



TESLA-FEL 2005-05

# Contributions to the FEL2005 conference

Compiled by O. Grimm

***fel2005***

**21-26 August 2005, Stanford University, Stanford**

<b>First Lasing at 32 nm of the VUV-FEL at DESY .....</b>	<b>1</b>
Siegfried Schreiber	
<b>Properties of the Radiation from VUV-FEL at DESY (Femtosecond Mode of Operation).....</b>	<b>8</b>
Evgeny Saldin, Evgeny Schneidmiller, Mikhail Yurkov	
<b>Accelerator Layout and Physics of X-Ray Free-Electron Lasers .....</b>	<b>12</b>
Winfried Decking	
<b>Bunch Compression Stability Dependence on RF Parameters .....</b>	<b>19</b>
Torsten Limberg, Martin Dohlus	
<b>Undulator Systems and Photon Diagnostic for the European XFEL Project .....</b>	<b>23</b>
Joachim Pflueger	
<b>Electron Beam Characterisation at PITZ and the VUV-FEL at DESY .....</b>	<b>28</b>
Katja Honkavaara, Florian Loehl, Martin Sachwitz, Elke Sombrowski, Dirk Noelle, Siegfried Schreiber, Luciano Catani, Alessandro Cianchi, Michele Castellano, Giampiero Di Pirro	
<b>High-Precision Optical Synchronization Systems for X-Ray Free Electron Lasers .....</b>	<b>35</b>
Axel Winter, Peter Schmüser, Holger Schlarb, Fatih Oemer Ilday, Jung-Won Kim, Jeff Chen, Franz Xaver Kaertner Jeff Chen, D. Cheever, T. Zwart, D. Wang	
<b>Optical Laser Synchronized to the DESY VUV-FEL for Two-Color Pump-Probe Experiments .....</b>	<b>41</b>
Ingo Will, Stefan Düsterer, Josef Feldhaus, Elke Plönjes, Harald Redlin	
<b>Properties of the Third Harmonic of the SASE FEL Radiation .....</b>	<b>45</b>
Evgeny Saldin, Evgeny Schneidmiller, Mikhail Yurkov	
<b>Detector Response and Beam Line Transmission Measurements with Far-Infrared Radiation .....</b>	<b>49</b>
Oliver Grimm, Hossein Delsim-Hashemi, Lars Fröhlich, Enrica Chiadroni	
<b>Upgrades of the Laser Beam-line at PITZ .....</b>	<b>53</b>
Juergen W. Baehr, Michael Hartrott, Dieter Richter, Hans-Juergen Grabosch, Jang Hui Han, Oleg kalekin, Sergiy Khodyachykh, Guido Klemz, Mikhail Krasilnikov, Shengguang Liu, Hartmut Luedecke, Velizar Miltchev, Anne Oppelt, Bagrat Petrosyan, Sabine Riemann, Lazar Staykov, Frank Stephan, Micheal Winde, Karen Abrahamyan, Galina Asova, Gancho Dimitrov, Vittorio Boccone, Ingo Will, Juliane Roensch	
<b>Bunch Length Measurements Using a Martin-Puplett Interferometer at the VUV-FEL.....</b>	<b>58</b>
Lars Fröhlich, Oliver Grimm	

<b>Next Generation Synchronization System for the VUV-FEL at DESY .....</b>	<b>62</b>
Holger Schlarb, Valeri Ayvazyan, Frank Ludwig, Dirk Noelle, Bernhard Schmidt, Stefan Simrock, Franz Xaver Kaertner, Axel Winter	
<b>Transverse Electron Beam Diagnostics at the VUV-FEL at DESY .....</b>	<b>66</b>
Katja Honkavaara, Florian Loehl, Martin Sachwitz, Elke Sombrowski, Dirk Noelle, Siegfried Schreiber, Luciano Catani, Alessandro Cianchi, Michele Castellano, Giampiero Di Pirro	
<b>The Infrared Undulator Project at the VUV-FEL .....</b>	<b>70</b>
Oliver Grimm, Josef Feldhaus, Jörg Rossbach, Evgeny Saldin, Evgeny Schneidmiller, Mikhail Yurkov	
<b>Misconceptions regarding Second Harmonic Generation in X-Ray Free-Electron Lasers .....</b>	<b>74</b>
Gianluca Geloni, Evgeny Saldin, Evgeny Schneidmiller, Mikhail Yurkov	
<b>Influence of an Energy Chirp on SASE FEL Operation .....</b>	<b>78</b>
Evgeny Saldin, Evgeny Schneidmiller, Mikhail Yurkov	
<b>Design Considerations for the 4GLS XUV-FEL .....</b>	<b>82</b>
Brian W.J. McNeil, Gordon Robb, James Jones, Michael W. Poole, Neil Thompson, Christopher Gerth	
<b>Broadband Single Shot Spectrometer .....</b>	<b>86</b>
Hossein Delsim-Hashemi, Oliver Grimm, Jörg Rossbach, Holger Schlarb, Bernhard Schmidt, Peter Schmüser, Alexander van der Meer	
<b>Commissioning of TTF2 Bunch Compressors for 20 fs SASE Source .....</b>	<b>90</b>
Yujong Kim, Klaus Floettmann, Siegfried Schreiber, Dongchul Son	
<b>Observation of Femtosecond Bunch Length Using a Transverse Deflecting Structure .....</b>	<b>94</b>
Markus Huening, Andy Bolzmann, Holger Schlarb, Josef Frisch, Douglas McCormick, Marc Ross, Tonee Smith, Jörg Rossbach	
<b>Measurement of Slice-Emittance using a Transverse Deflecting Structure .....</b>	<b>97</b>
Michael Roehrs, Andy Bolzmann, Markus Huening, Holger Schlarb, Katja Honkavaara	
<b>The Injector of the VUV-FEL at DESY .....</b>	<b>101</b>
Siegfried Schreiber	
<b>Spectral Decoding Electro-Optic Measurements for longitudinal bunch diagnostics at the DESY VUV-FEL.....</b>	<b>105</b>
Bernd Steffen, Sara Casalbuoni, Ernst-Axel Knabbe, Bernhard Schmidt, Peter Schmüser, Axel Winter	

<b>Longitudinal Phase Space Studies at PITZ.....</b>	<b>108</b>
Juliane Roensch, Jörg Rossbach, Michael Hartrott, Dirk Lipka, Karen Abrahamyan, Galina Asova, Juergen W. Baehr, Gancho Dimitrov, Hans-Juergen Grabosch, Jang Hui Han, Sergiy Khodyachykh, Mikhail Krasilnikov, Shengguang Liu, Velizar Miltchev, Anne Oppelt, Bagrat Petrosyan, Sabine Riemann, Lazar Staykov, Frank Stephan	
<b>Modelling the Transverse Phase Space and Core Emittance Studies at PITZ.....</b>	<b>112</b>
Velizar Miltchev	
<b>Measurements of Thermal Emittance for Cesium Telluride Photocathodes at PITZ.....</b>	<b>116</b>
Velizar Miltchev, Juergen W. Baehr, Hans-Juergen Grabosch, Jang Hui Han, Mikhail Krasilnikov, Anne Oppelt, Bagrat Petrosyan, Lazar Staykov, Frank Stephan, Michael Hartrott	
<b>Status and First Results from the Upgraded PITZ Facility .....</b>	<b>120</b>
Anne Oppelt, Karen Abrahamyan, Galina Asova, Juergen W. Baehr, Gancho Dimitrov, Ulrich Gensch, Hans-Juergen Grabosch, Jang Hui Han, Sergiy Khodyachykh, Mikhail Krasilnikov, Shengguang Liu, Velizar Miltchev, Bagrat Petrosyan, Sabine Riemann, Lazar Staykov, Frank Stephan, Michael Hartrott, Eberhard Jaeschke, Dieter Kraemer, Dirk Lipka, Frank Marhauser, Dieter Richter, Klaus Floettmann, Siegfried Schreiber, Vittorio Boccone, Luciano Catani, Enrica Chiadroni, Alessandro Cianchi, Paolo Michelato, Laura Monaco, Carlo Pagani, Daniele Sertore, David Alesini, Manuela Boscolo, Giampiero Di Pirro, Massimo Ferrario, Daniele Filippetto, Luigi Palumbo, Carlo Vicario, Ivan Tsakov, Terence Garvey, Wolfgang Sandner, Ingo Will, Valentin Paramonov, Wolfgang Ackermann, Wolfgang F.O. Müller, Sascha Schnepf, Thomas Weiland, Juliane Roensch	
<b>Commissioning of the SPARC Movable Emittance Meter and Its First Operation at PITZ ..</b>	<b>124</b>
Luciano Catani, Enrica Chiadroni, Alessandro Cianchi, Michael Hartrott, Mikhail Krasilnikov, Anne Oppelt, Frank Stephan, Michele Castellano, Giampiero Di Pirro, Daniele Filippetto, Carlo Vicario	

# FIRST LASING AT 32 NM OF THE VUV-FEL AT DESY

S. Schreiber\*, DESY, Hamburg, Germany  
for the VUV-FEL team†

## Abstract

The VUV-FEL is a free electron laser user facility being commissioned at DESY. It is based on the TTF-FEL, which was in operation until end of 2002 providing a photon beam for two pilot experiments in the wavelength range of 80 to 120 nm.

In its final configuration, the new VUV-FEL is designed to produce SASE FEL radiation with a wavelength down to 6 nm with high brilliance. The commissioning started in fall 2004, and in January 2005 succeeded in first lasing in the SASE mode at a wavelength of 32 nm with a radiation power close to saturation. This is a major milestone of the facility and of SASE FELs in general.

This contribution reports on the present electron linac driving the FEL, on properties of the electron beam and on the characterization of the FEL photon beam.

## INTRODUCTION

The VUV-FEL project at the TESLA Test Facility (TTF) at DESY [1] is the first user facility for VUV and soft X-ray coherent light experiments providing an impressive peak and average brilliance. The SASE process generates ultra-short coherent radiation pulses in the femtosecond range with peak powers in the GW level opening new fields of experiments in a broad range of scientific disciplines.

The VUV-FEL is also a pilot facility for the European XFEL project [2] and a test bed for further research and

development for linear collider related superconducting accelerator technologies.

It is based on the TTF-FEL [3, 4], which provided beam until end 2002 for user experiments in the wavelength range of 80 to 120 nm [5, 6]. In 2001, saturation has been achieved at a wavelength of 98.1 nm [7]. The experiments carried out lead to out-standing results in atomic cluster [8] and ablation experiments [9].

The TTF-FEL has been completely redesigned to meet the demands on beam energy and beam properties for lasing down to 6 nm. For the present start-up phase, emphasis is given on lasing around 30 nm with smaller wavelengths down to 12 nm being within the present energy reach. The start-up installation has been completed in 2004, and will be finalized in 2006 with an additional accelerating module to reach an electron beam energy of 1 GeV required for 6 nm operation.

After the commissioning runs in 2004 and early 2005, first lasing has been achieved at a wavelength of 32 nm in January 2005 [10]. Since then, the VUV-FEL has been optimized to serve the first user experiments which started in June 2005.

Figure 1 gives a schematic overview of the present configuration of the linac. Table 1 summarizes the present beam and FEL properties for the start-up lasing around 30 nm and the design goal for 6 nm. For a more detailed discussion of parameter choices refer to [1, 11].

In the following, main sections of the linac are described, starting from the injector down to the undulator and photon diagnostic section.

## THE LINAC

### Injector

Based on the experience with the TTF phase 1 injector [12], the injector has been redesigned to meet the tighter demands on the electron beam quality for the VUV-FEL [13]. The design follows the proposal for the XFEL [14]. The performance of the injector is crucial for the successful generation of FEL radiation. For this reason, a photoinjector test facility (PITZ) [15] has been set-up to optimize electron sources for FELs and other applications. The injector has been successfully commissioned in the first half of 2004.[16]

Some electron beam properties required are listed in Table 1. Most important is to generate a train of electron bunches with a charge of 1 nC each and a normalized transverse emittance of less than  $2 \mu\text{m}$ . The bunch train length

\* siegfried.schreiber@desy.de

† W. Achermann, V. Ayvazyan, N. Baboi, J. Bähr, V. Balandin, B. Beutner, A. Brandt, I. Bohnet, A. Bolzmann, R. Brinkmann, O.I. Brovko, J.P. Carneiro, S. Casalbuoni, M. Castellano, P. Castro, L. Catani, E. Chiodroni, S. Choroba, A. Cianchi, H. Delsim-Hashemi, G. Di Pirro, M. Dohlus, S. Düsterer, H.T. Edwards, B. Faatz, A.A. Fateev, J. Feldhaus, K. Flöttmann, J. Frisch, L. Fröhlich, T. Garvey, U. Gensch, N. Golubeva, H.-J. Grabosch, B. Grigoryan, O. Grimm, U. Hahn, J.H. Han, M. v. Hartrott, K. Honkavaara, M. Hüning, R. Ischebeck, E. Jaeschke, M. Jablonka, R. Kammering, V. Katalev, B. Keitel, S. Khodyachyhh, Y. Kim, V. Kocharyan, M. Körfer, M. Kollwe, D. Kostin, D. Krämer, M. Krassilnikov, G. Kube, L. Lilje, T. Limberg, D. Lipka, S. Liu, F. Löhler, M. Luong, C. Magne, J. Menzel, P. Michelato, V. Miltchev, M. Minty, W.D. Möller, L. Monaco, W. Müller, M. Nagl, O. Napoly, P. Nicolosi, D. Nölle, T. Nuñez, A. Oppelt, C. Pagani, R. Paparella, B. Petersen, B. Petrosyan, J. Pflüger, P. Piot, E. Plönjes, L. Poletto, D. Proch, D. Pugachov, K. Rehlich, D. Richter, S. Riemann, J. Rönsch, M. Ross, J. Rossbach, M. Sachwitz, E.L. Saldin, W. Sandner, H. Schlarb, B. Schmidt, M. Schmitz, P. Schmüser, J.R. Schneider, E.A. Schneidmiller, S. Schnepf, H.-J. Schreiber, S. Schreiber, D. Sertore, S. Setzer, A.V. Shabunov, S. Simrock, E. Sombrowski, L. Staykov, B. Stefan, F. Stephan, F. Stulle, K.P. Sytchev, H. Thom, K. Tiedtke, M. Tischer, R. Treusch, D. Trines, I. Tsakov, A. Vardanyan, R. Wanzenberg, T. Weiland, H. Weise, M. Wendt, I. Will, A. Winter, K. Wittenburg, M.V. Yurkov, I. Zagorodnov, P. Zambolin, K. Zapfe

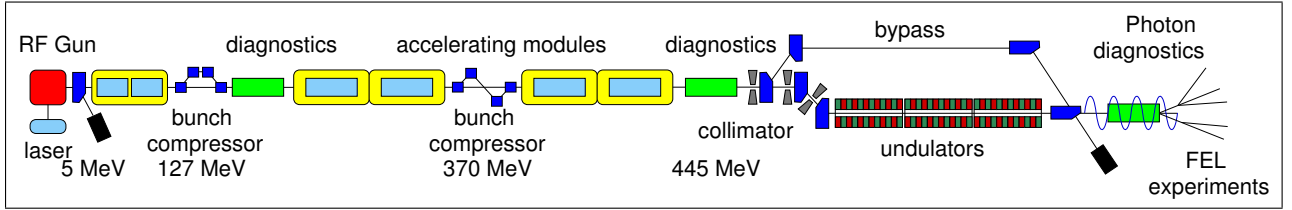


Figure 1: Schematic overview of the VUV-FEL linac (not to scale). Beam direction is from left to right, the total length is about 250 m.

Table 1: Present parameters of the VUV-FEL (start-up). For comparison, the design parameters for the femtosecond mode of operation for 30 nm are shown as well (from [11]). (The peak brilliance, peak power, and peak photon flux are calculated from the average achieved photon pulse energy, where the data are most complete.)

		start-up	design
<b>Electron beam</b>			
Energy	MeV	445	450
Peak current	kA	2.0	1.3-2.2
Emittance, norm. (x,y)	$\mu\text{m rad}$	2-4	1.5-3.5
Nb. of bunches/train		30	7200
bunch train length	ms	0.03	0.8
Rep. rate	Hz	2	10
$\Delta E/E$ (rms)	%	0.1	0.1
<b>Undulator</b>			
Period	cm	2.73	
Gap	mm	12	
Peak magnetic Field	T	0.48	
K		1.23	
total length	m	27.3	
<b>FEL radiation</b>			
Wavelength	nm	32	30
Max. pulse energy	$\mu\text{J}$	40	50-150
Average pulse energy	$\mu\text{J}$	16	
spot size (fwhm)	$\mu\text{m}$	$\approx 150$	180-270
divergence (fwhm)	$\mu\text{rad}$	160	140-160
Bandwidth (fwhm)	%	0.8	0.8
Pulse duration (fwhm)	fs	25	15-50
Peak Power	GW	0.6	2-4
Peak photon flux	ph/s	$1 \cdot 10^{26}$	$3\text{-}6 \cdot 10^{26}$
Peak spectral Brilliance	*	$\approx 10^{28}$	$\approx 10^{29}$

\* photons/s/mrad<sup>2</sup>/mm<sup>2</sup>/(0.1% bw)

of 800  $\mu\text{m}$  and the repetition rate of up to 10 Hz are adapted to the superconducting TESLA accelerating structures.

A normal conducting laser-driven photocathode RF gun provides a rapid acceleration from the cathode and allows to generate a low emittance beam from the source.

The RF gun and an upgraded laser system have been successfully tested and optimized at PITZ [15] and installed at the VUV-FEL in January 2004. It is a 1.5 cell L-band cav-

ity (1.3 GHz,  $\text{TM}_{010}$  mode) powered by a 5 MW klystron. A longitudinal coupler is used to keep the cylindrical symmetry around the beam axis as perfect as possible. The RF gun is operated with an RF power of 3 MW (41 MV/m on the cathode) and an RF pulse length of up to 0.9 ns. A low level RF system based on digital signal processors reads the forward and reflected power from the gun and regulates the RF power and RF phase in the gun by acting on the low level RF input to the klystron with a vector modulator. The phase stability achieved is below  $0.5^\circ$ , the amplitude stability within 0.1 %.

A  $\text{Cs}_2\text{Te}$  photocathode is inserted into the RF gun back-plane via a load-lock system and can be changed if required. The cathode quantum efficiency achieved (for UV light) is initially high (more than 5 %) and drops to a level of 1 % after months of usage.

The laser is based on a pulsed mode-locked pulse train oscillator synchronized to the 1.3 GHz RF of the accelerator. The phase stability is better than 0.5 ps. A chain of linear Nd:YLF amplifiers provides the laser pulse energy to convert the initial infrared wavelength into UV (262 nm) with a single pulse energy of about  $1 \mu\text{J}$  required for a charge of a few nC on  $\text{Cs}_2\text{Te}$ . The system produces pulse trains with up to 800  $\mu\text{s}$  length at a repetition rate of up to 10 Hz. The pulse spacing is usually 1  $\mu\text{s}$  (1 MHz), a 9 MHz mode is in preparation. The charge fluctuation of a single electron bunch from shot to shot is better than 2 % rms, if averaged over a train better than 1 %. The pulses length in the UV measured with a streak camera is  $\sigma_1 = 4.4 \pm 0.1$  ps.

A complete TESLA module with eight accelerating structures boosts the beam energy to 127 MeV before the first bunch compressor. With the digital feedback system regulating the phase and amplitude of the accelerating structures, the energy stability  $\delta E/E$  is better than  $8.5 \cdot 10^{-4}$  rms. The uncorrelated energy spread has been estimated to be smaller than 25 keV, probably limited by the resolution of the present imaging system.

The uncompressed rms bunch length has been measured with a streak camera to be  $1.7 \pm 0.2$  mm as expected.

A small transverse emittance below  $2 \mu\text{m}$  normalized is achieved by two measures. A solenoid (0.163 T) compensates the emittance growth induced by space charge in the drift after the gun. The beam is then matched into the acceleration section [17] which is operated with a moderate gradient of 12 MV/m in the first four cavities.

## Bunch compressors

The peak current of the uncompressed bunch is about 70 A. In order to achieve a peak current exceeding 1 kA, a compression of the bunch using magnetic chicanes is done in two steps at energies of 127 MeV and 370 MeV. Care is taken to avoid an unacceptable emittance growth due to space charge, wakefield, and coherent synchrotron radiation effects.[18, 11]

The rms bunch length in the first accelerating section before compression is long compared to the RF wavelength (about 2 mm or  $3^\circ$  in RF). The beam is accelerated about  $10^\circ$  off-crest in order to impose an energy chirp along the bunch for compression. Due to the length of the bunch and the sinusoidal RF field, a curvature in the energy-phase plane develops. To remove this curvature, it is planned to install a superconducting third harmonic cavity (3.9 GHz) [19] before the first bunch compressor. This cavity is not available for the initial run this year.

However, the compression with the imposed curvature leads to a bunch with a sharp high current spike and a long tail. Moreover, varying the compression ratio in the two bunch compressors, a tailoring of the spike shape is to some extent possible. This effect has already been experimentally verified at TTF phase 1 [20] and successfully used for SASE operation [6, 21].

Therefore, we follow – until the third harmonic cavity is installed – the TTF phase 1 femtosecond mode of operation [11].

## Undulator

Single pass high gain FELs require long undulator systems. The VUV-FEL undulator system consists of six modules with a length of 4.5 m each [22]. The fixed gap is 12 mm with a peak magnetic field of 0.48 T ( $K=1.23$ ) realized with permanent NdFeB magnets. The undulator period is 27.3 mm. In contrast to TTF phase 1, the undulators have no internal focusing. A pair of electromagnetic quadrupoles between each of the six modules provides a large acceptance in beam energy. In terms of FEL radiation it covers the wavelength range of 120 to 6 nm. Each quadrupole doublet is aligned on a stable granite base plate together with beam position monitors and a vertical and horizontal wirescanner. The absolute alignment in respect to the undulator axis is better than  $100 \mu\text{m}$ . The SASE process requires an alignment of the electron beam with the undulator axis of better than  $20 \mu\text{m}$ . Therefore, the quadrupoles are equipped with movers allowing a fine adjustment of their position.

A collimation section [23] protects the undulators from radiation due to off-energy and off-orbit particles. The design includes two copper collimators in the straight and two in a dogleg section allowing to collimate off energy particles as well. The energy acceptance is  $\pm 3\%$ .

## Diagnostics

The linac includes a large variety of diagnostic tools to measure the transverse and longitudinal beam properties, beam positions, current etc.

Remarkable results have been achieved in the measurements of the transverse projected emittance and the longitudinal bunch structure.

The transverse beam size is measured using optical transition radiators (OTR). Twenty-four stations with movable radiators are installed, equipped with a high resolution imaging system each [24].

An impressively small transverse emittance for the uncompressed beam is measured in the injector at 127 MeV. The normalized projected rms emittance for a 1 nC bunch is  $\epsilon_n=1.4 \mu\text{m}$  [25]. For this analysis, 90 % of the bunch intensity is used, the statistical error is 4 %, the systematic error estimated with 6 % [26].

A powerful method to measure the bunch length is a deflecting cavity integrated into the linac. At 445 MeV just before the collimation section, an S-band deflecting cavity [27] (length 3.66 m) in combination with an OTR beam size monitor is installed. The resolution of the system is smaller than  $15 \mu\text{m}$ . First measurements of the longitudinal bunch structure reveals a sharp spike with a length of  $36 \mu\text{m}$  or 120 fs (fwhm) and a long tail of 2 ps. The longitudinal structure varies from run to run depending on the specific tuning of the machine. Please refer to [28] for details.

## Photon diagnostics

Another important diagnostic section is located in the FEL beam line to measure the properties of the FEL radiation. An overview of the various tools is given in [29].

An important instrument for tuning the onset of laser amplification and optimizing the lasing is a detector based on gold wires and a micro-channel plate (MCP) [30]. The dynamic range of this detector is sufficient to cover several orders of magnitude of radiation energy, from spontaneous (7 nJ for 1 nC) to the amplified emission (50 to  $100 \mu\text{J}$ ). The detector has been carefully calibrated, its relative accuracy is in the order of 1 %. The radiation energy has been cross-calibrated with the gas monitor detector which has an absolute measurement uncertainty of 25 %. After calibration, the energies measured with both methods agree within 5 %.

View screens using Ce:YAG crystals are placed at various locations. A monochromator is used to measure single shot spectra. It is equipped with an intensified CCD camera and has a resolution of 0.02 nm with an absolute calibration error of less than 0.03 nm [31].

## Experimental Hall

The FEL experimental hall is presently equipped with three experimental stations. Two more will follow in the

near future. A variety of experiments in basic and applied research of multiple scientific fields, from life science, chemistry to physics are scheduled including pump-probe experiments. Three experiments already started to take data; their results will be published elsewhere.

## OPERATION AT A WAVELENGTH OF 32 NM

In January 2005, lasing at 32 nm has been observed for the first time. Figure 2 shows the image of a single VUV-FEL pulse on a Ce:YAG crystal. The pattern of the gold mesh in front of the crystal is clearly visible. From the distance between the grid wires a size of 3 mm (fwhm) is measured yielding an angular divergence of  $160 \mu\text{rad}$  (fwhm). The spot size at the undulator exit is estimated to be about  $150 \mu\text{m}$  (fwhm).

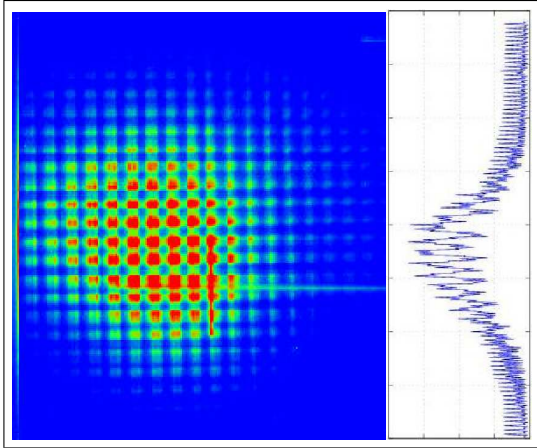


Figure 2: Image of a the FEL beam on a Ce:YAG crystal (single shot) and its projection.[10] The gold mesh of the radiation detector in front of the screen is visible and allows to estimate the width of the beam to 3 mm (fwhm) at 18.5 m distance from the undulator (wire distance 0.31 mm). This results in an angular divergence of  $160 \mu\text{rad}$  (fwhm).

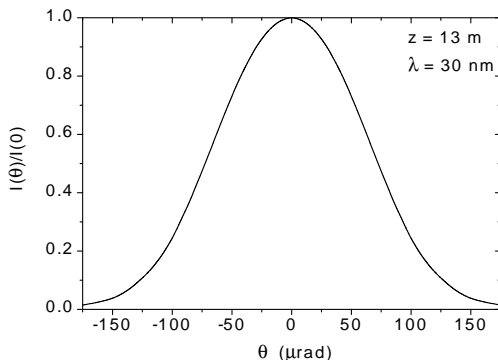


Figure 3: Simulated intensity distribution of the FEL radiation in the far zone.[11] The angular divergence is  $150 \mu\text{rad}$  (fwhm) in good agreement with the measurement.

The measured angular divergence fits well to the estimate from simulation (Fig. 3). We conclude, that the beam is close to the diffraction limit and thus has a high degree of transverse coherence. First measurements of the coherence with a slit system confirm this.

## Energy in the radiation pulse

The energy of the SASE FEL radiation pulses fluctuates due to the statistical nature of the SASE process starting from noise. When the fluctuations caused by machine induced instabilities of the beam are small, we can measure this fluctuation. Figure 4 shows the measured energy of the FEL radiation during a certain time period together with a histogram of the same data yielding a probability distribution  $p(E)$  of the energy  $E$ . From theoretical considerations of the SASE process [32], the probability follows the distribution  $p(E) = M^M / \Gamma(M) E^{M-1} e^{-ME}$  with the gamma function  $\Gamma(M)$ ,  $E$  is the energy normalized to its average. The parameter  $M = 1/\sigma_E^2$  is interpreted as the number of modes in a radiation pulse. In the case shown, the measured rms width  $\sigma_E$  of the distribution is 49.6% (normalized to the average energy) yielding the estimate of the number of lasing modes  $M = 4.1$ . The measured distribution follows the expectation of a high-gain FEL operating in the exponential regime.

In the example shown in Fig. 4, the average energy was  $1 \mu\text{J}$ . This is well within the exponential regime of the FEL, where the Gamma-distribution defined above should apply. After tuning the VUV-FEL, an average energy of  $16 \mu\text{J}$  with a peak energy of  $40 \mu\text{J}$  has been reached in June 2005. At the same time, the width of the energy distribution is getting smaller, indicating the approach of saturation.

## Radiation Spectra

From the statistical analysis of the energy fluctuation, we cannot distinguish between transverse and longitudinal modes. Given the high degree of transverse coherence supported by the measurement of the angular divergence, we estimate, that about 2 or more modes should show up as spikes in the frequency domain. Figure 5 shows examples of measured single shot spectra supporting this assumption. The data agree well with simulations of the FEL process in the exponential regime (Fig. 6).

The duration of one longitudinal spike  $\tau_{\text{rad}}$  itself is too short to be measured directly. However, it can be estimated from the width of the single shot spectra using the relation  $\tau_{\text{rad}} = 2\pi/\delta\omega$ . The fwhm width of the spectra is typically 0.25 nm (or 0.8% at 32 nm). This leads to a spike duration of  $\tau_{\text{rad}} = 14 \text{ fs}$ . With the presence of several modes, the total length of the radiation pulse is roughly speaking increased by the number of modes. The results agree well with simulations of the process. Including the presence of more than one longitudinal modes, the total pulse length is estimated with 25 fs. Averaging several single shot spectra yield a center wavelength of 31.8 nm and a width of 0.275 nm.

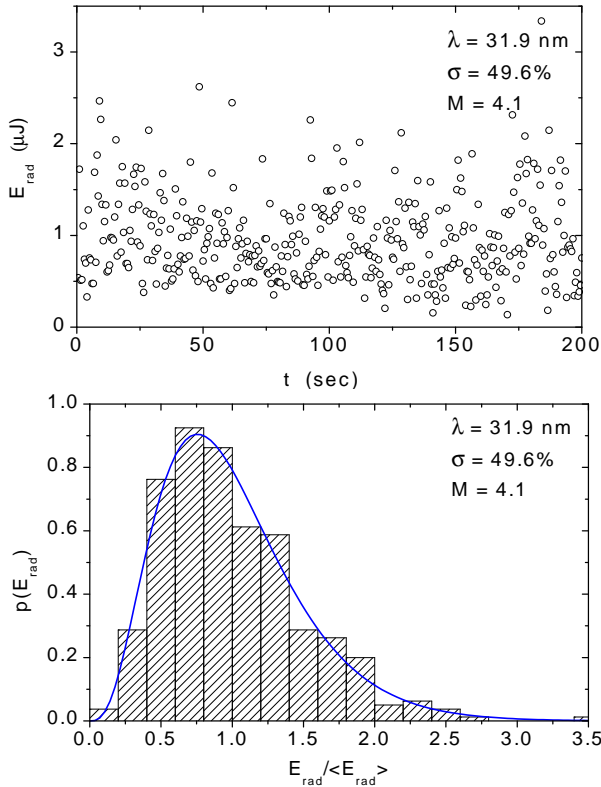


Figure 4: Example of the measured energy in the FEL radiation pulses for a certain period of time (top). The same data normalized to the average energy are shown as a histogram giving the probability distribution (bottom).[10] The rms energy fluctuation  $\sigma$  of 49.6% gives the number of lasing modes  $M$  of 4.1, which determines the Gamma-distribution drawn as a solid line. (The data bins are scaled such that the area is equal to the integrated Gamma-distribution.)

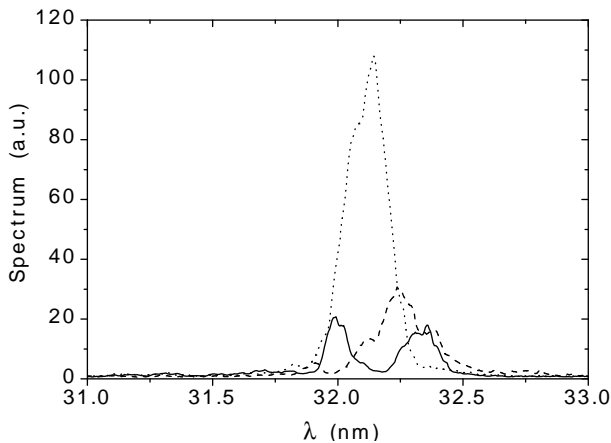


Figure 5: Example of three measured single shot spectra with different line shapes.[10] The center wavelength is 32 nm, the spectral width typically 0.25 nm.

With an average measured energy of  $16 \mu\text{J}$ , this corresponds to 0.6 GW average power. The maximum energy

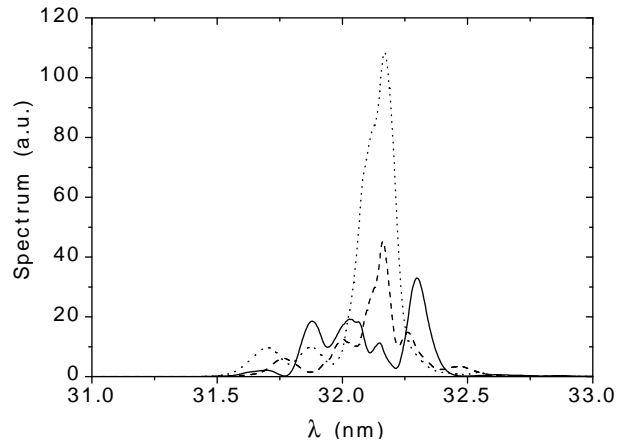


Figure 6: Simulation of the spectra operating in the exponential regime.[11] They are in good agreement with the measurements.

of  $40 \mu\text{J}$  measured so far would lead to a peak power of 1.6 GW. However, the analysis of the spectra for this case indicate a larger total length by a factor of 2 reducing the peak power to 0.8 GW. The numbers are summarized in Table 1.

A figure of merit for many experiments is the brilliance, the spectral photon flux per area and solid angle. With the data given in Table 1, the peak brilliance at the exit of the undulator amounts to  $B = 2.7 \cdot 10^{28}$  photons/s/mrad<sup>2</sup>/mm<sup>2</sup>/(0.1% bw) with a large uncertainty due to the rough estimate of the spot size at the undulator. This is several orders of magnitude above the state-of-the-art synchrotron radiation sources.

Assuming fully coherent radiation, the product of the radiation beam area and the solid angle is given by  $(\lambda/2)^2$ . Using  $B_c = \text{spectral photon flux} / (\lambda/2)^2$  we get  $B_c = 4.6 \cdot 10^{28}$  photons/s/mrad<sup>2</sup>/mm<sup>2</sup>/(0.1% bw). This is only by a factor of 2 larger than the calculated brilliance from the measured angle and estimated spot size. This indicates a good coherence and the presence of more than one transverse modes, in agreement with the statistical analysis discussed above.

The SASE process also generates higher harmonics radiation. In June 2005, the second and third harmonics have been measured for the first time. Figure 7 shows their averaged spectra. The center wavelengths are 15.86 nm and 10.53 nm respectively, the spectral width is 1.1% (fwhm) in both cases. The monochromator has been calibrated for wavelengths down to 20 nm, the calibration for smaller wavelengths has been extrapolated from this. Therefore, the absolute wavelength is preliminary.

## SUMMARY AND OUTLOOK

The VUV-FEL at DESY started to produce laser-like radiation with a wavelength of 32 nm and a peak brilliance orders of magnitude above the state-of-the-art synchrotron radiation sources. Moreover, the radiation pulses exhibit

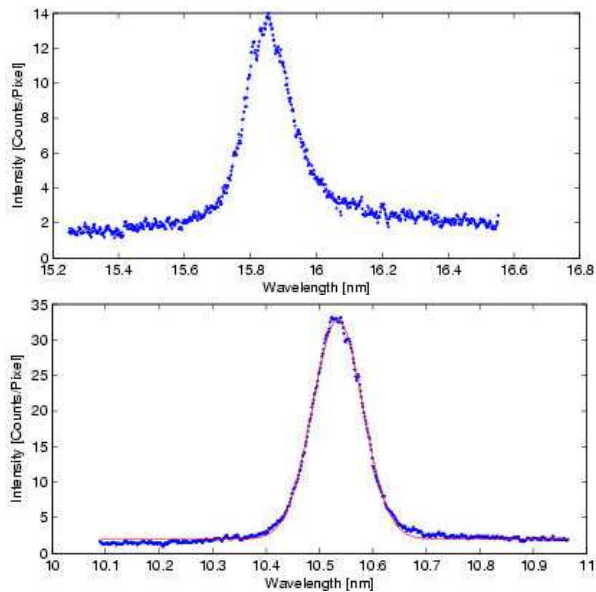


Figure 7: Measured average spectra of the second (top) and third (bottom) harmonic of 32 nm. The center wavelengths are 15.86 nm and 10.53 nm respectively.

spikes with a width in the 10 fs range opening a new window of research.

The facility includes five beamlines for experiments. Three beamlines have been commissioned so far, experiments started to take data. The other beamlines will be commissioned soon. For this year, several experiments are scheduled, including pump-probe experiments.

Later in 2006, an additional accelerating module will be installed which enables beam energies up to 1 GeV opening the window to wavelength down to 6 nm. The injector will be upgraded with a third harmonic superconducting cavity to improve the longitudinal structure of the beam. Additional equipment and undulators will be added for a seedings scheme to provide fully coherent radiation.

## ACKNOWLEDGMENT

On behalf of the VUV-FEL group, I would like to thank all colleagues from DESY and the collaborating institutes for their enthusiastic commitment in the construction and installation of the VUV-FEL. I would also like to thank the TTF operators who carried out their difficult tasks with great dedication.

## REFERENCES

- [1] "SASE FEL at the TESLA Facility, Phase 2," DESY-TESLA-FEL-2002-01
- [2] R. Brinkmann *et al.*, "TESLA XFEL: First stage of the X-ray laser laboratory. Technical design report, supplement," DESY-02-167
- [3] "A VUV Free Electron Laser at the TESLA Test Facility at DESY," DESY Print TESLA-FEL 95-03
- [4] J. Rossbach, "A VUV Free Electron Laser at the TESLA Test Facility at DESY," Nucl. Instrum. Meth. A **375** (1996) 269.
- [5] J. Andruszkow *et al.* [TESLA Collaboration], "First observation of self-amplified spontaneous emission in a free-electron laser at 109-nm wavelength," Phys. Rev. Lett. **85**, 3825 (2000) [arXiv:physics/0006010].
- [6] V. Ayvazian *et al.*, "Generation of GW radiation pulses from a VUV free-electron laser operating in the femtosecond regime," Phys. Rev. Lett. **88** (2002) 104802.
- [7] V. Ayvazian *et al.*, "A new powerful source for coherent VUV radiation: Demonstration of exponential growth and saturation at the TTF free-electron laser," Eur. Phys. J. D **20** (2002) 149.
- [8] H. Wabnitz *et al.*, "Multiple ionization of atom clusters by intense soft X-rays from a free-electron laser," Nature **420** (2002) 482.
- [9] J. Krzywinski *et al.*, "Interaction of intense ultrashort XUV pulses with different solids: Results from the Tesla Test Facility FEL phase I," Proc. FEL 2004, Trieste, Italy, 29 Aug - 3 Sep 2004
- [10] V. Ayvazian *et al.*, "First operation of a Free-Electron Laser generating GW power radiation at 32 nm wavelength", submitted to Eur. Phys. J. D.
- [11] E. L. Saldin, E. A. Schneidmiller and M. V. Yurkov, "Expected properties of the radiation from VUV-FEL at DESY (femtosecond mode of operation)," DESY-TESLA-FEL-2004-06
- [12] S. Schreiber *et al.*, "Performance of the TTF Photoinjector for FEL Operation", Proc. of the workshop "The physics and applications of high brightness electron beams", Chia Laguna, Sardinia, July 1-6, 2002, World Scientific, ISBN 981-238-726-9.
- [13] K. Flöttmann and P. Piot, "An upgraded injector for the TTF FEL-user facility," Proc. EPAC 2002, Paris, France, 3-7 Jun 2002
- [14] K. Flöttmann, P. Piot, M. Ferrario and B. Grigorian, "The TESLA X-FEL injector," DESY-M-01-06O, Proc. PAC 2001, Chicago, Illinois, 18-22 Jun 2001
- [15] M. Krasilnikov *et al.*, "Optimizing the PITZ electron source for the VUV-FEL," DESY-M-04-03U, Proc. EPAC 2004, Lucerne, Switzerland, 5-9 Jul 2004
- [16] S. Schreiber, "Commissioning of the VUV-FEL injector at TTF," EPAC-2004-MOPKF022, Proc. EPAC 2004, Lucerne, Switzerland, 5-9 Jul 2004
- [17] Y. Kim *et al.*, "First Experimental Demonstration of Ferrario's Matching Principle in TTF2 Booster Linac," these proceedings, THPP037.
- [18] T. Limberg, P. Piot and F. Stulle, "Design and performance simulation of the TTF-FEL II bunch compression system," Proc. EPAC2002, Paris, France, 3-7 Jun 2002
- [19] J. Sekutowicz, R. Wanzenberg, W. O. Müller and T. Weiland, "A design of a 3rd harmonic cavity for the TTF2 photoinjector," DESY-TESLA-FEL-2002-05
- [20] K. Honkavaara, S. Schreiber, C. Gerth and P. Piot, "Electron bunch shape measurements at the TTF-FEL," DESY-M-03-01L, Proc. PAC 2003, Portland, Oregon, 12-16 May 2003

- [21] V. Ayvazian *et al.*, “Study of the statistical properties of the radiation from a VUV SASE FEL operating in the femtosecond regime,” *Nucl. Instrum. Meth. A* **507** (2003) 368.
- [22] J. Pflüger, U. Hahn, B. Faatz and M. Tischer, “Undulator system for the VUV-FEL at the TESLA Test Facility phase-2,” *Nucl. Instrum. Meth. A* **507** (2003) 228.
- [23] V. Balandin, N. Golubeva and M. Körfer, “Studies of the collimation system for the TTF FEL at DESY,” *Nucl. Instrum. Meth. A* **483** (2002) 340.
- [24] A. Cianchi, L. Catani, E. Chiadroni, M. Raparelli, M. Castellano, G. Di Pirro and K. Honkavaara, “Commissioning of the OTR beam profile monitor system at the TTF/VUV-FEL injector,” EPAC-2004-THPLT058, *Proc. EPAC 2004, Lucerne, Switzerland, 5-9 Jul 2004*
- [25] K. Honkavaara *et al.*, “Electron Beam Characterization at PITZ and the VUV-FEL at DESY,” these proceedings, WEOB001.
- [26] K. Honkavaara *et al.*, “Transverse Electron Beam Diagnostics at the VUV-FEL at DESY”, these proceedings, MOPP038.
- [27] The deflecting cavity project is a cooperation between SLAC and DESY.
- [28] M. Hüning *et al.*, “Observation of Femtosecond Bunch Length Using a Transverse Deflecting Structure”, these proceedings, THPP035.
- [29] C. Gerth, B. Faatz, T. Lokajczyk, R. Treusch and J. Feldhaus, “Photon diagnostics for the study of electron beam properties of a VUV SASE-FEL,” *Nucl. Instrum. Meth. A* **475** (2001) 481.
- [30] A. Bytchkov *et al.*, “Development of MCP-based photon diagnostics at the TESLA Test Facility at DESY”, *Nucl. Instrum. Meth. A* **528** (2004) 254.
- [31] P. Nicolosi *et al.*, “On-line spectral monitoring of the VUV FEL beam at DESY,” *Proc. FEL 2004, Trieste, Italy, 29 Aug - 3 Sep 2004*
- [32] E. L. Saldin, E. A. Schneidmiller and M. V. Yurkov, “Statistical Properties of Radiation from VUV and X-ray Free Electron Lasers”, *Opt. Commun.* **148** (1998) 383.

# Properties of the radiation from VUV-FEL at DESY (femtosecond mode of operation)

E.L. Saldin, E.A. Schneidmiller, and M.V. Yurkov  
Deutsches Elektronen-Synchrotron (DESY), Hamburg, Germany

## Abstract

Present bunch compression scheme at the VUV FEL is essentially nonlinear and naturally results in a formation of a short high-current leading peak (spike) in the density distribution that produces FEL radiation. The main feature of the considered mode of operation is the production of short, down to 20 fs radiation pulses with GW-level peak power and contrast of 80%.

## INTRODUCTION

The project of the VUV FEL at DESY is realized in two phases. Phase I (1999-2002) served for a proof-of-principle of SASE FEL operation and for system tests of the hardware. Phase II of the VUV FEL has been built as an extension of Phase I to shorter wavelengths (down to 6 nm) and will be used as the first VUV FEL user facility starting in spring, 2005. VUV FEL Phase I demonstrated unique femtosecond mode of operation which was not considered at an early design stage of the project [1, 2]. Thorough analysis has shown that due to nonlinear compression and small local energy spread the short high-current (3 kA) leading peak (spike) in the bunch density distribution was produced by beam formation system. Despite strong collective effects (of which the most critical was the longitudinal space charge after compression) this spike was bright enough to drive FEL process up to the saturation for the wavelengths around 100 nm [3]. In addition to the possibility for production of high-power femtosecond pulses this mode of FEL operation demonstrated high stability with respect to drifts of machine parameters. Successful operation of the VUV FEL Phase I in the femtosecond regime encouraged us to extend such a mode of operation for shorter wavelengths. Relevant theoretical study has been performed in [5]. It has been found that the beam formation system of the linac can be tuned for production of bunches with a high-peak-current spike capable for effective driving of the FEL process such that the VUV FEL can safely saturate even at the shortest design wavelength of 6 nm with a GW level of the peak power in short pulses of 15-50 fs duration.

Optimum parameters determined in [5] have been chosen for the commissioning of the VUV FEL. First experimental results obtained at the VUV FEL operating at the radiation wavelength around 30 nm did show perfect agreement with predictions [6]. Commissioning of the VUV FEL proceeded in parallel with first user experiments. Our

contacts with user community did show that planning of future user experiments at the VUV FEL requires more detailed knowledge of the expected statistical properties of the source, and present paper covers this gap.

## RADIATION PROPERTIES

Operation of the bunch formation system has been studied in details in [5]. We considered two possible options of operation with a nominal charge of 0.5 nC, and with higher charge, 1 nC (see Fig. 1). Both options can be realized experimentally and provide different modes of the VUV FEL operation in terms of output characteristics of the radiation. Complete set of the electron beam properties at the undulator entrance can be found in [5].

Some output characteristics of VUV FEL (energy in the radiation pulse, angular divergence, etc) have been described in our previous paper [5]. Here we present more detailed features of the radiation related to ultra-short pulse duration. To extract more detailed information about photon beam properties, we performed 500 statistically independent runs with FEL code FAST [7]. Figure 2 shows mean energy in the radiation pulse and rms fluctuations as functions of position along the undulator. One can see that for both charges (0.5 and 1 nC) saturation is expected in the middle of the undulator for the wavelength of 30 nm.

Expected level of the output energy at saturation is approximately the same, of about 100  $\mu$ J, while the saturation length is shorter for the case of 0.5 nC. More pronounced

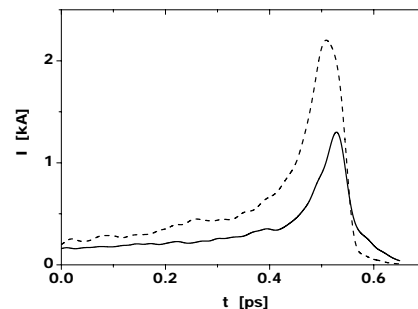


Figure 1: Current along the electron bunch. Solid and dashed line correspond to bunch charge 0.5 and 1 nC, respectively. Bunch head is on the right side

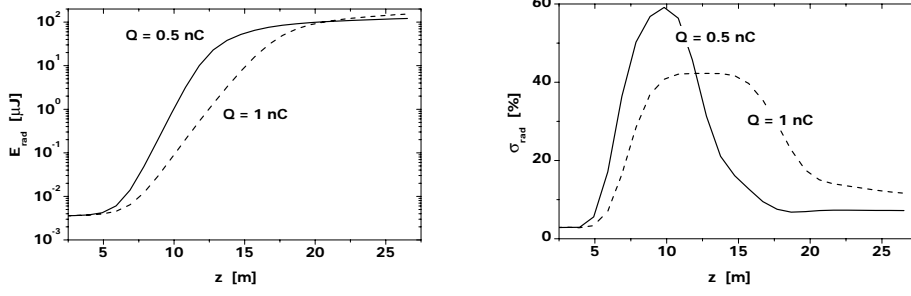


Figure 2: Expected performance of the VUV FEL at the radiation wavelength 30 nm. Left: energy in the radiation pulse versus undulator length. right: fluctuations of the energy in the radiation pulse versus undulator length. Solid and dashed lines refer to bunch charge 0.5 nC and 1 nC, respectively

difference is in the behavior of the fluctuations of the radiation energy. Larger level of fluctuations in the linear regime indicates that the radiation pulse length should be shorter for the case of 0.5 nC. Numerical analysis shows that in the linear regime the VUV FEL driven by 0.5 nC electron bunches reproduces twice shorter, down to 20 fs (FWHM) radiation pulses (see Fig. 3). The reason for this is that 0.5 nC bunch has more narrow lasing part. Group velocity of the radiation in the high gain FEL regime is much less than kinematic slippage which prevents lengthening of the radiation pulse [8]. Figure 4 shows time structure of

radiation pulses at saturation. We find that at saturation the 0.5 nC case has no benefit in terms of pulse duration. Radiation pulse lengthening occurs mainly due to two effects. First, there is no suppression of the group velocity in the nonlinear regime. Second, tail of the electron bunch starts to produce visible amount of radiation. Using plots in Fig. 5 one can trace evolution of the radiation pulse envelope from linear regime to the saturation. Figure 6 shows evolution of the FWHM pulse length along the undulator.

For time-resolved experiments it is important to know the degree of contrast of the radiation pulse, i.e. ratio of the

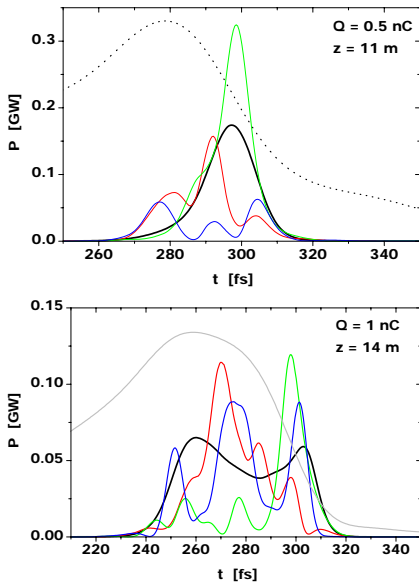


Figure 3: Radiation power along the bunch for the VUV FEL operating in the linear regime. Top: bunch charge 0.5 nC,  $z = 11 \text{ m}$ . Bottom: bunch charge 1 nC,  $z = 14 \text{ m}$ . Thin curves show single shots. Bold curves show averaged profiles. Grey curves show profile of electron bunch.

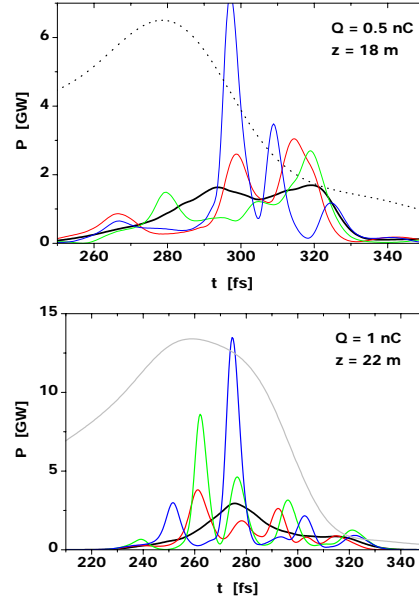


Figure 4: Radiation power along the bunch for the VUV FEL operating in the saturation regime. Top: bunch charge 0.5 nC,  $z = 18 \text{ m}$ . Bottom: bunch charge 1 nC,  $z = 22 \text{ m}$ . Thin curves show single shots. Bold curves show averaged profiles. Grey curves show profile of electron bunch.

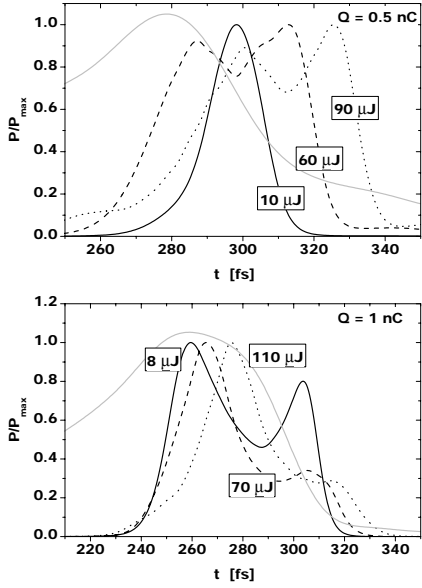


Figure 5: Evolution of the radiation pulse shape versus average energy in the radiation pulse. Grey line shows electron bunch profile. Top: bunch charge is 0.5 nC. Bottom: bunch charge is 1 nC

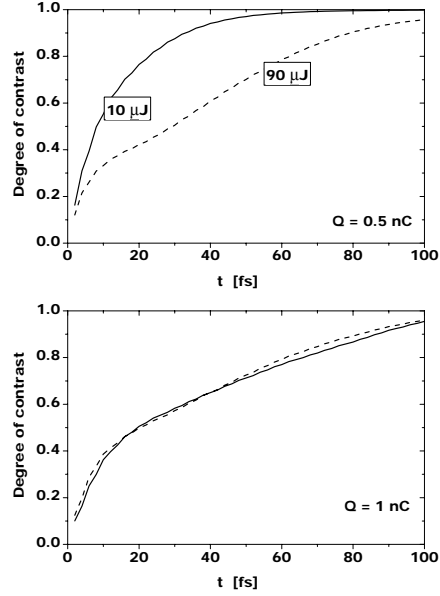


Figure 7: Degree of contrast versus time gate around a spike with maximum intensity. Top: bunch charge is 0.5 nC. Bottom: bunch charge is 1 nC. Solid and dashed line corresponds to the case of the linear regime and saturation, respectively

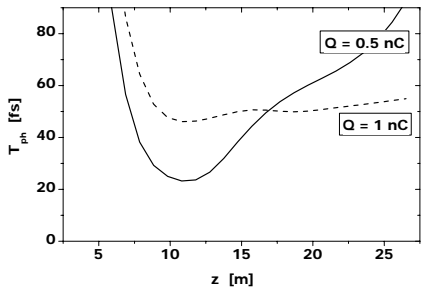


Figure 6: Evolution of the FWHM radiation pulse length along undulator. Solid and dashed line correspond to the charge of 0.5 and 1 nC, respectively

radiation energy within a time window around a spike with maximum peak power to the total energy in the radiation pulse. Relevant function is plotted in Fig. 7.

The radiation from SASE FEL operating in the linear regime possesses properties of completely chaotic polarized light [8, 9]. This means that probability distribution of the energy in the radiation pulse follows gamma-distribution.

$$p(E) = \frac{M^M}{\Gamma(M)} \left( \frac{E}{\langle E \rangle} \right)^{M-1} \frac{1}{\langle E \rangle} \exp \left( -M \frac{E}{\langle E \rangle} \right),$$

where  $\Gamma(M)$  is the gamma function,  $M = 1/\sigma_E^2$ , and  $\sigma_E^2 = \langle (E - \langle E \rangle)^2 \rangle / \langle E \rangle^2$ . The number of mode,  $M$ ,

reaches its minimum value in the end of the linear regime (see Fig. 2). Simulations show that statistics of the radiation change drastically near the saturation point on a scale of one field gain length. Such a fast drop of fluctuations is the feature of ultra-short pulse duration [10]. Nature of this phenomenon can be understood by analyzing structure of the radiation pulse (see Fig. 4). amplification process enters nonlinear stage, radiation power is saturated, and pulses sleep forward. Further growth of the total energy occurs due to the radiation of bunched electron beam. Since maximal bunching of the electron beam is limited to the unity, this additional radiation is well stabilized, leading to the overall stability of the total energy in the radiation pulse.

Radiation spectra for VUV FEL operating in the linear regime and saturation are shown in Fig. 8 and 9. One can obtain that spectrum bandwidth for 1 nC case is visibly wider. This is a consequence of larger energy chirp along the lasing part of the electron bunch which appears due to more stronger space charge effects.

Another subject is statistics of SASE FEL radiation filtered through narrow-band monochromator. In the linear stage of SASE FEL operation the value of normalized energy deviation is equal to unity, and energy fluctuates in accordance with negative exponential distribution. This is consequence of the fact that in this case radiation is gaussian random process. However, in the nonlinear mode of operation we obtain significant decrease of fluctuations when the pulse length goes down (see Fig. 10). This effect

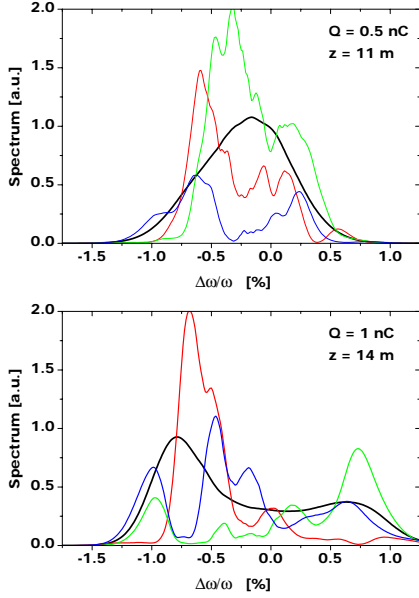


Figure 8: Radiation spectrum of the VUV FEL operating in the linear regime. Top: bunch charge 0.5 nC,  $z = 11$  m. Bottom: bunch charge 1 nC,  $z = 14$  m. Thin curves show single shots. Bold curves show averaged profiles

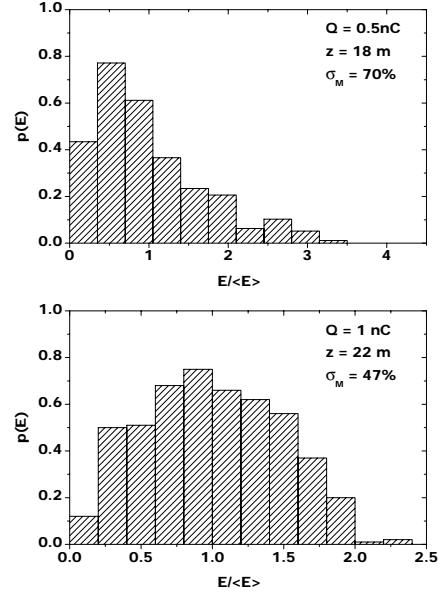


Figure 10: Probability distribution of the energy in the radiation pulse after narrow band monochromator. VUV FEL operates at saturation. Top: bunch charge is 0.5 nC. Bottom: bunch charge is 1 nC

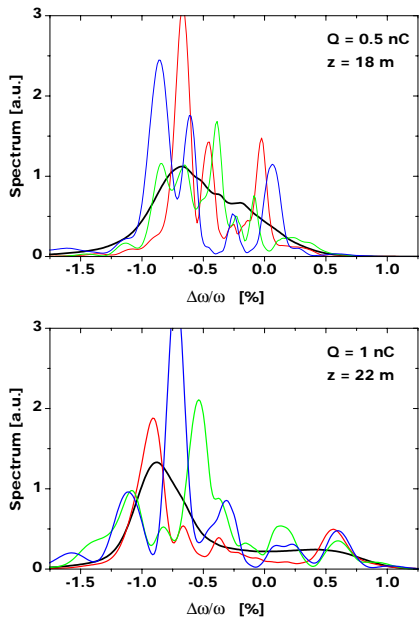


Figure 9: Radiation spectrum of the VUV FEL operating at the saturation. Top: bunch charge 0.5 nC,  $z = 18$  m. Bottom: bunch charge 1 nC,  $z = 22$  m. Thin curves show single shots. Bold curves show averaged profiles

always takes place for SASE FELs having pulse duration comparable with cooperation length [10].

## REFERENCES

- [1] V. Ayvazyan et al., Phys. Rev. Lett. 88(2002)104802.
- [2] V. Ayvazyan et al., Eur. Phys. J. D20(2002)149.
- [3] M. Dohlus et al., Nucl. Instrum. and Methods A530(2004)217.
- [4] The TTF FEL team, DESY Print TESLA FEL 2002-01, June 2002.
- [5] E.L. Saldin, E.A. Schneidmiller, M.V. Yurkov, DESY Print TESLA-FEL 2004-06, July 2004.
- [6] V. Ayvazyan et al., First operation of a free electron laser generating GW radiation power at 32 nm wavelength. Submitted to Eur. Phys. J. D.
- [7] E.L. Saldin, E.A. Schneidmiller and M.V. Yurkov, Nucl. Instrum. and Methods **A429**(1999)233.
- [8] E.L. Saldin, E.A. Schneidmiller, M.V. Yurkov, "The Physics of Free Electron Lasers" (Springer-Verlag, Berlin, 1999).
- [9] E.L. Saldin, E.A. Schneidmiller and M.V. Yurkov, Opt. Commun. **148**(1998)383.
- [10] E.L. Saldin, E.A. Schneidmiller and M.V. Yurkov, Nucl. Instrum. and Methods **A507**(2003)101.

# ACCELERATOR LAYOUT AND PHYSICS OF X-RAY FREE-ELECTRON LASERS

W. Decking, DESY, Notkestraße 85, 22603 Hamburg, Germany

## Abstract

X-ray Free-Electron Lasers facilities are planned or are already under construction around the world. This talk covers the X-Ray Free-Electron Lasers LCLS (SLAC), European XFEL (DESY) and SCSS (Spring8). All aim for self-amplified spontaneous emission (SASE) FEL radiation of approx. 0.1 nm wavelengths. The required excellent electron beam qualities pose challenges to the accelerator physicists. Space charge forces, coherent synchrotron radiation and wakefields can deteriorate the beam quality. The accelerator physics and technological challenges behind each of the projects will be reviewed, covering the critical components low-emittance electron gun, bunch-compressors, accelerating structures and undulator systems.

## INTRODUCTION

X-rays have played for many decades a crucial role in the study of structural and electronic properties of matter on an atomic scale. Free electron laser X-ray sources can provide ultra-high brilliant and sub-100fs pulse length coherent radiation. This will allow the research in this field to enter a new era. Linear accelerator driven FELs using the principle of self-amplified spontaneous emission (SASE) [1] appear to be the most promising approach to produce this radiation in the Å wavelength regime. Approaching this short wavelength requires large beam energies and thus rather huge linear accelerator installations. Consequently, only three projects are proposed so far which aim for shortest radiation wavelength.

The first facility of this type, using part of the existing SLAC linac, is under construction here at Stanford and will become operational in 2009 [2].

The XFEL was originally proposed as integral part of the TESLA project together with a 500 – 800 GeV e+e- Linear Collider based on superconducting RF (SRF) technology [3]. In 2003 the German government decided to approve the XFEL as an European project located at DESY in Hamburg. Construction is expected to start in 2006 with first beam in 2012.

The SCSS is proposed at SPRING8 in Japan with the aim to start operation in 2010. This layout relies on C-Band acceleration technology developed for the Japanese Linear Collider (JLC) [4].

In addition to this large scale facilities their exist proposals for FELs reaching the soft X-ray/VUV regime. These projects have lower electron energies and reach the X-ray regime by higher order FEL processes like **H**igh **G**ain **H**armonic **G**eneration

(HGFG). An overview of the present FEL projects is given in [5].

## ELECTRON BEAM REQUIREMENTS

The electron beam quality and stability required by the SASE process presents considerable challenges to the linear accelerator community. The following basic scaling laws for a Self-Amplified Spontaneous Emission FEL drive the layout of all facilities:

$$\varepsilon_N < \gamma \frac{\lambda_r}{4\pi}, \quad (1)$$

with  $\varepsilon_N$  the normalized emittance,  $\lambda_r$  the FEL resonant wavelength and  $\gamma$  the relativistic factor. The resonance condition is written as:

$$\lambda_r = \frac{\lambda_u(1+K^2)}{2\gamma^2} \quad (2)$$

with  $K = 93.4\lambda_u B_{RMS}$  being the undulator parameter ( $B_{RMS}$  the RMS undulator field,  $\lambda_u$  the undulator period length). The gain length  $L_g$  is given by

$$L_g = \frac{\lambda_u}{4\pi\sqrt{3}\rho} \quad (3)$$

with the FEL parameter  $\rho$

$$\rho \approx \frac{1}{4} \left( \frac{1}{2\pi^2} \frac{I_{PK}}{I_A} \frac{\lambda_u}{\beta\varepsilon_N} \left( \frac{K}{\gamma} \right)^2 \right)^{\frac{1}{3}}, \quad (4)$$

where  $I_{PK}$  is the peak current,  $I_A \approx 17\text{kA}$  and  $\beta$  the average beta-function in the undulator.

Finally the energy spread has to be smaller than the FEL parameter

$$\frac{\sigma_E}{E} < \rho. \quad (5)$$

The gain length is underestimated in this 1d-model, and saturation is usually reached after 10–20 gain length. To keep the gain length short means increasing the peak current while decreasing the normalized emittance. Optimized FEL parameters call thus for peak currents of 2-5 kA and a normalized emittance of around 1 mm mrad.

An important feature of X-Ray FELs is the fact that the stringent electron beam parameters have to be reached for a ‘slice’ of the bunch only. The slippage length, i.e. the difference between the electron and photon path length equals one radiation wavelength per undulator period, or approx.  $0.5 \mu\text{m}$  ( $\approx 1.7 \text{ fs}$ ) along a typical XFEL undulator. Many of the collective effects deteriorate mainly the ‘global’ bunch properties, while leaving the slice parameters unaffected.

SASE test facilities in the visible and vacuum-ultra-violet wavelength range were built and operated during the last years. The results have demonstrated the viability of the challenging accelerator subsystems and the good understanding of the SASE process in this wavelength regime.

## OVERALL LAYOUT

### XFEL

The layout of the XFEL is sketched in Figure 2. It is laid out as a multi-user facility. In its first stage, it will have 5 undulator beamlines, 3 of which are SASE-FELs (two for the Å wavelength regime, one for softer X-rays), the other two for hard X-ray spontaneous radiation. The site allows extending the user facility for more beam lines in a later stage.

The undulator sections have a maximum total length of 250 m. Variable gap 5 m long undulator segments are foreseen, which not only permits to independently adjust the photon energy within certain limits, but also facilitates the precise steering of the electron beam for optimum overlap with the photon beam.

The undulator parameters have been optimized for one Å wavelength at beam energy of 17.5 GeV. This implies that at the nominal maximum beam energy from the linac of 20 GeV at 23MV/m accelerating gradient, the  $^{57}\text{Fe}$  line at 0.8 Å, of interest for certain experiments, will be accessible. Furthermore, the expected higher performance of the superconducting cavities (see below) will permit to operate at even shorter wavelength, provided that the electron beam

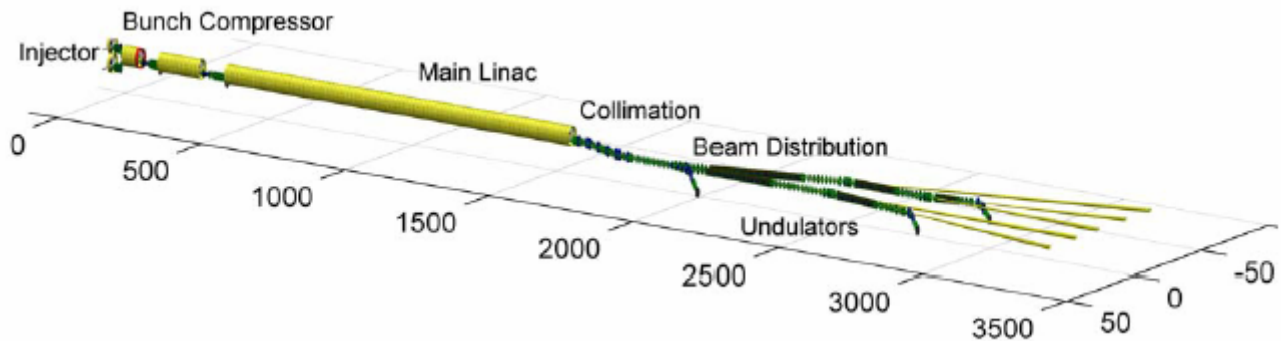


Figure 2: Layout of the XFEL

### LCLS

The LCLS makes use of the last third of the SLAC linac. One fixed gap, 112 m long undulator is foreseen for the initial phase, with an extension to more undulator beamlines being straight forward. The undulator parameters are optimized for 1.5 Å wavelength at a beam energy of 15 GeV.

Undulator system procurement is underway, with the complete delivery of the undulator system in 2007. The LCLS construction will start in 2006, FEL commissioning is planned in 2008 and operation is then foreseen for 2009. The project budget amounts to 379 M\$.

quality can also be further improved to guarantee saturation in the SASE FEL process.

The site for the XFEL has the linac starting on the DESY site, permitting to make optimum use of existing infrastructure, and the user facility in a rural area about 3km west-northwest from DESY (see Figure 1). The legal procedure to obtain permission for construction is expected to be completed by end of 2005. The project organization at the European level is ongoing with the goal to prepare the documents required for the technical definition and organizational structure of the project by 2005. The final decision to move into the construction phase is expected for 2006. The construction time until beam operation will be 6 years. The total project cost is estimated at 684 M€ (year 2000 price level).



Figure 1: Site for the XFEL starting at DESY and extending approx. 3.3 km to the North-West.

### SCSS

The SCSS site is located in parallel to the long SPRING8 beamline. A total length of approx. 1 km is available on the SPRING8 site, which drives the layout towards a high gradient linac and small gap undulator. A 250 MeV test facility is being constructed to test the crucial components (thermionic gun, buncher, C-band acceleration, bunch compression and in-vacuum undulator) starting end of 2005. With input from this

test facility construction of the SCSS can start in 2006 with FEL commissioning planned for 2010-11[6].

An overview of the main X-ray FEL parameters is given in Table 1.

Table 1: Selected Parameters of X-ray FELs

	LCLS	XFEL	SCSS
Radiation Properties			
Wavelength [nm]	0.15	0.08-6.4	0.1
Sat. length [m]	87	140	80
# of Undulators	1	5 (10)	1
Electron Beam Properties			
Energy [GeV]	15	6-20	6-8
Bunch Charge [nC]	0.2 – 1	1	0.4
Bunch Length [ $\mu\text{m}$ ]	8-22	25	25
Energy Spread	1e-4	1.5e-4	1.5e-4
Emittance [mm mrad]	0.85-1.2	1.4	0.85
Peak Current [kA]	2.1-3.4	5	3
Main Linac Parameters			
RF Frequency [GHz]	2.85 S-Band	1.3 L-Band	5.71 C-Band
Gradient [MV/m]	20	23	35
Linac Length [m]	0.9	1.5	0.4
Rep. Rate [Hz]	120	10	60
# Bunches/Pulse	1	3000	1
Avg. Beam Power [kW]	0.36-1.8	650	0.2

## INJECTOR

A sketch of the XFEL injector complex is shown in Figure 3. Two injectors are foreseen. This increases the availability of the XFEL and facilitates independent injector tuning and development. The injector layout is similar to the present installation at TTF. It uses an RF-gun, directly followed by an eighth-cavity TESLA accelerating module. Each injector will be equipped with a diagnostic section. This section consists of a FODO lattice which comprises four beam size measurement stations, allowing to measure the emittance and optical functions before entering the bunch compressor (four screen method) [7]. Using this setup, a projected emittance of 1.4 mm mrad has been regularly measured at TTF.

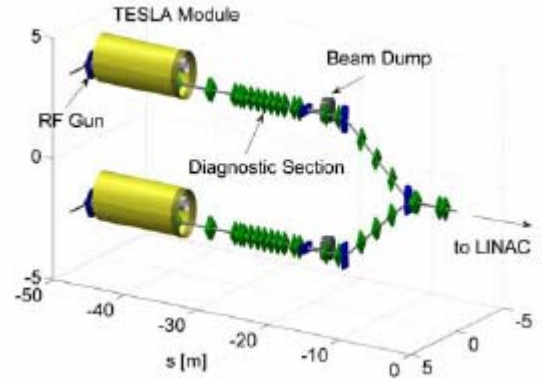


Figure 3: Injector layout of the XFEL

Figure 4 shows the development of the emittance along the XFEL injector as simulated with ASTRA. Further improvements of the gun are needed to reach the emittance goal of 1 mm mrad at 1 nC charge. This includes the processing and operation of the gun at higher gradients (presently 40 MV/m, foreseen 60 MV/m) and continuous improvements of the laser profile. These measures are implemented in the present upgrade of the Photo injector test stand in Zeuthen (PITZ) [8].

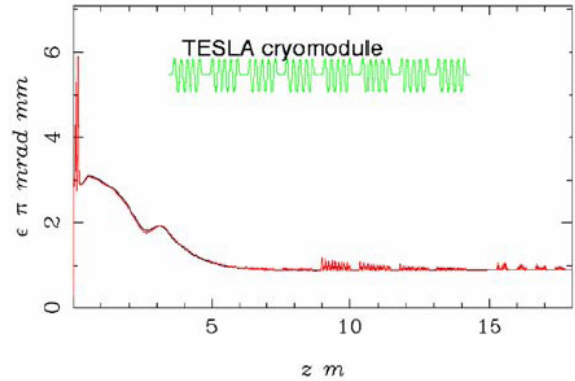


Figure 4: Development of transverse emittance in the XFEL injector (ASTRA simulation). Laser profile with uniform transverse distribution and longitudinal flat-top with 2 ps rise time.

An alternate approach to high-brightness electron beam generation is being pursued at SCSS using a low emittance HV-pulsed gun with a  $\text{CeB}_6$ -cathode and a reduced bunch charge level of 0.1 to 0.5 nC. An emittance of 1.1 mm mrad has been measured in their test facility [9].

The Paul Scherrer Institute (PSI) in Switzerland currently develops a Low-Emittance electron-Gun (LEG) based on field-emitter technology [10]. The target is a normalized transverse emittance of 0.05 mm mrad or less. Such a source is particularly interesting for X-ray FELs since it permits a reduction of the required beam-energy and hence, a reduction of the construction- and operational costs.

## BUNCH COMPRESSION

The large peak currents are reached with a bunch compression system. The basic layout is always very similar. Electrons are accelerated after the gun to an energy where space charge forces are small enough to not deteriorate the beam qualities. This acceleration is performed off-crest to add a momentum-longitudinal position correlation (chirp) to the bunch. In addition the bunch energy spread increases within the curved RF acceleration potential. A higher harmonic cavity system is then used to linearize the longitudinal phase space again, before the first bunch compression is performed [11]. After this a second acceleration takes place (again to mitigate space charge effects), and a second bunch compression is performed. Splitting the compression has several reasons: The first compression is performed as early as possible to decrease the nonlinear effects of the accelerating fields. Because of space charge effects the bunches are not compressed to the final peak current values. The second compression is thus at higher energies and weaker to decrease the coherent synchrotron radiation forces, which scale with the bunch compressor dipole bending strength and inversely with the bunch length.

The bunches are not fully compressed at the end of the second bunch compression. The remaining momentum-longitudinal correlation is taken out by the wake-fields in the main linac. This leads to subtle differences in the bunch compressor set-ups: With stronger wakefields in the main linac the LCLS can allow for a larger chirp and smaller  $r_{56}$  leading to reduced CSR effects (see Table 2).

Figure 5 shows the initial and final longitudinal beam profile for the LCLS. Due to the longitudinal compression the bunch develops sharp spikes - or ‘horns’ - at the tail and the head. The reason for this is a combination of strong wakefields in the accelerating structures and the coherent synchrotron radiation wakefield. These spikes will lead to very strong wakefield effects in the undulator vacuum chamber. An alternative set of parameters with lower charge has been developed which reduces the spikes to a much smaller level [12].

Figure 6 shows the initial and final beam profile for the XFEL. Due to the smaller wakefields in the TESLA cavities and optimized settings of the bunch compressor parameters spikes can be avoided.

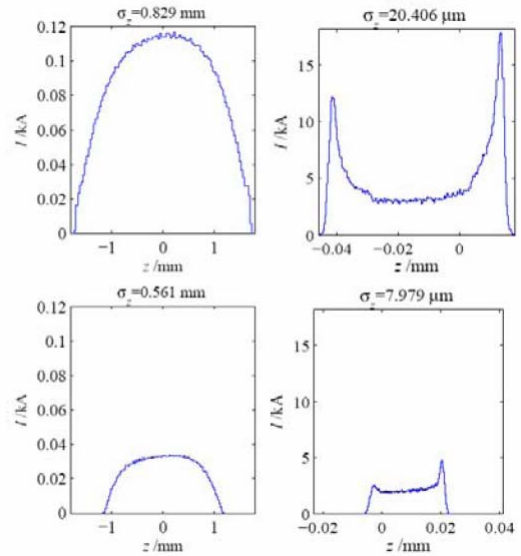


Figure 5: Initial (left) and final (right) longitudinal beam profile for the LCLS using a low charge (0.2 nC) in the bottom line and a high charge (1 nC) working point in the top line. The bunch head is at  $z < 0$ .

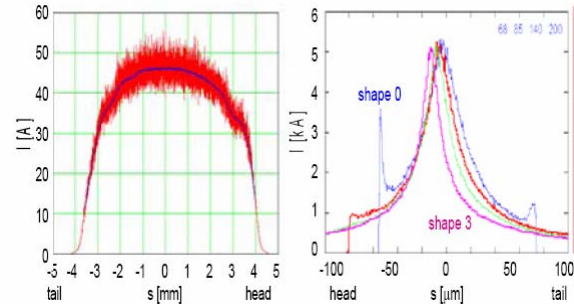


Figure 6: Initial (left) and final (right) longitudinal beam profile for the XFEL. The four colors in the left plot indicate the possibility of tuning the final beam distribution with the help of the orthogonal tuning ‘knobs’ constructed out of the first and higher harmonic RF parameters [13].

Table 2: Bunch Compressor Parameters

	LCLS	XFEL	SCSS
Initial peak current [kA]	0.1	0.05	0.04
1 <sup>st</sup> bunch compression stage			
Energy [MeV]	250	500	450
Compression	4.3	14	15
$r_{56}$ [m]	$\approx 36$	$\approx 90$	$\approx 50$
Peak current [kA]	0.5	0.7	0.6
2 <sup>nd</sup> bunch compression stage			
Energy [MeV]	4540	2000	790
Compression	8.8	7	5
$r_{56}$ [m]	$\approx 22$	$\approx 30$	$\approx 4$
Final peak current [kA]	3.2	5	2-3

## MAIN LINEAR ACCELERATOR

The most striking difference between the X-ray FEL projects is the choice of the main accelerator rf. LCLS relies on the well proven SLAC linac. A basic S-band accelerating structure is 3 m long and comprises 84 cells. 4 structures are powered by one klystron, with a total of 77 klystrons (including spares) used for the LCLS main linac.

The SCSS main linac is based on C-Band technology developed for the Japanese linear collider project. This leads to higher gradients and thus shorter linac length. All mayor rf parts have been developed in the past years. The accelerating structure will use choke mode damped cavity cells [15] to effectively damp long range wakefields. This will allow the acceleration of multi-bunch beams as a future option for the SCSS. A first 1.8 m long C-band (with 100 cells) structure was successfully tested with high power in 2004. The 8 GeV linac will use 144 of these structures, grouped into units of 4. Each unit is fed by two 50 MW klystrons running in parallel.

The XFEL linac is based entirely on the technology which was over the past years developed by the TESLA collaboration as the most essential part of the R&D program towards a superconducting linear collider. The TESLA Test Facility (TTF) has demonstrated that superconducting 9-cell Nb cavities can be reliably produced and operated with beam with the XFEL design performance of 23MV/m. With the electro polishing (EP) method to improve the Nb surface quality, 9-cell cavities were tested at gradients of 35 – 40MV/m. The main linac for the XFEL will be built with the EP technique.

The main linac uses 116 12m long accelerator modules with 8 superconducting cavities each, grouped in 29 rf stations. The linac is housed in a tunnel (Figure 7) 15 – 30m underground. The klystrons are in the tunnel and connected to the modulators in a surface building by pulse cables. The required klystron power per station is 4.8MW, well below the maximum power of 10MW of the multi-beam klystrons developed in industry for the TESLA project. This will not only cover the power needs for operation at higher energies, but also allow operating the linac at higher repetition rates (and duty cycles) at lower energy (the main limitation then being the *average* power of the RF system).

In contrast to conventional linacs, with the superconducting accelerator technology even a continuous wave (CW, 100% duty cycle) operation of the linac is conceivable, although only at reduced energy/accelerating gradient in order to avoid excessive cryogenic load into the Helium at 2K. Such an option is not part of the initial stage of the facility, but becomes attractive if lower-emittance, high duty cycle beam sources become available. We estimate that with a gradient of 7 – 8 MV/m (~7 GeV beam energy)

this mode of operation would be compatible with the foreseen cryogenic plant.

Table 3: Parameters for XFEL CW operation

Beam Energy [GeV]	6.5
Gradient [MV/m]	7
Beam current [mA]	0.18
Bunch spacing [ $\mu$ s]	5.5
rf power/module [kW]	20 (requires new low power rf system)
beam power [MW]	1.2
cryo load [kW]	2.4

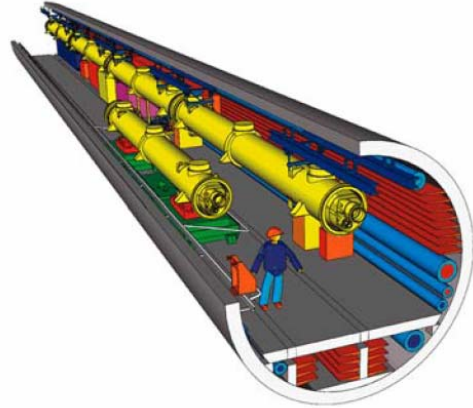


Figure 7: Layout of the XFEL accelerator tunnel

## UNDULATORS

All FEL projects use permanent magnet based undulator technology. Different philosophies are followed in view of gap variability and vacuum installation. The XFEL will use variable gap undulators to allow some independent tuning of the output radiation wavelength. In the case of the XFEL this allows a true multi-user facility with an independent choice of the radiation wavelength [16]. The SCSS Undulators will be placed inside the vacuum chamber, thus allowing for smaller gaps and shorter periods with higher K values. This technique has been pioneered at SPRING8. The possibility of opening the undulator gap has also the advantage that an alignment/diagnosis of individual undulator segments with spontaneous synchrotron radiation becomes possible. At the LCLS with their fixed gap devices this can be realized by moving the undulators sideways away from the vacuum chamber.

Table 4: Undulator parameters

	LCLS	XFEL			SCSS
Half aperture [mm]	2.5	3.8	3.8	3.8	1.75
Period length [mm]	30	35.6	48	56	15
K-Value	3	3.3	2.8-6.1	5.2-11	1.3

The undulator segments (3-5 m long) are embedded in a FODO lattice. Trajectory tolerances in the undulator sections are extremely tight. The rms deviation of the electron beam path should not exceed approx. 5  $\mu\text{m}$ , the slope not 5  $\mu\text{rad}$ . BPMs are aligned along a straight line using a laser system (Figure 8) or wire positioning system. Trajectory control is performed by moving the focussing quadrupoles to steer the beam through the BPM center or to minimize the dispersion (beam based alignment).

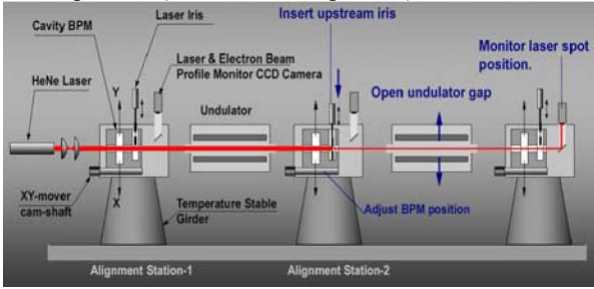


Figure 8: BPM alignment system for SCSS. The image of an alignment iris attached to the RF-BPM can be observed with an HeNe laser beam inside the beam pipe [4].

## WAKEFIELDS

Wakefields play an important role for the final bunch shape of short bunches. The wakefields of the accelerating structures lead for instance to the current spikes at the head and tail of the LCLS and SCSS bunches. In the small gap undulator vacuum chambers resistive wall wakes, geometric wakes and surface roughness wakes play an important role. Reference [18] gives a comprehensive overview.

By proper design of the vacuum chamber components it is possible to reduce the contribution of the geometric wake to a fraction of the resistive wake (see Figure 9). The same is true for the surface roughness wake, which amounts to 10-20% of the resistive wake for a roughness of 300 nm [20].

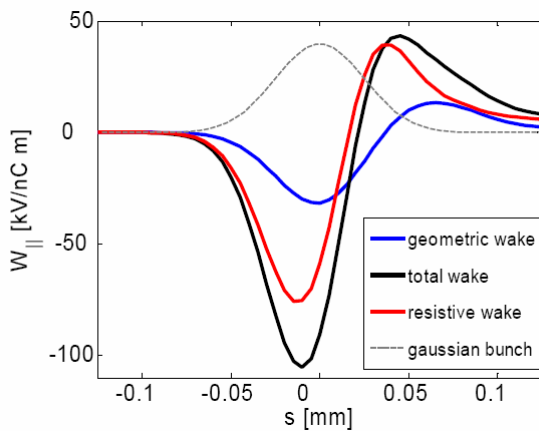


Figure 9: Wake field contributions including the geometric wakes (tapered absorber, pump, bellow, flange gap) and the resistive wake (25  $\mu\text{m}$  Cu, 4.5 mm radius) of one segment of the XFEL undulator section [19].

For the resistive wake the material properties of the vacuum chamber play a crucial role. So-called AC-conductivity effects differ for different materials like Cu and Al. In the case of the LCLS with its strong leading spike this leads to the conclusion that an Al vacuum pipe may be of advantage because the AC wake is damped faster [21]. In the case of the XFEL with its ‘Gaussian’ bunch shape this effect is negligible (see Figure 11).

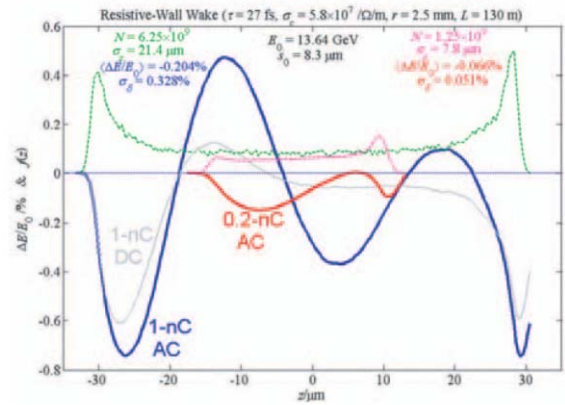


Figure 10: Resistive Wake in the LCLS undulator for the 1 nC (blue) and 0.2 nC setup [12].

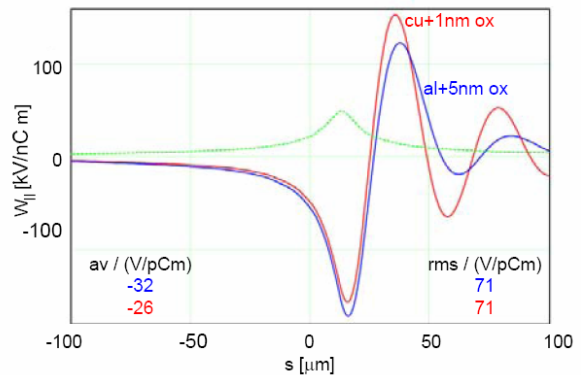


Figure 11: Resistive and Surface Roughness Wake for bunch shape 3 (see Figure 6). Beam pipe radius is 3.8mm, roughness 300 nm.

## OUTLOOK

X-ray free electron lasers will become reality in the upcoming years. While many of the accelerator physics challenges are understood, the focus will move towards commissioning and operation of these facilities.

## REFERENCES

- [1] Ya. S. Derbenev, A. M. Kondratenko and E. L. Saldin, Nucl. Instr. Meth. 193(1982)415.

- [2] „LCLS Conceptual Design Report“, SLAC-R-593, 2002.
- [3] F. Richard et al. (eds.), “TESLA Technical Design Report“, DESY 2001-011, 2001.
- [4] “SCSS XFEL Conceptual Design Report”, Riken, 2005.
- [5] G. Dattoli and A. Renieri, “Reviews of Existing Soft and Hard X-Ray FEL Projects”, FEL2005.
- [6] T. Tanaka, “Status of R&D for SCSS Project”, FEL2005.
- [7] K. Honkavaara, F. Löhl, “Transverse Electron Beam Diagnostics at the VUV-FEL at DESY”, FEL2005.
- [8] A. Oppelt et. al., “Status and First Results from the Upgraded PITZ Facility”, FEL2005.
- [9] T. Hara, “Current Status of SCSS Project at SPring-8”, Workshop on Undulator Systems (WUS2005), Hamburg, 2005.
- [10] R.J. Bakker, “Low Emittance X-FEL Development”, FEL2005.
- [11] P. Piot et. al., “Conceptual Design for the XFEL Photoinjector”, DESY TESLA-FEL 01-03, 2001.
- [12] P. Emma et. al., “An Optimized Low-Charge Configuration of the Linac Coherent Light Source“, SLAC-PUB-11243, also PAC05.
- [13] T. Limberg and M. Dohlus, “XFEL Bunch Compression System Set Up”, ICFA Mini-Workshop on Commissioning of X-Ray Free-Electron Lasers, Zeuthen, 2005.
- [14] T. Limberg and M. Dohlus, “Bunch Compression Stability Dependence on RF Parameters”, FEL2005.
- [15] T. Shintake, “The Choke Mode Cavity”, Jpn. J. Appl. Phys. Vol.31, p.1567, No.11A, 1992.
- [16] J. Pflüger, “Undulator Systems and Photon Diagnostic Plans for the European XFEL Project”, FEL2005.
- [17] H.D. Nuhn, “LCLS Undulator Commissioning”, ICFA Mini-Workshop on Commissioning of X-Ray Free-Electron Lasers, Zeuthen, 2005.
- [18] K.L.F. Bane, “Emittance Control for very short bunches”, EPAC2004.
- [19] I. Zagorodnov, “Geometric Wake in the XFEL Undulator”, XFEL Beam Dynamics Seminar, 2005, [www.xfel-beam.de](http://www.xfel-beam.de).
- [20] M. Dohlus, “Impedance of Beam Pipes with Smooth Shallow Corrugations”, TESLA 2001-26, 2001.
- [21] K.L.F. Bane and G. Stupakov, “Resistive wall wakefield in the LCLS undulator, SLAC-PUB-11227, also PAC05.

# BUNCH COMPRESSION STABILITY DEPENDENCE ON RF PARAMETERS

M. Dohlus, T. Limberg, DESY, Hamburg, Germany

## Abstract

In present designs for FEL injector linacs with high electron peak currents and short bunch lengths, higher harmonic rf systems are often used to optimize the final longitudinal charge distributions [4]. This opens degrees of freedom for the choice of rf phases and amplitudes to achieve the necessary peak current with a reasonable longitudinal bunch shape. It had been found empirically that different working points result in different tolerances for phases and amplitudes.

We give an analytical expression for the sensitivity of the compression factor on phase and amplitude jitter for a bunch compression scheme involving two rf systems and two magnetic chicanes. A cancellation scheme which loosens the rf jitter tolerances is discussed and numerical results for the case of the European XFEL are presented.

## INTRODUCTION

A two-stage bunch compression system as it is used for instance in the XFEL or the LCLS is shown schematically in Fig.1. It consists of the dipole magnet chicanes BC1 and BC2, their upstream accelerating RF sections and, upstream of the first chicane, a higher harmonic rf section.

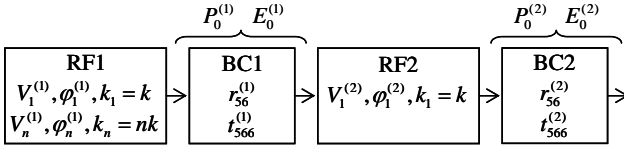


Fig. 1: Two-stage bunch compression system scheme

The basic parameters which have to be chosen are the beam energies at the chicanes BC1 and BC2 ( $E^{(1)}$  and  $E^{(2)}$ ), their compression factors  $C^{(1)}$  and  $C^{(2)}$ , the required rf chirps ( $p_0^{(1)}$  and  $p_0^{(2)}$ ) and the corresponding values for the ‘longitudinal dispersion’  $r_{56}$ . The total compression is determined by the ratio of the required peak current in the undulator ( $\sim 5$  kA for the XFEL) and the available current from the gun. The XFEL requires a total compression of  $C^{(1+2)} \approx 100$ .

The higher harmonic rf system (3<sup>rd</sup> harmonic in the XFEL case) is used to compensate higher order effects of the dispersion and the rf voltage. The (normalized) amplitudes  $a_{1\text{or}n}$  and phases  $\varphi_{1\text{or}n}$  of the fundamental mode rf and the  $n^{\text{th}}$  harmonic rf are related to the normalized total voltage, or, which is equivalent, to the normalized beam momentum and its derivatives by the following condition:

$$\begin{bmatrix} 1 & 0 & 1 & 0 \\ 0 & -k & 0 & -(nk) \\ -k^2 & 0 & -(nk)^2 & 0 \\ 0 & k^3 & 0 & (nk)^3 \end{bmatrix} \cdot \begin{bmatrix} a_1 \cos \varphi_1 \\ a_1 \sin \varphi_1 \\ a_n \cos \varphi_n \\ a_n \sin \varphi_n \end{bmatrix} = \begin{bmatrix} 1 \\ p_0^{\prime(1)} \\ p_0^{n(1)} \\ p_0^{m(1)} \end{bmatrix} \quad (1)$$

Eq. 1 determines the rf settings for four ‘knobs’, which allow independent control of the (normalized) final beam energy, the rf induced momentum chirp and the second and third derivative of the momentum deviation.

The first two knob settings, determining the beam energy and the momentum chirp, are obviously fixed and  $p_0^{n(1)}$  is needed to compensate 2nd order effects in the bunch compressor to avoid partial over-compression and thus spikes in the longitudinal charge distribution, which then cause strong wake fields [3].

The influence of higher order momentum deviations on the final bunch shape is weaker, so that  $p_0^{m(1)}$  is a relatively free parameter. In the numerical simulations shown in the last section of this paper,  $p_0^{m(1)}$  is scanned to find the working point with the lowest jitter sensitivities for rf phases and amplitudes.

## ERROR SENSITIVITY OF THE FIRST STAGE

We consider only the first stage and skip for this section the upper index ‘<sup>(1)</sup>’. The energy after the first linac section and the 3<sup>rd</sup> harmonic section is

$$E(s_a) = E_0^{(\text{gun})} + qV_1 \cos(ks_a + \varphi_1) + qV_3 \cos(3ks_a + \varphi_3)$$

$s_a$  is the relative longitudinal particle position in the bunch and  $E_0^{(\text{gun})}$  the beam energy at the entrance of RF1.

The reference energy is  $E_0 = E(0)$  and the relative momentum deviation is approximately

$$p(s_a) \approx E(s_a)/E_0 - 1.$$

The longitudinal position after compression is

$$s_b = s_a - (r_{56}p + t_{566}p^2 + O_3(p)),$$

and the bunch is compressed by the ratio

$$C = \left[ \frac{\partial s_b}{\partial s_a} \right]^{-1} = \left[ 1 - (r_{56} + 2t_{566}p + O_2(p)) \frac{\partial p}{\partial s_a} \right]^{-1}.$$

The nominal compression at design working point ( $p_0 = 0$  and  $p_0' = p'(0)$ ) is  $C_0 = (1 - r_{56}p_0')^{-1}$ , with  $p' = \partial p / \partial s_a$ . To estimate the error sensitivity with respect to the variation of an rf parameter (e.g.,  $\varphi = \varphi_{\text{design}} + x$  for the phase or  $A = A_{\text{design}} + x$  for the

amplitude), we write the relative momentum deviation  $p = p(s_a, x)$  explicitly as function of the error parameter  $x$  and the longitudinal bunch position  $s_a$ . The relative error sensitivity of the compression factor is:

$$\frac{1}{C_0} \frac{\partial C}{\partial x} = A \frac{\partial p}{\partial x} + B \frac{\partial p'}{\partial x}, \quad (2)$$

with  $A = -2(C_0 - 1)t_{566}/r_{56}$  and  $B = -C_0 r_{56}$ . It depends on the sensitivity of the momentum ( $\partial p/\partial x$ ) and that of the chirp ( $\partial p'/\partial x = \partial^2 p/\partial x \partial s_a$ ).

To calculate the effect of phase jitter of the fundamental harmonic rf we write for the momentum:

$$p(s_a, x) = a_1 \cos(k s_a + \varphi_1 + x) + a_n \cos(nk s_a + \varphi_n),$$

with  $p(0,0) = 0$  and  $p'(0,0) = (1 - C_0^{-1}) \cdot r_{56}^{-1}$ .

The phase sensitivity of the compression factor with respect to fundamental harmonic rf-jitter then follows as

$$\frac{1}{C_0} \frac{\partial C}{\partial x} = -a_1 (A \sin \varphi_1 + B k_i \cos \varphi_1). \quad (3)$$

This expression is derived for a single stage compression system, but as we show in the next chapter, the presence of the second compression stage causes only minor changes for the case of the XFEL parameters.

For the special case of one rf system on the fundamental mode and a simple chicane consisting of four dipole magnets, where  $r_{56} < 0$  and  $t_{566} \approx -1.5r_{56}$ , the phase sensitivity is given by (if  $E_0^{(\text{gun})} \ll E_0$ ):

$$\frac{1}{C_0} \frac{\partial C}{\partial x} \approx (1 - C_0) \cdot \left( 3 \tan \varphi_1 + \frac{1}{\tan \varphi_1} \right).$$

In the case of high compression ( $C_0 \gg 1$ ) and acceleration not too far off crest ( $|\varphi_1| \ll 1$ ), the relative compression error in such a system is approximately

$$\Delta C/C_0 \approx -C_0 \Delta \varphi_1 / \varphi_1.$$

The tolerances for the phase stability and absolute phase are by the bunch compression factor tighter than the tolerance on the final peak current. In the case of the XFEL, phase stability requirements become as demanding as a few hundredth of a degree.

## ERROR SENSITIVITY OF A TWO-STAGE COMPRESSION SYSTEM

In the following, we extend our sensitivity analysis to a two-stage compression system. In this case, the energy length correlation after RF2 is

$$E^{(2)}(s_b(s_a)) = E^{(1)}(s_a) + qV_1^{(2)} \cos(k s_b(s_a) + \varphi_1^{(2)}).$$

The reference energy is  $E_0^{(2)} = E^{(2)}(0)$  and the relative momentum deviation is given by:

$$p^{(2)}(s_b) \approx E^{(2)}(s_b) / E_0^{(2)} - 1$$

$$p^{(2)}(s_b) \approx u p^{(1)}(s_a) + p^{(2r)}(s_b)$$

with  $u = E_0^{(1)} / E_0^{(2)}$  and

$$p^{(2r)}(s_b) = V_1^{(2)} \cos(k s_b + \varphi_1^{(2)}) / E_0^{(2)} - 1$$

is the chirp created by the second fundamental mode rf system RF2 (see Fig. 1). The longitudinal position after the 2<sup>nd</sup> compressor follows as

$$s_c = s_b - (r_{56}^{(2)} p^{(2)} + O_2(p^{(2)})).$$

The total compression factor of the two stages is

$$C^{(1+2)} = \frac{1}{(C^{(1)} \tilde{C}^{(2)})^{-1} - (r_{56}^{(2)} + O(p^{(2)})) \cdot u \frac{\partial p^{(1)}}{\partial s_a}},$$

$C^{(1)}$  being the compression of the 1<sup>st</sup> stage and

$$\tilde{C}^{(2)} = \left[ 1 - (r_{56}^{(2)} + O(p^{(2)})) \frac{\partial p^{(2r)}}{\partial s_b} \right]^{-1}$$

the compression of the 2<sup>nd</sup> stage without the chirp of the 1<sup>st</sup> stage. With the help of the nominal parameters

$$\tilde{C}_0^{(2)} = [1 - r_{56}^{(2)} p_0'^{(2r)}]^{-1},$$

$$C_0^{(2)} = [1 - r_{56}^{(2)} p_0'^{(2)}]^{-1},$$

$$C_0^{(1+2)} = C_0^{(1)} C_0^{(2)} = \left[ (C_0^{(1)} \tilde{C}_0^{(2)})^{-1} - r_{56}^{(2)} u p_0'^{(1)} \right]^{-1}$$

where

$$p_0'^{(2)} = \left( \partial p^{(2)} / \partial s_b \right)_{s_b=0}$$

and

$$p_0'^{(2r)} = p_0'^{(2)} - C_0^{(1)} u p_0'^{(1)},$$

we can write the sensitivity of the total compression factor to errors of parameters of the first rf system as

$$\frac{\partial C^{(1+2)}}{C_0^{(1+2)} \partial x} = \frac{C_0^{(1+2)}}{C_0^{(1)} \tilde{C}_0^{(2)}} \left\{ \frac{\partial C^{(1)}}{C_0^{(1)} \partial x} \right\} - C_0^{(1+2)} r_{56}^{(2)} u \frac{\partial p'^{(1)}}{\partial x},$$

neglecting second order effects downstream of the first magnet chicane.

For the parameter range of the XFEL bunch compression system the second term is small, so that the error sensitivity behaves similar to that of the 1<sup>st</sup> stage (multiplied with  $C_0^{(1+2)} / C_0^{(1)} \tilde{C}_0^{(2)}$ ). For the case that the beam is on crest in RF2, the two-stage system has the same sensitivity as the single stage compressor (for the same total compression factor). Adding chirp in the second linac by operating the beam off-crest reduces the sensitivity somewhat (in principle of up to the compression factor of the 2<sup>nd</sup> stage), but for reasonable penalty in rf power the gain for XFEL parameters is small (see last chapter).

## PHASE JITTER COMPENSATION

A possible way to loosen the extremely tight phase tolerances is suggested by Eq. 2. For the four-magnet chicane, the constants  $A$  and  $B$  have the same sign. Since  $r_{56}$  is negative and a negative chirp is needed for compression, a shift in phase which increases the beam momentum must be accompanied with an increased chirp (more negative!) to reduce the sensitivity. The effectively reduced longitudinal dispersion of the magnet chicane due

to the higher beam energy is then compensated by the stronger chirp.

An rf system with a single frequency cannot provide this compensation, as for instance Eq. 3 shows: As, again, the constants  $A$  and  $B$  have the same sign, the right hand terms can compensate each other only if  $\cos \varphi_i > 0$  and  $\sin \varphi_i < 0$  (acceleration, but with positive (de-compressing) chirp) or if  $\cos \varphi_i < 0$  and  $\sin \varphi_i > 0$  (negative (compressing) chirp, but de-acceleration).

In the presence of a higher harmonic rf system, it is possible to find a working point where the terms of Eq. 2 compensate each other to a significant degree for both systems.

Such a working point for the case of the XFEL is sketched in Fig. 2. The sum of the fundamental and 3<sup>rd</sup> harmonic field is shown in red. The total field accelerates and has a negative slope  $p' = (1 - C_0^{-1}) \cdot r_{56}^{-1}$  as it is required for compression. The fundamental mode rf provides the acceleration and the higher harmonic system the chirp.

The compensation is shown in the lower graphs of Fig. 2: Increasing amplitude due to phase offsets in both rf systems is always accompanied by a stronger chirp.

To determine the optimal rf parameters which provide the required beam energy, rf chirp and 2nd momentum derivative (see Eq. 1) as well as the minimum phase sensitivity for both systems, we varied the third derivative of the momentum  $p_0^{(3)}$ . The results of this scan are shown in the next chapter.

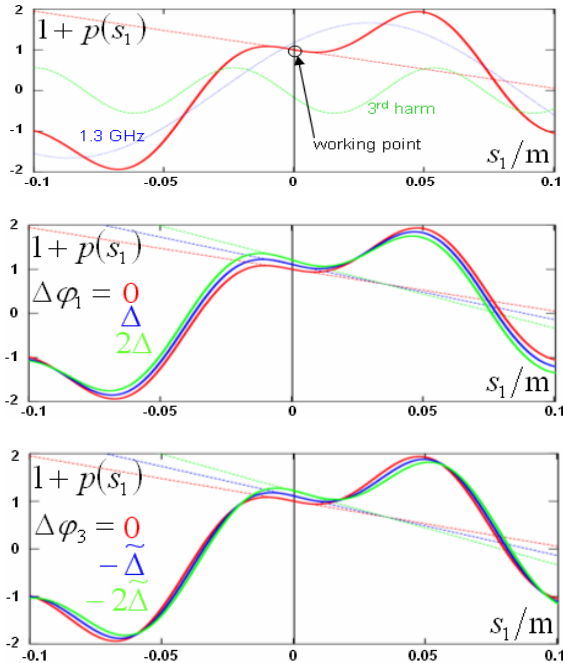


Fig. 2: On top: Voltages of fundamental and 3rd harmonic rf and the sum voltage. The lower graphs show the sum voltage and its slope at the working point for different phase offsets for the fundamental mode rf system (middle) and for the 3rd harmonic system (bottom).

## OPTIMAL WORKING POINT FOR THE XFEL BUNCH COMPRESSION SYSTEM

In [1] it has been shown that growth of the projected emittance due to CSR effects is minimal for  $C^{(1)} \approx 20$ .

Space charge effects give a lower limit for the beam energy for the compression stages: Simulation calculations [2] for the XFEL suggest that  $I / \gamma^2 > \sim 1$  mA is a good criterion to avoid emittance growth, requiring  $E_0^{(1)} > \sim 0.5$  GeV and  $E_0^{(2)} > \sim 1$  GeV for design peak currents. Actually, the design beam energy for stage 2 has been chosen to be  $E_0^{(2)} = 2$  GeV to provide head room for higher peak currents.

To compensate the energy offsets caused by the wake fields of the accelerating structures of the main linac, we choose the chirp for the 1<sup>st</sup> stage to be about 10 MeV per RMS bunch length. In the linac section upstream of the second magnet chicane, the bunch travels on crest.

To find the working point for the rf systems upstream of the first chicane, we scanned different settings of the third momentum derivative  $p_0^{(3)}$ , while keeping the accelerating voltage, the chirp and the second derivative constant.

The sensitivities of the total compression factor with respect to amplitude and phase jitter of these rf systems were calculated with a longitudinal tracking code which includes the non-linearities of rf systems and compressor chicanes, wake field effects and the longitudinal space charge forces.

The resulting necessary voltage for the fundamental harmonic system (Fig. 3) and the phase and amplitude sensitivities of both rf systems (Fig. 4-7) turn out to be mostly smooth functions of the 3<sup>rd</sup> harmonic rf amplitude, which is plotted on the horizontal axis.

The phase and amplitude offsets which are plotted on the vertical scale cause a change of the final peak current of 10%.

The different curves refer to different settings of chicane beam energies and compression factors (see Table 1). For all cases, the total compression factor is  $C^{(1+2)} = 100$ .

Table 1: Parameters for different compression scenarios.

	1	2	3	4	5	6
$E_0^{(1)}/\text{MeV}$	500	500	500	500	400	400
$C^{(1)}$	20	14	20	14	14	14
$r_{56}^{(1)}/\text{mm}$	84.4	82.3	101.4	109.3	89.1	68.4
$\varphi_1^{(2)}/\text{deg}$	0	0	20	20	20	20
$r_{56}^{(2)}/\text{mm}$	19.2	29.0	19.0	29.3	29.3	23.5

Case 1 represents the present design values. For phase jitter compensation, the integrated voltage of the 3<sup>rd</sup> harmonic rf has to be around 250 MV (see Fig. 4 and 5). Perfect compensation of the terms in Eq. 3 for the

fundamental mode rf occurs at a setting of 250 MV for the 3<sup>rd</sup> harmonic system. At 240 MV, the 3<sup>rd</sup> harmonic system itself is perfectly compensated. For a voltage a little less than 250 MV, both systems have phase tolerances looser than one degree. The fundamental mode rf needs close to 800 MV to reach the 500 MeV beam energy at the exit of the 1<sup>st</sup> compression stage (see Fig. 2).

In the cases two to four, bunch compression factors are varied and the linac upstream of BC2 is run 20 degrees off-crest (3 and 4).

The cases 5 and 6 have reduced beam energy after BC1 and a consequently reduced voltage requirement for the 3<sup>rd</sup> harmonic rf system (200 kV). For the cases 1 to 5, chirp and cavity wakes (of the next 100 linac rf modules) approximately compensate each other; in case 6 we drop that requirement.

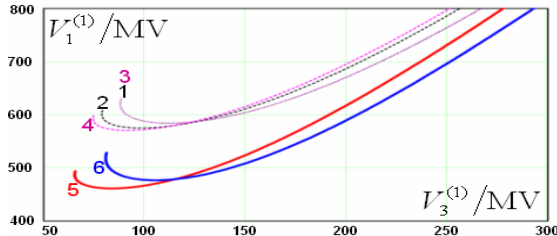


Fig.3: Amplitude of fundamental harmonic rf system vs. 3<sup>rd</sup> harmonic rf amplitude. The varied parameter is  $p_0'''^{(1)}$ .

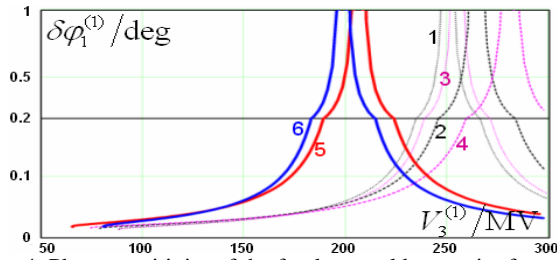


Fig. 4: Phase sensitivity of the fundamental harmonic rf system vs. 3<sup>rd</sup> harmonic rf amplitude

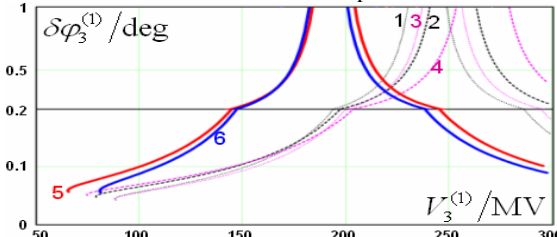


Fig. 5: Phase sensitivity of the 3<sup>rd</sup> harmonic rf system vs. 3<sup>rd</sup> harmonic rf amplitude.

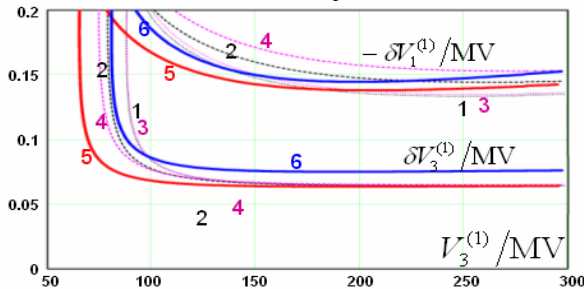


Fig. 6: Amplitude sensitivity of both rf systems vs. 3<sup>rd</sup> harmonic rf amplitude

The amplitude sensitivities in Fig. 6 are voltage offsets in units of MV. Over the most part of the scan, the relative amplitude sensitivity is constant at a level of  $1.5 \cdot 10^{-4}$  for the 3<sup>rd</sup> harmonic rf and  $3 \cdot 10^{-4}$  for the fundamental mode. In the parameter regime where the amplitude jitter sensitivity would be reduced, the phase tolerances become extremely tight.

Fig. 7 shows the variation in the charge profile during the scan for the example of case 5 at three points.

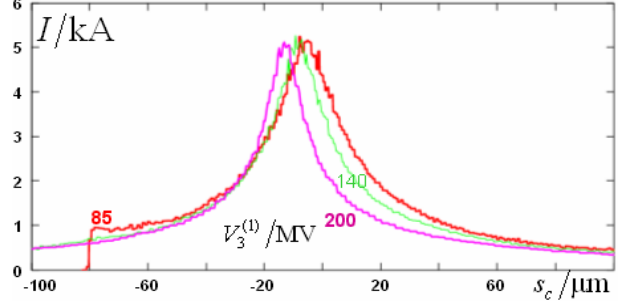


Fig. 7: Final longitudinal beam distribution for three different third harmonic rf voltages (case 5)

## CONCLUSION

The phase jitter sensitivity of a bunch compression system can be reduced by more than an order of magnitude if the amplitudes and phases of the fundamental mode rf and the higher harmonic rf system are correctly chosen to provide phase jitter compensation.

For the case of the European XFEL, the 3<sup>rd</sup> harmonic system has to be operated with an amplitude of 250 MV, more than twice the minimum value necessary to compensate the non-linearities of the fundamental mode rf and the magnet chicanes. At that working point, phase jitter tolerances are of the order of a degree for both rf systems, compared to a few hundredth of a degree in the previous design. Amplitude jitter tolerances are  $1.5 \cdot 10^{-4}$  for the 3<sup>rd</sup> harmonic rf and  $3 \cdot 10^{-4}$  for the fundamental mode rf.

## REFERENCES

- [1] M. Dohlus, T. Limberg: "Optics, Geometry and CSR-related Emittance Growth in Bunch Compressor Chicanes". PAC 2005.
- [2] V. Balandin et al.: "Optimized Bunch Compression System for the European XFEL". PAC 2005
- [3] M. Dohlus, T. Limberg: "XFEL Bunch Compression System Set Up". Commissioning Workshop, Zeuthen 2005.  
<http://commissioning2005.desy.de/>
- [4] P. Piot et al., "Conceptual Design for the XFEL Photoinjector", DESY TESLA-FEL 01-03, 2001.

# UNDULATOR SYSTEMS AND PHOTON DIAGNOSTICS FOR THE EUROPEAN XFEL PROJECT

Joachim Pflüger<sup>#</sup>

DESY, HASYLAB, Notkestr 85, 22603 Hamburg, Germany

## Abstract

For the European XFEL project very long undulator systems are required. Due to the nature of the SASE process there are stringent requirements and tolerances on these systems. An extensive R&D phase to solutions has been started. In this contribution an overview over this R&D work is given.

FELs. They are much longer and have to meet different requirements and specifications. Design ideas and requirements for the undulator systems based on parameters found in [1] were already published [3]. This contribution focuses on recent upgrades and new design ideas not published before.

## INTRODUCTION

Over the past years the design of the XFEL Laboratory has undergone several major changes. Initially it was linked to the TESLA Linear collider using a fraction of the 500 GeV  $e^-$  Linac in a time sharing fashion. This was the basis for the TDR, which is described in [1]. In 2002 the XFEL was proposed with a separate Linac [2], which is now the basis for the European XFEL project. Presently the project is in a defining stage. Despite of all these changes the intended scientific use and the wavelength range remain unchanged. The principle of self amplified

## UNDULATOR SYSTEM

### Systems Overview

The whole XFEL will be built in underground tunnels. The total length of the accelerator, the FEL and the photon beam lines will be about 3.3km. Fig.1 shows a schematic overview of the beam distribution and the arrangement of the undulator systems of the Phase I of the European XFEL. In a later upgrade the number of beamlines can be doubled. The outgoing beamline in the bottom of Fig.1 belongs to beam distribution of Phase II, which will be built later. Table 1 shows parameters of the proposed undulator systems. Undulator and photon beam lines extend over a total length up to approximately 1150m. The beam is split in two beam lines, which serve SASE1 and SASE2. Both can be operated at 1Å. SASE1 is designed to operate at fixed wavelength while SASE 2 can be tuned from 1 to 4 Å. It therefore needs to be longer by about 25%.

After passing through the undulator the beam after SASE1 is still of sufficient quality to drive a second FEL called SASE3 which operates in the soft X-ray regime at wavelength  $> 4\text{Å}$ . An helical undulator of the APPLE 2 type is planned [4, 5] since in this wavelength range there is no alternative to generating circularly polarized X-rays.

The spend beam of SASE2 is used in two spontaneous radiators, which can generate hard x-rays at wavelength as short as 0.1 Å. In total there are five photon beamlines serving the experiments in the experimental hall.

The undulator systems will be segmented in 5m long undulator segments and 1.1m long intersections (see also ref [3].)

In the tunnels there is free space left as can be seen in Fig.1. There are numerous upgrade options, which can be used to generate radiation for more beam lines ultrashort pulses, or ultra high resolution [6], which need additional space.

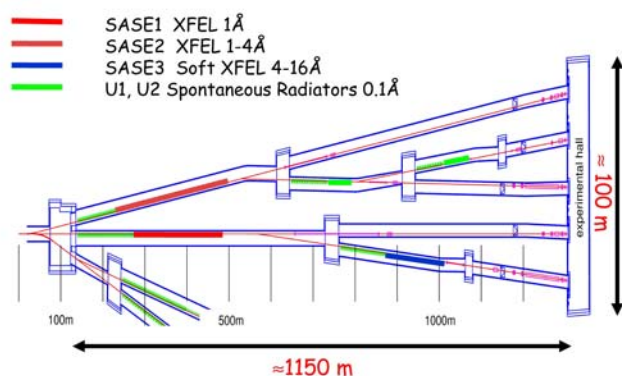


Fig. 1 Baseline layout of the beam distribution, the undulator systems, photon beam lines and experimental hall.

spontaneous radiation (SASE) will be used for the European XFEL. It will predominantly operate in the hard X-ray regime around 1 Å, but also use soft X-rays at wavelengths  $> 4\text{Å}$

Undulator systems for SASE X-FELs differ quite a bit from those for Synchrotron Radiation sources or cavity

<sup>#</sup>joachim.pflueger@desy.de

Table 1: Parameters for the proposed undulator systems

	$\lambda_R$ [Å]	$\lambda_0$ [mm]	Gap # [mm]	$B_0$ [T]	K	$\beta_0$ [m]	$L_{Sat}^+$ [m]	$N_{Tot}^+$	$L_{Tot}^{+++}$ [m]	
SASE 1 *	1	35.6	10	1.0	3.3	32	133	33	201.3	
SASE 2 *	1-4	48	19-10	0.63-1.37	2.8-6.1	46-15	174-72	42	256.2	
SASE 3 **	4-16	65	20-10	0.85-1.76	5.2-11	15	88-55	22	134.	
U1, U2 ***	0.09- 0.25	20.9	22-6	0.1-0.98	0.2-1.9	15	50	10	61.0	
							Total	495	107	652.5

\* Planar Hybrid Undulator

\*\* Apple II Helical Undulator

\*\*\* Spontaneous Emitters operated on 1. Harmonic

# Magnetic gap of SASE FELs is 10mm, that of Spontaneous emitters is 6mm

+ Net saturation length with no contingency, spontaneous emitters are limited to 50m magnetic length

++ Number of 5m undulator segments plus 20% contingency

+++ Total system length includes 1.1m long intersection after each undulator segment

## Undulator Segments

### Tolerances

The linewidth of FEL radiation is of the order of the Pierce parameter  $\rho$ , which for the XFEL amounts to  $3 \times 10^{-4}$  at 1Å. For the undulator system this means that the first harmonic has to be tuned with an accuracy given by:

$$\frac{\Delta\lambda}{\lambda} \leq \rho \quad (1)$$

The nature of the FEL process is such that in order to have an effect on the radiated power an error has to act over a power gain length, which for the XFEL is in the order of 10m. A conservative requirement would be to require eq.(1) for a 5m long undulator segment. There are different error sources having an effect on the harmonic: Temperature via the temperature coefficient of the magnet material, vertical alignment via the hyperbolic cosine like field distribution, Gap and flatness errors via the exponential field dependence. If all error sources are equally weighted and using:

$$\Delta\lambda = \left| \frac{\partial\lambda}{\partial B} \right| \sqrt{\Delta B_{Temp}^2 + \Delta B_{Align}^2 + \Delta B_{Gap}^2 + \Delta B_{Flat}^2} \quad (2)$$

the values reproduced in Table 2 result. These values are the basis for the designs shown in this contribution.

Table 1: Tolerances for the Undulator systems and 5m segments

Temperature	$\Delta T$	$\pm 0.08$	K
Alignment	$\Delta Y$	$\pm 100$	$\mu m$
Gap	$\Delta g$	$\pm 1$	$\mu m$
Flatness	$\Delta g$	$\pm 1$	$\mu m$

### Mechanic Support

Fig. 2 shows the design of the undulator segments for the XFEL. It is planned to have a standard drive system. Its design should meet the requirements for all XFEL

undulator systems. There are several points, which deserve being mentioned:

1. The girders have a substantial rectangular cross section of 500 by 100mm. The reason for the rectangular cross section is to minimize shear deformation, which, in the  $\mu m$  range dominates over elastic deformation.
2. The materials for girders and support structures need to be identical in order to avoid any bimetallic bending as a function of temperature. Stainless steel will be taken for magnetic and stability reasons.
3. The girders are supported on four equidistant points. This

reduces the deformation under magnetic load dramatically. Two auxiliary, intermediate girders are needed, which are shown in the rear view shown in Fig.3.

4. The girders are connected to massive guideways and leadscrews integrated in the support columns using spherical supports. In this way the magnetic forces are transmitted and a rotational degree of freedom is provided. The exact parallel alignment of top and

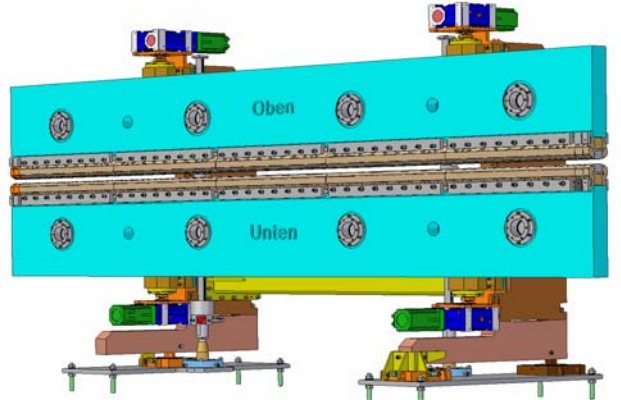


Fig.2 : View of a 5m long Undulator segment

bottom girder is achieved through a separate individual guiding system also shown in Fig 3. It also integrates the encoders needed for the feedback for the motors. There are no forces on this guiding system. It provides the precision alignment.

5. There are four motors, one for each spindle. They are electronically synchronized.

### Magnetic structures

The mechanical design of the magnetic structure is strongly influenced by the experience made with TTF1. It will be subdivided into 90cm long support segments for magnets and poles, which are clamped onto the girders. Stainless steel, the same as for the girders, will be used

for the support structures in order to reduce bimetallic bending. The method of field fine tuning by pole height adjustment will be further refined and used to fine tune the field distribution [7]. It requires each pole to be height adjustable by about  $\pm 100\mu\text{m}$ .

### Intersections

#### Planar Permanent Magnet Quadrupoles (PPMQs)

The intersections were already described in [3]. It is currently investigated if electromagnetic (EM)

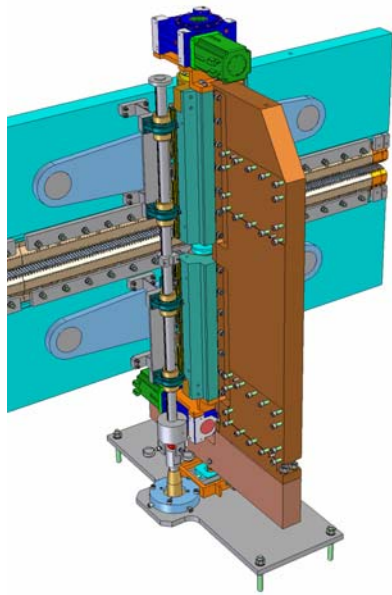


Fig. 3: Rear view showing the girder support column of one end, the auxiliary intermediate girder for the four point support and the guiding system, which integrates the position encoders for the top and bottom motor.

components such as quadrupoles and phase shifters can be replaced by those using permanent magnets (PM). These efforts are driven by the request to 1.) avoid any sources of heat in the undulator section, 2.) make components in the intersection as compact as possible and 3.) have sufficient accuracy for adjustments.

Fig 4 shows the principle of an adjustable PPMQ. It is an improvement of a proposal by Tatchyn [8]. A strong quadrupolar field is created in the center of the PM array, which consists of PM parallelepipeds separated by a gap. The top and bottom separation distance may be changed independently by moving the blocks along the z direction symmetrically to the Y-axis. In this way the gradient and the exact vertical center position can be adjusted. These relations are shown in the contour plots, Fig. 5. XFEL parameters were assumed: a gap of 12mm, a maximum integrated gradient of about 8T and a vertical center adjustability of  $\pm 1\text{mm}$ . Magnet dimensions are given in Fig. 5. It is seen that vertical center adjustment capability requires some compromise with the integrated gradient,

which has to be smaller than the maximum achievable one: 12T are possible, but at almost no adjustability. As a compromise 8T were chosen, which allow for the required  $\pm 1\text{mm}$ . Horizontal adjustability is trivial: All four magnets may be moved by the desired amount along the Z-direction.

The good field area is about  $\pm 1.5\text{mm}$  which is sufficient for an electron beam of a Linac with an RMS beam size of  $25\mu\text{m}$ . Although looking exotic PPMQs were heavily and successfully used in the undulator for the VUV-FEL at the Tesla Test Facility Phase I (TTF1). Magnet arrays similar to that in Fig.4 were superimposed to the field of an PM undulator [9]. A total of 30 planar PM quadrupoles were integrated in the 15m long undulator section. They were forming a FODO lattice superimposed to the periodic field of the undulator and allowing for a beta function in the undulator of 1m only. Adjustment and alignment of the quadrupoles were done

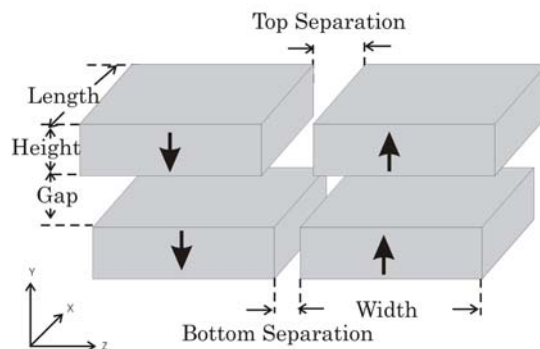


Fig. 4: Principle of a planar permanent magnet quadrupole

in a similar fashion as discussed above [9, 10].

A PPMQ may replace an EM quadrupole mounted on movable supports for beam steering.

For the XFEL accurate control of the quadrupole center positions to  $1\text{-}2\ \mu\text{m}$  is desirable. The accuracy of the

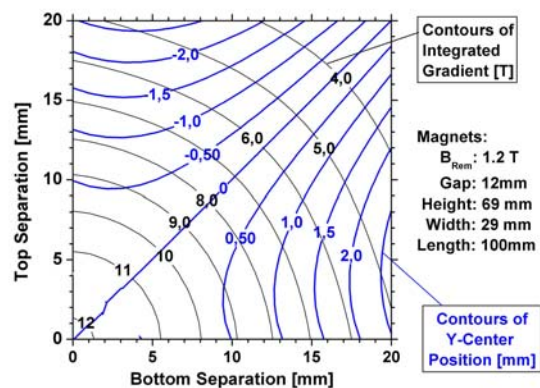


Fig. 5: Contour plot of the field gradient and the position of the vertical center as a function of Top and Bottom separation

PPMQ principle depends on the stability and reproducibility of the PM material and on the accuracy of the mechanical components used to move the magnets. It also has to be compared with that of an EM quadrupole. This will be subject to investigations in the next future.

### Phase shifter

In undulator systems with variable gaps a phase shifters are needed to exactly adjust the phase between segments so that constructive superposition occurs. The simplest way is to use a three magnet chicane using EM. This is

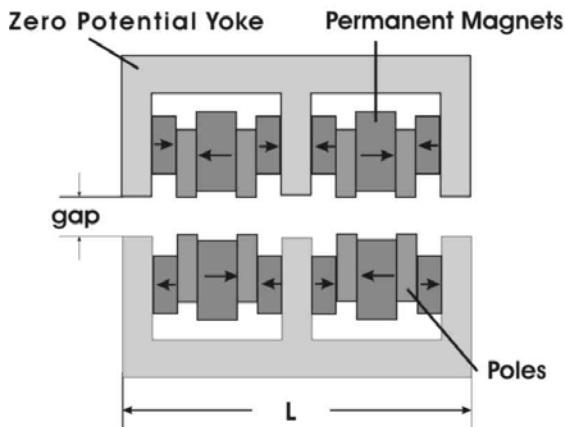


Fig. 6: Proposed PM phase shifter. The soft iron zero potential yoke avoids stray fields. The strength can be adjusted by changing the gap. The length  $L$  is about 200mm

described in [12]. Drawbacks of this solution systems are: 1.) Hysteresis in the magnets, 2.) Asymmetries in the magnets and 3) space requirements.

Fig. 6 shows a sketch of a PM phase shifter. It uses a zero potential yoke made of soft iron, PMs and poles in a similar configuration as in the case of a hybrid undulator. The full center magnets excite flux in the poles next to them with the same strength but opposite sign. So the field integral is balanced. Additional magnets between poles and the zero potential yoke can be used to enhance the pole strength. Slight vertical movement of the short magnets can be used for error correction. In addition the zero potential yoke very effectively terminates outside fields. The strength of the phase shifter is controlled via the gap. First estimates indicate that the length can be shortened by a factor of 2 as compared to the EM version of [12]. A prototype is presently under construction.

## CONTROL SYSTEM

There are several requirements on the control system:

- It has to control and synchronize the motion of the four motors of an undulator segment with high precision. The gap should be adjusted with an accuracy of  $< 1\mu\text{m}$ . In addition operational safety, i.e. proper failure recognition has to be guaranteed.

- It has to allow for synchronization of additional components, for example current settings of corrector coils, gap values for phase shifter settings etc. It should be possible to implement these corrections in a flexible manner.
- It must provide control of the whole undulator system i.e. synchronization of all individual undulator segments.
- It should be designed for a life of 15-20 years minimum.
- High reliability and availability of components is essential.
- Industrial Standards and components should be used.

Over the past years there has been a tremendous development of control systems and components for industrial applications such as automatation, robotics, numerical machining, process- and motion control, handling etc. Components are available off the shelf and prices become more and more moderate. For these systems field-buses such as SERCOS, Profibus, CAN-bus, Ethernet or EtherCAT are used. Some of them are vendor independent. There are very fast solutions for triggering and synchronization of an arbitrary number of components in a system. To some extent even hardware compatibility between different manufacturers exists. The undulator control system will take advantage of these developments.

To gain first experience an old decommissioned wiggler used at HASYLAB for many years has been converted to a motion control test undulator. Before there was central 3-Phase motor and five gear boxes, which powered four spindles, which moved the girders. These component were replaced by four servo motors and one central control unit manufactured by Beckhoff Industrie Elektronik, Germany. Each motor has its own high resolution position encoder feedback with submicron resolution. First tests show that the gap can be controlled with submicron resolution reproducibly back and forth: Mechanical play and backlash although detectable in the spindles is fully compensated by the encoder feedback. The 'In Position' gap with enabled feedback jitters by  $0.2\mu\text{m}$ . The synchronization works reliably and the hardware allows for the synchronization of external components. These results are encouraging and therefore the concept will be the basis for further developments.

## UNDULATOR RELEVANT OPTICAL DIAGNOSTICS

An undulator system consisting of 42 segments like SASE2 (see table1) has an enormous number of parameters to adjust. The purpose of the photon beam diagnostic system is to check and verify the most important and critical ones. A diagnostic station for the XFEL has been proposed, which can be used to control settings of the undulator and the alignment of the  $e^-$  beam in the undulator section [13]. It uses the 5<sup>th</sup> harmonic of the fundamental at a wavelength around  $0.2\text{\AA}$ . A single crystal monochromator in Laue geometry is used. Its

design could be similar to the beam diagnostic system for PETRA [14]. The spontaneous radiation emitted either by a single segment or by groups of segments is analyzed. There are three basic measurements, which can be performed:

1. Position measurement of the photon beam
2. Exact measurement of the radiation wavelength or equivalently the K parameter
3. Measurement of the phasing between undulator segments

These measurements may be used to check settings of individual undulator segments, segment pairs or groups of segments. This will be facilitated by the possibility to open the gaps in all undulator segments to a 'switch off' position. Using the fast control system it is straightforward to implement automated procedures, which allow the following gap dependent measurement on any segment of an undulator system with high accuracy:

- Proper corrector setting to keep the beam position fixed
- In situ calibration of photon wavelength
- Phase shifter settings

Operational experience will show to what extent these measurements need to be repeated to allow for a safe routine operation of the undulator system.

The bunch charge may fluctuates by several percent and the bunch energy by  $10^{-4}$ . This makes the precision measurements more difficult. Two alternative solutions were proposed by Yang [15]: Using his idea any two undulator segments of a system are compared. One of them, the last of the system is taken as 'reference undulator'. The same bunch passes through both undulators. A steerer magnet deflects the  $e^-$  beam before it entering the second. The radiation of both is now spacially separated and is passed through the same Laue monochromator, but intensities are analyzed individually. Differences in count rates are very sensitive to differences in the K parameter. A resolution of  $\Delta K/K < 10^{-5}$  has been reported, which is even more than required for an XFEL using eq. (1).

Alternatively charge and energy could be measured for each bunch and used for correction for the spectrum.

## SUMMARY AND CONCLUSION

New design ideas for the undulator systems of the European XFEL project were presented. The specification requirements fully determine the design of the mechanical support system. In order to achieve stability on the  $\mu\text{m}$  level large cross section for the girders, four fold support and proper material pairing is needed. The control system has to support these accuracy requirements. Novel ideas for planar adjustable PM quadrupoles and phase shifters were presented. They are more compact than EM and avoid any heat dissipation.

These ideas are the basis for the first prototypes of undulator segments, phase shifters and PPMQs to be built in the near future.

## ACKNOWLEDGEMENT

The help, discussions and support of my colleagues: M. Bräuer, P. Illinski, U. Hahn, H. Schulte-Schrepping, K. Tiedke, M. Tischer is gratefully acknowledged.

## REFERENCES

- [1] TESLA Technical Design Report Part V, The X-ray Free Electron Laser, G. Materlik, T. Tschentscher (Eds.) DESY 2001-011, ECFA 2001-209, TESLA-FEL2001-05, March 2001, [http://tesla.desy.de/new\\_pages/0000\\_TESLA\\_Project.html](http://tesla.desy.de/new_pages/0000_TESLA_Project.html)
- [2] TESLA XFEL Technical Design Report Supplement, R. Brinkmann, B. Faatz, K. Flöttmann, J. Rossbach, J. Schneider, H. Schulte-Schrepping D. Trines, T. Tschentscher, H. Weise, DESY 2002-167, TESLA-FEL2002-09, October 2002, [http://tesla.desy.de/new\\_pages/0000\\_TESLA\\_Project.html](http://tesla.desy.de/new_pages/0000_TESLA_Project.html)
- [3] J. Pflüger, M. Tischer, NIM A483, (2003), 388
- [4] S. Sasaki, Nucl. Instr. and Methods A347, (1994), 83
- [5] J. Bahrtdt, A. Gaupp, U. Englisch, W. Frentrup, M. Scheer, TESLA-FEL2000-11, [http://tesla.desy.de/new\\_pages/0000\\_TESLA\\_Project.html](http://tesla.desy.de/new_pages/0000_TESLA_Project.html)
- [6] E.L. Saldin, E.A. Schneidmiller, M.V. Yurkov, "The Potential for the Development of the X-Ray Free Electron Laser", TESLA-FEL 2004-02, [http://tesla.desy.de/new\\_pages/FEL\\_Reports/2004](http://tesla.desy.de/new_pages/FEL_Reports/2004)
- [7] J. Pflüger, H. Lu, T. Teichmann, NIM A429, (1999), 368
- [8] R. Tatchyn, NIM A341, (1994), 449
- [9] J. Pflüger, Y. Nikitina, NIM A381, (1996), 554
- [10] J. Pflüger, H. Lu, D. Köster, T. Teichmann, NIM A407, (1998), 386
- [11] J. Pflüger, P. Gippner, A. Swiderski, T. Vielitz, "Magnetic Characterization of the Undulator for the VUV-FEL at the TESLA Test Facility", Proceedings of the FEL99, August 23-26, 1999, Hamburg, Germany
- [12] J. Pflüger, M. Tischer, "A Prototype Phase Shifter for the Undulator Systems at the TESLA X-ray FEL", TESLA-FEL 2000-08 [http://tesla.desy.de/new\\_pages/0000\\_TESLA\\_Project.html](http://tesla.desy.de/new_pages/0000_TESLA_Project.html)
- [13] M. Tischer, P. Illinski, U. Hahn, J. Pflüger, H. Schulte-Schrepping, NIM A483, (2002), 418
- [14] U. Hahn, H. Schulte-Schrepping, "Crystal Monochromator based Emittance Measurements at the PETRA Undulator Beamline", SRI 2003, AIP Conference Proc. Vol 705, 533-536
- [15] BingXin Yang, "High resolution undulator measurements using angle-integrated spontaneous radiation", Proceedings of the PAC05, May 16-20, 2005, Knoxville, USA

# ELECTRON BEAM CHARACTERIZATION AT PITZ AND THE VUV-FEL AT DESY

K. Honkavaara\*, Hamburg University, 22761 Hamburg, Germany  
for the VUV-FEL team†

## Abstract

The VUV-FEL at DESY Hamburg is a user facility for SASE FEL radiation in the VUV wavelength range. The quality of the high brightness electron beam driving the VUV-FEL plays an important role for the performance of the facility. Prior to installation, the VUV-FEL electron RF gun has been fully optimized and characterized at the PITZ photoinjector test facility at DESY, Zeuthen, dedicated to develop high brightness electron sources for FEL projects like the VUV-FEL and the XFEL. We summarize here the results of transverse emittance optimization at PITZ and report on the upgrade of the PITZ facility presently under construction. At the VUV-FEL normalized projected transverse emittances around 1.4 mm mrad for 90% of a 1 nC bunch have been regularly measured. These emittance measurements are described here, as well as recent measurements of the longitudinal bunch profile using a transverse deflecting cavity.

## INTRODUCTION

The VUV-FEL [1], a SASE FEL user facility at DESY (Hamburg) operating in the wavelength range from vacuum ultraviolet to soft x-rays, has been commissioned during 2004 and in the beginning of 2005. The first lasing, at the wavelength of 32 nm, was achieved in January 2005 [2, 3], and the first user experiments started in summer 2005. Besides providing FEL radiation for the FEL studies and ex-

periments, the VUV-FEL is a piloting project of the European X-Ray Free Electron Laser Facility (XFEL) [4]. The electron linac driving the VUV-FEL is used also as a test bench for the International Linear Collider (ILC) [5].

The RF gun of the VUV-FEL has been optimized and characterized, prior its installation to the VUV-FEL accelerator tunnel in January 2004, at the PITZ photoinjector test facility at DESY, Zeuthen [6]. The PITZ facility has operated since 2002 as a test bench for the development of high brightness electron sources for FEL projects, and it is presently being upgraded to an electron beam energy up to 30 MeV.

The FEL process demands a bunched electron beam with a high peak current, a small transverse emittance, a small momentum spread, and a short bunch length. In order to achieve these high demands, accurate characterization of the electron beam is necessary. We summarize here measurements and optimization of the transverse emittance at PITZ and at the VUV-FEL. Measurements of the longitudinal phase space at PITZ are shortly described as well as the longitudinal bunch structure measurements at the VUV-FEL using a transverse deflecting cavity.

## PHOTOINJECTOR CONCEPT

The injector is a key element of a linear accelerator producing high brightness electron beams. The photoinjector consists of a laser driven RF gun with solenoid magnets, a booster cavity, and magnetic bunch compressors. In order to suppress the space charge induced emittance growth, a homogeneous transverse and longitudinal distribution of the laser pulse is desired. For the same reason, the accelerating field on the photocathode is as high as possible. The solenoid magnet located close to the photocathode is used to counteract the space charge induced emittance growth. It also contributes to a reduction of the correlated emittance via a so-called emittance compensation process [7]. A second solenoid (the bucking coil) is used to compensate the magnetic field on the photocathode to zero. In order to reduce the space charge induced emittance growth, a matching technique based on the so-called “invariant envelope” [8] is used: The beam should be at a waist on the entrance of the booster, and the energy gain of the booster should be selected correctly according to the beam size, the incoming beam energy, and the peak current. More details of this matching scheme is in [9].

The high peak current required for the FEL process is achieved by compressing the electron bunch. Typically a magnetic chicane bunch compressor downstream of a

\* katja.honkavaara@desy.de

† W. Achermann, V. Ayvazyan, N. Baboi, J. Bähr, V. Balandin, B. Beutner, A. Brandt, I. Bohnet, A. Bolzmann, R. Brinkmann, O.I. Brovko, J.P. Carneiro, S. Casalbuoni, M. Castellano, P. Castro, L. Catani, E. Chiodroni, S. Choroba, A. Cianchi, H. Delsim-Hashemi, G. Di Pirro, M. Dohlus, S. Düsterer, H.T. Edwards, B. Faatz, A.A. Fateev, J. Feldhaus, K. Flöttmann, J. Frisch, L. Fröhlich, T. Garvey, U. Gensch, N. Golubeva, H.-J. Grabosch, B. Grigoryan, O. Grimm, U. Hahn, J.H. Han, M. v. Hartrott, K. Honkavaara, M. Hüning, R. Ischebeck, E. Jaeschke, M. Jablonka, R. Kammering, V. Katalev, B. Keitel, S. Khodyachyhh, Y. Kim, V. Kocharyan, M. Körfer, M. Kollwe, D. Kostin, D. Krämer, M. Krasilnikov, G. Kube, L. Lilje, T. Limberg, D. Lipka, S. Liu, F. Löhler, M. Luong, C. Magne, J. Menzel, P. Michelato, V. Miltchev, M. Minty, W.D. Möller, L. Monaco, W. Müller, M. Nagl, O. Napoly, P. Nicolosi, D. Nölle, T. Nuñez, A. Oppelt, C. Pagani, R. Paparella, B. Petersen, B. Petrosyan, J. Pflüger, P. Piot, E. Plönjes, L. Poletto, D. Proch, D. Pugachov, K. Rehlich, D. Richter, S. Riemann, J. Rössch, M. Ross, J. Rossbach, M. Sachwitz, E.L. Saldin, W. Sandner, H. Schlarb, B. Schmidt, M. Schmitz, P. Schmüser, J.R. Schneider, E.A. Schneidmiller, S. Schnepp, H.-J. Schreiber, S. Schreiber, D. Sertore, S. Setzer, A.V. Shabunov, S. Simrock, E. Sombrowski, L. Staykov, B. Steffen, F. Stephan, F. Stulle, K.P. Sytchev, H. Thom, K. Tiedtke, M. Tischer, R. Treusch, D. Trines, I. Tsakov, A. Vardanyan, R. Wanzenberg, T. Weiland, H. Weise, M. Wendt, I. Will, A. Winter, K. Wittenburg, M.V. Yurkov, I. Zagorodnov, P. Zambolin, K. Zapfe

booster cavity is used. A sinusoidal accelerating field of the booster cavity induces a curvature in the longitudinal phase space. Thus, the compression of an off-crest accelerated bunch leads to a longitudinal bunch structure with a high peak current spike and a long tail. The energy-phase plane curvature can be removed by using a superconducting third harmonic cavity (3.9 GHz) [10] before the bunch compressor. The third harmonic cavity of the VUV-FEL is still under construction, and therefore the start-up lasing strategy of the VUV-FEL is similar than at the TTF-FEL [11]: A spike is used to produce the required peak current.

## PITZ

The PITZ facility has been built to develop and optimize high brightness electron sources for FEL projects. The first stage of the facility (PITZ 1) consisted of a laser system providing long trains of short, spatially and temporally homogeneous UV pulses, a 1.5 cell RF gun (1.3 GHz) with a Cs<sub>2</sub>Te photocathode, a solenoid system to compensate space charge induced emittance growth, and a diagnostic section for measurements of transverse emittance, bunch length, momentum, and momentum spread. Electron beam momentum of 4.7 MeV/c is reached when operating the RF gun with an input power of 3.3 MW. Since 2004 it is possible to operate the gun with a higher power resulting in an increased beam momentum (up to 5.2 MeV/c). The nominal bunch charge is 1 nC. A schematic overview of the PITZ 1 facility is shown in Fig. 1.

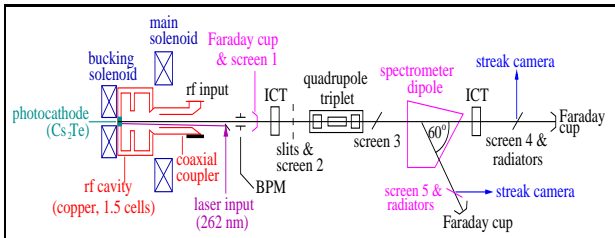


Figure 1: Schematic overview of PITZ 1. Beam direction is from left to right, and the total length is about 6 m.

In the following we concentrate on the optimization of the transverse emittance. Other results and more details of the PITZ facility are in [6, 12, 13, 14, 15].

### Emittance optimization

The transverse projected emittance at PITZ is measured using a single slit technique. The advantage of the slit technique is that the space charge effects, which otherwise need to be taken into account at low electron beam energies, are strongly suppressed. A 1 mm thick tungsten plate with a 50  $\mu\text{m}$  slit opening is used as a slit mask to produce a beamlet, which is imaged 1.01 m downstream on a Ce:YAG screen. Beamlets from three slit positions are taken into account in the emittance calculations. More details of the measurement technique and calculations are in [16, 17].

Optimization of the longitudinal and transverse profile of the photocathode laser pulse plays an important role when attempting to reach small emittances. A pulse shaper producing laser pulses with longitudinal flat-top profile is used at PITZ. The typical laser pulse length is around 20 ps with a rise and decay time of about 7 ps. When a flat-top laser pulse is used, the measured emittance is reduced at least by a factor of two compared to emittances measured with a gaussian laser pulse [14]. In order to find an optimum balance between the thermal (initial) and the space charge induced emittance, the transverse size of the laser pulse has been varied. The optimal transverse laser profile is radially homogeneous with a size of  $\sim 0.55$  mm (rms).

Besides the laser profile, also the RF phase of the gun cavity with respect to the laser phase, as well as settings of the two solenoids need to be optimized. A systematic optimization of these parameters has been performed at PITZ for the RF gun now in use at the VUV-FEL. The minimum normalized average emittance ( $\sqrt{\epsilon_x \epsilon_y}$ ) measured for a 1 nC bunch was around 1.7 mm mrad [6].

After the delivery of the VUV-FEL gun to DESY Hamburg, an other RF gun cavity, with a similar design, has been installed to PITZ. This cavity is operated with a higher gradient on the photocathode: 45 MV/m instead of 42 MV/m. This, in combination with some other subsystem upgrades, has resulted in an improved transverse emittance. Figure 2 shows measured horizontal ( $\epsilon_x$ ) and vertical ( $\epsilon_y$ ) normalized emittances as a function of the main solenoid current. A geometrical average ( $\epsilon_{\text{tr}} = \sqrt{\epsilon_x \epsilon_y}$ ) and results from ASTRA simulations [18] using a rotational symmetrical model are presented as well. The bucking solenoid is tuned to compensate the main solenoid field at the cathode for each main solenoid current. The RF phase is chosen to be close the phase providing the maximum electron beam energy. We can see that the behavior as function of the solenoid current agree with the prediction from simulations, and that the minimum measured average emittance is around 1.6 mm mrad.

### Longitudinal phase space

Besides the optimization of the transverse emittance, it is important to study and optimize the beam parameters also in the longitudinal phase space. At PITZ correlated measurements of the beam momentum and the temporal structure of the electron bunch (longitudinal bunch shape) are possible. The momentum distribution is measured on a Ce:YAG screen in a dispersive section of the spectrometer dipole (see Fig. 1). The temporal structure of the electron bunch is measured using a streak camera detecting light emitted when an electron beam traverses a Cherenkov radiator (silica aerogel). These measurements are possible both in the straight and in the dispersive section (see Fig. 1). Streak camera measurements in the dispersive section provide a combined measurement of the temporal and the momentum distribution of the electron bunch.

Figure 3 shows first results of longitudinal phase space

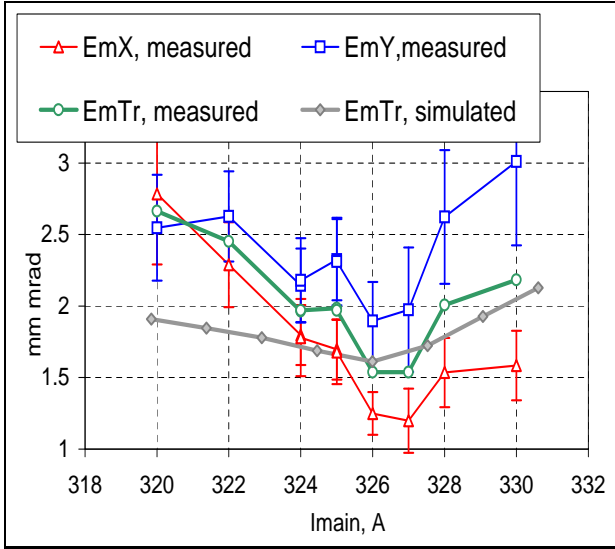


Figure 2: Normalized emittance measured at PITZ as a function of the main solenoid current. The electron beam momentum is 5.2 MeV/c, and the bunch charge 1 nC. The bucking solenoid is optimized for each main solenoid current. Horizontal (red) and vertical (blue) normalized emittances as well the geometrical average  $\sqrt{\epsilon_x \epsilon_y}$  (green) are shown. The grey curve is a result from simulations.

measurements. The left plot is the phase space distribution measured by the streak camera in the dispersive section. The right plot shows the simulated [19] phase space. We can see that the experimental results agree relatively well with the simulations. However, further studies and analysis are required in order to understand in detail the beam parameters in the longitudinal phase space. More details and recent results are in [15, 20].

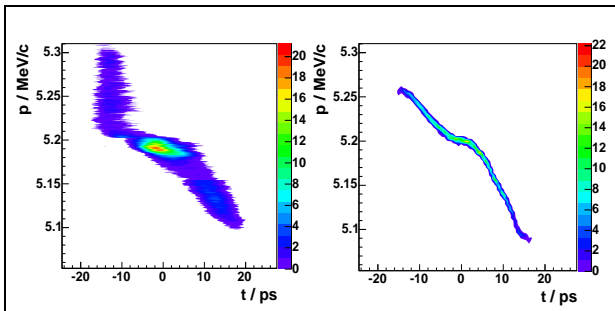


Figure 3: Measured (left) and simulated (right) longitudinal phase space. The vertical axis represents the electron beam momentum and the horizontal the temporal distribution of the bunch. Bunch charge is 1 nC.

### Upgrade of PITZ (PITZ 2)

Presently, the PITZ facility is being upgraded. The main goal of the upgraded facility (PITZ 2) is to further improve

of the transverse emittance and to study in detail the emittance conservation scheme.

The 5 MW klystron providing RF power for the gun cavity is now replaced by a 10 MW klystron. With this new klystron it is possible to operate the RF gun with a higher accelerating field, which improves the beam quality due to reduced space charge forces. A second major upgrade is the installation of a booster cavity. With the booster presently installed at PITZ the beam energy can be increased up to  $\sim 16$  MeV. Later, with a special booster designed for PITZ, the beam energy can be further increased up to  $\sim 30$  MeV. The location of the booster is chosen such that the distance from the photocathode to the entrance of the cavity is identical to the corresponding distance at the VUV-FEL injector. The beam diagnostic sections are being upgraded as well. With the new diagnostics tools it will be possible to measure the transverse emittance by different methods in several locations along the linac. Also slice emittance measurements will be possible in the future. An upgrade of the photocathode laser system, including replacement of the flashlamps by diode-pumped amplifiers and improvements on the laser beam line, has been already done. A laser system providing longitudinal flat-top laser pulses with a very short rise and decay time ( $< 2$  ps) is under development. More details and the first results of the upgraded PITZ facility are in [21].

## THE VUV-FEL

In the present stage, the VUV-FEL linac consists of a laser driven photoinjector, five accelerator modules with eight 9-cell superconducting TESLA cavities, two magnetic chicane bunch compressors, and six undulator segments to produce SASE FEL radiation. Figure 4 shows a schematic overview of the linac. With this layout electron beam energies up to  $\sim 730$  MeV can be achieved. Later, one or two accelerator modules can be added to increase the beam energy up to 1 GeV. During the commissioning emphasis has been on lasing at a wavelength of 32 nm, which requires an electron beam energy of 445 MeV.

The RF gun is operated with a gradient of 41 MV/m. The longitudinal laser pulse shape is nearly gaussian with an rms size of  $\sim 4.5$  ps. Later, if required, a similar laser pulse shaper as tested at PITZ providing longitudinally flat-top laser pulses can be installed to the VUV-FEL laser system. A complete TESLA module with eight superconducting cavities, placed about 2.5 m downstream of the photocathode, is used as a booster. In order to make use of the matching conditions discussed above the first four cavities are operated with a moderate gradient (12 MV/m). The last four cavities accelerate with the nominal gradient of  $\sim 20$  MV/m increasing the electron beam energy to 125 - 130 MeV before the first bunch compressor. At the second compression stage, the beam energy is about 370 MeV. The design normalized emittance is 2 mm mrad.

More details of the VUV-FEL photoinjector are in [22].

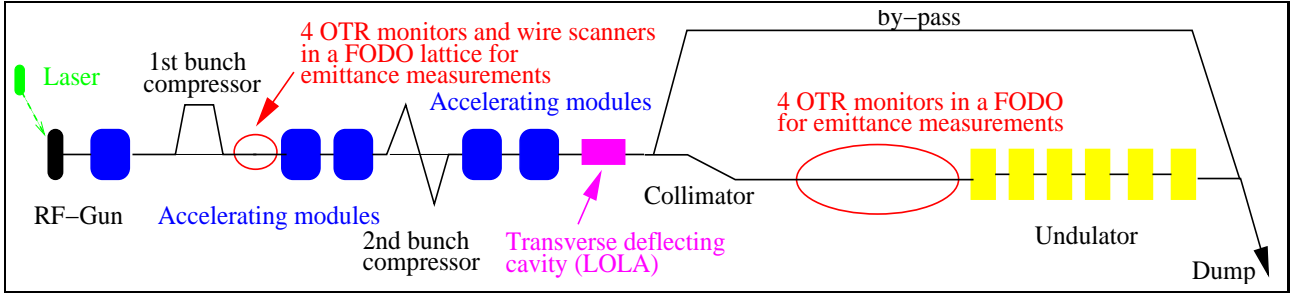


Figure 4: Present layout of the VUV-FEL linac (not to scale). Beam direction is from left to right. The total length is about 250 m. The LOLA cavity as well as the locations of the diagnostic sections dedicated to emittance measurements are indicated.

### Emittance measurements

Measurements of the transverse projected emittance are performed using a four-monitor method. In this method the transverse beam distribution (shape and size) is measured at four locations with a fixed beam optics. Along the linac there are two diagnostics sections dedicated to these measurements (see Fig. 4). The first one is a FODO lattice of six quadrupoles with a periodic beta function located downstream of the first bunch compressor at the beam energy of 127 MeV. The beam distribution is measured with four optical transition radiation (OTR) monitors combined with wire scanners. The second FODO lattice with four OTR monitors is upstream of the undulator at the full beam energy. The OTR monitor system is designed and constructed by INFN-LNF and INFN-Roma2 in collaboration with DESY. Detailed description of this system is in [23, 24, 25].

The transverse emittance is determined from the measured beam distribution and the known transport matrices using two techniques. The first one is based on least square fitting of the Twiss parameters and the emittance to the measured beam sizes. The second one uses tomographic reconstruction of the transverse phase space. The results obtained by both methods agree well with each other [26].

Since a small fraction of particles in the tails of the transverse beam distribution can have a significant influence on the transverse emittance, we are interested in, besides the emittance of the entire beam, the emittance of the high density core. This core is determined by cutting away 10% (an arbitrary choice) of particles in the tails of the two-dimensional transverse beam distribution. Horizontal and vertical emittances are calculated for the entire beam and for the core containing 90% of the beam intensity. All the calculations use the rms definition of the beam size.

Figure 5 shows the measured normalized horizontal ( $\epsilon_x$ ) and vertical ( $\epsilon_y$ ) rms emittances as well as the geometrical average ( $\epsilon_{tr} = \sqrt{\epsilon_x \epsilon_y}$ ) as a function of the current in the main solenoid. The measurements are performed in the diagnostic section after the first bunch compressor using OTR monitors. During these measurements the injector was operated with the nominal parameters, but it was not tuned to obtain the minimum emittance. The electron

beam was transported through the bunch compressor without compression (on-crest acceleration in the first accelerator module). The beam energy was 125 MeV, and the bunch charge 1 nC. The experimental results are shown both for 100% and 90% beam intensity. The solid line is the result

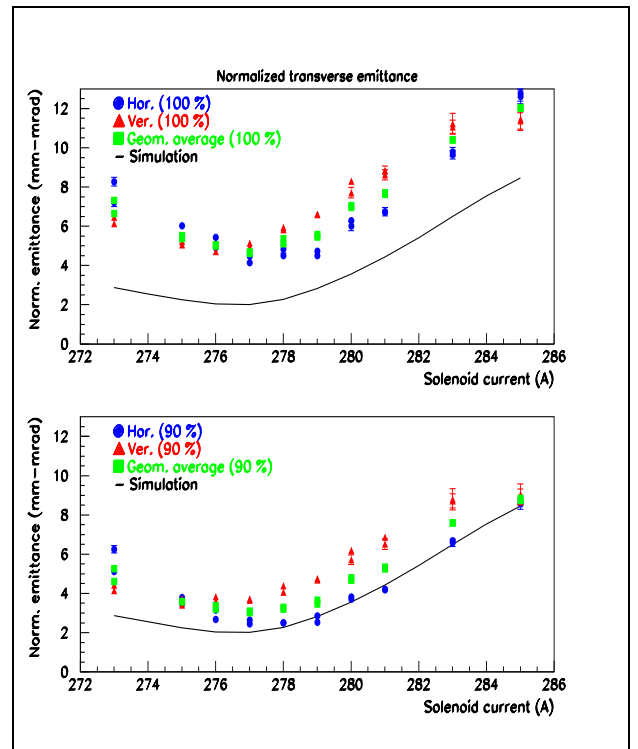


Figure 5: Normalized emittance measured at the VUV-FEL as function of the main solenoid current. Measurements have been repeated twice for each solenoid current. Electron beam energy is 125 MeV and bunch charge 1 nC. Bucking solenoid current is 20 A. Horizontal (blue) and vertical (red) normalized emittances as well as the geometrical average  $\sqrt{\epsilon_x \epsilon_y}$  (green) are shown both for the entire beam (top) and for the 90% beam intensity (bottom). The solid curve is a prediction from simulations. Emittances are calculated by the least square fitting technique, and the errors shown are statistical errors only.

from simulations [27] using 2 mm mrad normalized emittance. The observed behavior as a function of the solenoid current agrees well with the prediction from the simulation: the optimal solenoid current from the emittance point of view is 277 A, which corresponds to a magnetic field of 0.163 T.

In order to reach small emittances, we need to optimize, besides the laser and solenoid settings, also the beam injection to the first accelerator module. When the injector is carefully tuned, we regularly measure normalized emittances around 1.4 mm mrad for 90% of a 1 nC bunch at beam energy of 127 MeV. For the entire beam this value is typically around 2 mm mrad.

More details of the emittance measurements, as well as of the transverse electron beam diagnostics in general, are in [26], and a complete description of the emittance measurement set-up, image analysis, emittance calculations, and error analysis in [28].

When comparing the results obtained at PITZ and at the VUV-FEL, we need to keep in mind the differences in the measurement conditions. First of all, at PITZ flat laser pulses are used, while at the VUV-FEL the longitudinal laser pulse is shorter and nearly gaussian. Secondly, at PITZ the emittance has been measured and optimized at a low beam energy ( $\sim 5$  MeV) about 1.6 m downstream of the photocathode. At the VUV-FEL the emittance measurements are performed after the first accelerator module at the electron beam energy of 127 MeV about 29 m downstream of the cathode. The gradient and the location of the module is chosen such that the conditions fit for the matching conditions discussed above. The fact that the minimum emittance at PITZ and at the VUV-FEL is achieved with different setting of the solenoids can be explained by the emittance optimization at different locations. The emittances measured at PITZ and at the VUV-FEL agree with the expectations from simulations, and, taking into account the differences in measurement conditions, are consistent with each other.

Sofar, the emittance measurements at the VUV-FEL have been performed using the OTR monitors only. The commissioning of the wire scanners combined with the OTR monitors in the first FODO lattice is on-going, and a first cross-check of the results obtained by the OTR monitors and the wire scanners has been recently done showing a good agreement [26]. Optimization of the emittance measurement conditions in the second FODO lattice before the undulator has not yet finished, and therefore accurate emittance measurement have not yet been done there. Along the undulator there are seven wire scanners. The first tests to use these wire scanners for emittance measurements have been successfully done, and they are now available for emittance measurements.

### *Measurements of longitudinal bunch structure*

Measurements of the longitudinal bunch distribution are performed using different methods. In the injector, syn-

chrotron radiation emitted by the last dipole of the first bunch compressor is guided out of the accelerator tunnel and used for bunch length measurements by a streak camera and an interferometer [29]. A detailed description of the interferometer measurements is in [30]. After the both bunch compressors, a slit providing coherent diffraction radiation can be inserted into the beam pipe. The coherent (THz) radiation is used for on-line measurements of the bunch compression by means of a pyrodetector, and it can be used for bunch length measurements with interferometers as well. Additional experimental set-ups using THz radiation are under construction.

In order to resolve the bunch structure at the full bunch compression, two sophisticated diagnostics tools have been implemented to the VUV-FEL linac. The first one, still under commissioning, uses electro-optical sampling technique [31], and the second one, described more in detail below, is based on the use of a transverse deflecting cavity [32].

A transverse deflecting cavity, a powerful tool to measure the bunch structure of a compressed electron beam, has been installed to the VUV-FEL in a collaboration between SLAC and DESY. It is a 3.66 m long disk-loaded S-band waveguide structure. This structure, called LOLA according to its designers, was built at SLAC in 1968. At the VUV-FEL, it is mounted between the last accelerator module and the collimator section (see Fig. 4). This structure provides a time dependent electric field, which deflects the electron beam transversally such that the temporal distribution of the electron bunch is transformed to a spatial distribution. The streaked beam image, having the temporal distribution in the vertical direction, is measured on an off-axis OTR screen downstream of the LOLA cavity. A kicker magnet is used to select only one bunch from the bunch train to be streaked. Depending on the transverse

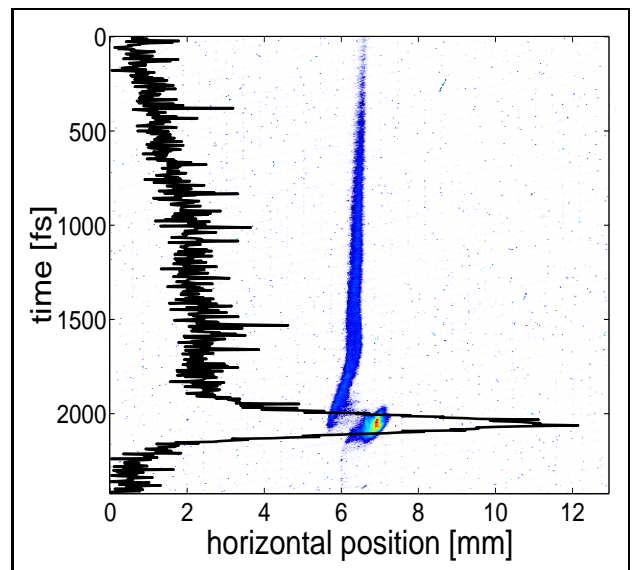


Figure 6: Longitudinal bunch distribution measured with the LOLA cavity during FEL operation.

focusing of the electron beam before the LOLA cavity, a resolution between 10 - 50 fs can be achieved.

Figure 6 shows an example of a streaked beam image measured during the FEL operation. The vertical direction represents the temporal structure of the bunch, which, as expected, has a leading spike and a long tail. The width of the spike depends on the FEL operation mode. In this example the width is  $\sim 120$  fs (FWHM). More details and results are in [33].

## SUMMARY AND OUTLOOK

In order to meet the high beam quality demands of the FELs, accurate characterization of the driving electron beam is essential. Dedicated beam diagnostics systems to measure and to optimize the beam parameters are implemented both at PITZ and at the VUV-FEL. In the transverse phase space the emphasis is presently on the measurements of the projected emittances, but both PITZ and the VUV-FEL have plans for slice emittance measurements in the future.

Since the VUV-FEL is already operated as a user facility, the time allocated to a detailed electron beam characterization is limited. Therefore, the emphasis of beam diagnostics will be more and more on the on-line measuring and monitoring of the beam parameters. The upgraded PITZ facility will continue detailed studies of the beam parameters and further develop high brightness electron sources.

## ACKNOWLEDGMENT

The author like to thank colleagues and collaborators contributing in the successful operation of PITZ and the VUV-FEL. Special thanks are due to M. Hüning, M. Krasilnikov, J. Rönisch, S. Schreiber, and F. Stephan for help in preparation of this paper.

## REFERENCES

- [1] The TTF FEL Team, "SASE FEL at the TESLA Test Facility, Phase 2", DESY-TESLA-FEL-2002-01
- [2] B. Faatz for the DESY VUV-FEL project team, "First results from the VUV-FEL at DESY", PAC 2005, Knoxville, Tennessee, May 16-20, 2005
- [3] S. Schreiber for the VUV-FEL team, "First lasing at 32 nm of the VUV-FEL at DESY", these proceedings
- [4] "TESLA XFEL: First stage of the X-ray laser laboratory. Technical design report, supplement", eds. R. Brinkmann *et al.*, DESY-2002-167 (2002). See also <http://xfel.desy.de>
- [5] <http://www.interactions.org/linearcollider>
- [6] M. Krasilnikov *et al.*, "Optimizing the PITZ electron source for the VUV-FEL", EPAC 2004, Luzern, Switzerland, July 5-9, 2004
- [7] B.E. Carlsten, "New photoelectric injector design for the Los Alamos National Laboratory XUV FEL accelerator", Nucl. Instr. Meth. **A285** (1989) 313-319
- [8] L. Serafini, "Overview on production and beam dynamics of high brightness beams", AIP Conference Proceedings CP395, *Nonlinear and Collective Phenomena in Beam Physics*, eds. S. Cattopadhyay, M. Cornacchia, C. Pellegrini, 1997
- [9] M. Ferrario *et al.*, "Conceptual design of the XFEL photoinjector", DESY-TESLA-FEL 2001-03, and references therein
- [10] J. Sekutowicz *et al.*, "A design of a 3rd harmonic cavity for the TTF2 photoinjector", DESY-TESLA-FEL-2002-05
- [11] S. Schreiber *et al.*, "Performance of the TTF photoinjector for FEL operation", Workshop "The physics and applications of high brightness electron beams", Chia Laguna, Sardinia, July 1-6, 2002, ed. J. Rosenzweig, G. Travish, L. Serafini, World Scientific, Singapore, 2003
- [12] A. Oppelt *et al.*, "The Photo Injector Test Facility at DESY Zeuthen: Results of the first phase", LINAC 2004, Lübeck, Germany, Aug 16-20, 2004
- [13] F. Stephan *et al.*, "Recent results and perspectives of the low emittance photo injector at PITZ", FEL 2004, Trieste, Italy, Aug 29 - Sep 3, 2004
- [14] V. Miltchev *et al.*, "Transverse emittance measurements at the Photo Injector Test Facility at DESY Zeuthen", FEL 2004, Trieste, Italy, Aug 29 - Sep 3, 2004
- [15] J. Rönisch *et al.*, "Longitudinal phase space studies at PITZ", these proceedings
- [16] V. Miltchev *et al.*, "Transverse emittance measurements at the Photo Injector Test Facility at DESY Zeuthen (PITZ)", DIPAC 2003, Mainz, Germany, May 5-7, 2003
- [17] M. Krasilnikov *et al.*, "Characterization of the electron source at the Photo Injector Test Facility at DESY Zeuthen", FEL 2003, Tsukuba, Japan, September 2003
- [18] ASTRA simulations by M. Krasilnikov (DESY, Zeuthen); ASTRA manual: <http://www.desy.de/~mpyfb>
- [19] ASTRA simulations by J. Rönisch (DESY, Zeuthen); ASTRA manual: <http://www.desy.de/~mpyfb>
- [20] J. Rönisch *et al.*, "Measurement of the longitudinal phase space at the photoinjector test facility at DESY in Zeuthen (PITZ)", DIPAC 2005, Lyon, France, June 6-8, 2005
- [21] A. Oppelt *et al.*, "Status and first results from the upgraded PITZ facility", these proceedings
- [22] S. Schreiber, "The injector of the VUV-FEL at DESY", these proceedings
- [23] K. Honkavaara *et al.*, "Design of OTR beam profile monitors for the TESLA Test Facility, phase 2 (TTF2)", PAC 2003, Portland, Oregon, May 12-16, 2003
- [24] A. Cianchi *et al.*, "Commissioning of the OTR beam profile monitor system at TTF/VUV-FEL injector", EPAC 2004, Luzern, Switzerland, July 5-9, 2004
- [25] L. Catani *et al.*, "A large distributed digital camera system for accelerator beam diagnostics", Review of Scientific Instruments **76**, 073303 (2005)
- [26] K. Honkavaara *et al.*, "Transverse electron beam diagnostics at the VUV-FEL at DESY", these proceedings
- [27] ASTRA simulations by Y. Kim (DESY, Hamburg); ASTRA manual: <http://www.desy.de/~mpyfb>

- [28] F. Löhle, "Measurements of the transverse emittance at the VUV-FEL", to be published as DESY-THESIS 2005-014 and TESLA-FEL 2005-03, Diploma Thesis, Hamburg University, 2005.
- [29] L. Fröhlich and O. Grimm, "Bunch length measurements using a Martin-Puplett interferometer at the VUV-FEL", these proceedings
- [30] L. Fröhlich, "Bunch length measurements using a Martin-Puplett interferometer at the VUV-FEL", DESY-THESIS-2005-011 and TESLA-FEL 2005-02, Diploma Thesis, Hamburg University, 2005
- [31] B. Steffen *et al.*, "Electro optic bunch length measurements at the VUV-FEL at DESY", PAC 2005, Knoxville, Tennessee, May 16-20, 2005
- [32] P. Emma *et al.*, "A transverse RF deflecting structure for bunch length and phase space diagnostics", PAC 2001, Chicago, Illinois, June 18-22, 2001
- [33] M. Hünig *et al.*, "Observation of femtosecond bunch length using a transverse deflecting structure", these proceedings

# High-precision optical synchronization systems for x-ray free electron lasers

Axel Winter, Peter Schmüser, Universität Hamburg, Hamburg, Germany,  
 Holger Schlarb, DESY, Hamburg, Germany,  
 F. Ömer Ilday, Jung-Won Kim, Jeff Chen, Franz X. Kärtner,  
 Massachusetts Institute of Technology, Cambridge, MA, USA,  
 D. Cheever, T. Zwart, D. Wang  
 MIT Bates R&E Center, Middleton, MA 01949, USA.

## Abstract

Next generation free electron lasers aim to generate x-ray pulses with pulse durations down to 30 fs, and possibly even sub-fs. Synchronization of the probe system to the x-ray pulses with stability on the order of the pulse width is necessary to make maximal use of this capability. We are developing an optical timing synchronization system in order to meet this challenge. Optics has two fundamental advantages over traditional RF technologies: (i) optical frequencies are in the 100 THz range, enabling femtosecond resolution, and (ii) photons are immune to electromagnetic interferences, easing noise-free transportation of the signals. In the scheme described here, a train of short optical pulses, with a very precise repetition frequency, are generated from a mode-locked laser oscillator and distributed via length-stabilized optical fibers to points requiring synchronization. The timing information is imbedded in the repetition frequency and its harmonics. First results achieved in an accelerator environment are reported.

## INTRODUCTION

One of the key challenges for the new fourth generation light sources such as the XFEL is to implement a timing stabilization and distribution system that allows the full exploitation of the potentially  $\sim 10$  fs x-ray pulse for time-resolved studies. To this end, an ultra-stable timing and synchronization system must be implemented, covering the critical subsystems of the machine and the experimental area, which are spread over distances as large as several kilometers.

The electron beam needs to enter the undulator with timing jitter comparable to the pulse duration, which puts significant pressure on the synchronization system of the XFEL and requires point-to-point stabilization of various RF frequencies for the critical components (booster section, injector, bunch compressors and experimental area) with femtosecond precision. This translates to an amplitude and phase stability of the RF in the critical cavities of  $10^{-4}$  and 0.01 deg respectively. The required amplitude stability levels have already been achieved in present day facilities, e.g. at JLAB and the DESY VUV-FEL [1, 2]. The best phase stability reported for superconducting cavities is on the order of 0.03 degrees; improving this to the 0.01 deg level (21 fs at 1.3 GHz) seems feasible. However, in order to accurately measure the phase stability, one

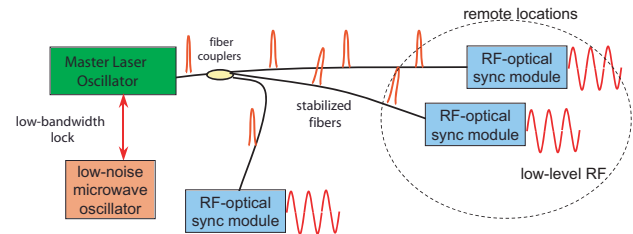


Figure 1: Schematic of the optical timing synchronization system.

requires a high-quality reference with much smaller phase jitter than the signal to be measured. A key challenge is to provide this reference in facilities spanning a few kilometers in length.

These requirements on the timing stability appear to be beyond the capability of traditional RF distribution systems based on temperature-stabilized coaxial cables. A promising way to reach this goal is by using an optical transmission system, depicted schematically in Figure 1 [3]. A train of sub-picosecond pulses of light generated from a mode-locked laser with very low timing jitter is distributed over actively length-stabilized optical fiber links to an arbitrary number of remote locations. The precise repetition frequency of the pulse train, as well as its upper harmonics, contain the synchronization information. At the remote locations, low-level RF signals can be extracted simply by using a photodiode and a suitable bandpass filter to pick the desired harmonic of the laser repetition rate, or by phase locking an RF source to a harmonic of the pulse train [4].

## TIMING STABILITY REQUIREMENTS FOR THE X-RAY PULSES

The layout of the European XFEL is shown in Figure 2 as an example of a fourth generation light source. The most critical sections of the machine in terms of inducing timing jitter onto the electron bunch are the injector and booster sections. Here, the electron bunch is accelerated off-crest to induce a chirp to make bunch compression possible. If amplitude and phase of the RF inside the cavities varies, this translates to a change in the centroid energy of the electron bunch, which is in turn directly converted into timing jitter by the bunch compressor chicane. A timing jitter on the order of the desired x-ray pulse width requires amplitude

and phase stability of  $10^{-4}$  and 0.01 deg respectively. This condition is relaxed by an order of magnitude in the main drive linac, as the on-crest acceleration makes the electron bunch less susceptible to amplitude and phase errors. If a seeding option is considered requiring an external laser system, as proposed for e.g. the FERMI facility [5], the timing jitter between the seed laser pulse and the electron bunch becomes a crucial issue for the quality of the x-ray pulse generated. Ideally, the seed laser pulse should have a flat-top profile and its pulse-width should be comparable to the electron bunch length. If a large timing jitter is present, the efficiency will drop dramatically and this timing jitter will directly transfer onto the final x-ray pulse. The seed laser is one of the components of the accelerator requiring the most stable reference and tightest lock possible. A similar argument is true for the probe laser systems in the experimental hall. To fully exploit the potential of a  $\sim 10$  fs long x-ray pulse, the timing jitter between the probe pulse and the x-ray pulse must be kept to a minimum. Single-shot arrival time measurements might make it possible to sort the data taken afterwards according to the arrival time of the electron bunch, but a reliable arrival time measurement with 10 fs resolution has not been shown to date. Furthermore, the time it takes to accumulate a full data set increases drastically as a result of timing jitter between pump and probe pulses. Therefore, the probe laser systems also require a tight synchronization to the accelerator reference frequency, which makes a the stable distribution of that reference frequency to the experimental hall a key challenge [6]. A possible solution is direct seeding of fiber amplifiers and Ti:Sapphire-based amplifiers with the optical pulses, distributing the timing information, or their second harmonics, respectively. This scenario has the inherent advantage that no timing jitter is added due to the generation of the seed pulse. Additional jitter imparted during the amplification process must be minimized.

## MODE-LOCKED FIBER LASERS

Mode-locked fiber lasers are a natural choice to realize an optical master oscillator, because of the ease of coupling to the fiber distribution system, their excellent long-term stability, and the well-developed and mature component base available at the optical communications wavelength of 1550 nm. Recently, their technical capabilities have also improved significantly [7, 8]. Yb-doped and Er-doped fiber lasers offer stable and practical platforms for short pulse generation, at  $1\mu\text{m}$  and  $1.5\mu\text{m}$ , respectively. Fiber lasers can generate pulses from picosecond down to 35 fs in duration by simultaneous phase coherent lasing of multiple longitudinal modes spaced in frequency by the pulse repetition rate of the laser. During photodetection, these optical modes beat in the photodetector and generate all harmonics of the repetition rate within the bandwidth of the photodetector.

Mode-locking is initiated by a mechanism providing lower loss (hence, higher net gain) for a pulse than for

continuous wave (cw) radiation, leading to pulse formation from intra-cavity noise as soon as the laser reaches a certain intracavity power. In the case of active mode-locking, this is a high-speed modulator. For passively mode-locked lasers, this is achieved by a real or artificial saturable absorber. For brevity, we restrict the following description to passive mode-locking. Once the pulses are shortened, the laser dynamics are dominated by an interplay of group velocity dispersion (different frequencies have different speeds) and Kerr nonlinearity (the refractive index depends on intensity), leading to the formation of soliton-like pulses, which intrinsically balance dispersion and nonlinearity [9]. As the gain has a finite bandwidth, the generated pulses need to be stabilized by the saturable absorber, which favors the pulse and suppresses any cw-radiation. At the simplest level, short-pulse laser dynamics can be characterized by four processes: gain, saturable absorption, Kerr nonlinearity, and dispersion interacting in a repetitive way, defined by the physical cavity (Fig. 3a).

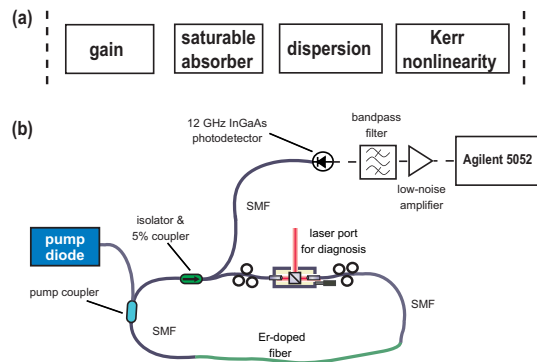


Figure 3: (a) The four effects governing pulse shaping in mode-locked lasers. (b) Schematic of the experimental setup: SMF, single-mode fiber.

In fiber lasers, the fiber assumes multiple roles, providing nonlinear and dispersive effects that dictate the soliton-like pulse shaping mechanism and moreover shielding against fast environmental fluctuations. The Er- or Yb-doped fiber segments form the gain medium, pumped conveniently by low-cost, fiber-coupled 980 nm diode lasers. A representative schematic of the laser is presented in Figure 3b, where saturable absorption is implemented by nonlinear polarization rotation in the fiber.

## NOISE PERFORMANCE OF MODE-LOCKED FIBER LASERS

It is essential that the laser serving as the master oscillator has extremely low timing jitter, particularly at high frequencies ( $> 10$  kHz), where further suppression through feedback is difficult. The timing of the pulse circulating in the laser cavity is affected by the intrinsic noise sources such as pump noise and amplified spontaneous emission noise from the amplification process. Ultimately, the timing jitter is limited by quantum fluctuations in the number

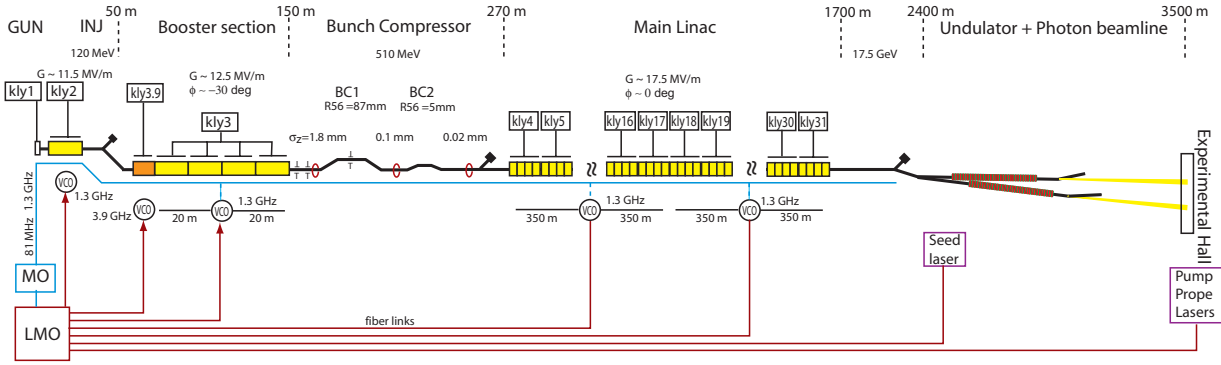


Figure 2: Layout of a 4th generation light source.

of photons making up the pulse and the incoherent photons added in the cavity due to spontaneous emission.

The noise characteristics of mode-locked lasers is well-described using soliton-perturbation theory, along with quantum noise sources [10, 11]. These perturbations cause fluctuations in amplitude, phase, timing and center frequency. The last of these further contributes to timing in the presence of dispersion, *i.e.* a shift in center frequency is translated into timing shift *via* dispersion, which is known as the Gordon-Haus effect [12]. For a fundamentally mode-locked fiber laser with small net dispersion and otherwise typical parameters, the quantum-limit is extremely small, on the order of 1 fs (from 1 kHz to 25 MHz, for a repetition rate of 50 MHz).

The noise performance of both an Er-doped fiber laser (EDFL) and an Yb-doped fiber laser (YDFL) were characterized. The EDFL is a stretched-pulse laser, implementing dispersion management [13] producing pulses compressible down to 100 fs and 1 nJ of energy at a repetition rate of 40 MHz, centered at 1550 nm. A schematic of the EDFL and the experimental setup is shown in Figure 3. The YDFL is configured to produce pulses compressible down to 70 fs with 2 nJ energy content, with a repetition rate of 36 MHz, centered at 1030 nm [7]. The YDFL (not shown) has a cavity similar to that of the EDFL. Both of the lasers are free-running, in the sense that the cavity length is uncontrolled and subject to slow, thermally induced fluctuations.

The amplitude noise of the fiber lasers has been characterized. Figure 4 shows the relative intensity noise (RIN) of both lasers from 10 Hz to 1 MHz. The EDFL shows slightly lower high-frequency noise than the YDFL, which may be due to the different amplifier media and pulse shaping processes at work. The integrated RIN measured from 10 kHz to 1 MHz is about 0.04% rms for the YDFL, and 0.03% rms for the EDFL, compared to the average power level. Figure 5 shows the single sideband phase noise spectrum of the harmonic at 1.3 GHz extracted from the pulse train upon photodetection and filtering. This phase noise

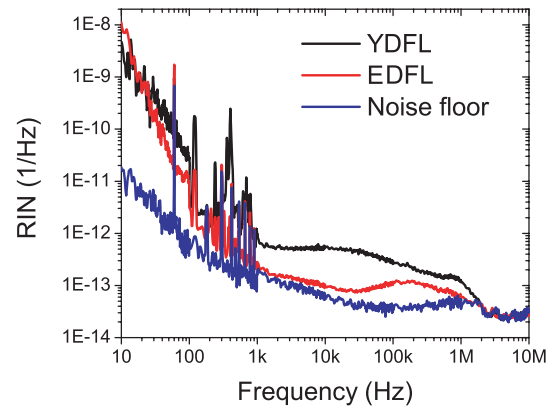


Figure 4: Relative intensity noise (RIN) of the EDFL and YDF, along with the measurement noise floor.

spectrum can be converted into a timing jitter using

$$\Delta t = \frac{\sqrt{2 \int L(f') df'}}{2\pi f_0}. \quad (1)$$

The integrated timing jitter from 1 kHz to the respective Nyquist bandwidths, *i.e.*, half of the laser repetition rate, is measured to be about 18 fs and 10 fs for the YDFL and EDFL, respectively. For comparison, the phase noise of a very low noise frequency generator, a Marconi 2041, is also plotted. As the lasers are free running, the performance of the microwave oscillator is slightly superior in the low frequency regime ( $< 10$  kHz), but at frequencies of  $\sim 100$  kHz, the mode locked lasers reach a comparable level of stability, with the EDFL having the lowest noise among the three at frequencies higher than 20 kHz. Both lasers would be already suitable for an overall sub-100 fs timing distribution system, which is an important next step to achieve in several FEL facilities. On the long run, the EDFL seems to be a stronger candidate for a master oscillator due to the availability of a larger variety of components at 1550 nm, and perhaps more importantly, transmission fibers with both signs of dispersion, which allow the construction of dispersion-compensated fiber links.

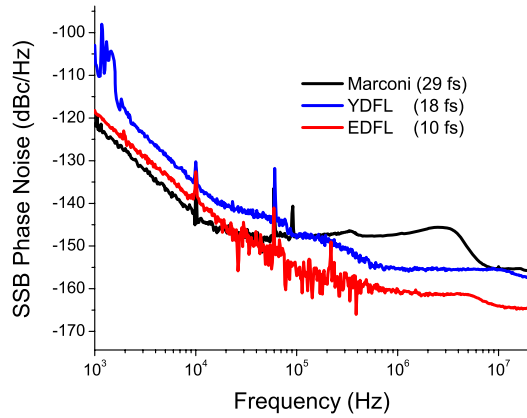


Figure 5: Single-sideband phase noise spectral density for the EDFL, YDFL, and a Marconi 2041 signal generator.

The measured timing jitter for both lasers is substantially higher than the noise limit given by the spontaneous emission noise. Several effects in the photodetection process lead to significant distortion of the actual phase noise spectrum. Due to the limited optical power that can be applied to a photodiode and subsequent filtering of a single harmonic of the laser repetition rate, the power level of this harmonic is on the order of  $-20$  dBm, even when saturating a typical photodetector. The thermal noise floor of the 50 Ohm resistor used to terminate the photodiode is at  $-178$  dBm. These limitations results in a minimum noise floor of  $-158$  dBc for the single sideband phase noise. The phase noise measurement device employed in this study (Agilent 5052) implements a correlation technique, which provides an additional noise suppression of up to 10 dB. Even with this improvement, the phase noise of the reference oscillator itself constitutes another measurement limit. Another effect, which plagues phase noise measurements, is amplitude to phase conversion in the photodiode [14]. The EDFL and YDFL have extremely low intensity fluctuations, nevertheless amplitude to phase conversion may contribute as much as 5 fs additional timing jitter.

## MEASUREMENTS IN AN ACCELERATOR ENVIRONMENT

In order to verify that laboratory performance can be transferred to an accelerator environment without degradation, measurements were conducted at the MIT-Bates Linear Accelerator Center. We utilized a 500 m-long single-mode optical fiber link, which was already installed to achieve picosecond-stability optical signal transmission. The experiment consisted of three separate parts:

- (i) Locking of the EDFL to the S-band master oscillator at the Bates Facility to reduce the close-in noise of the laser system,
- (ii) Stabilizing the fiber link with a RF-based feedback to reduce the timing jitter added by the transmission to a few

femtoseconds,

- (iii) Recovering a returning RF signal after 1 km of total travel through the fiber link with minimal added jitter.

The entire experiment was conducted over a time span of 3 weeks. The fiber laser worked reliably during this time without loss of mode-locking or significant increase of its phase noise.

### Locking of the EDFL to the S-band reference

A schematic of the experiment is shown in Figure 6. The EDFL runs at a repetition rate of 40.22 MHz, such that the 72nd harmonic is at the desired synchronization frequency of 2.856 GHz. The laser is locked to the reference using a phase-locked loop (PLL), generating an error signal by comparing the 72nd harmonic of the laser repetition rate to the S-band reference. This signal is fed back to a fiber stretcher, onto which 2 meters of the laser cavity fiber are wound. By controlling the fiber length, the repetition rate is adjusted. The unity gain point of the PLL has to be chosen carefully to ensure that the final phase noise of the signal is as low as possible. In fact, the EDFL becomes the *de facto* master oscillator of the facility. By locking to an RF reference for better low frequency stability, the resulting phase noise of the laser combines the good low-frequency properties of the RF oscillator and the excellent high-frequency properties of the free-running EDFL. Hence, a net improvement of the phase noise is achieved.

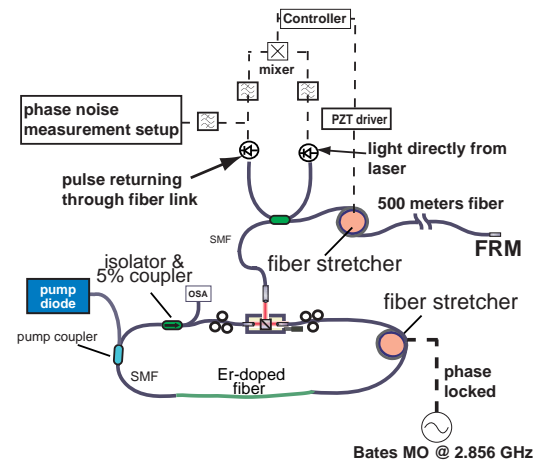


Figure 6: Schematic setup of the setup at MIT Bates Laboratory.

### Stabilization of the fiber link

Optical fibers exhibit a temperature dependent change of the refractive index, which causes arrival time jitter of a pulse propagating through the fiber. A typical value is  $10^{-6}/\text{C}^\circ$  [15], which corresponds to a fluctuation of 5 ps for a link length of 1 km and a temperature stability of  $1 \text{ C}^\circ$ . This makes a stabilization scheme mandatory. Presently, there are two different approaches to stabi-

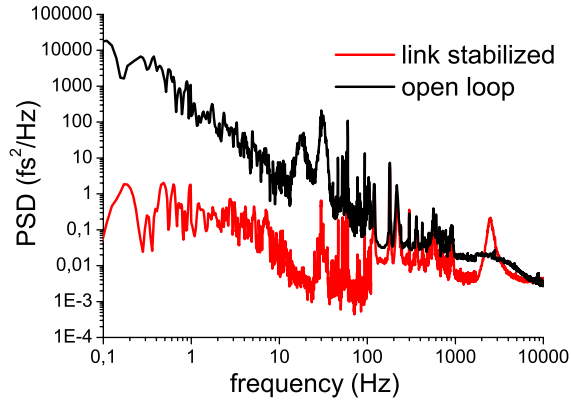


Figure 7: Mixer output signal of the RF fiber link stabilization.

lize the fiber length, both relying on a fiber stretcher with sufficient stretch to adjust for length fluctuations. One approach is to interferometrically stabilize the link: light from a single-frequency laser is sent through the link and beat with the returning, frequency-shifted light, thus generating an RF frequency equal to the difference frequency of the optical waves. The phase difference of the optical waves is directly transferred into a phase difference of the recovered RF frequency, which results in a very high resolution phase detector and facilitates the locking [16]. However, this scheme stabilizes the phase velocity and not the group velocity. If any information is transmitted over the fiber link, it will travel with the group velocity. The difference between these two velocities is on the order of  $10^{-2}$  and any temperature and stress dependent changes are difficult to control.

Stabilizing the fiber link using optical pulses has the inherent advantage of directly stabilizing the group velocity unlike schemes based on interferometric stabilization. Part of the light at the end of the link is reflected back into the same fiber using a Faraday rotator mirror. This mirror reflects the light with a 90 degree rotation of the polarization, counteracting the effects of residual birefringence in the fiber. There are two possible feedback schemes that can be employed. For a coarse lock, an RF-based scheme is used and optical cross-correlation can be utilized for a fine lock. In the former scheme, part of the light directly from the laser and light returning through the fiber link are photodetected using two high-bandwidth photodiodes. Out of the resulting RF spectrum a harmonic is selected (1 GHz, in the present study) and combined in quadrature in a mixer. The resulting phase error signal is fed back to the fiber stretcher. The mixer output is monitored with a high-resolution signal analyzer to assess the performance of the lock.

The results for both open and closed loop scenarios stabilizing the MIT-Bates fiber link mentioned above, is shown in Figure 7. If the loop is open, the jitter in a bandwidth between 0.1 Hz and 5 kHz amounts to 66 fs, which

is reduced to 12 fs when the feedback is active. It should be emphasized that these results are by no means the limit achievable using this simple RF feedback approach. Operating at a higher harmonic will lead to a linear increase of the resolution of the mixer. We expect to be able to decrease the residual timing jitter by a factor 5-10 if comparison frequencies in the 5-10 GHz range are used.

We conclude that a fiber link of 500 meters length can readily be stabilized to the 10 fs level using RF techniques alone. For a fine lock, it is possible to employ optical cross-correlation of the pulse coming directly from the laser with the one returning through the fiber. Here, the resolution depends predominantly on the pulse width used. For the proposed distribution system with a pulse length of several hundred femtoseconds, the resolution of the cross correlator can easily surpass the resolution presently achieved by an RF-based feedback by a factor of 100. If optical cross correlation is used as a second, additional feedback scheme, a stability of below a femtosecond is feasible [17]. Here, both pulses are overlapped either inside a crystal for second-harmonic generation or on a two-photon absorption detector. This results in a strong signal with a duration on the order of the pulse length of the incident pulses. This increases the resolution of this optical phase detector by a factor of 50 compared to the RF approach.

### Recovering the RF signal after Transmission

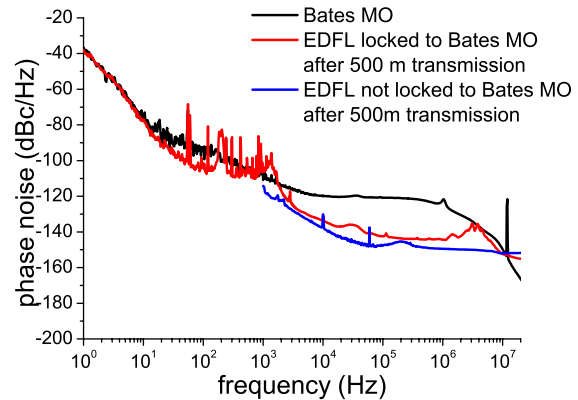


Figure 8: Single sideband phase noise of the Bates Reference Oscillator, the EDFL locked to the reference after transmission through the link and the free running EDFL.

The crucial question for any timing distribution system is the transmission of various RF signals with the required level of stability. After stabilizing the fiber link (500 m-long) and locking the EDFL to a local RF source, the phase noise of the signal at the end of the fiber link is the relevant parameter. Figure 8 shows the phase noise of the RF master oscillator at the MIT-Bates Facility and of the EDFL locked to the RF source after returning through the fiber link (total travel distance of 1 km). It is clear that the laser follows the

RF master oscillator extremely well for the lower frequency range. For offset frequencies between 100 Hz and 10 kHz, there is technical noise added showing as spurs at 60 Hz and its harmonics. This is due to the driver of the pump diode and can be eliminated by running the pump diodes on battery power, or better isolation of the diode driver. At an offset frequency of 1.5 kHz, the free running spectra of the laser and the RF source meet, which corresponds to the optimal unity gain frequency for the PLL. As can be seen in Figure 8, the locked EDFL phase noise spectrum is almost identical to the free running laser spectrum inside the locking bandwidth (blue line). The difference in these two is due to technical issues in the photodetection process, rather than additional noise due to the fiber transmission. The phase locking of the EDFL to the MIT-Bates master oscillator source adds around 30 fs timing jitter. This is reduced to a few femtoseconds, if one ignores the technical noise spurs. The absolute phase noise is reduced, even taking the excess timing jitter due to the phase-lock into account, from 272 fs to 178 fs in a bandwidth of 10 Hz to 20 MHz. Including the residual noise of the fiber link stabilization, the complete system adds less than 50 fs of timing jitter in a bandwidth of 0.1 Hz to 20 MHz.

## CONCLUSION AND OUTLOOK

In conclusion, mode-locked fiber lasers producing sub-ps pulses can serve as ultra-low noise master oscillators for timing distribution in next-generation light sources. The main advantage of mode-locked fiber laser is the excellent noise performance at high frequencies, the high quality and availability of pump sources and components in the 1550 nm wavelength range. Measurements show a high-frequency performance surpassing that of microwave oscillators with ultra-low phase noise. We have demonstrated sources with record low timing jitter of 10 fs in a bandwidth of 1 kHz to the Nyquist frequency. Such sources can be made readily available for sub-100 fs and potentially sub-50 fs timing distribution. We have demonstrated the operation of a complete timing distribution system consisting of the master laser oscillator locked to the S-band reference oscillator and one 500 m-long stabilized fiber link. The residual timing jitter due to the fiber link is 12 fs rms between 0.1 Hz and 5 kHz using a basic RF feedback system. Sub-fs timing jitter for the fiber link is feasible with optical cross correlation. The total added jitter due to locking of the laser to the microwave oscillator is 30 fs, leading to sub-50 fs of added jitter in a bandwidth of 0.1 Hz to 20 MHz. Overall, the way to a timing distribution system, with point-to-point jitter of 10 fs is outlined. Finally, it should be noted that transition from a laboratory implementation of this scheme to operation in a real-world accelerator environment has been remarkably smooth. We gratefully acknowledge the support from the MIT Bates staff during these experiments.

## REFERENCES

- [1] M. Liepe, "Superconducting RF and RF Control" Proceedings of the ERL 2005 Workshop, Jefferson Lab, Newport News, VA.
- [2] S. Simrock, "Overview of options for RF control & state of the art, simulation results and performance test results" Proceedings of the ERL 2005 workshop, Jefferson Lab, Newport News, VA.
- [3] J. W. Kim, F. Ö. Ilday, F. X. Kärtner, O. D. Mücke, M. H. Perrott, W. H. Graves, D. E. Moncton, and T. Zwart, "Large scale timing distribution and RF-synchronization for FEL facilities," FEL Conference 2004, Trieste, Italy, 2004.
- [4] J. Kim, F. X. Kärtner, and M. H. Perrott, "Femtosecond synchronization of radio frequency signals with optical pulse trains," *Opt. Lett.* **29**, 2076-2078 (2004).
- [5] C. J. Boccetta et. al., "FERMI @ Elettra: A seeded harmonic cascade FEL for EUV and soft x-rays", Proceedings of the FEL 2005, Stanford, CA.
- [6] A. Winter, E.-A. Knabbe, S. Simrock, B. Steffen, N. Ignachin, A. Simonov, S. Sytov, "Femtosecond synchronization of ultrashort pulse lasers to a microwave RF clock," Proceedings of the PAC 2005, Knoxville TN.
- [7] F. Ö. Ilday, J. R. Buckley, H. Lim, and F. W. Wise, "Generation of 50-fs, 5-nJ pulses at 1.03  $\mu\text{m}$  from a wave-breaking-free fiber laser," *Opt. Lett.* **28**, 1365-1367 (2003).
- [8] F. Ö. Ilday, J. R. Buckley, W. G. Clark, F. W. Wise, "Self-similar evolution of parabolic pulses in a laser," *Phys. Rev. Lett.* **92**, 3902 (2004).
- [9] H. A. Haus, "Mode-locking of lasers," *IEEE J. Sel. Top. Quantum Electron.* **6**, 1173-1185 (2000).
- [10] S. Namiki, and H. A. Haus, "Noise of the stretched pulse fiber ring laser: part I - theory," *IEEE J. Quantum Electron.* **33**, 649-659 (1997).
- [11] C. X. Yu, S. Namiki, and H. A. Haus, "Noise of the stretched pulse fiber ring laser: part II - experiments," *IEEE J. Quantum Electron.* **33**, 660-668 (1997).
- [12] J. P. Gordon, and H. A. Haus, "Random walk of coherently amplified solitons in optical fiber transmission," *Opt. Lett.* **11**, 665-667 (1986).
- [13] K. Tamura, E. P. Ippen, H. A. Haus, and L. E. Nelson, "77-fs pulse generation from a stretched-pulse mode-locked all-fiber ring laser," *Opt. Lett.* **18**, 1080-1082 (1993).
- [14] E. N. Ivanov, S. A. Diddams and L. Hollberg, "Analysis of noise mechanisms limiting the frequency stability of microwave signals generated with a femtosecond laser," *IEEE J. Sel. Top. Quantum Electron.* **9**, 1059-1065 (2003).
- [15] C. E. Lee, H. F. Taylor, A. M. Markus, and E. Udd, "Optical-fiber Fabry-Perot embedded sensor," *Opt. Lett.* **14**, 1225-1227 (1989).
- [16] J. W. Staples, and R. Wilcox, "Fiber transmission stabilization by optical heterodyning techniques and synchronization of mode-locked lasers using two spectral lines", Proceedings of the FEL 2005, Stanford, CA, and references therein.
- [17] T. R. Schibli, J. Kim, O. Kuzucu, J. T. Gopinath, S. N. Tandon, G. S. Petrich, L. A. Kolodziejski, J. G. Fujimoto, E. P. Ippen, and F. X. Kärtner, "Attosecond active synchronization of passively mode-locked lasers by balanced cross correlation," *Opt. Lett.* **28**, 947 (2003).

# OPTICAL LASER SYNCHRONIZED TO THE DESY VUV-FEL FOR TWO-COLOR PUMP-PROBE EXPERIMENTS

Ingo Will (MBI, Berlin)

Harald Redlin, Stefan Düsterer, Josef Feldhaus, Elke Plönjes (DESY, Hamburg)

## Abstract

The VUV-FEL at DESY provides ultra-short pulses with pulse durations below 50 fs. In order to utilize the short pulse duration for time resolved experiments, an OPCPA laser system has been installed delivering 150 fs pulses at a wavelength of 800 nm with 50  $\mu\text{J}$  pulse energy at 1 MHz repetition rate during the FEL burst. The laser is synchronized to the FEL with an accuracy better than 0.5 ps. In addition, the delay between optical laser and FEL pulses can be precisely adjusted, enabling high-resolution two-color pump-probe experiments.

The paper describes the laser system and the synchronization concept. First results of measurements of the synchronization accuracy by using a streak camera are presented.

## INTRODUCTION

The VUV-FEL at DESY [1] presently provides ultra-short pulses with pulse durations below 50 fs in the VUV wavelength range. To explore a wide field of time resolved applications using two-color pump-probe experiments, a supplementary laser providing ultrashort pulses in the visible and near-infrared spectral range is required. Such a laser should generate femtosecond pulses with the same temporal structure as the pulses from the VUV-FEL. A particularly important feature of this FEL is that it generates trains (bursts) of femtosecond pulses instead of single pulses in its standard operation mode. The typical spacing of the individual pulses ("micropulses") in the train presently amounts to 1  $\mu\text{s}$ , i.e. the repetition rate in the train is 1 MHz. Consequently, the solid-state laser should be able to generate similar pulse trains which may be up to 800  $\mu\text{s}$  long in future operation of the FEL. Naturally, the individual femtosecond pulses

of the train should be precisely synchronized to the output pulses of the FEL.

It turned out that particularly the requirement to generate trains (bursts) of synchronized femtosecond pulses severely influenced the decision on the type of the laser and on its general layout.

## LAYOUT OF THE OPCPA LASER

Fig. 1 shows the general scheme of the laser system that generates the desired trains of femtosecond pulses. It is based on Optical-Parametric Chirped-Pulse Amplification (OPCPA) [3, 4]. The initial seed pulses generated by a Titanium Sapphire (Ti:Sa) oscillator are amplified in two stages by Optical-Parametric Amplification (OPA). Both OPA stages consist of nonlinear LBO crystals which are pumped by a special burst-mode Nd:YLF laser. The pump laser is an appropriately adapted version of the photocathode laser [5, 6] that drives the photo injector of the linear accelerator of the VUV-FEL.

In order to pump the OPA an additional flashlamp-pumped amplifier is required to boost the available output energy to 1.1 mJ per micropulse. The number of micropulses per burst is adjustable by appropriately programming the window of the second pulse-picking Pockels cell of the amplifier chain. A whole pulse train (fig. 2) can contain up to 800 micropulses, the total energy amounts to 0.88 J in this case. The pump laser can operate at a 5...10 Hz repetition rate. Conversion to the second harmonic is accomplished using a 10 mm long LBO crystal with a typical efficiency of 60%. The duration of the individual micropulses in the train is 15 ps at 1047 nm wavelength and 12 ps after conversion to green light ( $\lambda = 524 \text{ nm}$ ).

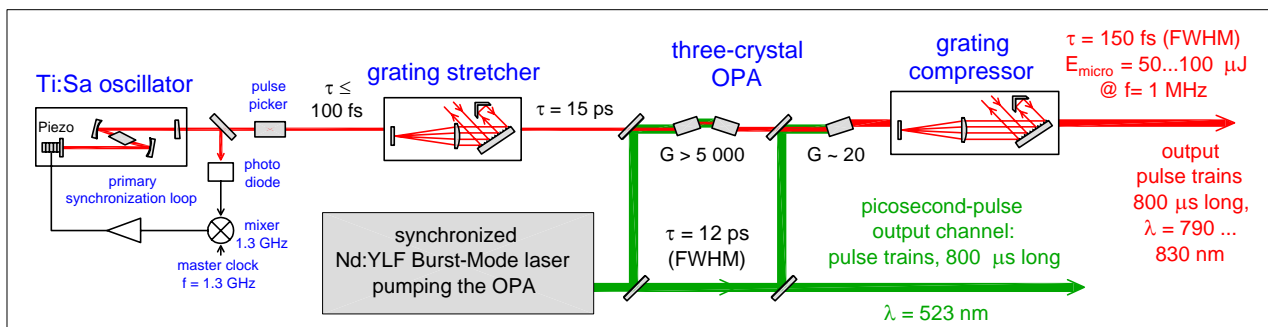


Figure 1: Basic scheme of the OPCPA laser system

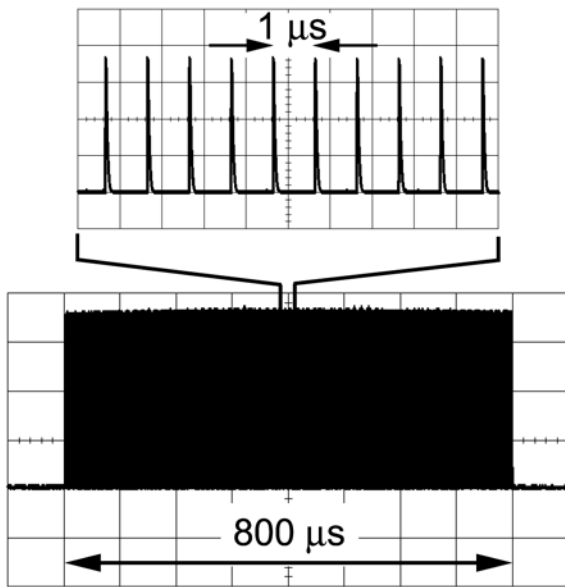


Figure 2: Pulse trains from a Nd:YLF burst-mode laser which is used as the pump laser of the optical-parametric amplifier

In order to utilize the energy of the pump laser efficiently, the seed pulses from the Ti:Sa oscillator are stretched to  $\tau \geq 15$  ps (FWHM) by means of a stretcher that contains a grating of 1200 lines/mm. These pulses are

fed into the preamplifier, which consists of two LBO crystals of 12 mm length and reaches an amplification of 5000. Subsequently, the pulses pass the final amplifier stage containing a single 8 mm long LBO crystal. This amplifier is operated near saturation. It reaches a typical gain of twenty and increases the energy of the micropulses up to  $\sim 100 \mu\text{J}$ .

Naturally, the parametric amplification process selects only those pulses from the uninterrupted 108 MHz train of the Ti:Sa oscillator which coincide with the micropulses of the bursts from the Nd:YLF laser. An additional Pockels cell between the Ti:Sa oscillator and the stretcher reduces the load of the target due to the unamplified Ti:Sa pulses by nearly three orders of magnitudes.

At the output of the laser system, the pulses are recompressed by a grating compressor. We typically reach an output pulse duration of 150 fs. This is a significant increase of the pulse width in comparison with the pulses of the Ti:Sa oscillator. It is mainly caused by spectral narrowing during the amplification process as well as by accumulation of a nonlinear chirp in the pulse stretcher, the compressor, the LBO crystals and in the other optical components within the optical beam path.

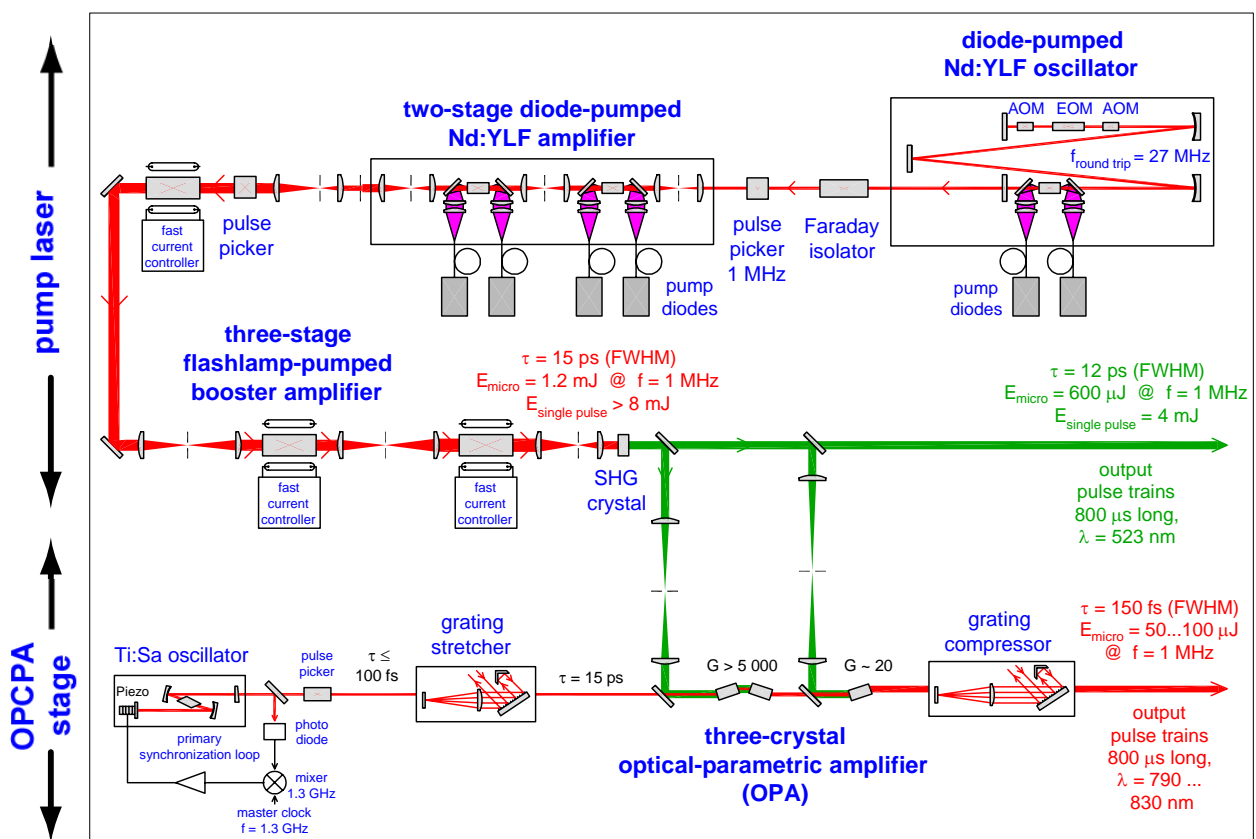


Figure 3: Optical layout of the OPCPA laser system

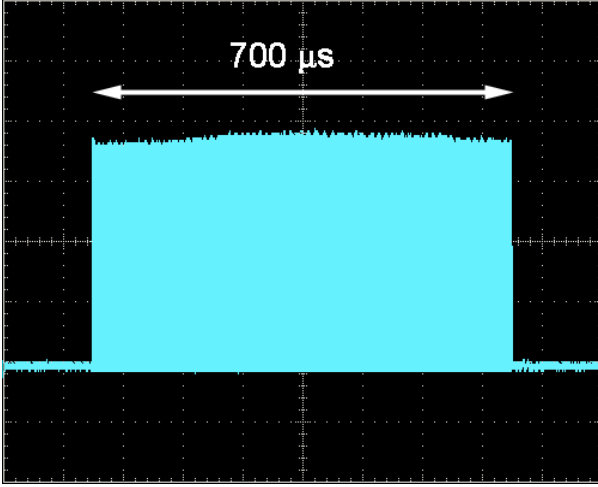


Figure 4: Output pulse trains of the OPCPA system containing 700 micropulses

## SYNCHRONIZATION

Synchronization between the FEL and the OPCPA laser system is accomplished using the signals from a common RF master oscillator of the linear accelerator (LINAC) as the reference. Consequently, the quality of the master oscillator and the distribution network strongly determines the synchronization accuracy actually reached.

Synchronization of the OPCPA system means that both the pump laser and the Ti:Sa master oscillator have to be synchronized to the external RF clock. The pump laser uses an actively modelocked oscillator which allows for a straightforward synchronization with sub-picosecond accuracy [5]. The synchronization system for the passively modelocked Ti:Sa oscillator is based on electronic synchronization loops which contain appropriate phase detectors. In these phase detectors, a fast photodiode is used to electronically detect the optical pulses from the laser. After passing through a band-pass filter, the signal is amplified and the phase is compared to the phase of the reference signal by means of a standard double balanced mixer. The output signal from this phase detector is further amplified in an appropriate feedback amplifier. It is then transferred to a fast piezo-electric translator, which carries the high-reflecting end mirror of the resonator of the Ti:Sa oscillator. This allows to control the mechanical length of the laser resonator. When the loop is closed, the system adjusts the resonator length in such a way that the output of the mixer becomes zero, i.e. the mutual phase between the laser and the RF reference signal is constant. Adjustment of the absolute phase is accomplished by manually adjustable phase shifters.

In order to efficiently reduce the unfavourable influence of electrical noise and imperfections of the mixer, the feedback loop actually contains two different phase detectors that compare the phase of the laser signal to the 108 MHz and to the 1300 MHz signals from the electronic master oscillator of the LINAC that drives the FEL. Initially, a pre-synchronization is performed using

the low-resolution phase detector that operates with the 108 MHz reference signal, which is equal to the round-trip time of the oscillator. In a second step, a more precise synchronization is achieved by selecting the high-resolution phase detector, which uses the 1300 MHz reference signal. We use this 12-th harmonics instead of the round-trip frequency itself as the reference, since this improves the obtainable accuracy of the synchronization loop significantly. Automatic switching between both phase detectors is accomplished by means of an appropriate electronic TTL circuitry.

We determine the actually reached synchronization accuracy by imaging both the pulses from the OPCPA laser and the radiation from a bending magnet that is located at the output of the LINAC simultaneously on to the photocathode of a synchroscan streak camera (type Hamamatsu C5680). The distance of the centre of mass between both pulses determines their mutual timing ( $\Delta t$  in Fig. 5). A jitter between both pulses should translate linearly into a variation of their vertical distance on the screen of the streak camera. Fig. 6 shows the jitter measured with this method over a period of 10 minutes. The jitter obtained by this method is  $\sigma = 0.5$  ps. This includes both the jitter of the synchronization of the OPCPA system as well as the timing stability of the whole LINAC with respect to the RF master oscillator. That is why we regard this value of the jitter as an upper limit for the accuracy of the synchronization loop of the laser.

In the future, we plan to use the described measurement technique to automatically correct the phase of the reference RF signal delivered to the primary synchronization of the laser. Alternatively, one can shift the OPCPA output pulse using an adjustable optical delay. This should enable us to compensate for effects of slow thermally induced drifts in the cables and the synchronization electronics of the OPCPA laser system.

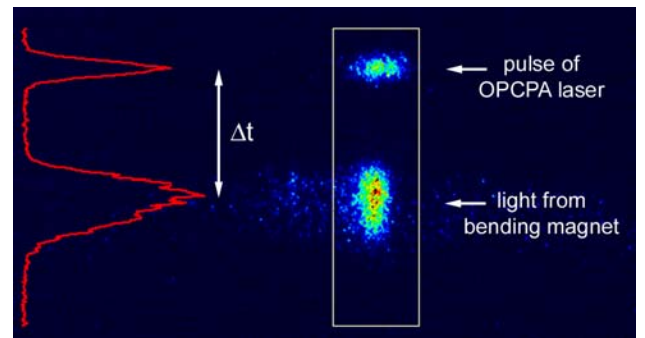


Figure 5: Streak camera image obtained by simultaneously imaging the pulses from the OPCPA system and the light from a bending magnet onto the photocathode of the synchroscan streak camera. (The time axis goes in vertical direction)

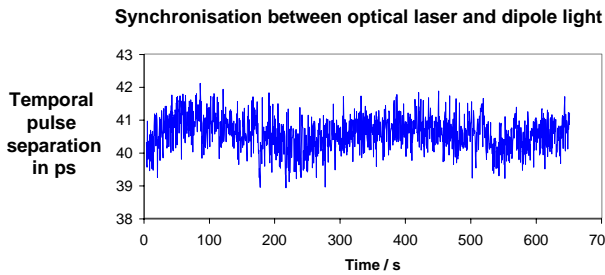


Figure 6: Synchronization jitter between OPCPA and light from a bending magnet measured with a streak camera

## SUMMARY

We have developed a special laser system, which provides the ultrashort pulses needed for two-color pump-probe experiments with the VUV-FEL at DESY Hamburg. This laser system uses the Optical-Parametric Chirped-Pulse Amplification (OPCPA) technique for generating trains of intense femtosecond pulses with the same time structure as the FEL radiation. Their centre wavelength is presently tuneable between 790 and 830 nm.

We have measured that the pulses are synchronized to the electron bunches of the LINAC with an accuracy better than 0.5 ps.

The laser system was installed in an air-conditioned hutch near the experimental area of the FEL in 2004. Appropriate software controls, beam transport to the experimental stations and suitable delay lines have been implemented. First pump-probe experiments are underway.

## ACKNOWLEDGEMENT

This work was funded by the European Commission under Contract no. HPRI-CT-1999-50009.

## REFERENCES

- [1] J. Rossbach et al., "A VUV free electron laser at the TESLA test facility at DESY", *Nuclear Instruments and Methods in Physics research A* 375, pp. 269-273 (1996).
- [2] S. Schreiber et al., "First lasing at 32 nm of the VUV-FEL at DESY", *Proc. FEL 2005*
- [3] I.N. Ross, P. Matousek, M. Towrie, A.J. Langley, J.L. Collier, "The prospects for ultrashort pulse duration and ultrahigh intensity using optical parametric chirped pulse amplification", *Opt. Comm.* 144 (1997), pp. 125-133
- [4] X. Yang et al., "Multiterawatt laser system based on optical parametric chirped pulse amplification", *Opt. Lett.* 27 (2002), pp. 1135-1137
- [5] I. Will, G. Koss, I. Templin, "The upgraded photocathode laser of the TESLA Test Facility", *Nuclear Instruments and Methods in Physics research A* 541 (2005), pp. 467-477
- [6] I. Will, A. Liero, D. Mertins, and W. Sandner, "Feedback-Stabilized Nd:YLF Amplifier System for Generation of Picosecond Pulse Trains of an Exactly Rectangular Envelope", *IEEE J. of Quant. Electron.* QE 34, pp. 2020-2028 (1998).

# PROPERTIES OF THE THIRD HARMONIC OF THE SASE FEL RADIATION

E.L. Saldin, E.A. Schneidmiller, and M.V. Yurkov  
Deutsches Elektronen-Synchrotron (DESY), Hamburg, Germany

## Abstract

Recent theoretical and experimental studies have shown that SASE FEL with a planar undulator holds a potential for generation of relatively strong coherent radiation at the third harmonic of the fundamental frequency. Here we present detailed study of the nonlinear harmonic generation in SASE FEL obtained with time-dependent FEL simulation code FAST. Using similarity techniques we present universal dependencies for temporal, spectral, and statistical properties of the third harmonic radiation from SASE FEL. In particular, we derived universal formulae for radiation power of higher harmonics at saturation. It was also found that coherence time at saturation falls inversely proportional to harmonic number, and relative spectrum bandwidth remains constant with harmonic number.

## INTRODUCTION

During last years a significant efforts of researchers have been devoted for studying the process of the higher harmonic generation in the high-gain free electron lasers [1]-[11]. Such an interest has been mainly driven by practical needs for prediction of the properties of X-ray free electron lasers. Analytical techniques have been used to predict properties of the higher harmonics for FEL amplifier operating in the linear mode of operation [8, 9]. However, the most fraction of the radiation power is produced in the nonlinear regime, and a set of assumptions needs to be accepted in order to estimate saturation power of higher harmonics on the base of extrapolation of analytical results. A lot of studies has been performed with numerical simulation codes. These studies developed in two directions. The first direction is investigations of higher harmonic phenomena by means of steady-state codes [4, 5, 6, 7]. Despite the results of these studies are applicable to externally seeded FEL amplifiers only, it is relevant to appreciate that they gave the first predictions for high radiation power in higher harmonics of SASE FEL [2, 4]. Another direction was an extraction of time structure for the beam bunching from time-dependent simulation code with subsequent use of analytical formulae of the linear theory [8]. Giving an estimate for the power, such an approach does not allow to describe statistical properties of the output radiation.

In this paper we perform comprehensive study of the statistical properties of the odd harmonic radiation from SASE FEL. The study is performed in the framework of one-

dimensional model with time-dependent simulation code FAST [12, 13] upgraded for simulation of higher harmonic generation. We restrict our study with odd harmonics produced in the SASE FEL. We omit from consideration an effect of self-consistent amplification of the higher harmonics. In other words, we solve only electrodynamic problem assuming that particle motion is governed by the fundamental harmonic. The latter approximation is valid when power in higher harmonics is much less than in the fundamental. This does not limit practical applicability of the results: it has been shown in earlier papers that the growth rate of higher harmonics is too small to produce visible increase of the coherent amplification above shot noise in X-ray FELs [8]. Under this approximation and using similarity techniques we derive universal relations describing general properties of the odd harmonics in the SASE FEL: power, statistical and spectral properties. The results are illustrated for the 3rd and 5th harmonic having practical importance for X-ray FELs.

## BASIC RELATIONS

The one-dimensional model describes the amplification of the plane electromagnetic wave by the electron beam in the undulator. When space charge and energy spread effects can be neglected, operation of an FEL amplifier is described in terms of the gain parameter  $\Gamma = [\pi j_0 K_1^2 / (I_A \lambda_w \gamma^3)]^{1/3}$ , efficiency parameter  $\rho = \lambda_w \Gamma / (4\pi)$ , and detuning parameter  $\hat{C} = [2\pi / \lambda_w - \omega(1 + K^2/2) / (2c\gamma^2)] / \Gamma$  (see, e.g. [13]). Here  $K_1$  is coupling factor of the radiation to the first harmonic  $h = 1$ ,  $K_h = K(-1)^{(h-1)/2} [J_{(h-1)/2}(Q) - J_{(h+1)/2}(Q)]$ , and  $Q = K^2 / [2(1 + K^2)]$ . Other parameters of the electron beam, undulator and radiation are:  $\lambda_w$  is undulator period,  $K = e\lambda_w H_w / 2\sqrt{2}\pi m c^2$  is rms undulator parameter,  $\gamma$  is relativistic factor,  $H_w$  is undulator field,  $j_0$  is the beam current density,  $(-e)$  and  $m$  are charge and mass of electron,  $I_A = mc^3/e \simeq 17$  kA, and  $\omega$  is frequency of electromagnetic wave. When describing start-up from shot noise, one more parameters of the theory appears – number of particles in coherence volume,  $N_c = I / (e\rho\omega)$ , where  $I$  is beam current.

Main advantage of accepted approximation (particle's dynamics is governed by the fundamental harmonic) is that we can factorize coupling of the harmonics of the radiation and relevant time-dependent integrals of the harmonic

of the beam bunching. Thus, with omission of a common factor, complex amplitude of electric field of harmonic is

$$E_h(z, t) \propto K_h \int_0^z a_h(z', t - (z - z')/c) dz',$$

where  $a_h$  is  $h$ -th harmonic of the beam bunching. Subsequent application of similarity techniques allows us to extract universal dependencies from numerical simulations.

## RADIATION PROPERTIES

The input parameter of the system is the number of co-operating electrons  $N_c$ . A typical range of the values of  $N_c$  is  $10^6$ – $10^9$  for the SASE FELs of wavelength range from X-ray up to infrared. The numerical results, presented in this paper, are calculated for the value  $N_c = 3 \times 10^7$  which is typical for a VUV FEL. Note that the dependence of the output parameters of the SASE FEL on the value of  $N_c$  is rather weak, in fact logarithmic [13]. Therefore, the obtained results are pretty general and can be used for the estimation of the parameters of actual devices with sufficient accuracy.

A plot for the averaged power of the 1st harmonic is shown in Fig 1 with a solid line (normalized power of  $h$ -th harmonic is defined as  $\hat{\eta}_h = W_h \times (K_1/K_h)^2 / (\rho W_b)$ ).

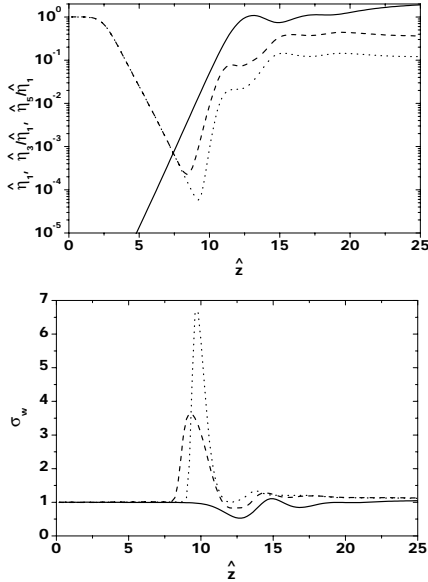


Figure 1: Top: normalized averaged power of a fundamental harmonic of SASE FEL,  $\hat{\eta}_1 = P_1 / (\rho P_{\text{beam}})$ , normalized power ratio,  $\hat{\eta}_h / \hat{\eta}_1 = (W_h / W_1) \times (K_1 / K_h)^2$ , for the 3rd and 5th harmonic. Bottom: Normalized rms deviation of the fluctuations of the instantaneous radiation power. Solid, dashed, and dotted lines correspond to the fundamental, 3rd, and 5th harmonic, respectively

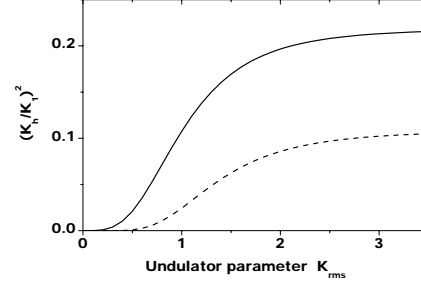


Figure 2: Ratio of coupling factors,  $(K_h/K_1)^2$ , for the 3rd (solid line) and the 5th (dashed line) harmonics with respect to the fundamental harmonic versus rms value of undulator parameter  $K_{\text{rms}}$

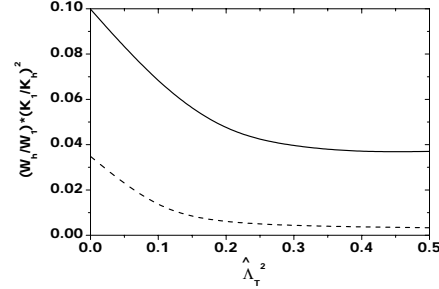


Figure 3: Normalized power ratio at saturation,  $(W_h/W_1) \times (K_1/K_h)^2$ , for the 3rd (solid line) and 5th (dashed line) harmonic as a function of energy spread parameter  $\hat{\Lambda}_T^2$ . SASE FEL operates at saturation

Saturation is achieved at the undulator length  $\hat{z} = 13$ . Dashed and dotted lines show a normalized power ratio,  $\hat{\eta}_h / \hat{\eta}_1 = (W_h / W_1) \times (K_1 / K_h)^2$ , for the 3rd and the 5th harmonic. One can notice that power of the higher harmonics becomes to be above the shot noise level only in the end of linear regime. This becomes clear if one takes into account that the shot noise level of the beam bunching is about  $1/\sqrt{N_c}$ , and is rather high [8]. For the saturation we find a universal formulae for the power of the 3rd and 5th harmonic:

$$\frac{\langle W_3 \rangle}{\langle W_1 \rangle} = 0.094 \times \frac{K_3^2}{K_1^2}, \quad \frac{\langle W_5 \rangle}{\langle W_1 \rangle} = 0.03 \times \frac{K_5^2}{K_1^2}. \quad (1)$$

Universal functions for the ratio  $(K_h/K_1)^2$  are plotted in Fig. 2. Asymptotic values for at large value of undulator parameter are:  $(K_3/K_1)^2 \simeq 0.22$ , and  $(K_5/K_1)^2 \simeq 0.11$ . Thus, we can state that contribution of the 3rd harmonic into the total radiation power of SASE FEL at saturation could not exceed a level of 2%. Thus, its influence on the beam dynamics should be small. This result justifies a basic assumption used for derivation of a universal relation (1).

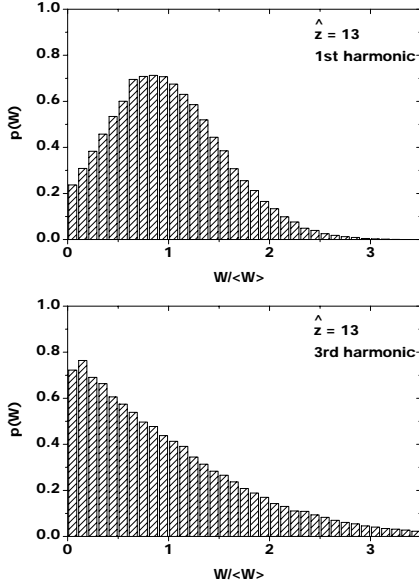


Figure 4: Probability distribution of instantaneous radiation power from SASE FEL operating in saturation regime at  $\hat{z} = 13$ . Upper and lower plots correspond to the fundamental and 3rd harmonic, respectively

A contribution of the 5th harmonic into the total power at saturation could not exceed the value of 0.3%.

Another important topic is an impact of the electron beam quality on the nonlinear harmonic generation process. In the framework of the one-dimensional theory this effect is described with the energy spread parameter  $\hat{\Lambda}_T^2 = \langle (\Delta E)^2 \rangle / (\rho^2 E_0^2)$  where  $\langle (\Delta E)^2 \rangle$  is the rms energy spread. Result given by (1) for the case of "cold" electron beam is generalized with the plots presented in Fig. 3. We see that the energy spread in the electron beam suppresses power of the higher harmonics. Within practical range of  $\hat{\Lambda}_T^2$  this suppression can be about a factor of 3 for the 3rd harmonic, and about an order of magnitude for the 5th harmonic. Note that typical range of the effective energy spread parameter (taking into account energy spread and emittance, see, e.g., [13]) for X-ray FELs is covered by the plot in Fig. 3. The saturation length at  $\hat{\Lambda}_T^2 = 0.5$  is increased by a factor of 1.5 with respect to the "cold" beam case  $\hat{\Lambda}_T^2 = 0$ .

Instantaneous radiation power is subjected to fluctuations because start-up from shot noise. In Fig. 1 we show the normalized rms deviation of the instantaneous radiation power,  $\sigma_w = \langle (W - \langle W \rangle)^2 \rangle^{1/2} / \langle W \rangle$ , as a function of the undulator length. The next step in our investigation is the behavior of the probability density distribution of the instantaneous power. In the linear stage of amplification the radiation of the fundamental harmonic is described with Gaussian statistics. As a result, the probability distribution of the instantaneous radiation intensity  $W$  should be the negative exponential probability density distribu-

tion  $p(W) = \exp(-W/\langle W \rangle) / \langle W \rangle$  [13, 14]. The same refers to the higher harmonics when the shot noise dominates above the process of nonlinear harmonic generation. When the latter process becomes to be dominant the statistics of the high-harmonic radiation from the SASE FEL changes significantly with respect to the fundamental harmonic (e.g., with respect to Gaussian statistics). In this case the probability density function  $p(W)$  of the fundamental intensity is subjected to a transformation  $z = (W)^h$ . It can be readily shown that this probability distribution is  $p(z) = z^{(1-h)/h} \exp(-z^{1/h}/\langle W \rangle) / (h\langle W \rangle)$  [15]. Using this distribution we get the expression for the mean value:  $\langle z \rangle = h! \langle W \rangle^h$ . Thus, the  $h$ th-harmonic radiation for the SASE FEL has an intensity level roughly  $h!$  times larger than the corresponding steady-state case, but with more shot-to-shot fluctuations compared to the fundamental [8]. Note that this regime of nonlinear harmonic generation which can be described with analytical techniques happens only in the end of linear regime. When amplification process in the SASE FEL enters nonlinear regime, statistical properties of the radiation can be found only from numerical simulations. Relevant probability distributions for saturation are shown in Fig. 4. It is seen that the distributions change significantly with respect to the linear regime for both, the fundamental and the 3rd harmonic. An important message is that at the saturation point the 3rd harmonic radiation exhibits much more noisy behavior (nearly negative exponential) while stabilization of the fluctuations of the fundamental harmonics takes place.

Temporal properties of the radiation are described in terms of the first and the second order time correlation functions  $g_1(t - t') = \langle \tilde{E}(t) \tilde{E}^*(t') \rangle / [\langle |\tilde{E}(t)|^2 \rangle \langle |\tilde{E}(t')|^2 \rangle]^{1/2}$ , and  $g_2(t - t') = \langle |\tilde{E}(t)|^2 |\tilde{E}(t')|^2 \rangle / [\langle |\tilde{E}(t)|^2 \rangle \langle |\tilde{E}(t')|^2 \rangle]$ . In Fig. 5 we show the time correlation functions at saturation. The nontrivial behavior of the second order correlation function reflects the complicated nonlinear evolution of the SASE FEL process. In classical optics, a radiation source with  $g_2(0) < 1$  cannot exist but the case of  $g_2(0) > 2$  is possible. As one can see from Fig. 5, the latter phenomenon (known as superbunching) occurs for higher harmonics of SASE FEL.

In Fig. 6 we present the dependence on the undulator length of the normalized coherence time  $\hat{\tau}_c = \rho \omega_0 \tau_c$ , where  $\tau_c$  is  $\tau_c = \int_{-\infty}^{\infty} |g_1(\tau)|^2 d\tau$ . For the fundamental harmonic the coherence time achieves its maximal value near the saturation point and then decreases drastically. The maximal value of  $\hat{\tau}_c$  depends on the saturation length and, therefore, on the value of the parameter  $N_c$ . With logarithmic accuracy we have the following expression for the coherence time of the fundamental harmonic  $(\hat{\tau}_c)_{\max} \simeq \sqrt{\pi \ln N_c} / 18$ . The coherence time at saturation for higher harmonics falls approximately inversely proportional to the harmonic number  $h$ .

Radiation spectra are described in terms of the normalized spectral density,  $h(\hat{C})$ , defined as  $\int_{-\infty}^{\infty} d\hat{C} h(\hat{C}) = 1$ .

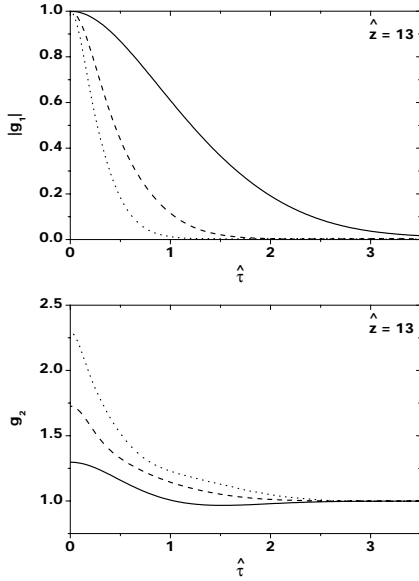


Figure 5: First and second order correlation functions. SASE FEL operates in saturation regime at  $\hat{z} = 13$ . Solid, dashed, and dotted lines correspond to the fundamental, 3rd and 5th harmonic, respectively. Here  $\hat{\tau} = \rho\omega_0(t - t')$

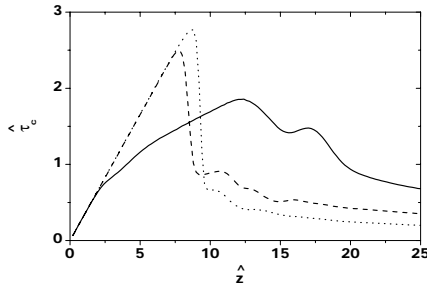


Figure 6: Normalized coherence time of a SASE FEL as a function of normalized undulator length. Solid, dashed, and dotted lines correspond to the fundamental, 3rd, and 5th harmonic, respectively

The frequency deviation,  $\Delta\omega$ , from the nominal value of  $\omega_h$  can be recalculated as  $\Delta\omega = -2\rho\omega_h\hat{C}$ . Normalized envelope of the radiation spectrum and the first order time correlation function are connected by the relation  $G(\Delta\omega) = (2\pi)^{-1} \int_{-\infty}^{\infty} d\tau g_1(\tau) \exp(-i\Delta\omega\tau)$  [16]. Figure 7 shows spectra of the SASE FEL radiation at saturation. Note that spectrum width of the higher harmonics from SASE FEL differs significantly from that of incoherent radiation. For the case of incoherent radiation relative spectrum width,  $\Delta\omega/\omega_h$  scales inversely proportional to the harmonic number  $h$  (see, e.g. [17]). One can see that situation changes dramatically for the case when nonlinear harmonic generation process starts to be dominant. At sat-

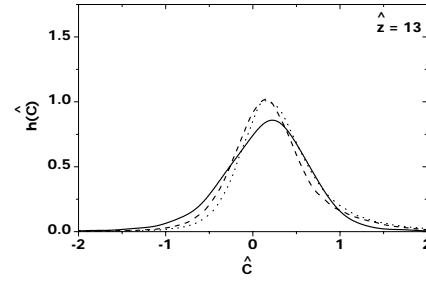


Figure 7: Normalized spectrum from SASE FEL operating in the saturation regime. Solid, dashed, and dotted lines correspond to the fundamental, 3rd and 5th harmonic, respectively

uration we find that relative spectrum bandwidth becomes to be nearly the same for all harmonics.

## REFERENCES

- [1] M. Schmitt and C. Elliot, Phys. Rev. A, 34(1986)6.
- [2] R. Bonifacio, L. De Salvo, and P. Pierini, Nucl. Instr. Meth. A293(1990)627.
- [3] W.M. Fawley, Proc. IEEE Part. Acc. Conf., 1995, p.219.
- [4] H. Freund, S. Biedron and S. Milton, Nucl. Instr. Meth. A 445(2000)53.
- [5] H. Freund, S. Biedron and S. Milton, IEEE J. Quant. Electr. 36(2000)275.
- [6] S. Biedron et al., Nucl. Instr. Meth. A 483(2002)94.
- [7] S. Biedron et al., Phys. Rev. ST 5(2002)030701.
- [8] Z. Huang and K. Kim, Phys. Rev. E, 62(2000)7295.
- [9] Z. Huang and K. Kim, Nucl. Instr. Meth. A 475(2001)112.
- [10] A. Tremaine et al., Phys. Rev. Lett. 88, 204801 (2002)
- [11] W. Brefeld et al., Nucl. Instr. Meth. A 507(2003)431.
- [12] E.L. Saldin, E.A. Schneidmiller, and M.V. Yurkov, Nucl. Instr. Meth. A 429(1999)233.
- [13] E.L. Saldin, E.A. Schneidmiller, and M.V. Yurkov, The Physics of Free Electron Lasers, Springer-Verlag, Berlin, 1999.
- [14] E.L. Saldin, E.A. Schneidmiller, and M.V. Yurkov, Opt. Commun. 148(1998)383.
- [15] E.L. Saldin, E.A. Schneidmiller, and M.V. Yurkov, Opt. Commun. 212(2002)377.
- [16] J. Goodman, Statistical Optics, Wiley, New York, 1985.
- [17] H. Wiedemann, Synchrotron Radiation, Springer-Verlag, Berlin, 2003.

# Detector response and beam line transmission measurements with far-infrared radiation

H. Delsim-Hashemi, L. Fröhlich, O. Grimm\*, DESY, Hamburg, Germany  
E. Chiadroni, University of Rome Tor Vergata, Italy

## Abstract

Good understanding of radiation generation and transport mechanisms and of detector characteristics is essential in attempting to use frequency-domain techniques for longitudinal bunch diagnostics which are of crucial importance at short-wavelength free-electron lasers. This paper summarizes the current state of experimental verification of the far-infrared performance of a synchrotron radiation beam line at the TTF2 accelerator at DESY, Hamburg. Measurement of the polarization as function of frequency has also been found a useful tool to characterize the beam line. Furthermore, several approaches for detector response measurements are reported.

## INTRODUCTION

Various activities at the TTF2 linear accelerator which drives the VUV-FEL at DESY, Hamburg, are geared towards measuring the longitudinal charge distribution of electron bunches with coherent far-infrared radiation. All such approaches require a good understanding of the radiation generation and transport mechanism and of the detector characteristics to extract useful information on the charge distribution. Simulations and measurements of the expected transverse intensity distribution and polarization of synchrotron radiation emitted at the first bunch compressor of TTF2 have been performed. The transverse intensity scanning provided for the first time at DESY a visual image of the footprint of terahertz radiation. Detector response measurements have been performed at the FELIX facility for the wavelength range (100-210)  $\mu\text{m}$ , and first considerations on using blackbody radiation together with suitable band pass filters in the terahertz regime have been made. A Goly cell detector has been characterized with this 'hot-cold' calibration method, as well as with a method based on using a mm-wave source.

## MODEL VERIFICATION OF THE CSR BEAMLINE AT TTF2

The synchrotron radiation beam line at the first bunch compressor of TTF2 [1] has been successfully used for streak camera measurements with visible and interferometric measurements with far-infrared radiation. The initial design has been based upon simple geometric optics considerations. Recent measurements and numerical calculations taking full account of diffraction effects using a

Fourier optics code suggest however a low transport efficiency in the THz regime of only a few percent. The simulations indicate that an order of magnitude better far-infrared transmission is achievable. Before installing an improved version according to such simulations, confidence in the numerical calculations needs to be gained by comparison with measurements.

As an example, the intensity distribution measured by transversely scanning with a 2 mm diameter pyroelectric detector at the end of the beam line is shown in Fig. 1, together with the result from the simulation. Similar comparisons were done in the focal point of the final paraboloid mirror and in front of the beam line, close to the vacuum view port of the bunch compressor magnet. Agreement is currently seen on a broad scale, but fine details of the measurements are not yet fully reproduced by the calculations.

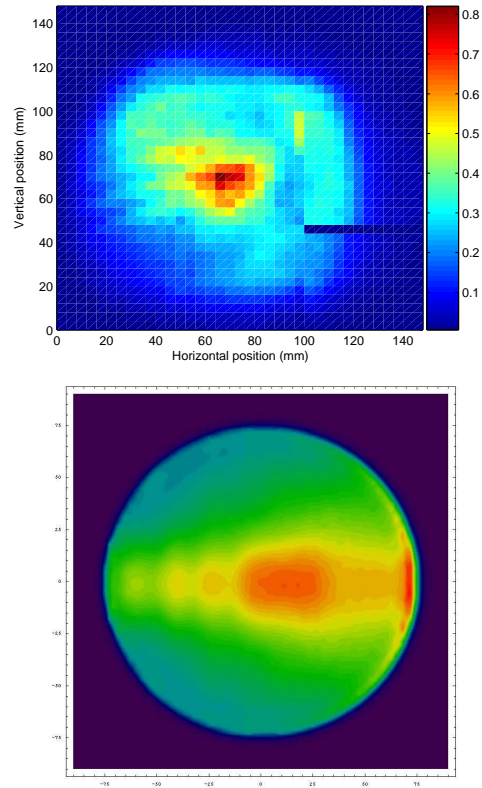


Figure 1: Measured (top) and calculated (bottom) transverse intensity distribution at the end of the beam line. A 50  $\mu\text{m}$  low-pass filter was used. The measurement is given in terms of detector voltage. The calculation covers the same area and uses a similar colour scale.

\* Corresponding author. E-Mail: oliver.grimm@desy.de

A further handle for verification purposes is the synchrotron radiation polarization as function of frequency. The source itself is expected to show a strong dependence. The measurement shown in Fig. 2 was taken after the beam line, so additional modifications to the source characteristics due to the different emission characteristics of the two orthogonal polarization components enter and are taken into account in on-going calculations.

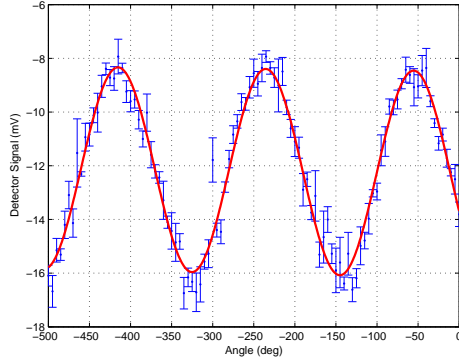


Figure 2: Detector intensity as function of the rotation angle of a polarizing wire grid. A 1.4 mm band-pass filter was used. The fit (1) yields  $p=0.52\pm 0.01$  and  $\phi_0=(-35\pm 0.6)^\circ$ .

The fit function is given by

$$I(\phi) = (I_0 + I'\phi) (\cos^2(\phi + \phi_0) + p \sin^2(\phi + \phi_0)), \quad (1)$$

where the polarization  $p = I_v/I_h$  is the ratio of two orthogonal components and  $I'$  takes into account a possible slow drift of the incoming intensity. The two components are taken with reference to a coordinate system rotate by  $\phi_0$  with respect to laboratory horizontal.

## DETECTOR RESPONSE MEASUREMENTS AT FELIX

Straightforward values for detector sensitivities are obtained by using a radiation source with narrow wavelength spectrum and known intensity. Such a source is provided by the far-infrared free-electron laser FELIX, at the FOM Rijnhuizen institute, Netherlands. The sensitivities of LiTaO<sub>3</sub> and DTGS pyroelectric detectors used for bunch length diagnostics at TTF2 were measured over the range (100-210)  $\mu\text{m}$ , an example is shown in Fig. 3.

The calculation includes the absorption in the detector crystal of thickness  $d$  and reflection at the gold back electrode, although its 15  $\mu\text{m}$  grit was not modelled [2]. This would tend to smooth the interference structure.

The FEL intensity has been monitored with a reference Joulemeter. To operate both pyroelectric and reference detector within their respective dynamic range, different attenuators had to be introduced into the FELIX beam line. Frequency-dependencies of these attenuators or of the reference detector itself cannot be separated in the results.

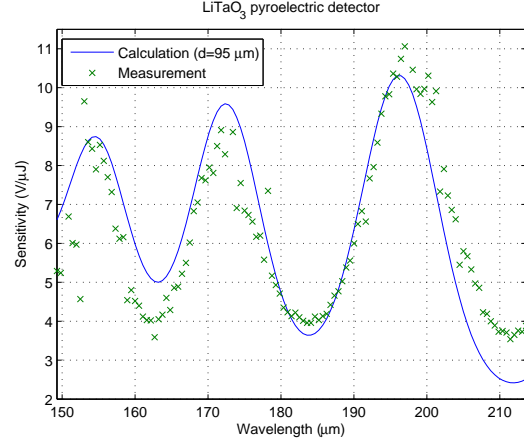


Figure 3: Sensitivity of a LiTaO<sub>3</sub> pyroelectric detector ( $\varnothing 5$  mm) measured at FELIX. The calculation takes into account absorption in the crystal, reflection at the back electrode and a Gaussian FEL linewidth (2% sigma).

A similar measurement with a 2 mm diameter DTGS detector yielded a sensitivity of about 35 V/ $\mu\text{J}$  and an interference structure compatible with 85  $\mu\text{m}$  thickness. The noise level of this slow detector, when equipped with a suitable low-pass filter, is of the order of 2 mV, thus pulse energies down to 60 pJ are measurable.

## DETECTOR CALIBRATION USING COUPLED OSCILLATORS

A local oscillator, which directly drives a mm-wave source module to 110 GHz in waveguide, has been used to produce monochromatic, linearly polarized radiation to characterise a Golay cell detector<sup>1</sup>. The waveguides are built such that only the fundamental mode TE<sub>10</sub> can propagate within the frequency band (75-110) GHz. Each waveguide is equipped with directional couplers which feed a scalar network analyzer and are used to pick up part of the signal from the source (10%) for calibration purposes and part of the reflected signal to measure the return loss. For detector calibration, a chopper to modulate the CW signal is needed and the waveguide series is interrupted, causing the emitted power to be strongly dependent on the frequency as it is shown in Fig. 4.

To reduce power losses and to ensure an almost perfect RF coupling, thus preventing back-scattered radiation and resonance effects, a conical tapered waveguide with 30° aperture has been studied (HFSS code) and built by shaping anticorodal (an Aluminium alloy) with the electroerosion technique to have at one end a standard flange with rectangular aperture ( $x=2.54$  mm,  $y=1.27$  mm) and a custom circular flange with radius of 3 mm to match the detector window at the other end.

An initial power of 1 dBm has been attenuated and modulated at 10 Hz chopper frequency, locked to a lock-in

<sup>1</sup>Collaboration with the University of Milano-Bicocca

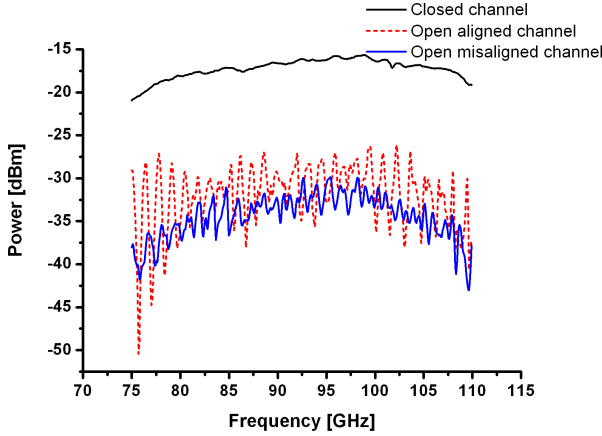


Figure 4: Source power spectrum for open (aligned and misaligned) and close channel.

amplifier to eliminate the background radiation. The frequency has been selected in the 75 GHz - 110 GHz bandwidth with a step width of 0.1 GHz. The responsivity, defined as the ratio between the measured voltage response and the incident power, is shown in Fig. 5.

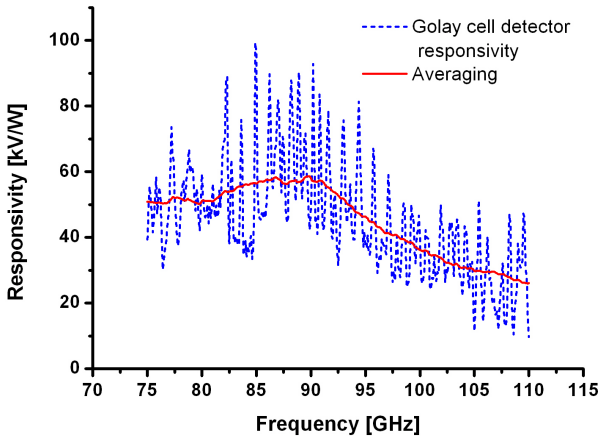


Figure 5: Golay cell detector responsivity.

On average, the responsivity follows an almost flat behaviour. The peaks are strongly dependent on the aperture between the waveguides necessary for chopping and are not a detector characteristic.

## PRINCIPLES OF DETECTOR CALIBRATION WITH BLACKBODY RADIATION

A radiation spectrum that is known from first principles is that of a blackbody, following the Planck radiation law

$$\frac{dL}{d\lambda d\Omega} = \frac{2hc^2}{\lambda^5} \frac{1}{\exp(hc/\lambda kT) - 1}, \quad (2)$$

and emitting isotropically. Isolating part of the spectrum with appropriate filters will then allow a geometry-independent relative sensitivity measurement at different wavelengths, or, with careful consideration of the geometry, even an absolute calibration. The main problem is that at temperatures for which there is sufficient intensity in the far-infrared range of interest, the spectrum rises very steeply towards short wavelengths as  $1/\lambda^4$ , requiring efficient blocking.

Specially made low-pass and band-pass filters from QMC<sup>2</sup> have been obtained to this end, but since even a small leakage at mid-infrared wavelengths would dominate any signal measured with a frequency-integrating detector, additional blocking is required. This can be achieved with fused Quartz, HDPE or Yoshinaga<sup>3</sup> filters, as can be inferred from the transmission curves in Fig. 6.

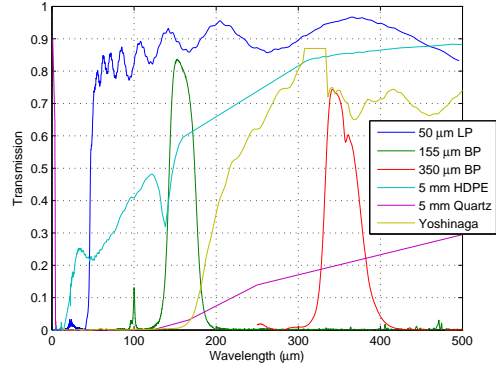


Figure 6: Filters for isolating long-wavelength contributions from a blackbody spectrum.

Infrared detectors are usually only sensitive to changing illumination, therefore a chopping setup as sketched in Fig. 7 is used. The cold blackbody is immersed in liquid Nitrogen at 77 K, the hot one at room temperature. It is essential to enclose detector and filters to avoid any chopped stray radiation to bypass the filters. The emission power in the far-infrared is proportional to temperature, so only significant rising of the hot blackbody temperature above room temperature has a useful effect, bringing a possible conflict with the operation parameters of the emitting material.

It is generally not easy to find materials that are actually black in the far-infrared, as required for the validity of (2). Reviews of suitable materials, mostly paints, can be found in [3, 4]. Studies how to construct a well-defined cavity blackbody are currently on-going at the Physikalisch-Technische-Bundesanstalt, Berlin [5], but for current experiments ECCOSORB foam, type AN-72, is used<sup>4</sup>. It is known to be a good absorber in the THz range, and thus

<sup>2</sup>QMC Instruments Ltd., <http://www.terahertz.co.uk>

<sup>3</sup>Transmission filter made from polyethylene sheets loaded with varieties of powdered crystals

<sup>4</sup>Emerson & Cuming Microwave Products, Inc., <http://www.eccosorb.com>

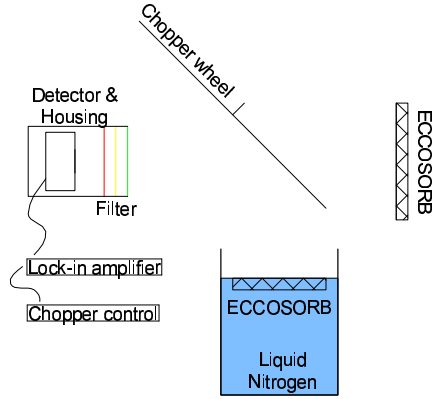


Figure 7: Setup for chopping between two blackbody sources.

expected to have a high emissivity as well.

At the University of Rome "La Sapienza" measurements with a Goly cell<sup>5</sup>, a slightly modified chopping setup (the warm emitter was directly attached to the chopper wheel) and different filters were made. By taking into account the solid angle subtended by the detector,

$$\Omega(L) = \int_0^{2\pi} \int_0^{\vartheta_0(L)} RA(\vartheta, \phi) \sin \vartheta \cos \vartheta, d\vartheta d\phi \quad (3)$$

and the emission spectrum (2), the power  $\Delta P$  on the detector can be calculated.  $L$  is the distance between the detector and the source and  $RA(\vartheta, \phi)$  the detector angular response (Fig. 8) which, assuming cylindrical symmetry, depends only on  $\vartheta$ .

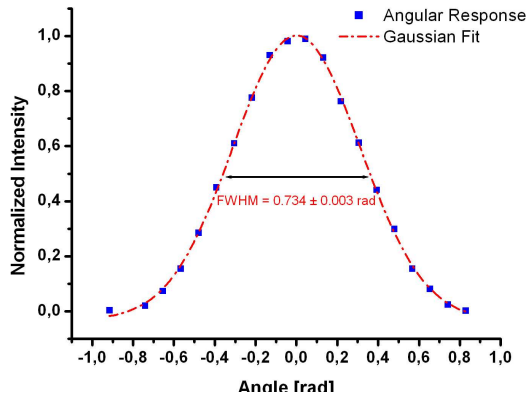


Figure 8: Goly cell detector measured angular acceptance.

Band-pass filters<sup>6</sup> with centre wavelengths of  $850 \mu\text{m}$ ,  $1.1 \text{ mm}$ ,  $1.4 \text{ mm}$  and  $2.1 \text{ mm}$  and 15% bandwidth have been used. To reduce the power reaching the detector and to cut visible and NIR contributions, additional Yoshinaga ( $\hat{\nu}_{cutoff} = 55 \text{ cm}^{-1}$ ) and Fluorogold ( $\hat{\nu}_{cutoff} = 30 \text{ cm}^{-1}$ ) blockers have been used.

<sup>5</sup>Property of ELETTRA - Synchrotron Light Laboratory - and provided in the framework of the SPARC collaboration, see <http://www.lnf.infn.it/acceleratori/sparc>

<sup>6</sup>Free-standing mesh filters manufactured by IKI in Moscow, cf. [6]

With the detector positioned at 3 cm from the source, the output voltage  $\Delta S$  has been recorded (Fig. 9) for the four band-pass filters. An absolute value of the detector responsivity as function of frequency can then be calculated as

$$R(\nu) = \frac{\Delta S(\nu)}{\Delta P(\nu)}.$$

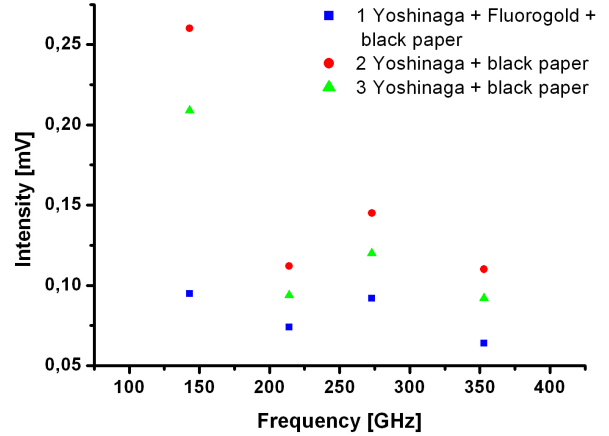


Figure 9: Detector output voltage with different blockers.

The large signal at 143 GHz (red dot and green triangle), corresponding to the 2.1 mm mesh filter, is due to the wide mesh of the filter for long wavelengths, and thus greater contribution of leaking short wavelengths. With more blockers the leakage is reduced, and complete attenuation of the visible light contribution (blue squares) is achieved if a fluorogold filter is also added.

#### Acknowledgment

We are much obliged to Dr. B. Redlich at FELIX and Dr. J. Hollandt at PTB for their assistance in preparing and carrying out the respective measurements and tests. Dr. B. Schmidt kindly supplied the Mathematica code THZ-Transport. We wish to thank also Dr. M. De Petris (Phys. Dept. of the University of Rome "La Sapienza") and Dr. M. Gervasi (Phys. Dept. of the University of Milano-Bicocca) and their groups for sharing knowledge, instrumentations and time with us.

## REFERENCES

- [1] S. Casalbuoni et al., *The Synchrotron Radiation Beamline at TTF2*, Proceedings EPAC'04, Lucerne, Switzerland, 5-9 July 2004
- [2] H. Schlarb, DESY, private communication
- [3] S.M. Smith, Proc. SPIE **0967**, 248 (1998)
- [4] M.J. Persky, Rev.Sci.Instr. **70**, 2193 (1999)
- [5] J. Hollandt, PTB Berlin, private communication
- [6] R. Ulrich, *FIR Properties of Metallic Mesh and its Complementary Structure*, Infrared Physics, **7**, n.1 (1967)

## Upgrades of the Laser Beam-line at PITZ<sup>&</sup>

J.Bähr<sup>\*</sup>, K.Abrahamyan<sup>#</sup>, G.Asova<sup>§</sup>, G.Dimitrov<sup>§</sup>, H.Grabosch, J.H.Han, H.Henschel,  
S.Khodyachykh, M.Krasilnikov, S.Liu, H.Lüdecke, V.Miltchev, A.Oppelt, B.Petrosyan,  
S.Riemann, L.Staykov, F.Stephan, M.Winde, DESY, D-15738 Zeuthen, Germany  
M.v.Hartrott, D.Richter, BESSY, D-12489 Berlin, Germany  
I.Will, G.Klemz, Max-Born-Institute D-12489 Berlin, Germany  
V.Boccone, O.Kalekin, Humboldt University, D-12489 Berlin, Germany  
J.Rönsch, University of Hamburg, D-22761 Hamburg, Germany

### Abstract

In spring of 2005 an essential upgrade of the photocathode laser and of the 20 m long laser beam-line took place at PITZ. A detectable improvement of the laser beam profile at the photocathode is observed. This improvement should lead to an additional reduction of the transverse emittance of the electron beam. The upgraded laser consists of a fully laser diode pumped scheme of pulse train oscillator, pre-amplifiers and booster amplifiers. The main advantages of this upgrade are improved stability, easier maintenance and long-term operations at 10 Hz repetition rate. In addition, the scheme of the optical beam-line was changed: The distance between the beam shaping aperture and the cathode was strongly reduced. Therefore a further improvement of the laser beam profile at the photocathode is expected. The laser beam-line is upgraded by an enlarged number of remotely controlled optical elements that allows the fine tuning of the laser beam characteristics during the running. New diagnostics tools are included in the laser beam-line. The paper focuses on the design of the new optical beam-line.

### INTRODUCTION

The photo injector PITZ at Zeuthen [1] is a dedicated facility for the investigation of rf-guns for FELs, i.e. the VUV-FEL and the XFEL at DESY. An essential upgrade program is ongoing in the years 2004-2006 resulting in the project phase PITZ2 [2]. The essential goals of PITZ2 are the proof of the emittance conservation principle [3] by using a booster cavity and the running of the rf-gun with a higher gradient using a 10 MW Multi-Beam Klystron (MBK) which should lead to an improved emittance immediately behind the gun. The diagnostics beam-line of the first milestone of PITZ2 was

commissioned in spring 2005 and has gone into operation. One of the most important sub-systems of a photo injector is the photocathode laser including the laser beam transport system. Especially in the case of FELs the transverse emittance is one of the basic characteristics which determine the performance of the SASE lasing. As simulations [4] and the results of PITZ [5] show, flat-top shape of the transverse and longitudinal profile of the laser beam are essential pre-conditions for a low transverse emittance of the electron beam. The photocathode laser at PITZ is developed by the Max-Born Institute Berlin (MBI) [6]. The laser produces pulses in a rather complicated time scheme according to the needs of the VUV-FEL and the XFEL. The maximum repetition rate at present is 10 Hz. The bunch train consists of 1...800 pulses emitted with a frequency of 1 MHz. The emitted wavelength is 262 nm which matches to the used Cesium-Telluride cathodes.

The last upgrade of the laser was performed in spring 2005. The essential improvement consists in the change of the pumping scheme of the amplifier stages. After the upgrade all amplifier stages are laser-diode pumped. It is expected, that this will result in a higher lifetime and more stability. Exchange of flash-lamps is not needed anymore. The laser can be operated now with a repetition rate of 10 Hz instead of 5 Hz before. Furthermore, the tuning of the laser pulse energy is realized exclusively by an attenuator behind the laser. This results in the advantage that the change of the laser pulse energy will not influence anymore on the transverse and longitudinal beam profile. Besides this, the laser control was improved.

The essential property of the laser beam-line should consist in the undisturbed transport of laser pulses to the photocathode keeping the transverse and longitudinal laser beam profile produced in the laser and in the laser beam-line. To improve the characteristics an upgrade of the laser beam-line was performed in spring 2005 as described in the next chapters.

<sup>\*</sup> presenting author: [juergen.baehr@desy.de](mailto:juergen.baehr@desy.de)

<sup>&</sup> This work has partly been supported by the European Community, contract numbers RII3-CT-2004- 506008 and 011935, and by the "Impuls-und Vernetzungsfonds" of the Helmholtz Association, contract number VH-FZ-05

<sup>#</sup> on leave from YERPHI, 375036 Yerevan, Armenia

<sup>§</sup> on leave from INRNE 1784 Sofia, Bulgaria

## THE LASER BEAM-LINE

The basic idea of the laser beam-line is the imaging of the beam-shaping aperture (BSA) onto the cathode such, that a flat-top transversal laser beam profile is produced. The BSA is illuminated by the laser beam, whereby the laser spot on the BSA is essentially larger than the inner diameter of the BSA.

During the upgrade of the laser beam-line in 2005 the distance of the BSA to the cathode has been essentially reduced. Besides this, more optical elements are remotely controlled, which gives the possibility of fine tuning of the laser beam parameters during running.

Furthermore the laser beam diagnostics is extended, this upgrade is still ongoing. All this upgrades should result in an improvement of the laser beam spot on the photocathode which should result in a decreased transverse emittance. The optical scheme of the upgraded laser beam-line was proposed and calculated by I. Will [7], see fig.1. This beam-line was commissioned in spring 2005. Fig.2 shows a schematic containing part of the laser beam-line diagnostics elements and the arrangement in the 3D-space. The overall length of the beam-line is about 20 m.

For 10 optical elements a remote control was developed. Usually 2 degrees of freedom – translation or rotation - are remotely controlled. For the technical solution an integrated system of MICOS [8] is used. A zero-position detector is added to all axes. The motor control is realized by a LabView program which itself is connected to the general control of PITZ. In fig.3 the main window of the laser beam-line control is shown.

The BSA consists of a metal plate with about 10 apertures of different diameter which can be positioned exactly and reproducibly on the axis of the laser beam. It can be moved by about 80 mm along the optical axis to optimize the focus.

## LASER BEAM DIAGNOSTICS

Several properties of the laser beam have to be controlled all the time. For this purpose appropriate diagnostics elements are needed. In Tab.1 these properties, the diagnostics elements and the tools to control the properties are shown.

## Virtual Cathodes

The virtual cathodes are realized by CCD-cameras which are UV sensitive and mounted exactly in a position corresponding to the gun photocathode. The analogous cameras of type M10SX (former: M10RS) are produced by JAI [9]. The cameras have a small but not negligible UV sensitivity in the range of the laser wavelength. The cameras are externally triggered, gain and shutter speed can be controlled using a RS232 interface. The pixel number is 782 x 582, the pixel size is 8.37 microns in both dimensions.

There are 2 virtual cathodes in use for different ranges of mean laser pulse train energy. The cameras are integrated in the general PITZ TV-system. The virtual cathodes are used for relative laser beam spot positioning and for the measurement of the transverse laser beam profile. A problem in the application is the limited radiation hardness of the cameras. Lead bricks are used to shield the cameras. Besides this, we observe a space dependent sensitivity of the camera sensor after some weeks or months running of the virtual cathode. We try to limit this effect by a shutter before the virtual cathode. An example for a laser beam transverse profile measured by the virtual cathode is shown in fig.4.

The measurement of the position jitter of the laser beam spot on the virtual cathode measured over 9 hours is shown in fig. 5. The amplitude of the jitter is of the order of 10 microns which is roughly the size of one camera pixel. The systematic increase the y-coordinate of about 10 microns has to be investigated.

The virtual cathodes do not resolve single laser pulses in the pulse train but measure mean values over all pulses in one pulse train. This will partly be improved in the near future by applying a quadrant diode. Using the quadrant diode one will be able to monitor the beam position with a pulse to pulse resolution. This option is under development and will be commissioned in a few weeks.

## Photomultiplier

A photomultiplier (PM) is used for the relative laser pulse energy monitoring. The applied PM type is H6780-03 by Hamamatsu[10]. The device is UV sensitive (quantum efficiency at 262 nm is about 14%) and the HV-power

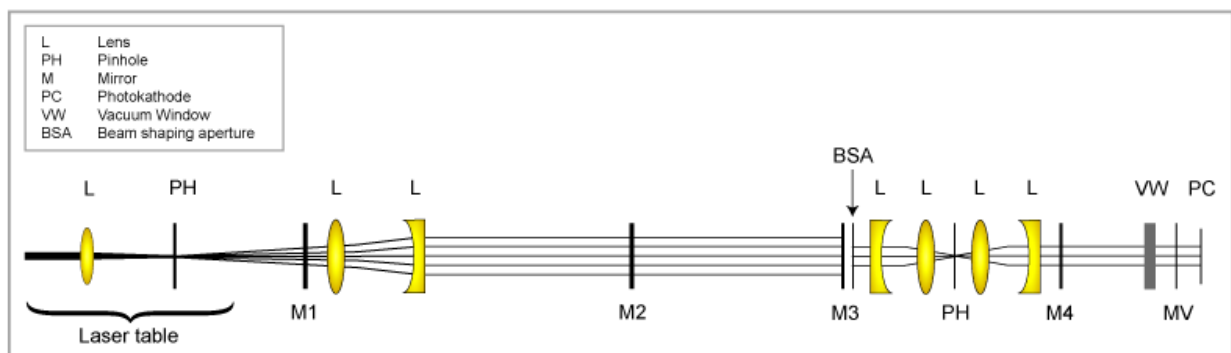


Fig. 1: Optical scheme of laser beam-line (I. Will)

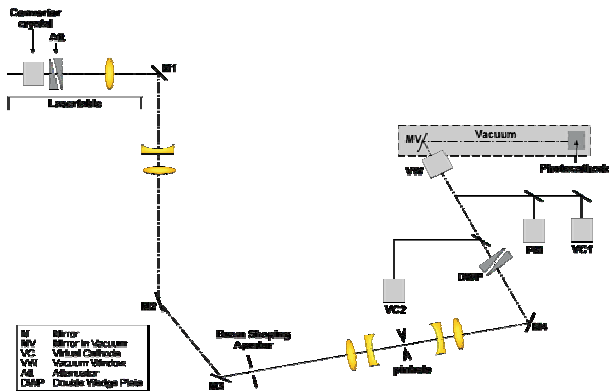


Fig. 2: Schematic of the laser beam-line

supply is integrated in the device. It has a metal channel dynode structure. The needed dynamic range is about 4 orders of magnitude. The device is commissioned, the calibration is ongoing.

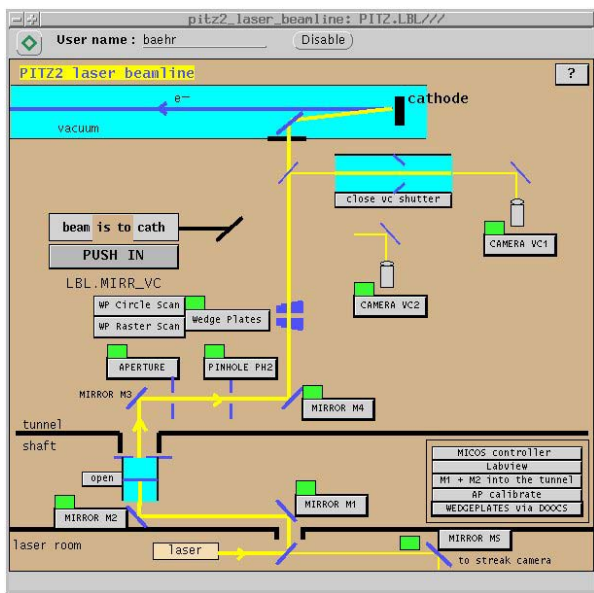


Fig. 3: Main control window of laser beam-line

### Streak camera

The longitudinal laser pulse profile is monitored using a streak camera. A fraction of the laser light is imaged by a second branch of the laser beam-line, which is not shown in fig. 2 onto the entrance slit of the streak camera. The used camera is of type C5680 produced by Hamamatsu. It is UV-sensitive and has a synchro-scan option. The resolution is 2 ps. An example of a longitudinal laser beam pulse profile is shown in fig. 6.

The parameters of the longitudinal profile measured at different days for two values of repetition rate are shown in table 2. The data show the relative stability of the longitudinal profile, the pulse shaper was not tuned between the measurements.

Tab.1: Laser beam properties, diagnostics elements and tuning tool for this property

Property	Measurement	Tuning
Pulse number	Oscilloscope	Laser control
Intensity envelope of pulse train	oscilloscope	Laser control
Pulse energy	Power meter	Attenuator on laser table
Relative pulse energy	Photomultiplier	Laser system tuning
Longitudinal profile	Streak camera	Pulse shaper in laser
Transverse beam profile	Virtual cathode VC1, VC2	Inclination of converter crystals, focus, laser system tuning
Nominal laser beam diameter	VC1, VC2	Beam shaping aperture
Laser beam inclination at entrance of laser beam-line	TV-system on laser table	Mirror at laser exit
Laser beam position on cathode, integrated	VC1, VC2 (relative)	Mirror4, double wedge system
Beam on virtual cathodes	VC1, VC2	x,y drive of cameras
Laser beam position on cathode, time resolved	Quadrant diode (relative)	Mirror4, double wedge system

### TV-cameras on laser table

A system of 2 TV-cameras will be arranged on the laser table. It allows the monitoring of the transverse beam profile, the relative laser beam position (near field) and the laser beam inclination (far field) immediately behind the laser.

Besides the monitoring of these properties it is useful for the laser beam-line alignment after laser adjustment. One can easily align the laser beam behind the laser in 4 degrees of freedom to match into the laser beam-line.

Table 2: Longitudinal laser beam profile

Date	Rep. rate/Hz	Width(FWHM)/ps	T(rise)/ps	Mod./%
01/08/05	10	23.5	6.5	5.0
10/08/05	10	25.5	6.9	5.7
11/08/05	5	25.3	7.5	6.5

The system is in preparation and will be commissioned in a few weeks.

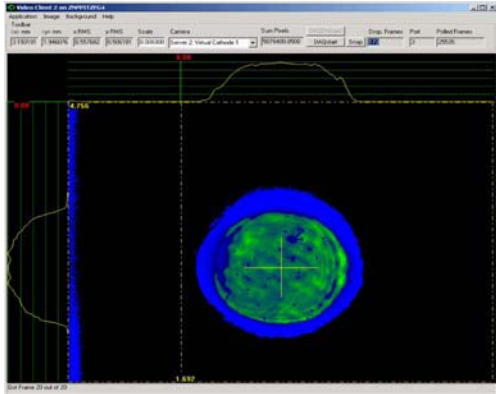


Fig. 4: Laser beam profile on virtual cathode

#### Resolution grid

A resolution grid is integrated into the plane of the BSA. The aim is to verify that a certain spatial resolution in the structure of the laser beam can be transferred onto the cathode. It is the aim to find this structure in the electron beam hitting a view-screen.

#### Laser pulse energy measurement

The laser pulse energy measurement is realized using a mobile absolutely measuring laser power meter. Ports for the detector are prepared immediately behind the laser

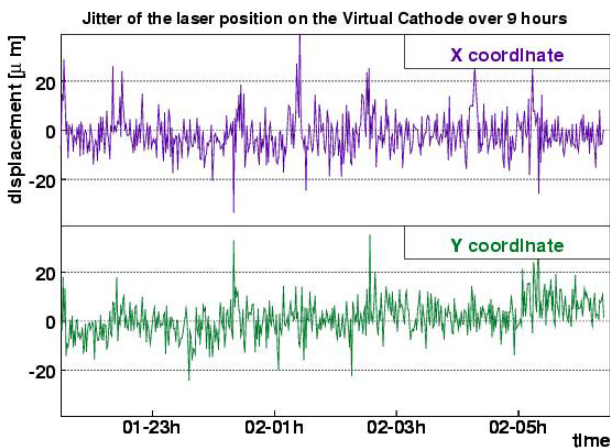


Fig. 5: Jitter of the laser position on VC1 over 9 hours

and just before the vacuum window near to the cathode. The PM announced above can be calibrated by the laser power meter.

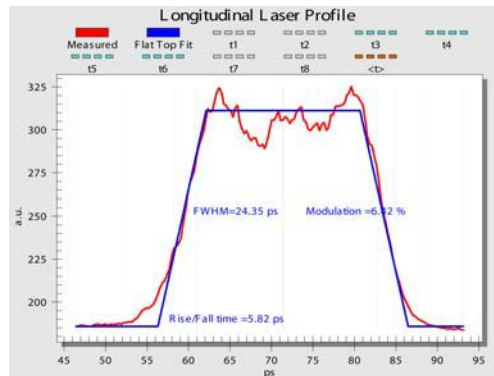


Fig. 6: Longitudinal laser pulse profile

## SUMMARY

At the PITZ facility an upgrade of the photocathode laser and the laser beam-line was performed. The essential change in the laser upgrade was the exchange of all flash-lamp pumped amplifier stages by laser-diode pumped amplifier stages. This leads to a higher laser stability and lifetime, easier maintenance and the possibility to run the laser with a repetition rate of 10 Hz. The goal of the upgrade of the laser beam-line was to improve the stability and the transversal optical profile on the photocathode. This should be reached by moving the beam shaping aperture closer to the photocathode. The optical scheme was completely changed. The number of remotely controlled optical elements was increased. Several diagnostics tools are integrated in the laser beam-line. First investigations on the stability of laser and the laser beam-line show an improved stability.

## REFERENCES

- [1] F.Stephan et al., Proc. FEL2000, Durham
- [2] A. Oppelt et al., "Status and first results from the upgraded PITZ facility", this conference
- [3] M.Ferrario et al. LNF-00-004(P)
- [4] M.Krasilnikov, "Experimental Characterization and Numerical Simulation of the Electron Source at PITZ" ICAP2004, St.Petersburg
- [5] V.Miltchev et al., "Transverse emittance measurement at the photo injector test facility at DESY Zeuthen", FEL 2004, Trieste, Italy
- [6] I.Will et al., Nucl.Instr.Meth.A472(2001), p.79
- [7] I.Will, seminar talk (unpublished), December 2004, DESY, Zeuthen
- [8] MICOS, Am Laidhoelzle 1, D-79224 Umkirch, Germany
- [9] JAI Corporation, Yokohama, Kanagawa 226-0006, Japan
- [10] Hamamatsu Photonics K.K. Electron Tube Division, Iwata-gun 438-01 Japan



# BUNCH LENGTH MEASUREMENTS USING A MARTIN-PUPLETT INTERFEROMETER AT THE VUV-FEL

L. Fröhlich\*, O. Grimm, DESY, Hamburg, Germany

## Abstract

The longitudinal charge distribution of short electron bunches can be characterized by a measurement of their coherent far-infrared radiation spectrum. This paper summarizes recent results obtained at the DESY VUV-FEL linear accelerator by observation of synchrotron radiation with a Martin-Puplett interferometer. The bunch shapes reconstructed with this method show a strong asymmetry with a full width at half maximum of about 1 ps.

## INTRODUCTION

The linac-driven Vacuum-Ultraviolet Free Electron Laser (VUV-FEL) at DESY, Hamburg produces short pulses of intense soft X-ray radiation. Because the high gain FEL process depends strongly on a high peak current of the electron bunches, it is necessary to measure and control the bunch length. As a technique for bunch length measurements with sub-picosecond resolution, we analyze coherent synchrotron radiation (CSR) with a Martin-Puplett interferometer. Once the spectrum of the coherent radiation is determined, the form factor and the longitudinal charge profile of the bunch can be reconstructed.

## EXPERIMENTAL SETUP

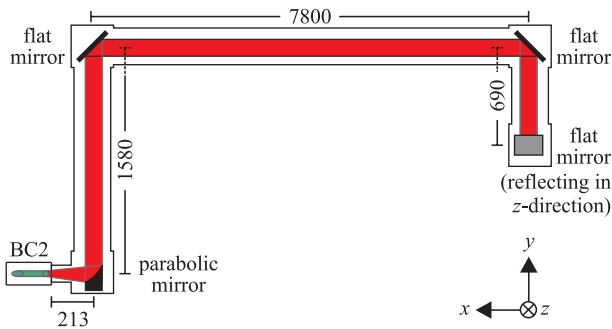


Figure 1: Setup of the CSR transfer line at bunch compressor BC2 (measures in mm)

The CSR beam is extracted from the last dipole magnet of a bunch compressor through a 4.8 mm thick vacuum window. To obtain good transmission properties up to 3.6 THz, a z-cut quartz single crystal has been chosen as the window material. By a series of mirrors, the radiation bundle is parallelized and reflected into a laboratory outside of the accelerator tunnel (Fig. 1). The transfer line can be flushed with dry nitrogen to reduce absorption by

water vapor. However, due to the large enclosed volume, it currently takes more than one day to achieve sufficient suppression of the absorption effects. Therefore, preparations are underway to evacuate the beam line.

The Martin-Puplett interferometer<sup>1</sup> (Fig. 2) is a polarizing version of the well-known Michelson version. Grids of gold-coated tungsten wires (thickness 15  $\mu\text{m}$ , distance 45  $\mu\text{m}$ ) are used as polarizers, permitting operation of the instrument up to frequencies of at least 3 THz. The far-infrared radiation intensity is measured with two pyroelectric DTGS detectors. Further details on the experimental setup and on the measurements can be found in [1].

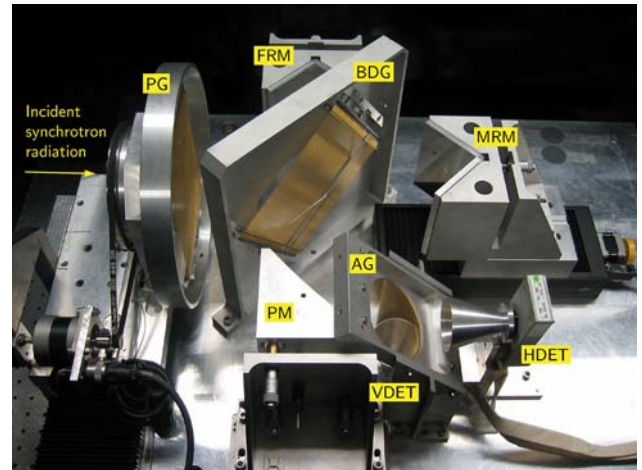


Figure 2: Setup of the interferometer. PG/BDG/AG – polarizer / beam divider / analyzer grid, FRM/MRM – fixed / moveable roof mirror, PM – parabolic mirror, VDET/HDET – detector for vertical / horizontal polarization.

## THE RECONSTRUCTION PROCESS

### Measuring principle

The direct result of an interferometer scan is a series of data points of the two detector signal amplitudes  $U_h$ ,  $U_v$  versus the time shift between the two partial beams in the instrument. While the interference signal is anti-correlated in the detectors, fluctuations and drifts in the incident radiation intensity affect both signals likewise. Therefore, the normalized *difference interferogram*  $\delta = (U_h - U_v) / (U_h + U_v)$  shows a much better signal-to-noise ratio than the single interferograms (Fig. 3 and 4).

\* lars.froehlich@desy.de

<sup>1</sup>Components manufactured at RWTH Aachen

The power spectrum  $I(\omega)$  is obtained by a Fourier transform of the difference interferogram. It is corrected by applying transfer functions for various optical elements of the radiation transfer line. Well understood transfer functions cover the absorption by residual water vapor and the transmission behavior of the quartz window, while important contributions like diffraction losses and detector sensitivity are still under investigation (cf. [4]).

As the 8 mm high vacuum chamber of the bunch compressor imposes an electromagnetic cutoff, frequencies below 275 GHz are almost completely suppressed in the measured spectra. An appropriate asymptotic curve is fitted to the data to replace the missing intensity information.

### Form factor analysis

The radiation emitted by a relativistic bunch of electrons is usually incoherent because the particles radiate under random phases. However, at wavelengths longer than the bunch itself, the emission is coherent. If  $I_1(\omega)$  is the spectral intensity distribution for a single electron, a bunch of  $N$  particles shows the spectrum

$$I(\omega) = I_1(\omega) \left( N + N(N-1) |F(\omega)|^2 \right), \quad (1)$$

with  $F(\omega)$  denoting the form factor of the bunch. In the case of tangential observation,  $F(\omega)$  can be expressed as the one-dimensional Fourier transform of the normalized longitudinal charge density  $\rho(t_z)$ :

$$F(\omega) = \int \rho(t_z) \exp(-i\omega t_z) dt_z$$

From a measurement of the spectrum, (1) allows to determine the modulus of the form factor.<sup>2</sup> To recover the missing phase information of the generally complex-valued  $F(\omega)$ , we use a *Kramers-Kronig relation* as proposed in [2]:

$$\eta(\omega) = \frac{2\omega}{\pi} \int_0^\infty \frac{\ln(|F(\omega')|/|F(\omega)|)}{\omega^2 - \omega'^2} d\omega'$$

It has been verified that this *minimal phase* is a good approximation of the actual phase of the complex form factor for typical bunch shapes (cf. [3]).

Finally, an inverse Fourier transform of the form factor gives access to the longitudinal charge distribution of the electron bunch.

### Resolution

The limits of the bunch length reconstruction are defined by the spectral range accessible to the measurement. In our case, the low-frequency cutoff limits the maximum length of reconstructible bunch features to about

$$l_{\max} = \frac{1}{2}(275 \text{ GHz})^{-1} \approx 1.8 \text{ ps (550 } \mu\text{m)}.$$

<sup>2</sup>This step requires a good knowledge of the single-particle spectrum  $I_0(\omega)$ . The subject is under continuous study with particle-tracking simulations.

Towards high frequencies, the absorption edge of the quartz window at 3.6 THz is a hard limit. Therefore, no structures smaller than

$$l_{\min} = \frac{1}{2}(3.6 \text{ THz})^{-1} \approx 140 \text{ fs (42 } \mu\text{m)}$$

can be resolved.

## MEASUREMENT RESULTS

### Scan during SASE FEL operation

Figures 3 and 4 show the results of a selected interferometer scan<sup>3</sup> during operation of the SASE FEL. As the scan took more than 20 minutes to complete, even comparatively slow drifts of machine parameters are visible in the total CSR intensity. The width of the difference interferogram, 0.51 ps (fwhm), is already a coarse indicator for the bunch length.

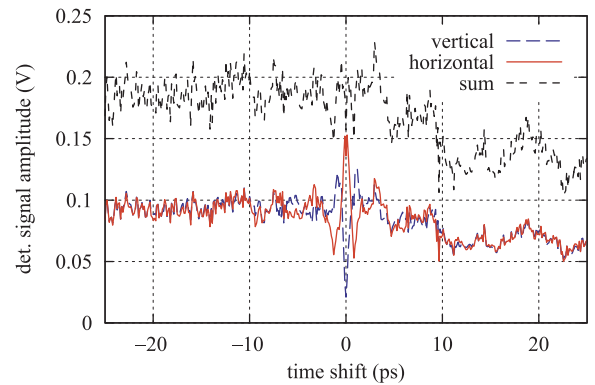


Figure 3: Raw interferograms. Drifts and fluctuations of the CSR intensity are visible.

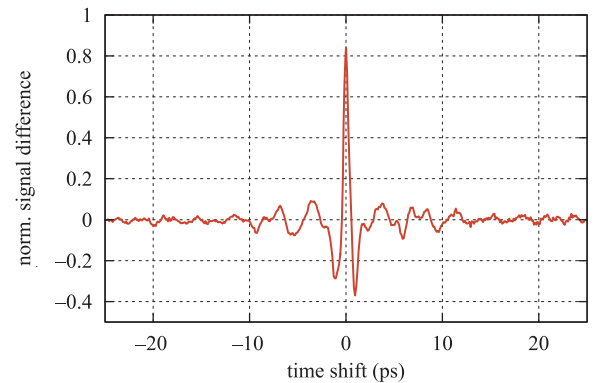


Figure 4: Difference interferogram. The distortions are well suppressed.

The corresponding spectrum (Fig. 5) shows that the measured coherent radiation power has almost no contribution above 2 THz. Even after correction with the known transfer

<sup>3</sup>Machine parameters: beam energy 125 MeV, acceleration phase  $-5^\circ$ , bunch charge 1.2 nC

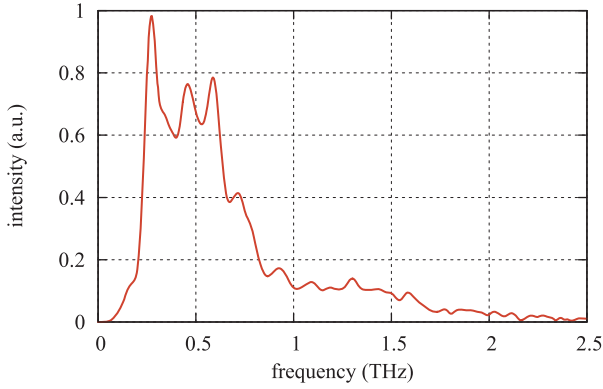


Figure 5: Power spectrum of the observed radiation after correction with the transfer functions.

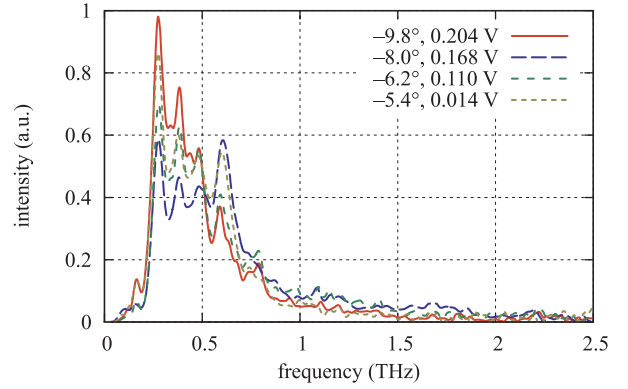


Figure 7: CSR spectra for various acceleration phases. The mean detector signal amplitudes are given.

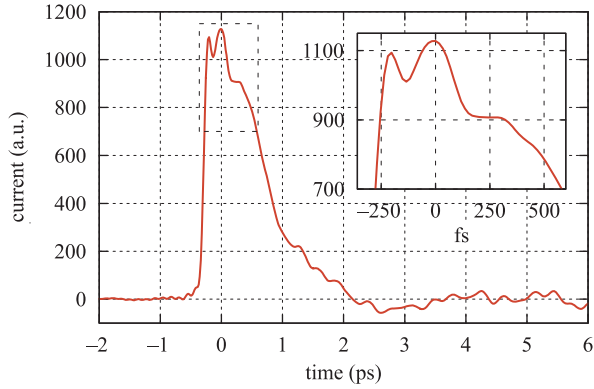


Figure 6: Reconstructed bunch shape. The width is 0.98 ps (fwhm) or 0.50 ps (rms).

functions, the spectrum reveals some unexplained oscillations, which might be an indication for as yet unconsidered effects, e.g. in the detector sensitivity.

The reconstructed bunch shape (Fig. 6) is clearly asymmetric, with a width of 0.98 ps (fwhm) or 0.50 ps (rms<sup>4</sup>). The small structures on top of the bunch have an extent below or very near the resolution limit and should therefore be considered as artifacts.

### Various degrees of bunch compression

The main parameter for tuning the compression of the electron beam is the relative phase between the electromagnetic RF wave and the electron bunch. If this phase is zero, the bunch is accelerated “on crest”, and no compression takes place in the magnetic chicane. At BC2, maximum compression is found at about  $-11^\circ$ . In the intermediate range, the coherent radiation intensity emitted by the bunch is very sensitive to changes of the phase.

Figure 7 shows CSR spectra measured at various acceleration phases. The plot illustrates that no clear correlation between the shape of the spectral distribution and the

<sup>4</sup>It should be noted that only points with a current above 5% of the maximum value are included in the calculation of the rms width to remove the influence of noise on the right side of the reconstructed bunch shape.

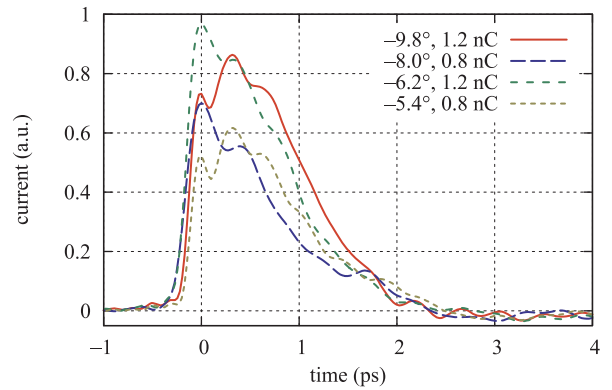


Figure 8: Reconstructed bunch shapes for various compression settings. The curves are scaled according to the respective bunch charge.

compression setting can be established. While the total radiation intensity increases with higher bunch compression, this increase is not accompanied by a shift to the high frequency range as expected in the case of a shortening of the coherently radiating part of the bunch.

From this observation, it is not surprising that also the reconstructed bunch shapes show little dependence on the phase, as seen in Fig. 8. The corresponding bunch lengths are found in Tab. 1 together with the relevant machine parameters.

Table 1: Measurement parameters

Phase (°)	Energy (MeV)	Charge (nC)	FWHM (ps)
-9.8	125	$1.16 \pm 0.07$	1.23
-8.0	127	$0.80 \pm 0.05$	0.92
-6.2	125	$1.16 \pm 0.07$	1.08
-5.4	127	$0.81 \pm 0.04$	1.17

## OUTLOOK

At present, a number of unknown quantities enter into the process of bunch shape reconstruction. To improve the accuracy of the method, especially two points need further investigation:

- The diffraction losses along the beam transfer line should be measured to obtain a reliable transfer function.
- The spectral responsivity of the detectors for far-infrared radiation needs to be determined. First steps in this direction have already been taken (cf. [4]).

At the moment, the low-frequency cutoff of the vacuum chamber constitutes a severe limitation of the achievable resolution. Experiments with different coherent radiation sources may help to widen the accessible spectral range.

## REFERENCES

- [1] L. Fröhlich, “Bunch length measurements using a Martin-Puplett interferometer at the VUV-FEL”, DESY report DESY-THESIS-2005-011/TESLA-FEL 2005-02, June 2005.
- [2] R. Lai and A. J. Sievers, “Examination of the phase problem associated with the determination of the longitudinal shape of a charged particle bunch from its coherent far IR spectrum”, *Phys. Rev. E*, vol. 50, pp. 3342–3344, 1994.
- [3] R. Lai and A. J. Sievers, “On using the coherent far IR radiation produced by a charged-particle bunch to determine its shape: I Analysis”, *Nucl. Instr. and Meth. A*, vol. 397, pp. 221–231, April 1997.
- [4] O. Grimm et al., “Detector response and beam line transmission measurements with far-infrared radiation”, this conference, paper ID MOPP033.

# Next Generation Synchronization System for the VUV-FEL at DESY

H. Schlarb\*, V. Ayvazyan, F. Ludwig, D. Noelle, B. Schmidt, S. Simrock, A. Winter, DESY, D-22607 Hamburg, Germany and F. Kaertner, MIT, Cambridge, Massachusetts

## Abstract

The control and stabilization of the longitudinal beam profile and the bunch arrival time in linac driven VUV or X-ray Free-Electron Lasers requires special effort and new developments in the fields of low-level RF controls, global synchronization systems, and longitudinal beam feedbacks. In this paper we describe the required upgrades for the VUV-FEL at DESY to synchronize the FEL pulse and optical lasers to the hundred femtoseconds (FWHM) level.

## INTRODUCTION

Pump-probe configurations are typically used to investigate the evolution of ultrafast systems in atomic physics, chemistry, biology or condensed matter. The time-dependent phenomena is stimulated by a high-power pump pulse, e.g. with an ultrafast optical laser, and then probed after a defined time delay. By repeating the experiment for different delays, the system changes can be recorded and the underlying dynamics understood.

In the standard setup, the pump and the probe beam have a common source, so that precise time delays can be produced with optical path-length differences. The time-resolution can be as short as a fraction of a femtosecond and is limited only by the overlap of the pump and the probe pulses [1, 2].

To carry out pump probe experiments at the VUV-FEL at DESY, a high-power optical laser has been installed. Since the VUV-pulse is generated by passing short electron bunches through a long undulator, the origin of the pump and probe sources is different. Special effort is required to precisely synchronize the electron bunch, thus the FEL-pulse, and the laser pulse to one another. In this paper we discuss the required upgrades of the facility, RF amplitude and phase tolerance and the resolution required of monitor systems serving beam based feedbacks.

## VUV-FEL LAYOUT AND TIMING JITTER

The layout of the VUV-FEL is shown in Fig. 1. The electron beam is generated by impinging a laser pulse on an CsTe-photocathode installed in a normal conducting 1.5-cell RF gun. The beam exits the gun with an energy of 4.5 MeV and is accelerated to 130 MeV in the superconducting module ACC1, housing 8 TESLA like cavities. To preserve the electron bunch emittance, the first four cavities are operated at a gradient of 12.5 MV/m. By off-crest acceleration in ACC1, an energy chirp in bunch is introduced, causing a longitudinal compression in the dispersive chicane 'BC2'. Then the energy is raised to 380 MeV

by the cryo-modules ACC2 and ACC3, before the final bunch compression takes place in BC3, an S-shape like chicane. Finally, the electron beam is accelerated to the energy needed to produce a wavelength between 6 nm (1 GeV) and 35 nm (380 MeV). The electron beam passes a collimator system to remove halo before entering the undulator magnets. The FEL beam then passes a 40 m long photon beam line to the experimental hall. The total distance from the RF photo-injector to the FEL experiment is about 260 m.

Presently, the third harmonic cavities (3.9 GHz) to linearize the longitudinal phase space are not yet installed. Thus, the initial, long electron bunch length of about 2 mm entering the ACC1 module receives a significant non-linear energy chirp due to the RF curvature. This causes only a small fraction of the electron beam to be compressed, leading to an ultra-short spike with peak currents of several kA. Strong collective forces such as space charge and coherent synchrotron radiation acting within the spike restrict the linac operation and the FEL pulse duration cannot be tuned.

The observed FEL pulse duration generated by the electron spike can be as short as 25 fs FWHM [3]. For pump probe experiments, ideally the electron beam is synchronized to the range of the photon pulse duration. The rms jitter of the electron bunch arrival time depends primarily on the RF stability and can be expressed as

$$(c_0\sigma_t)^2 = \left( \left[ R_{1,56} + \frac{E_1}{E_2} R_{2,56} \right] \frac{\sigma_{V_1}}{V_1} \right)^2 + \left( R_{2,56} \frac{E_2 - E_1}{E_2} \frac{\sigma_{V_2}}{V_2} \right)^2 + \left( \frac{\sigma_{\Phi_1}}{k_{rf}} \right)^2 \quad (1)$$

with  $V_1$  and  $V_2$  being the acceleration voltage of ACC1 and ACC2/ACC3, respectively. The energy and longitudinal dispersion of the first and the second chicane are denoted by  $E_1, E_2, R_{1,56}$ , and  $R_{2,56}$ . The RF phase jitter  $\Phi_1$  of ACC1 translates directly into the timing jitter of the electron bunch, since in this present compression mode the second acceleration section can not significantly contribute to the energy chirp and is thus operated on-crest ( $\Phi_2 = 0$ ).

With the nominal bending angles of  $18^\circ$  and  $3.8^\circ$  in BC2 and BC3, the ACC1 RF amplitude to beam arrival time conversion is (see Tab.)

$$\sigma_t = 658.1 [ps] \frac{\sigma_{V_1}}{V_1} \quad (2)$$

which dominates the rms jitter budget. For synchronization within the FEL pulse ( $< 10$  fs rms), an energy stability of  $\sigma_{V_1}/V_1 \approx 1 \cdot 10^{-5}$  is required. This is extremely difficult to achieve and has not been demonstrated for SRF cavities so far. The tolerance on the amplitude stability can be somewhat relaxed by reducing the  $R_{1,56}$  in BC2.

\*holger.schlarb@desy.de

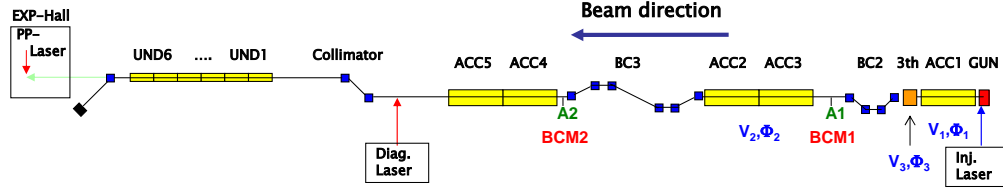


Figure 1: Layout of the VUV-FEL.

	no 3 <sup>th</sup>	with 3 <sup>th</sup>
$E_1$	130 MeV	130 MeV
$E_2$	380 MeV	450 MeV
$V_1$	126.7 MV	148 MV
$\Phi_1$	$-8^\circ$	$-3.9^\circ$
$V_2$	250 MV	368 MV
$\Phi_2$	$0^\circ$	$-29.6^\circ$
$V_3$	-	18.02 MV
$\Phi_3$	-	191.7 MV
$R_{1,56}$	-181 mm	-181 mm
$T_{1,566}$	295 mm	295 mm
$R_{2,56}$	-48.6 mm	-40.0 mm
$T_{2,566}$	73.3 mm	60.2 mm

Table 1: RF and BC parameters for simulation.

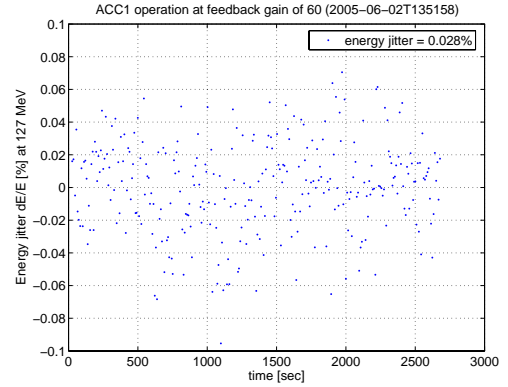


Figure 2: Energy jitter measured in BC2.

### Achieved energy stability at the VUV-FEL

The energy stability of the first acceleration module has been measured by imaging the beam with an OTR-screen in the straight section of the first bunch compressor. To avoid phase drifts during the measurement and to increase the resolution of the method, the cryo-module has been operated close to on-crest. The screen was calibrated by varying dipole current while monitoring the beam displacement on the screen.

After careful adjustment of the low-level RF parameters, such as loop phase, timing, phase and amplitude offsets, and a re-calibration of the cavity vector sum in the DSP system, shot-to-shot energy stability of  $2.8 \cdot 10^{-4}$  could be achieved. Figure 2 shows the energy jitter recorded during 45 min of operation.

The arrival times calculated from this energy jitter amounts to 180 fs rms, in agreement with measurements using spectral-decoding single-shot electro-optical techniques [4].

The measurement represents the energy variation of the first few bunches of each macro-pulse taken at a repetition rate of 2 Hz. The energy stability within a macro-pulse of  $800 \mu s$  duration can be much smaller. During superstructure tests (2002, TTF phase 1), the energy stability from macro-pulse to macro-pulse was 0.2%, but a factor of five better result has been achieved within the macro-pulse.

It is planned to replace the RF feedback DSP system

by an FPGA based board and to operated the RF down-converters at an intermediate frequency of 81 MHz instead of 250 kHz. This increases the resolution of the RF measurement and decreases the latency introduced by the data processing. With feedback regulation operated at a higher gain it becomes realistic to stabilize the energy to better than  $5 \cdot 10^{-5}$  within the macro-pulse train. In this case, the phase stability of the RF becomes more critical and will dominate the timing jitter unless special care is taken.

### Arrival jitter with the 3<sup>rd</sup>-harmonic cavities

In 2006, four cavities with an operation frequency of 3.9 GHz will be installed between the acceleration module ACC1 and the bunch compressor BC2. At a gradient of 15 MV/m and a length of 0.343 m per cavity, a maximum energy gain of 20.6 MV can be provided. The purpose of the cavities is to remove the non-linear energy-time correlation (chirp) of the bunch caused by the curvature of the 1.3 GHz RF acceleration in ACC1. The non-linear RF effect can be neglected after the beam is compressed in the first chicane.

At BC2 the energy of electrons at position  $z$  in the bunch ( $z < 0$  bunch head) is

$$E_1 = E_0 + V_1 \cos(k_{rf}z + \Phi_1) + V_3 \cos(3k_{rf}z + \Phi_3), (3)$$

where  $(V_1, \Phi_1, V_3, \Phi_3)$  are RF amplitude and phases shown in Fig. 1. The path length of the electrons through the mag-

netic chicane is written by

$$T(E_1) = L_0 + R_{56} \frac{E_1 - E_{10}}{E_{10}} + T_{566} \left( \frac{E_1 - E_{10}}{E_{10}} \right)^2 \quad (4)$$

with  $E_{10} \equiv E_1(z=0)$  the energy of the bunch center. The beam energy  $E_{10}$ , the linear energy chirp as function of the compression factor  $C_1$

$$E'_1 = -\frac{E_{10}}{R_{56}} \left( 1 - \frac{1}{C_1} \right) \quad (5)$$

and the compensation for the second order dispersion by a second order energy chirp

$$E''_1 = -2 \frac{T_{566}}{R_{56}} \frac{(E'_1)^2}{E_{10}} \quad (6)$$

defines three equations with four RF parameters ( $V_1, \Phi_1, V_3, \Phi_3$ ) in Eq. 3. The third order chirp  $E'''_1$  is a free parameter and its influence on the final bunch shape and bunch asymmetry is tolerable [5]. As discussed in [5], the third order energy chirp can be chosen such, that the dependency of the beam compression factor on the RF phase jitter for both 1.3 GHz and 3.9 GHz can be entirely removed. But significant RF power is required and the tolerances on the RF amplitudes are tighter. In addition, the sensitivity to arrival time jitter is enhanced, compromising pump probe experiments.

For the VUV-FEL, the parameter  $E'''_1$  can only be varied in a small range, due to limitations of the voltage generated by the 3<sup>rd</sup>-harmonic cavities. The dependence on phase and voltage is plotted in Fig. 3.

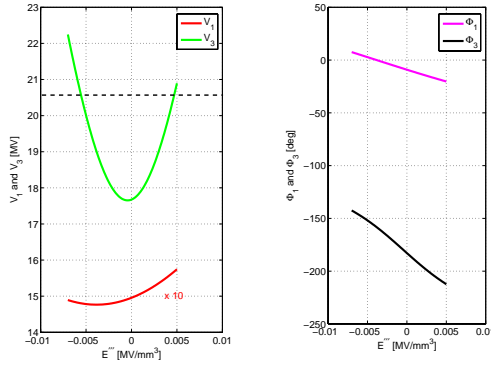


Figure 3: Amplitude and phase in first acceleration section as function of the third order chirp ( $C_1 = 5$ ). Dashed line indicates limit for  $V_3$ .

For pump probe experiments, only the arrival time jitter of the beam behind the last compressor (BC3) is important. This jitter depends on the compression factors  $C_1$  and  $C_2$ , for the first and the second chicane, and the RF stability of modules ACC1 and ACC2-ACC3.

In order to achieve an arrival stability of below 100 fs FWHM, the choice of RF and compression has been selected using the following criteria:

- an rms amplitude tolerance  $\sigma_{V_1}$  of ACC1  $\geq 5 \cdot 10^{-5}$ ,
- rms phase tolerance  $\sigma_{\Phi_1}$  and  $\sigma_{\Phi_3} \geq 0.02^\circ$ ,
- $\sigma_{\Phi_2} \geq 0.06^\circ$ , corresponding to timing jitter accuracy requirements for the phase measurement of 1.3 GHz and 3.9 GHz,
- moderate gradients in the acceleration structures (small Lorentz force detuning),
- a weak dependence of arrival time changes on bunch length variations
- independent correction of the arrival time jitter introduced by BC2 and BC3
- decoupling of amplitude and phase from the arrival time jitter.

Finally, the setting should allow a simple variation of the bunch length after BC3 without larger changes in feedback algorithms. A possible set of parameters that fulfill most of the above criteria is listed in Tab. .

$\sigma_{V_1}/V_1$	$\sigma_{V_3}/V_3$	$\sigma_{V_2}/V_2$	$\sigma_{\Phi_1}$	$\sigma_{\Phi_3}$	$\sigma_{\Phi_2}$
$5 \cdot 10^{-5}$	$4 \cdot 10^{-4}$	$1 \cdot 10^{-4}$	$0.02^\circ$	$0.06^\circ$	$0.02^\circ$
-684 ps	82 ps	-	-0.40	-0.40	-
-426 ps	51 ps	95 ps	-0.25	-0.25	-0.44

Table 2: RF jitter used in simulation. The last two lines lists the conversion factor RF to arrival time after BC2 and BC3. Phase is determined in terms of time jitter (conversion unit [fs/fs])

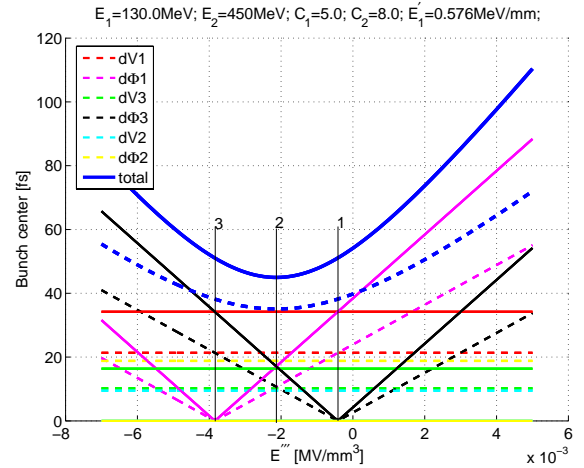


Figure 4: Arrival time jitter of beam behind BC2 (solid) and BC3 (dashed). The rms jitter used in the simulation are listed in Tab. 2

Figure 4 shows the rms arrival time jitter behind BC2 (solid lines) and BC3 (dashed lines) as a function of  $E'''_1$ . The effect of different RF parameters are shown, as well as

the overall jitter (blue) assuming that all parameters add independently from one another. The RF jitter for each parameter used in the simulation is listed in Tab. 2 .

The working points 1 or 3, indicated by vertical lines in Fig. 4, show that phase changes of the 3rd-harmonic or the ACC1 module do not contribute. Here,  $E_1'''$  is adjusted such that the operation phase is either  $180^\circ$  or  $0^\circ$  for the 3rd-harmonic or ACC1 cavities, respectively..

However, the minimum of the overall jitter is at work point 2, where 50% of the linear energy is generated by ACC1 and 50% by the 3<sup>rd</sup>-harmonic cavities. The longer bunch at the entrance of ACC2-ACC3 allows for operation of ACC2-ACC3 off-crest in order to compress some of the timing jitter introduced in BC2. The final bunch length is adjustable using  $\Phi_2$ , with  $-29.6^\circ$  for  $\sigma_z = 50 \mu\text{m}$  and  $-32.5^\circ$  for  $\sigma_z = 20 \mu\text{m}$ .

**Beam monitoring:** The arrival time is dominated by the amplitude stability of ACC1 and the phase stability of ACC2-ACC3. Both have to be measured by arrival time monitors, A1 and A2, shown in Fig. 1. To avoid larger correlated phase changes of  $\Phi_1$  and  $\Phi_3$  ( $\Phi_1 = 3\Phi_3$ ), or equivalently, an increasing arrival drift of the beam exiting the injector, careful measurement of the energy with BPMs in BC2 is required. An uncorrelated phase jitter ( $\Phi_1 = -3\Phi_3$ ), is the dominant source for bunch length jitter, which is monitored by the bunch compression monitor BCM2. The required accuracy of beam monitors A1 and A2 are 10 fs rms, and for the BPMs in the chicane 10  $\mu\text{m}$ .

## NEXT SYNCHRONIZATION SYSTEM FOR VUV-FEL

To achieve the timing jitter for the pump probe experiment, a laser based synchronization system is currently developed at DESY and MIT [6, 7]. Here a brief overview on the various devices, sketched in Fig. 5 will be given. Details and recent results can be found in [8].

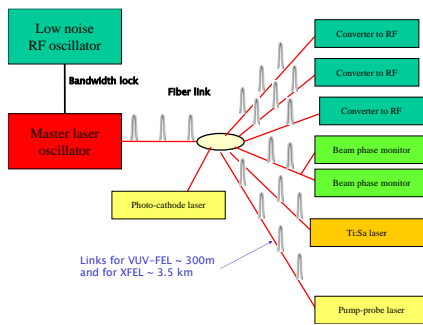


Figure 5: Next generation synchronization system.

**Master laser oscillator (MLO):** A passive mode-locked, ultra-stable Erbium-doped fiber laser with a repetition rate of 40.625 MHz serves as reference for all timing critical devices. The laser is locked with a piezo-stretcher to an ultra-low noise RF master oscillator. The laser pulses

of 0.5 ps duration (FWHM) and a central wavelength of 1550 nm are distributed in optical path-length stabilized fiber links. The integrated phase noise of the MLO has been measured to be  $<10$  fs in the frequency range between 1 kHz and 20 MHz, limited by the measurement method. The stream of pulses allows to extract any harmonics of the laser repetition rate, all phase locked to one another. The synchronization laser beam can be used to seed other lasers by generating higher harmonics of the 1550 nm. Due to the low repetition rate individual pulses can be used for electro-optical measurement to determine the bunch length or the beam arrival time (beam phase monitor) .

**Fiber length stabilization:** An RF phase lock loop comparing the back-reflected pulse with subsequent ones has demonstrated to be sufficient for a stabilization better than 20 fs. Using sum harmonic generation, the next step is to stabilize the optical path length to the fs-regime.

**Laser to RF conversion:** For synchronization in the order of 50 fs a photo-detector, bandpass-filter and RF amplifier is sufficient. To remove long term drifts and to achieve synchronization smaller than 10 fs, ultra-low noise VCO's and fiber loops controlled by optical phase modulators are planned.

In the final stage, to goal is to synchronize arbitrary points in (e.g. diag. laser, pump probe laser, VCO output, etc) better than 10 fs rms.

## SUMMARY

Pump probe experiments with time stability of 30 fs rms become realistic, by further improvements of the low level RF regulations which allows amplitude and phase stability of  $5 \cdot 10^{-5}$  and  $0.01^\circ$  within the pulse train. Mandatory for this timing stability is a laser based synchronization system that providing 10 fs point-to-point timing jitter to synchronize lasers and acceleration to one another.

## REFERENCES

- [1] M. Hentschel *et al.*, "Attosecond metrology", Nature 414, 509-513 (2001)
- [2] E. Goulielmakis *et al.*, "Direct Measurement of Light Waves", Science, Vol. 305, 1267-1269 (2004)
- [3] B. Faatz, "First Results from the VUV FEL at DESY", PAC'05, May 2005, Tennessee
- [4] B. Steffen, "Spectral Decoding", FEL'05, August 2005, San Francisco
- [5] M. Dohlus, T. Limberg, "Bunch Compression Stability Dependence on RF Parameters", FEL'05, August 2005, San Francisco
- [6] F. Kaertner *et al.*, "Progress in Large Scale Femtosecond Timing Distribution and RF-Synchronization", PAC'05, May 2005, Tennessee
- [7] A. Winter, "Synchronization of Femtosecond Pulses", FEL'05, August 2005, San Francisco
- [8] A. Winter *et al.*, "Femtosecond Timing Distribution", FEL'05, August 2005, San Francisco

# TRANSVERSE ELECTRON BEAM DIAGNOSTICS AT THE VUV-FEL AT DESY

K. Honkavaara\*, F. Löhl, Hamburg University, 22761 Hamburg, Germany  
 D. Nölle, S. Schreiber, E. Sombrowski, DESY, 22603 Hamburg, Germany  
 M. Sachwitz, DESY, 15738 Zeuthen, Germany  
 M. Castellano, G. di Pirro, INFN-LNF, 00044 Frascati, Italy  
 L. Catani, A. Cianchi, INFN-Roma2, 00133 Roma, Italy

## Abstract

The VUV-FEL is a new free electron laser user facility at DESY. High demands on the electron beam quality require sophisticated beam diagnostics tools and methods. At the VUV-FEL the transverse distribution of the electron beam is measured using optical transition radiation (OTR) monitors and wire scanners. This paper refers concepts, analysis, and results of the transverse phase space measurements. The main emphasis is on emittance measurements, in which we have regularly measured normalized projected rms emittances around 1.4 mm mrad for 90% of a 1 nC bunch at 127 MeV beam energy.

energy is low ( $\sim 5$  MeV), detect light emitted by Ce:YAG screens. The other 24 monitors are based on optical transition radiation (OTR). Eight of the OTR monitors are combined with wire scanners. In addition there are seven wire scanner stations in the undulator section. All of these monitors are used for on-line optimization of the beam transport through the linac as well as for characterization of the transverse phase space by measurements of the beam shape, size, and emittance. The OTR monitors located in the dispersive sections are used for energy and energy spread measurements as well as for determination of the on-crest phase of the accelerating modules.

## INTRODUCTION

The TESLA Test Facility (TTF) linac at DESY (Hamburg) has been extended to drive a new free electron laser user facility, the VUV-FEL [1], in the wavelength range from vacuum-ultraviolet to soft x-rays. The commissioning of the facility started in the beginning of 2004, and the first lasing was achieved in January 2005 [2, 3]. The first user FEL experiments started in summer 2005.

Figure 1 shows a schematic layout of the present stage of the VUV-FEL linac. Electron bunch trains with a nominal bunch charge of 1 nC are generated by a laser-driven RF gun. Five accelerating modules with eight 9-cell superconducting TESLA cavities are installed to provide electron beam energies up to  $\sim 730$  MeV. The electron bunch is compressed by two magnetic chicane bunch compressors. At the location of the first bunch compressor the beam energy is 127 MeV and at the second 370 MeV. During the commissioning the main emphasis has been on lasing with a wavelength of 32 nm, corresponding to an electron beam energy of 445 MeV.

The lasing process requires a high quality electron beam in terms of transverse emittance, peak current, and energy spread. In order to meet these demands, an accurate characterization of the electron beam properties is essential. In this paper we concentrate on measurements of the beam properties in the transverse phase space.

Presently, there are 27 optical beam profile monitors mounted along the VUV-FEL linac (see Fig. 1). Three of them, located in the RF gun area where the electron beam

## OTR MONITORS

The OTR monitors have been one of the main diagnostics tools during the commissioning of the VUV-FEL linac. Monitors in the injector area have been in operation since spring 2004, and the complete system since autumn 2004. Requirements for these monitors are demanding. They have to deliver on-line beam images to optimize the beam transport through the linac as well as provide high quality beam images for the characterization of the beam parameters in the transverse phase space. Since the electron beam size varies along the linac, as well as under different operation conditions, OTR monitors have to be able to measure transverse beam sizes from millimeter scale down to  $\sim 50 \mu\text{m}$  (rms) with a high resolution. In addition, they have to be reliable, robust, and remote controlled.

The OTR monitor system is designed and constructed by INFN-LNF and INFN-Roma2 in collaboration with DESY. OTR monitors are based on measurements of backward optical transition radiation emitted by a screen at an angle of  $45^\circ$  with respect to the beam trajectory. All monitors have a remotely controlled stepper motor actuator to insert the OTR screen into the beam pipe. All stations, except the ones in the dispersive sections, have two screens: a polished silicon screen, and a silicon screen with an aluminium coating. Between the two screens, on the same plane, there are marks to adjust and calibrate the optical system.

Most of the monitors (18) have an optical set-up specially designed and constructed to meet the demands of the VUV-FEL. This set-up consists of a mirror deflecting the OTR light downwards, three achromat doublet lenses, three neutral density filters, and a CCD camera. The lenses and

\* katja.honkavaara@desy.de

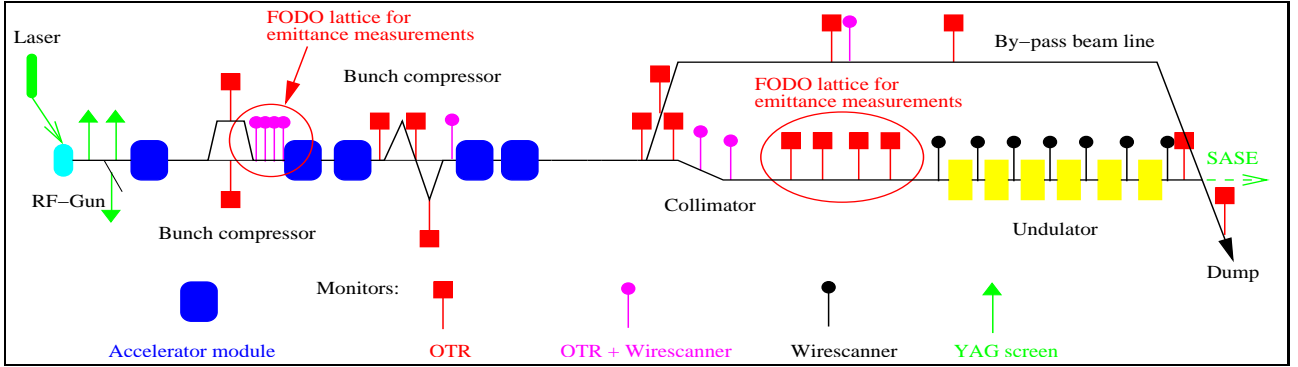


Figure 1: Present layout of the TTF VUV-FEL linac (not to scale). Beam direction is from left to right, and the total length is about 250 m. Locations of OTR monitors, wire scanners, and FODO lattices for emittance measurements are indicated.

the filters can be moved remotely in and out of the optical axis (transversal movement). Each of the lenses provides a fixed nominal magnification: 1.0, 0.39, and 0.25. The CCD camera has a lead shield against x-ray radiation, and the complete system is covered against external light. Prior to installation into the accelerator tunnel, all optical set-ups have been prealigned and calibrated in a laboratory. The measured resolution of the system is  $11 \mu\text{m}$  rms for the highest magnification.

The OTR monitors in the bunch compressors and in the by-pass line, as well as the YAG screens in the RF gun area, have a simplified optical set-up: a CCD camera with an objective providing one fixed image magnification. Upgraded set-ups with a higher dynamic range and the possibility to change remotely the magnification will be available later for the monitors in the dispersive sections of the bunch compressors.

The read out system is based on the use of digital CCD cameras with a firewire interface (IEEE1394). The cameras are connected to compact industrial PCs, located in the accelerator tunnel, via firewire links (2-6 cameras to each). These PCs (8) are connected via local Ethernet to an “image server” PC in the control room. The image server, using LabView based control and image analysis software, is the main interface for the complete system. It controls the PCs and the cameras, displays beam images on-line, runs locally measurements and analysis programs, and provides beam images for applications running in other computers. House-made remotely controlled power switches allow to reset the PCs and the cameras from the control room.

More details of the OTR monitor system are in [4, 5, 6].

## WIRE SCANNERS

Two different types of wire scanners are used at the VUV-FEL. Eight wire scanners along the linac are old devices, built in collaboration with CERN, and they are now combined with OTR monitors. Wire scanners at the undulator section have a new design, and they are constructed by DESY (Zeuthen and HASYLAB).

The first type has three tungsten wires with a diameter

of  $18 \mu\text{m}$ . The wires are mounted into a fork moving with an angle of  $45^\circ$  with respect to the beam. The wires are oriented such that one of them scans horizontally, another one vertically, and the third one provides information of the coupling between the two planes. Since these wire scanners are mounted into a common vacuum chamber with an OTR screen, only 5 mm downstream of the screen, they can be used for complementary measurements of the transverse beam profile and size. A first cross-check between profiles measured by the OTR monitors and the wire scanners on the four OTR/wire scanner monitors downstream of the first bunch compressor is recently done showing a good agreement (see Fig. 2).

Seven wire scanner stations are mounted along the undu-

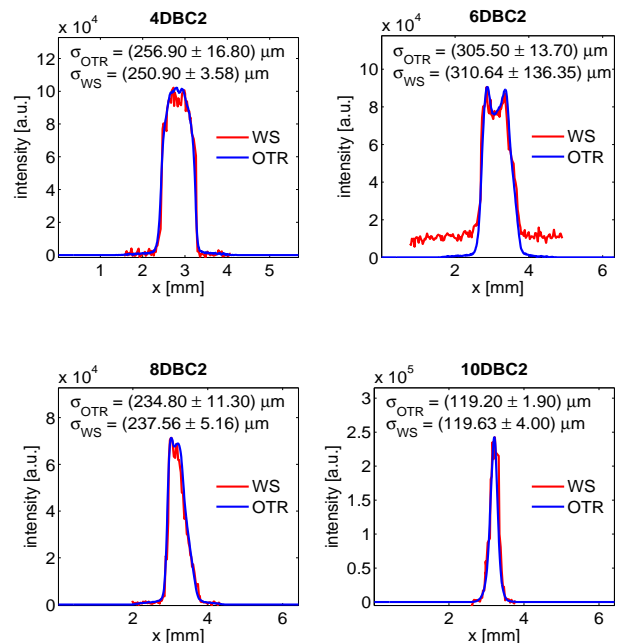


Figure 2: Comparison of transverse beam profiles measured by OTR monitors (blue) and wire scanners (red) downstream of the first bunch compressor. The measured rms beam sizes are shown as well.

lator. Each of these stations has two individual wire scanners: one scanning in horizontal direction and the other one in vertical. Each scanner has three wires: a  $10\ \mu\text{m}$  thick carbon wire, and two tungsten wires with diameters of  $10\ \mu\text{m}$  and  $50\ \mu\text{m}$ . At the moment, we use typically the carbon wire. The maximum scanning speed is  $1\ \text{m/s}$ . Since these wire scanners can measure the absolute beam position with respect to the undulator axis with a precision of  $50 - 100\ \mu\text{m}$  they are used, besides the measurements of the beam shape and size, also for measurements of the beam orbit along the undulator. More details of the undulator wire scanners are in [7].

Both wire scanner types use photomultipliers to detect secondary particles emitted when the wire passes the electron beam. The measured beam profile and size are calculated and displayed on-line. A sophisticated control and display software being an integral part of the VUV-FEL control system is under commissioning [8].

## EMITTANCE MEASUREMENTS

The transverse projected emittance is measured using a four-monitor method. This method is based on measurements of the transverse beam distribution (shape and size) at four locations along the linac with a fixed beam optics. A detailed description of the emittance measurements and analysis techniques presented here are in [9].

### *Experimental set-up and data-analysis*

There are two diagnostic sections dedicated to emittance measurements along the VUV-FEL linac (see Fig. 1). The first one is located downstream of the first bunch compressor at an electron beam energy of  $127\ \text{MeV}$ . This section has four OTR monitors combined with wire scanners mounted into a FODO lattice of six quadrupoles with a periodic beta function. A second FODO lattice with four OTR monitors is located upstream of the undulator.

The transverse emittance is determined from the measured beam distributions and the known transport matrices between the monitors using two different techniques. The first method is based on a least square (chi-square) fitting of the Twiss parameters and the emittance to the measured beam sizes. An application of this method for emittance measurements can be found in [10]. The second method is a tomographic reconstruction of the phase space using the maximum entropy algorithm [11].

Sofar, routine emittance measurements have been performed in the first diagnostics section using OTR monitors. In a typical measurement 20 beam and background images are recorded at each of the four OTR screens. After subtraction of an averaged background from each beam image, a sophisticated analysis procedure is applied to determine an elliptical region of interest (ROI) surrounding the entire beam, as well as to correct remaining off-sets. If required, a wavelet filter can be used to reduce the noise.

Besides the emittance of the entire beam, we are interested in the emittance of the high density core. This core

is determined by cutting away 10% (an arbitrary choice) of particles in the tails of the two dimensional transverse beam distribution. After that the horizontal and vertical rms beam sizes of the entire beam and of the core containing 90% of it are calculated. These rms beam sizes are used in the fitting method to calculate the emittance of the entire beam and the core emittance including 90% of the beam intensity.

In the tomographic reconstruction, an averaged beam profile at each screen is used. In order to avoid broadening of this profile due to a beam position jitter, the measured profiles are rebinned, and the center of each profile is moved to the same position before averaging. The phase space distribution is reconstructed using the maximum entropy algorithm, and the emittance is then determined from this distribution. In order to determine the 90% core emittance, 10% of the particles in the tails of the reconstructed phase space distribution is cut away.

An error estimation taking into account statistical and systematic errors has been performed for the fitting method. Statistical errors due to fluctuations of the measured beam sizes are calculated as in [10]. Systematical errors are estimated using a Monte Carlo simulation assuming a 5% error in the beam energy, a 6% error in the gradient of the FODO lattice quadrupoles, and a 3% error in the calibration of the optical system. Statistical errors are typically 2-4%, and systematical ones 5-6%. For the tomographic reconstruction, no error analysis is performed yet.

### *Experimental results*

The measurements presented here are performed in the first diagnostic section using OTR monitors. Figure 3 shows the normalized horizontal ( $\epsilon_x$ ) and vertical ( $\epsilon_y$ ) projected emittances measured ten times during 75 minutes without changing the machine parameters. The geometrical average ( $\sqrt{\epsilon_x \epsilon_y}$ ) is shown as well. The electron beam energy is  $127\ \text{MeV}$ , and the bunch charge  $1\ \text{nC}$ . The beam is transported through the first bunch compressor without compression (on-crest acceleration in the first accelerating module). The results obtained by fitting and by tomography are presented for 100% and 90% beam intensity. We can see that the results by the two techniques agree well, and that the stability of the measurements is good. The rms jitter of the 100% emittance in the horizontal plane is  $\sim 3.5\%$  and in the vertical  $\sim 2\%$ , in agreement with the statistical error estimated above.

During the measurements above the injector was operated with the nominal laser and RF settings. The optimal settings of the solenoid magnets were used [12], whereas the injection to the first accelerating module was not completely optimized. When the injector is carefully tuned, we regularly measure normalized projected emittances around  $1.4\ \text{mm mrad}$  for 90% of a  $1\ \text{nC}$  bunch. For the entire beam, this value is around  $2\ \text{mm mrad}$ .

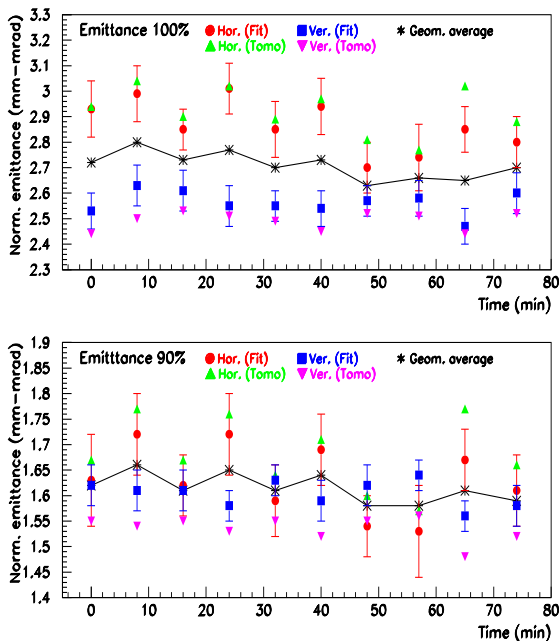


Figure 3: Horizontal (fitting=red, tomography=green) and vertical (fitting=blue, tomography=magenta) normalized emittances. The measurement is repeated 10 times during 75 minutes. Results obtained for 100% (top) and 90% (bottom) beam intensity are shown. Error is the statistical error only. The black curve shows the geometrical average ( $\sqrt{\epsilon_x \epsilon_y}$ ) of the horizontal and vertical emittances obtained by the fitting method.

## SUMMARY AND OUTLOOK

The OTR monitors are in routine use to measure and optimize the electron beam parameters along the VUV-FEL linac. A first cross-check of the beam profiles measured simultaneously by the OTR monitors and the wire scanners in the first diagnostics section has been done showing a good agreement. The control software for these wire scanners is still under commissioning, and therefore they are not yet routinely used. The wire scanners in the undulator section are regularly used to measure the beam sizes and the beam orbit along the undulator.

The emittance measurement system based on a four-monitor method using OTR monitors is commissioned and routinely used to measure projected emittances at the VUV-FEL injector. Normalized emittances around 1.4 mm mrad for 90% of a 1 nC bunch at 127 MeV beam energy are regularly measured.

Optimization of the emittance measurement conditions in the second diagnostics section is not yet finished, and therefore accurate emittance measurements are not yet performed there. First tests to use the undulator wire scanners for the emittance measurement have been successfully done, and they are now available for emittance measure-

ments along the undulator.

## ACKNOWLEDGMENT

We thank the colleagues and the technical staff at DESY (Hamburg and Zeuthen), and at INF-LNF/Roma2 contributing in the design, realization, and maintenance of the OTR and wire scanner systems. Special thanks are due to the VUV-FEL shift crew participating in the measurements and providing useful tips to improve the diagnostics tools.

## REFERENCES

- [1] The TTF FEL Team, "SASE FEL at the TESLA Test Facility, Phase 2", DESY-TESLA-FEL 2002-01
- [2] B. Faatz for the DESY VUV-FEL project team, "First Results from the VUV-FEL at DESY", PAC 2005, Knoxville, Tennessee, May 16-20, 2005
- [3] S. Schreiber for the VUV-FEL team, "First lasing at 32 nm of the VUV-FEL at DESY", these proceedings
- [4] K. Honkavaara *et al.*, "Design of OTR beam profile monitors for the TESLA Test Facility, phase 2 (TTF2)", PAC 2003, Portland, Oregon, May 12-16, 2003
- [5] A. Cianchi *et al.*, "Commissioning of the OTR beam profile monitor system at TTF/VUV-FEL Injector", EPAC 2004, Luzern, Switzerland, July 5-9, 2004
- [6] L. Catani *et al.*, "A large distributed digital camera system for accelerator beam diagnostics", Review of Scientific Instruments **76**, 073303 (2005)
- [7] M. Sachwitz *et al.*, "Wire scanners in the undulator section of the VUV-FEL at DESY", DIPAC 2005, Lyon, France, 6-8 June, 2005
- [8] E. Sombrowski *et al.*, "Wire scanner control and display Software", PCaPAC 2005, Hayama, Japan, March 22-25, 2005
- [9] F. L'ohl, "Measurements of the transverse emittance at the VUV-FEL", to be published as DESY-THESIS 2005-014 and TESLA-FEL 2005-03, Diploma Thesis, Hamburg University, 2005.
- [10] M. Minty and F. Zimmermann, *Measurements and control of charged particle beams*, Springer, 2003
- [11] J. Scheins, "Tomographic Reconstruction of Transverse and Longitudinal Phase Space Distribution using the Maximum Entropy Algorithm", TESLA Report 2004-08, May 2004
- [12] K. Honkavaara for the VUV-FEL team, "Electron beam characterization at PITZ and the VUV-FEL at DESY", these proceedings

## The infrared undulator project at the VUV-FEL

J. Feldhaus, O. Grimm\*, O. Kozlov, E. Plönjes, J. Rossbach, E. Saldin, E. Schneidmiller, M. Yurkov  
DESY, Hamburg, Germany

### Abstract

The VUV-FEL at DESY, Hamburg, will be complemented with an undulator producing radiation in the wavelength range (1–200)  $\mu\text{m}$  by autumn 2006. First, it will serve as a powerful radiation source naturally synchronized with the vacuum-ultraviolet (VUV) pulses from the FEL, thus allowing pump-probe experiments with high timing precision. Second, it will help to characterize the longitudinal charge distribution of the short electron bunches in a manner similar to other frequency-domain techniques using infrared radiation currently studied at the VUV-FEL.

### INTRODUCTION

Complementing the VUV-FEL at DESY, Hamburg, with an undulator working in the mid- and far-infrared regime was first proposed in [1]. There is growing interest in using such an undulator delivering up to 10 MW peak power in the THz-regime as a radiation source, allowing especially pump-probe experiments with high temporal resolution using either the infrared or the VUV pulse as probe. In addition, the undulator can be used as a diagnostics tool for longitudinal bunch shape measurements [2]. Funding has now been secured and it is planned to install the undulator described in this paper behind the FEL undulator in late 2006.

A further application under discussion is using the undulator as a radiator for a proposed bunch-length measurement technique based on generating an optical replica of the charge distribution and subsequent analysis with standard frequency-resolved optical gating (FROG) devices [3].

### UNDULATOR DESIGN

The undulator is designed as a planar electromagnetic device. The main parameters are collected in Table 1.

The main electric and cooling parameters allow using infrastructure already existing at DESY. The mechanical design is optimized for the tight spacial situation close to the descending branch of the electron bypass, see Fig. 1.

The undulator magnetic yoke, made from two girders of type 1010 plain carbon steel, supports poles milled to 50  $\mu\text{m}$  precision. The yoke itself rests on a C-shaped support made from non-magnetic steel, limiting a change of the undulator gap due to magnetic forces to no more than 10  $\mu\text{m}$ . The support is equipped with an alignment system

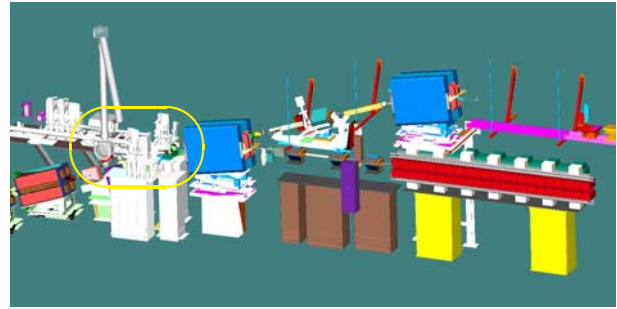


Figure 1: The infrared undulator (on the right, red) as planned to be installed in the VUV-FEL. Radiation out-coupling, focusing, and optionally detection occurs in the encircled region next to the large dipole magnet.

and allows, due to its shape, easy access to the gap, facilitating for example magnetic field measurements.

The windings of the main coils are produced from square pipes of 8.5 mm width, having an aperture of 5.3 mm diameter for circulation of cooling water (the conductor cross-section is thus 50 mm<sup>2</sup>). The electrical isolation is 0.4 mm thick. A basic coil consists of four layers with 15 windings each and a 1 mm diameter copper wire wound around to adjust the field strength. The end poles are wound in a similar manner, though with only one or three layers, and contain separately powered correction windings for adjusting the first and second field integrals.

Using the undulator for the replica-based bunch length diagnostics requires tunability down to wavelengths in the range (0.5–1)  $\mu\text{m}$ , demanding a sufficient field quality at small excitation currents, i.e. good control of remanence effects. This is part of the specification.

### INFRARED BEAM LINE

The infrared radiation will be transported to one of the end stations of the VUV-FEL user facility for pump-probe experiments combining the VUV-FEL with the infrared source. In addition, a laboratory designated for working with the infrared radiation alone is proposed in the user facility. A beam line design into a building next to the dump region of the TTF2 linac is currently kept as fall-back solution in case timely installation of beam line components would otherwise be impossible.

The beam line design into the experimental hall makes use of an existing beam pipe transporting visible synchrotron radiation from the dump magnet, currently used for synchronization purposes. As this pipe has a diam-

\* Corresponding author. E-Mail: oliver.grimm@desy.de

Gap	40 mm	Maximum field	1.18 T (K=44 @ 500 MeV)
Period	40 cm	Total weight	5100 kg
Number of full periods	9	Ampere-turns per coil	27520 A
Number of poles	44	Number of turns	64
Termination pattern	+1/4,-3/4,+1,...,-1,+3/4,-1/4	Maximum current	435 A
Good field region	$\pm 5$ mm ( $\Delta B/B < 3 \times 10^{-3}$ )	Conductor area	50 mm <sup>2</sup>
First field integral	$< 2 \times 10^{-4}$ Tm (@1 T)	Current density	8.7 A/mm <sup>2</sup>
Second field integral	$< 2 \times 10^{-4}$ Tm <sup>2</sup> (@1 T)	Resistance (main coil)	13.1 m $\Omega$
Iron yoke length	4.3 m	Inductance (main coil)	0.11 mH
Total cooling water flow	100l/min	Voltage (main coil)	5.7 V
Water temperature rise	20°C	Total resistance	0.55 $\Omega$
Temperature rise (water cut off)	0.4°C/s	Total inductance	4.4 mH
Total power	104 kW	Total voltage	238 V

Table 1: Main parameters of the infrared undulator.

eter of only 100 mm, intermediate focusing elements are needed as shown in Fig. 2 to transport far-infrared radiation efficiently. Plotted in the bottom of that figure are  $2\sigma$  beam radii for this lay-out calculated using Gaussian optics. A restriction towards long wavelengths is the limited aperture of the dump magnet, indicated in blue.

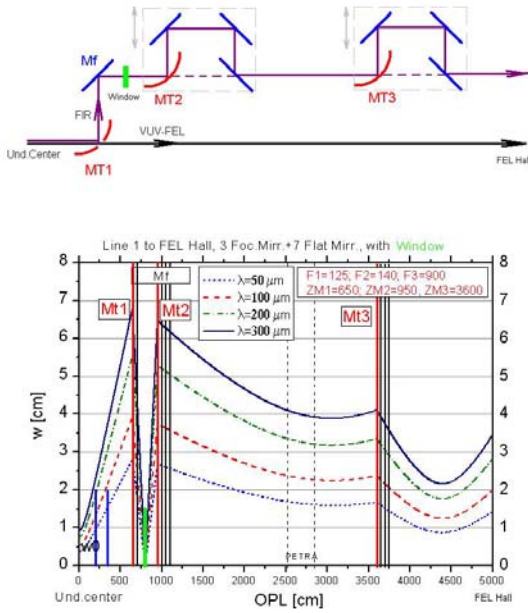


Figure 2: Mirror arrangement (top) and  $2\sigma$  beam radii calculated using Gaussian optics (bottom) for the beam line into the experimental hall.

The accelerator vacuum is separated from the rougher beam line vacuum by a diamond window located at the position of an intermediate focus. A larger crystal Quartz window is foreseen to allow easy viewing and alignment of the out-coupling region. For beam diagnostics, a broadband infrared detector will be installed in the accelerator tunnel, close to the out-coupling port.

Inevitably, the path length for the infrared radiation will

be significantly longer by several meters compared to that of the VUV pulses due to the intermediate focusing stations. To allow nevertheless pump-probe experiments, several options are currently pursued. Conceptually simplest is the combination of radiation from two consecutive bunches (FEL pulse from the second). At 9 MHz repetition rate this corresponds to 33 m path length, thus requiring additional delay of this order on the side of the infrared pulse. Alternatively, a delay line for the VUV-FEL pulses compensating for the path length difference can be fabricated using normal-incidence multilayer mirrors. As such mirrors are only reasonably reflective in a very narrow wavelength band such a design comes at the cost of losing the wavelength tunability of the FEL. Finally, the possibility to accelerate two electron bunches separated by several radio frequency buckets, each giving 23 cm delay at 1.3 GHz, is under investigation.

## RADIATION PROPERTIES

The radiation properties have been calculated numerically using the actual magnetic field of the current undulator design and the paraxial approximation described in [4]. Comparisons with the resonance approximation, as derived, for example, in [5, Chapter 11], show good agreement within the validity of the approximation. In Fig. 3 the normalized transverse intensity distribution of the horizontal polarization component of the fundamental is plotted for two values of  $K$  at the position of the out-coupling mirror MT1. The vacuum pipe has a diameter of 35 mm at this position, so part of the radiation cone will be cut due to aperture effects (cf. Fig. 2, bottom).

A typical pulse shape in time-domain for a Gaussian bunch with 1 nC charge and  $\sigma = 50 \mu\text{m}$  is shown in Fig. 4.

The on-axis spectral distribution of the radiation from a single electron is shown in Fig. 5 at the position of mirror MT1. To get the total spectrum emitted from a bunch this has to be multiplied with the bunch form factor according to (1). The modulus of the form factor for a Gaussian shape and a peaked shaped parametrized in [2] is also shown in the figure.

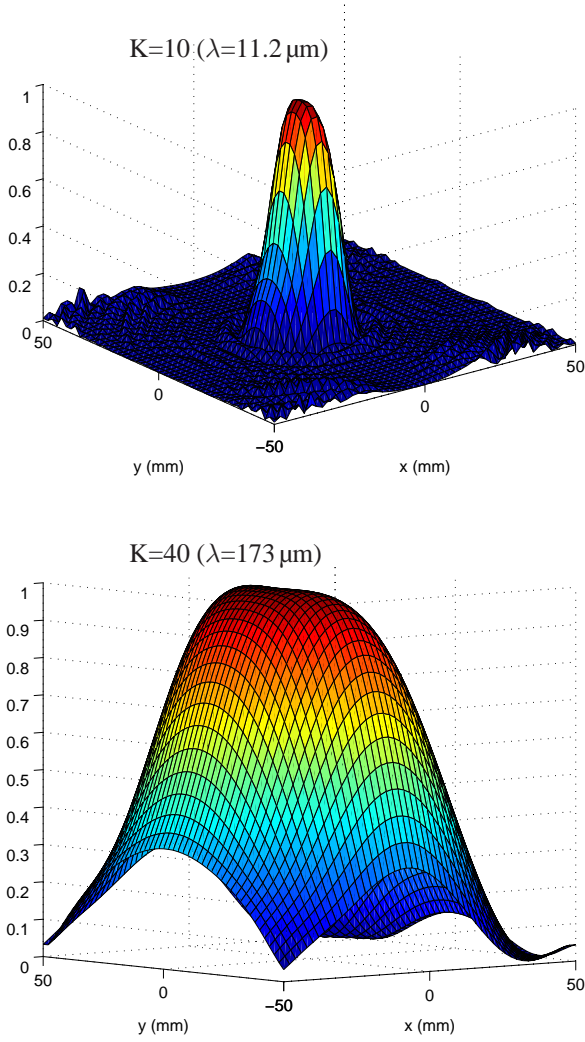


Figure 3: Transverse intensity distribution of the horizontal polarization component (fundamental frequency) at mirror MT1. No aperture effects are considered, normalization to the forward direction.

The resulting total spectrum in forward direction for two values of  $K$  is plotted in Fig. 6. Here, the form factor for the peaked shape has been used. For  $K=10$  the emission spectrum is dominated by small oscillations away from the resonance peak due to the boosting by the form factor. In case the actual bunch shape has structures on a smaller scale, the form factor will have non-negligible values up to higher frequencies, cf. (2), and the resonance peak can become more pronounced.

Diffraction at beam pipe and mirror apertures will be considered in currently on-going calculations using a Fourier optics approach. These will yield the full transmission characteristic of the beam line.

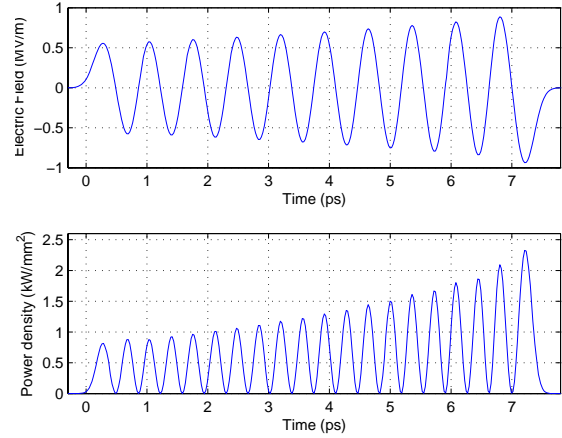


Figure 4: Electric field and power density in time-domain at position of mirror MT1 on-axis for a 1 nC Gaussian bunch with  $\sigma=50 \mu\text{m}$ . Edge effects not taken into account.

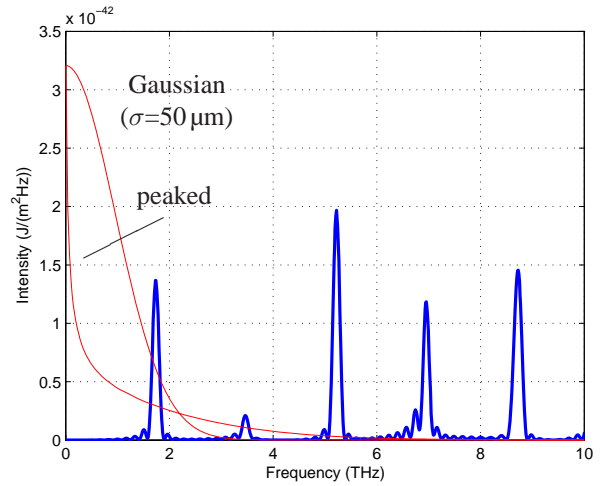


Figure 5: Single electron spectrum on-axis for  $K=40$ . The form factors for a Gaussian bunch and for a typical peaked bunch shape in the VUV-FEL given in [2] are also shown.

## LONGITUDINAL BEAM DIAGNOSTICS

Similar to synchrotron or transition radiation, the bunch shape is imprinted on the undulator radiation spectrum  $dU/d\lambda$  through the form factor  $F(\lambda)$ ,

$$\frac{dU}{d\lambda} = \left( \frac{dU}{d\lambda} \right)_0 \left( N + N(N-1) |F(\lambda)|^2 \right), \quad (1)$$

where  $(dU/d\lambda)_0$  is the emission spectrum of one single electron,  $N$  is the total number of electrons, and the form factor is the Fourier transform of the normalized longitudinal charge distribution  $S(z)$  ( $\int_{-\infty}^{\infty} S(z) dz = 1$ ),

$$F(\lambda) = \int_{-\infty}^{\infty} S(z) \exp\left(\frac{-2\pi i}{\lambda} z\right) dz. \quad (2)$$

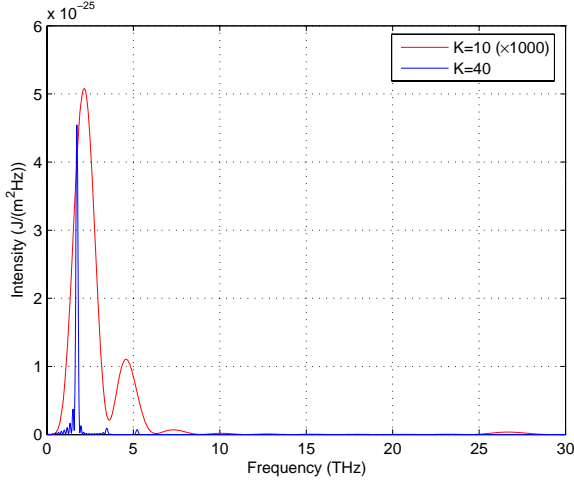


Figure 6: Total spectrum on-axis at position of mirror MT1 for a 1 nC bunch using a shape as parametrized in [2] for K values of 10 (curve multiplied by 1000) and of 40.

The basic assumption in the derivation of these equations is that each electron generates a time-dependent electric field at a given position that is the same for all electrons except a time delay (corresponding to a spacial distance).

Measurement of the total spectrum and knowledge of the number of electrons and the single-electron spectrum then gives access to the modulus of the form factor. The final step of inverse Fourier transforming this to arrive at the bunch shape requires knowledge of the phase of the Fourier transform. This, although not directly measured, is partially determined by the modulus through a Kramers-Kronig relation [6]. If one writes for the complex form factor  $F(\omega) = |F(\omega)| \exp(i\psi(\omega))$ , with  $\omega$  the angular frequency, then

$$\psi(\omega) = -\frac{2\omega}{\pi} \int_0^{\infty} \frac{\ln(|F(x)|/|F(\omega)|)}{x^2 - \omega^2} dx$$

yields a phase consistent with the measured modulus (but the solution is not unique) [7].

The electromagnetic undulator effectively replaces the spectrometer used in other frequency-domain approaches by its tuning capability, thus avoiding frequency-resolved measurements in (1). A pre-requisite for this to work is that the major intensity contribution is from the resonance peak. Also, good knowledge of the beam line transmission characteristics and the detector response is necessary.

The possibility to tune the undulator down to 1  $\mu\text{m}$  will give the unique chance to detect structures of the bunch on this scale, even if the precise longitudinal shape cannot be determined. Such micro-bunching is currently not excluded and could have a significant effect on beam dynamics in bunch compressors.

## REFERENCES

- [1] B. Faatz et al., Nucl. Instr. Meth. **A475**, 363 (2001)
- [2] G. Geloni et al., DESY 03-031 (March 2003)
- [3] E.L. Saldin et al., DESY 04-126 (July 2004)
- [4] G. Geloni et al., DESY 05-032 (February 2005)
- [5] H. Wiedemann, *Particle Accelerator Physics II*, Springer (1995)
- [6] J.S. Toll, Phys. Rev. **104**, 1760 (1956)
- [7] R. Lai, A.J. Sievers, Nucl. Instr. Meth. **A397**, 221 (1997)

# Misconceptions regarding Second Harmonic Generation in X-ray Free-Electron Lasers

G. Geloni, E. Saldin, E. Schneidmiller and M. Yurkov  
Deutsches Elektronen-Synchrotron (DESY), Hamburg, Germany

## Abstract

Nonlinear generation of coherent harmonic radiation is an important option in the operation of a X-ray Free-Electron Laser facility (XFEL) since it broadens the spectral range of the facility itself, thus allowing for a wider scope of experimental applications. We find that up-to-date theoretical understanding of second harmonic generation is not correct. Derivation of correct radiation characteristics will follow our criticism. A more detailed report of our study is given in [1].

## INTRODUCTION

The process of harmonic generation of coherent radiation can be considered as a purely electro-dynamical one. In fact, the harmonics of the electron beam density are driven by the electromagnetic field at the fundamental frequency, but the bunching contribution due to the interaction of the electron beam with the radiation at higher harmonics can be neglected. This leads to important simplifications. Namely, the solution to the self-consistent problem for the fundamental harmonic can be used to calculate the harmonic contents of the beam current. These contents enter as known sources in the calculation of the characteristics of harmonic radiation. As a result, numerical calculations dealing with harmonic generation simply compute the solution of Maxwell equations with sources obtained by means of FEL self-consistent codes.

Non-linear generation of the second harmonic radiation, in particular, is important for extending the attainable frequency range of an XFEL facility. The subject has been a matter of theoretical studies in high-gain Self-Amplified Spontaneous Emission (SASE) FELs both for odd [3] and even harmonics [4, 5, 9], where the electro-dynamical problem is dealt with. The practical interest of these studies is well underlined by both numerical analysis [6] and experiments in the infra-red and in the visible range of the electromagnetic spectrum [7, 8]. Experimental results are compared with numerical analysis and numerical analysis rely on analytical studies: this fact stresses the importance of a correct theoretical understanding of the subject. From this viewpoint we find that [4] includes arbitrary manipulations of the source terms in the paraxial wave equation, which are also proposed in [5, 9].

We find that a first incorrect step is the omission of a term depending on the gradient of the charge density. As we will see such term is responsible for a non-negligible contribution to the second harmonic field both for the horizontal and, surprisingly, for the vertical polarization component

and it should not go overlooked. Moreover, the beam distribution is modelled as a collection of individual point-particles, i.e. a sum of  $\delta$ -Dirac functions that is expanded in the  $x$  coordinate on the right hand side of the wave equation. Based on this manipulation, as it is discussed in [1], a main parameter is identified that has no theoretical support and will not play any role in our analysis. Also, (see, again, [1] for a detailed demonstration) the expansion of the  $\delta$ -Dirac functions cannot be performed as it corresponds to an incorrect expansion of the Green's function for Maxwell equation. Finally, the estimation of the second harmonic power is based on the (arbitrarily manipulated) source term alone, without actually solving Maxwell equations. Altogether, these works predict a wrong dependence of the second harmonic field on the problem parameters. The results in [5] are extended in [9] to the case of an electron beam moving off-axis through the undulator. The authors of [9] conclude that the second harmonic power increases when the beam moves off-axis. We find that, in this case the power of the second harmonic radiation never increases: in particular, as we will see, it may only decrease or remain unvaried.

In this paper, that was inspired by a method [11] developed to deal with Synchrotron Radiation from complex setups, we present a theory of second harmonic generation for high-gain FELs. We apply a Green's function technique to solve the wave equation. Our result is used to calculate, in a specific case, properties of the second harmonic radiation such as polarization, directivity diagram and total power including proper parametric dependencies. The most surprising prediction of our theory is that the electric field is not only horizontally polarized, as it is usually assumed, but exhibits, though remaining linearly polarized, a vertical polarization component too. A more detailed report of our study is given in [1].

## COMPLETE ANALYSIS OF THE SECOND HARMONIC GENERATION MECHANISM

Let us consider for simplicity a beam modulated at a single frequency  $\omega$ . The current density can be written as a sum of an unperturbed part independent of the modulation,  $(\vec{v}/c)j_o$ , and a term responsible for the beam modulation at frequency  $\omega$ , whose evolution through the beamline, accounting for emittance and energy spread, is described by the function  $\tilde{a}_2$ , to be considered a result from an external FEL code:

$$\vec{j}(z, t, \vec{\eta}) = \frac{\vec{v}(z, \vec{\eta})}{c} j_o \left( \vec{r}_\perp - \vec{r}_\perp^{(c)}(z, \vec{\eta}) \right)$$

$$\times \exp \left[ i\omega \int_0^z \frac{dz'}{v_z(z', \vec{\eta})} - i\omega t \right] + \text{C.C.} \left. \right\} . \quad (1)$$

Eq. (1) has been derived in the limit  $\gamma^2 \gg 1$ , where  $\gamma = \gamma(z)$  describes the (given) average Lorentz factor along the undulator. In the presence of energy spread the transverse size of the electron beam is assumed to be not smaller than the typical wiggling motion. Then, with accuracy  $\delta\gamma/\gamma$  all particles can be considered moving coherently according to  $\vec{r}_\perp^{(c)}$ , which corresponds to a velocity:

$$\begin{aligned} v_z(z, \eta) &= v_{z(nd)}(z) \left( 1 - \frac{\eta_x^2 + \eta_y^2}{2} \right) \\ \vec{v}_\perp(z, \eta) &= \vec{v}_{\perp(nd)}(z) + v_{z(nd)}(z) \vec{\eta}. \end{aligned} \quad (2)$$

Here  $\vec{\eta}$  is the direction of the beam deflection with respect to the undulator axis and  $\vec{v}_{(nd)}$  is the velocity with no deflection. The charge density can be written as

$$\rho = \frac{j_z}{v_z} \simeq \frac{j_z}{c}, \quad (3)$$

as we will be working in the paraxial approximation. Eq. (1) and Eq. (3) give the sources for Maxwell equation.

Looking for solutions in the form  $\vec{E}_\perp = \vec{\tilde{E}}_\perp \exp[i\omega(z/c - t)] + \text{C.C.}$  and applying the paraxial approximation one writes the Maxwell equation as [11]:

$$\begin{aligned} & \left( \nabla_\perp^2 + \frac{2i\omega}{c} \frac{\partial}{\partial z} \right) \vec{\tilde{E}}_\perp = \frac{4\pi}{c} \exp \left[ i\omega \right. \\ & \times \left. \left( \int_0^z \frac{dz'}{v_z(z', \vec{\eta})} - \frac{z}{c} \right) \right] \left( \frac{i\omega}{c^2} \vec{v}_\perp - \vec{\nabla}_\perp \right) j_o \tilde{a}_2. \end{aligned} \quad (4)$$

We will consider the case of a planar undulator thus modelling the electron transverse motion with:

$$\vec{r}_\perp^{(c)}(z', \vec{\eta}) = \left\{ \frac{K [\cos(k_w z') - 1]}{\gamma k_w} + \eta_x z' \right\} \vec{x} + [\eta_y z'] \vec{y}. \quad (5)$$

$K$  is the deflection parameter and  $k_w = 2\pi/\lambda_w$ ,  $\lambda_w$  is the undulator period. We will work in the far zone. Using a Green's function technique and the integration variable  $\vec{l} = \vec{r}' - \vec{r}_\perp^{(c)}(z', \vec{\eta})$  an exact solution of Eq. (4) reads:

$$\begin{aligned} \vec{\tilde{E}}_\perp &= \frac{i\omega}{c^2 z_o} \int d\vec{l} \int_{-\frac{L_w}{2}}^{\frac{L_w}{2}} dz' j_o(\vec{l}) \tilde{a}_2(z', \vec{l}) \exp[i\Phi_T] \\ &\times \left[ \left( \frac{K}{\gamma} \sin(k_w z') + (\theta_x - \eta_x) \right) \vec{x} + (\theta_y - \eta_y) \vec{y} \right], \end{aligned} \quad (6)$$

where

$$\Phi_T = \frac{\omega}{\omega_1} k_w z' - \frac{\omega K^2}{8\gamma^2 k_w c} \sin(2k_w z')$$

$$\begin{aligned} & - \frac{\omega K (\theta_x - \eta_x)}{\gamma k_w c} \cos(k_w z') + \omega \left\{ \frac{K}{k_w \gamma c} (\theta_x - \eta_x) \right. \\ & \left. - \frac{1}{c} (\theta_x l_x + \theta_y l_y) + (\theta_x^2 + \theta_y^2) \frac{z_o}{2c} \right\}, \end{aligned} \quad (7)$$

$\omega_1$  being defined by

$$\omega_1^{-1} = \frac{1}{2k_w c \gamma^2} \left[ 1 + \frac{K^2}{2} + \gamma^2 |\vec{\theta} - \vec{\eta}|^2 \right]. \quad (8)$$

Here  $\theta_x$  and  $\theta_y$  indicate the observation angles and  $L_w = N_w \lambda_w$  is the undulator length. Under the resonant approximation we will make use of the well-known expansion [12]:  $\exp[ia \sin(\psi)] = \sum_{p=-\infty}^{\infty} J_p(a) \exp[ip\psi]$ ,  $J_p$  being the Bessel function of the first kind of order  $n$ . We will be interested in frequencies  $\omega$  around the second harmonic:

$$\omega_{2o} = 4k_w c \gamma_z^2, \quad \text{where} \quad \gamma_z^2 = \frac{\gamma^2}{1 + K^2/2}. \quad (9)$$

The second harmonic contribution  $\vec{\tilde{E}}_{\perp 2}$  is then

$$\begin{aligned} \vec{\tilde{E}}_{\perp 2} &= \frac{i\omega_{2o}}{c^2 z_o} \exp \left[ i \frac{\omega_{2o}}{2c} z_o (\theta_x^2 + \theta_y^2) \right] [\mathcal{A}(\theta_x - \eta_x) \vec{x} \\ &+ \mathcal{B}(\theta_y - \eta_y) \vec{y}] \int_{-\infty}^{\infty} dl_x dl_y dz' \tilde{\rho}^{(2)}(z', \vec{l}, C) \\ &\times \exp \left[ -i \frac{\omega_{2o}}{c} (\theta_x l_x + \theta_y l_y) \right] \\ &\times \exp \left\{ i \frac{\omega_{2o}}{2c} [(\theta_x - \eta_x)^2 + (\theta_y - \eta_y)^2] z' \right\}. \end{aligned} \quad (10)$$

Here we have defined

$$\mathcal{A} = 2\xi [J_0(\xi) - J_2(\xi)] + J_1(\xi) \quad \text{and} \quad \mathcal{B} = J_1(\xi), \quad (11)$$

where  $\xi = K^2/(2 + K^2)$ . Moreover

$$C = (\omega - \omega_{2o})/\omega_{1o} \quad \text{and} \quad (12)$$

$$\tilde{\rho}^{(2)} = j_o(\vec{l}) \tilde{a}_2(z', \vec{l}) \exp[iCz'] H_{L_w}(z'). \quad (13)$$

$H_{L_w}(z')$  is equal to unity over the interval  $[-L_w/2, L_w/2]$  and zero everywhere else, and accounts for the fact that the integral in  $dz'$  should be performed over the undulator length. Also, the detuning parameter  $C$  should be considered as a function of  $z$ ,  $C = C(z)$  which can be retrieved from the knowledge of  $\gamma = \gamma(z)$ .

The terms in  $J_1$  in Eq. (11) are due to the presence of the gradient term  $\vec{\nabla}_\perp(j_o \tilde{a}_2)$  in Eq. (4), which has been omitted in [4, 5, 9]. The gradient term contributes for more than one fourth of the total field for the  $x$ -polarization component. Moreover, without that term, the entire contribution to the field polarized in the  $y$  direction would go overlooked.

Usually, computer codes present the functions  $\tilde{a}_2$  and  $\exp[iCz']$  combined in a single product, known as the complex amplitude of the electron beam modulation with respect to the phase  $\psi = 2k_w z' + (\omega/c)z' - \omega t$ . We will

regard  $\tilde{\rho}^{(2)}$  as a given function so that our description is independent on the particular presentation of the beam modulation.

We will now treat the particular case when  $\gamma(z) = \bar{\gamma} = \text{const}$ ,  $C(z) = 0$ ,

$$\tilde{a}_2 = a_{2o} \exp \left[ \frac{i\omega_{2o}}{c} (\eta_x l_x + \eta_y l_y) \right], \quad (14)$$

with  $a_{2o} = \text{const}$  and

$$j_o(\vec{l}) = \frac{I_o}{2\pi\sigma^2} \exp \left( -\frac{l_x^2 + l_y^2}{2\sigma^2} \right), \quad (15)$$

$I_o$  and  $\sigma$  being the bunch current and transverse size respectively. This corresponds to a modulation wavefront perpendicular to the beam direction of motion. Eq. (10) amounts, then, to a spatial Fourier transform and we obtain:

$$\begin{aligned} \tilde{E}_{\perp 2} &= \frac{iI_o a_{2o} \omega_{2o} L_w}{c^2 z_o} \exp \left[ i \frac{\omega_{2o}}{2c} z_o (\theta_x^2 + \theta_y^2) \right] \\ &\quad \times [\mathcal{A}(\theta_x - \eta_x) \vec{x} + \mathcal{B}(\theta_y - \eta_y) \vec{y}] \\ &\quad \times \text{sinc} \left\{ \frac{L_w \omega_{2o}}{4c} [(\theta_x - \eta_x)^2 + (\theta_y - \eta_y)^2] \right\} \\ &\quad \times \exp \left\{ -\frac{\sigma^2 \omega_{2o}^2}{2c^2} [(\theta_x - \eta_x)^2 + (\theta_y - \eta_y)^2] \right\}. \end{aligned} \quad (16)$$

The angular distribution of intensity along the  $\vec{x}$  and  $\vec{y}$  polarization directions will be denoted with  $I_{2(x,y)}$ . Definition of normalized quantities:  $\hat{\theta} = (\omega_{2o} L_w / c)^{1/2} \theta$ ,  $\hat{\eta} = (\omega_{2o} L_w / c)^{1/2} \eta$ ,  $\hat{l}_{x,y} = [\omega_{2o} / (c L_w)]^{1/2} l_{x,y}$  and of the Fresnel number  $N = \omega_{2o} \sigma^2 / (c L_w)$  give

$$\begin{aligned} I_{2(x,y)}(\hat{\theta}_x - \hat{\eta}_x, \hat{\theta}_y - \hat{\eta}_y) &= \text{const} \times (\hat{\eta}_{x,y} - \hat{\theta}_{x,y})^2 \\ &\quad \times \text{sinc}^2 \left\{ \frac{1}{4} \left[ (\hat{\theta}_x - \hat{\eta}_x)^2 + (\hat{\theta}_y - \hat{\eta}_y)^2 \right] \right\} \\ &\quad \times \exp \left\{ -N \left[ (\hat{\theta}_x - \hat{\eta}_x)^2 + (\hat{\theta}_y - \hat{\eta}_y)^2 \right] \right\}. \end{aligned} \quad (17)$$

$I_{2x}$  and  $I_{2y}$  have no azimuthal symmetry, contrarily with what happens for the first harmonic, where only the  $x$  polarization is present and has azimuthal symmetry [13]. The directivity diagram in Eq. (17) is plotted in Fig. 1 for different values of  $N$  as a function of  $\hat{\theta}_x - \hat{\eta}_x$  at  $\hat{\theta}_y - \hat{\eta}_y = 0$  for the  $x$  polarization component. The next step is the calculation of the second harmonic power for the  $x$ - and  $y$ -polarization components that is given by

$$W_{2(x,y)} = \frac{c}{2\pi} \int_{-\infty}^{\infty} dx_o \int_{-\infty}^{\infty} dy_o |\tilde{E}_{\perp x,y}(z_o, x_o, y_o)|^2 \quad (18)$$

It is convenient to present the expressions for  $W_{2x}$  and  $W_{2y}$  in a dimensionless form. After appropriate normalization they both are function of one dimensionless parameter:

$$\hat{W}_{2x} = \hat{W}_{2y} = F_2(N) = \ln \left( 1 + \frac{1}{4N^2} \right). \quad (19)$$

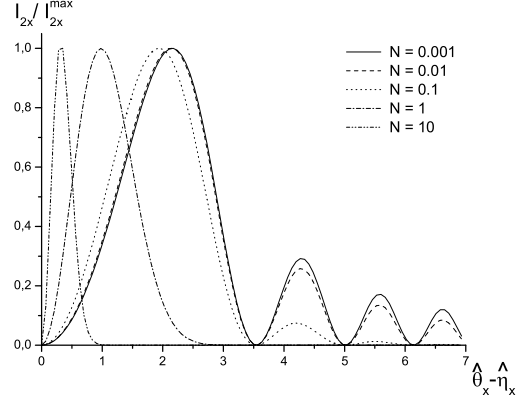


Figure 1: Plot of the directivity diagram for the radiation intensity as a function of  $\hat{\theta}_x - \hat{\eta}_x$  at  $\hat{\theta}_y - \hat{\eta}_y = 0$  for the  $x$ -polarization component, for different values of  $N$ .

Here  $\hat{W}_{2x} = W_{2x}/W_{ox}^{(2)}$  and  $\hat{W}_{2y} = W_{2y}/W_{oy}^{(2)}$  are the normalized powers. The normalization constants  $W_{ox}^{(2)}$  and  $W_{oy}^{(2)}$  are given by

$$\begin{pmatrix} W_{ox}^{(2)} \\ W_{oy}^{(2)} \end{pmatrix} = \begin{pmatrix} \mathcal{A}^2 \\ \mathcal{B}^2 \end{pmatrix} W_b \left[ \frac{a_{2o}^2}{2\pi} \right] \left[ \frac{I_o}{\gamma I_A} \right], \quad (20)$$

where  $W_b = m_e c^2 \gamma I_o / e$  is the total power of the electron beam and  $I_A = m_e c^3 / e \simeq 17$  kA is the Alfvén current.

The logarithmic divergence in  $F_2(N)$  in the limit for  $N \ll 1$  imposes a limit on the meaningful values of  $N$ . On the one hand, the characteristic angle  $\hat{\theta}_{\text{max}}$  associated with the intensity distribution is given by  $\hat{\theta}_{\text{max}}^2 \sim 1/N$ . On the other hand, the expansion of the Bessel function used in our derivation is valid only as  $\hat{\theta}^2 \leq N_w$ . As a result we find that Eq. (19) is valid only up to values of  $N$  such that  $N \geq N_w^{-1}$ . As  $N < N_w^{-1}$  the dimensionless problem parameter  $N$  is smaller than the accuracy of the resonance approximation scaling as  $N_w^{-1}$ . In this situation our electrodynamic description does not distinguish anymore between a beam with finite transverse size and a point-like particle and, for estimations, we should make the substitution  $\ln(N) \rightarrow \ln(N_w^{-1})$ .

The first harmonic study in [13] refers to a modulation wavefront orthogonal to the direction of propagation of the beam exactly as here and results have been presented in dimensionless form, which allows direct comparison between the powers of the second and of the first harmonic:

$$\frac{W_2(N)}{W_1(N)} = \frac{1}{(2\pi)^3 N_w} \frac{2 + K^2 a_{2o}^2 \mathcal{A}^2 + \mathcal{B}^2}{K^2 a_{1o}^2 \mathcal{A}_{JJ}^2} \frac{F_2(N)}{F_1(N)}, \quad (21)$$

where

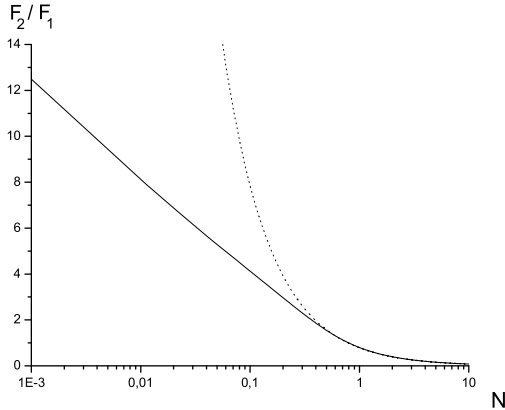


Figure 2: Solid line:  $F_2/F_1$  as a function of  $N$ . Dashed line: its asymptotic,  $\pi/(4N)$ , for  $N \gg 1$ .

$$F_1(N) = \frac{2}{\pi} \left[ \arctan\left(\frac{1}{N}\right) + \frac{N}{2} \ln\left(\frac{N^2}{N^2+1}\right) \right] \quad (22)$$

and  $A_{JJ} = J_0(\xi/2) - J_1(\xi/2)$ . Here  $a_{1o}$  is the analogous of  $a_{2o}$  for the first harmonic. For notational reasons,  $a_{1o}$  is one half of the original modulation level  $a_{in}$  in Eq. (27) of [13]. Moreover, all  $N$  in Eq. (22) are multiplied by a factor  $1/2$  with respect to [13], since  $N$  is defined for the second harmonic. In Fig. 2 we plot the behavior of  $F_2/F_1$  as a function of  $N$  and its asymptotic,  $\pi/(4N)$ , for  $N \gg 1$ .

The knowledge of the polarization contents of the radiation, even if relatively small as in this case, can be important from an experimental viewpoint. For example, in the VUV range, the reflection coefficients of many materials (e.g. SiC, that is widely used for mirrors) exhibit a complicated behavior, and there may be differences of even an order of magnitude depending on the polarization of the radiation. A study of  $R(K) = W_{2y}/W_{2x} = \mathcal{A}^2(K)/\mathcal{B}^2(K)$  shows that the relative magnitude of the  $y$  and the  $x$  polarization components of the second harmonic power ranges from 4% at  $K = 0$  to about 6% in the limit  $K \gg 1$ . Note that  $R(K)$  is independent of the particular model chosen for the beam modulation and that the second harmonic radiation is linearly polarized.

It is important to remark that we have treated a particular situation when the modulation wavefront is orthogonal to the direction of propagation of the beam. We have seen that the total power of the second harmonic radiation does not depend on the deflection angles  $\eta_x$  and  $\eta_y$ . In general, the second harmonic power can be independent of the beam deflection angle (like in this case) or can decrease due to the presence of extra oscillating factors in  $\vec{l}$  in Eq. (10). On the contrary in [9], an increase of the total power is reported, due to deflection angles: we find that such conclusion does not correspond to physical reality.

## CONCLUSIONS

In this paper we addressed the mechanism of second harmonic generation in Free-Electron Lasers. We find that available theoretical treatments of this phenomenon consist of estimations based on arbitrary manipulations of the source term of the wave equation that describes the electro-dynamical problem.

By solving analytically the wave equation with the help of the Green's function technique we derived an exact expression for the field of the second harmonic emission. We limited ourselves to the steady-state case which is close to practice in High-Gain Harmonic Generation (HG) schemes but, for the rest, we did not make restrictive approximations. Our solution of the wave equation may therefore be considered as a basis for the development of numerical codes dealing with second harmonic emission which should be using as input data the electron beam bunching for the second harmonic, as calculated by self-consistent FEL codes.

In general, the second harmonic field presents both horizontal and vertical polarization components and the electric field is linearly polarized. We calculated analytically the directivity diagram and the power associated with the second harmonic radiation assuming a particular beam modulation case. We expect that these expressions may be useful for cross-checking of numerical results.

A more detailed report of our study is given in [1].

## REFERENCES

- [1] G. Geloni, E. Saldin, E. Schneidmiller and M. Yurkov, Exact solution for the Second Harmonic Generation in XFELs, DESY 05-137, ISSN 0418-9833 (2005) and <http://arxiv.org/abs/physics/0508046>
- [2] E. Saldin, E. Schneidmiller and M. Yurkov, The Physics of Free Electron Lasers, Springer, 2000
- [3] Z. Huang and K. Kim, Phys. Rev. E, 62, 5 (2000)
- [4] M. Schmitt and C. Elliot, Phys. Rev. A, 34, 6 (1986)
- [5] Z. Huang and K. Kim, Nucl. Instr. and Meth. in Phys. Res. A 475, 112 (2001)
- [6] H. Freund, S. Biedron and S. Milton., Nucl. Instr. and Meth. in Phys. Res. A 445, 53 (2000)
- [7] A. Tremaine et al., Phy. Rev. Lett. 88, 204801 (2002)
- [8] S. Biedron et al. Nucl. Instr. Meth. A 483, 94 (2002)
- [9] Z. Huang and S. Reiche, Proceedings of the FEL 2004 Conference, Trieste, Italy
- [10] H. Wiedemann, Synchrotron Radiation, Springer-Verlag, Germany (2003)
- [11] G. Geloni, E. Saldin, E. Schneidmiller and M. Yurkov, Paraxial Green's functions in Synchrotron Radiation theory, DESY 05-032, ISSN 0418-9833 (2005)
- [12] D. Alferov, Y.A. Bashmakov et al. Sov. phys. - Tech. Phys. 18, 1336 (1974)
- [13] E. Saldin et al. Nucl. Instr. Meth. A 539, 499 (2005)

# INFLUENCE OF AN ENERGY CHIRP ON SASE FEL OPERATION

E.L. Saldin, E.A. Schneidmiller, and M.V. Yurkov  
Deutsches Elektronen-Synchrotron (DESY), Hamburg, Germany

## Abstract

Influence of a linear energy chirp in the electron beam on a SASE FEL operation is studied analytically and numerically using 1-D model. Explicit expressions for Green's functions and for output power of a SASE FEL are obtained for high-gain linear regime in the limits of small and large energy chirp parameter. Saturation length and power versus energy chirp parameter are calculated numerically. It is also shown that the effect of linear energy chirp on FEL gain is equivalent to linear undulator tapering (or linear energy variation along the undulator). A consequence of this fact is a possibility to perfectly compensate FEL gain degradation, caused by the energy chirp, by means of the undulator tapering (while keeping a frequency chirp in the radiation pulse) independently of the value of the energy chirp parameter. This opens up a possibility of a conceptual breakthrough: by a proper choice of energy chirp, undulator tapering, and bandwidth of a monochromator, installed behind the undulator, one can select a radiation pulse which is much shorter than inverse FEL bandwidth.

## INTRODUCTION

Start-to-end simulations [1] of TTF FEL, Phase 1 [2], have shown a presence of a strong energy chirp (energy-time correlation) within a short high-current leading peak in electron density distribution that has driven SASE FEL process. The energy chirp was accumulated due to the longitudinal space charge after compression. According to the simulations (that reproduced well the measured FEL properties), the energy chirp had a dramatical impact on SASE FEL saturation length and output characteristics. A similar effect takes place during the operation of VUV FEL at DESY in a "femtosecond mode" [3]. Such a mode of operation might also be possible in future X-ray SASE FELs.

There also exists a concept of frequency-chirped SASE FELs<sup>1</sup> aiming at the shortening of radiation pulse with the help of a monochromator [4]. Energy chirp can also be used to tune the output frequency of an FEL with coherent prebunching as it was demonstrated in the experiment at the DUV FEL facility [5]. Thus, a theoretical understanding of the energy chirp effect on the FEL performance is of crucial importance.

Analytical studies on this subject were performed in [6] in one-dimensional approximation. The general form of a time-domain Green's function as an inverse Laplace transform was derived in [6]. It was then reduced to the ex-

PLICIT expression in the limit of small energy chirp parameter up to the first order, resulting in phase correction (and ignoring the gain correction). This explicit solution for the Green's function was used to analyze statistical properties of a chirped SASE FEL in this limit. A second order correction to the FEL gain was presented in [4] but this result is incorrect.

The goal of this paper is to study the impact of energy chirp on SASE FEL performance and to find a possible way to cure the FEL gain degradation.

## GREEN'S FUNCTION

Electric field of the amplified electromagnetic wave is presented in the form<sup>2</sup>

$$E = \tilde{E} \exp[i\omega_0(z/c - t)] + C.C. ,$$

where  $\omega_0$  is a reference frequency and  $\tilde{E}$  is slowly-varying amplitude [7]. As it was shown in [6], for a SASE FEL, driven by an electron beam with linear energy chirp,  $\tilde{E}$  can be written as follows (we use notations from [7]):

$$\tilde{E} = 2E_0 \sum_j e^{-i\hat{s}_j / \rho} e^{2i\hat{\alpha}\hat{s}_j (\hat{s}_j - \hat{z}/2 - \hat{s}_j)} g(\hat{z}, \hat{s}_j - \hat{s}_j, \hat{\alpha}) \quad (1)$$

Here  $\rho$  is the efficiency parameter [7],  $E_0$  is the saturation field amplitude [7],  $\hat{z} = \Gamma z$  is a normalized position along the undulator,  $\Gamma = 2k_w \rho$ ,  $\lambda_w = 2\pi/k_w$  is the undulator period,  $\hat{s}_j = \rho\omega_0(z/\bar{v}_{z0} - t)$  is normalized position along the electron bunch,  $\bar{v}_{z0}$  is average longitudinal velocity (defined for a reference particle). Let the energy linearly depend on a particle position in the bunch (or arrival time). The energy chirp parameter

$$\hat{\alpha} = -\frac{d\gamma}{dt} \frac{1}{\gamma_0 \omega_0 \rho^2}$$

is defined such that, for positive sign of  $\hat{\alpha}$ , particles in the head of the bunch have larger energy than those in the tail. Relativistic factor  $\gamma_0$  for a reference particle (placed at  $\hat{s} = 0$ ) and reference frequency  $\omega_0$  are connected by the FEL resonance condition:  $\omega_0 = 2ck_w \gamma_0^2 / (1 + K^2)$ ,  $K$  being rms undulator parameter. Note that the theory is applicable when  $\rho\hat{\alpha} \ll 1$  [6]. It is also useful to define normalized detuning [7]:  $\hat{C} = [k_w - \omega(1 + K^2)/2c\gamma_0^2]/\Gamma$ .

The Green's function  $g$ , entering Eq. (1), is given by the inverse Laplace transform [6]:

<sup>1</sup>Frequency chirp of SASE FEL radiation is correlated with energy chirp in the electron beam due to the FEL resonance condition

<sup>2</sup>Plane wave and planar undulator are considered in this paper

$$g(\hat{z}, \hat{s}, \hat{\alpha}) = 2 \int_{\gamma' - i\infty}^{\gamma' + i\infty} \frac{dp}{2\pi ip} \exp[f(p, \hat{z}, \hat{s}, \hat{\alpha})], \quad (2)$$

where

$$f(p, \hat{z}, \hat{s}, \hat{\alpha}) = p(\hat{z} - 2\hat{s}) + \frac{2i\hat{s}}{p(p + i\hat{\alpha}\hat{s})} \quad (3)$$

We use a saddle point approximation to get an estimate of the integral (2) for large values of  $\hat{z}$  [6]. The saddle point is determined from the condition  $f' = 0$  which leads to the 4th power equation with three parameters:

$$p^4 + 2i\hat{\alpha}\hat{s}p^3 - \hat{\alpha}^2\hat{s}^2p^2 - \frac{4i\hat{s}}{\hat{z} - 2\hat{s}}p + \frac{2\hat{\alpha}\hat{s}^2}{\hat{z} - 2\hat{s}} = 0 \quad (4)$$

Once the saddle point,  $p_0$ , is found, the Green's function can be approximated as follows:

$$g(\hat{z}, \hat{s}, \hat{\alpha}) = \frac{2 \exp[f(p_0, \hat{z}, \hat{s}, \hat{\alpha})]}{p_0 [2\pi f''(p_0, \hat{z}, \hat{s}, \hat{\alpha})]^{1/2}} \quad (5)$$

Let us first consider the case when the energy chirp is a small perturbation,  $|\hat{\alpha}|\hat{z} \ll 1$ ,  $\hat{z} \gg 1$ . A second-order expansion of the Green's function takes the following form

$$g(\hat{z}, \hat{s}, \hat{\alpha}) \simeq \frac{e^{-i\pi/12}}{\sqrt{\pi\hat{z}}} \exp \left[ i^{1/3}\hat{z} + i^{2/3}\frac{\hat{\alpha}\hat{s}}{2} \left( 1 + i\frac{\hat{\alpha}\hat{z}^2}{36} \right) - 9i^{1/3} \left( 1 - \frac{\hat{\alpha}^2\hat{z}^2}{216i^{2/3}} \right) \frac{(\hat{s} - \hat{z}/6)^2}{\hat{z}} - \frac{i}{2}\hat{\alpha}\hat{s}(\hat{z} - 2\hat{s}) \right] \quad (6)$$

The leading correction term is the last term in the argument of the exponential function. It was found in [6] (note difference in definition of normalized parameters). Setting  $\hat{\alpha} = 0$ , one gets from (6) the well-known Green's function for unchirped beam [8].

Now let us consider the case  $\hat{\alpha} > 0$  and  $1 \ll \hat{\alpha} \ll \hat{z}$ . The Green's function for  $\hat{s} \gg \hat{\alpha}^{-1}$  is approximated by:

$$g(\hat{z}, \hat{s}, \hat{\alpha}) \simeq \left( \frac{\hat{\alpha}}{2\pi^2\hat{z}} \right)^{1/4} \exp \left( 2\sqrt{\frac{2\hat{z}}{\hat{\alpha}}} - 2\sqrt{\frac{2}{\hat{\alpha}\hat{z}}} \hat{s} \right) \quad (7)$$

More thorough analysis for small values of  $\hat{s}$  shows that the Green's function is peaked at  $\hat{s}_m = 2^{1/3}\hat{\alpha}^{-1}$ , i.e. the position of maximum is independent of  $\hat{z}$  while the width of the radiation wavepacket is proportional to  $\sqrt{\hat{\alpha}\hat{z}}$ . The mean frequency of the radiation wavepacket corresponds to a resonant frequency at  $\hat{s} = 0$ . Note also that the beam density excitation is concentrated near  $\hat{s} = 0$  within much shorter range, of the order of  $\hat{\alpha}^{-7/4}\hat{z}^{-1/4}$ .

In the case  $\hat{\alpha} < 0$  and  $1 \ll |\hat{\alpha}| \ll \hat{z}$  the Green's function is given by:

$$g(\hat{z}, \hat{s}, \hat{\alpha}) \simeq \frac{2^{1/4}e^{-i\pi/2}}{\pi^{1/2}|\hat{\alpha}|^{5/4}\hat{z}^{3/4}\hat{s}} \exp \left( 2\sqrt{\frac{2\hat{z}}{|\hat{\alpha}|}} \right)$$

$$+ i|\hat{\alpha}|\hat{z}\hat{s} + \frac{2i}{|\hat{\alpha}|^2\hat{s}} - \frac{2\sqrt{2}}{|\hat{\alpha}|^{7/2}\hat{z}^{1/2}\hat{s}^2} - 2\sqrt{\frac{2}{|\hat{\alpha}|\hat{z}}} \hat{s} \quad (8)$$

The width of the radiation wavepacket (and of beam density excitation as well) is of the order of  $|\hat{\alpha}|^{-7/4}\hat{z}^{-1/4}$ . The maximum of the wavepacket is positioned at  $\hat{s}_m = 2^{5/4}|\hat{\alpha}|^{-7/4}\hat{z}^{-1/4}$ , i.e. the wavepacket is shrinking and back-propagating (with respect to the electron beam) with increasing  $\hat{z}$ . The mean frequency of the wavepacket is blue-shifted with respect to resonant frequency at  $\hat{s} = 0$ . In normalized form this shift is  $\Delta\hat{C} = -|\hat{\alpha}|\hat{z}/2$ .

## LINEAR REGIME OF SASE FEL

The normalized radiation power (normalized efficiency),  $\langle \hat{\eta} \rangle = P_{\text{SASE}}/\rho P_{\text{beam}}$ , can be expressed as follows [7]:

$$\langle \hat{\eta} \rangle = \frac{\langle |\tilde{E}|^2 \rangle}{4E_0^2}, \quad (9)$$

where  $\langle \dots \rangle$  means ensemble average. One can easily get from (1):

$$\langle \hat{\eta}(\hat{z}, \hat{\alpha}) \rangle = \frac{1}{N_c} \int_0^\infty d\hat{s} |g(\hat{z}, \hat{s}, \hat{\alpha})|^2. \quad (10)$$

Here  $N_c = N_\lambda/(2\pi\rho)$  is a number of cooperating electrons (populating  $\Delta\hat{s} = 1$ ),  $N_\lambda$  is a number of electrons per wavelength. The local power growth rate [9] can be computed as follows:

$$G(\hat{z}, \hat{\alpha}) = \frac{d}{d\hat{z}} \ln \langle \hat{\eta}(\hat{z}, \hat{\alpha}) \rangle. \quad (11)$$

Applying Eqs. (10), (11) to the asymptotical cases, considered in the previous Section, we get the following results. For the case  $|\hat{\alpha}|\hat{z} \ll 1$ ,  $\hat{z} \gg 1$  the FEL power is given by

$$\langle \hat{\eta} \rangle \simeq \frac{\exp \left\{ \sqrt{3}\hat{z} \left[ 1 - (\hat{\alpha}\hat{z}/12)^2/3 \right] + \hat{\alpha}\hat{z}/12 \right\}}{3^{5/4}\sqrt{\pi\hat{z}}N_c} \quad (12)$$

and the local power growth rate is

$$G(\hat{z}, \hat{\alpha}) \simeq \sqrt{3} \left[ 1 - \left( \frac{\hat{\alpha}\hat{z}}{12} \right)^2 \right] - \frac{1}{2\hat{z}} + \frac{\hat{\alpha}}{12}. \quad (13)$$

It reaches maximum  $G_m = \sqrt{3} \left[ 1 - (|\hat{\alpha}|/16)^{2/3} \right] + \hat{\alpha}/12$  at the position  $\hat{z}_m = 3^{1/2}2^{2/3}/|\hat{\alpha}|^{2/3}$ . Although the condition  $|\hat{\alpha}|\hat{z} \ll 1$  was used to derive Eqs. (12), (13), they are pretty accurate up to the values  $|\hat{\alpha}|\hat{z}$  of the order of unity as it was seen from comparison with numerical simulations.

For the case  $\hat{\alpha} > 0$  and  $1 \ll \hat{\alpha} \ll \hat{z}$  we get rather simple expressions:

$$\langle \hat{\eta}(\hat{z}, \hat{\alpha}) \rangle \simeq \frac{\hat{\alpha}}{8\pi N_c} \exp \left( 4\sqrt{\frac{2\hat{z}}{\hat{\alpha}}} \right), \quad (14)$$

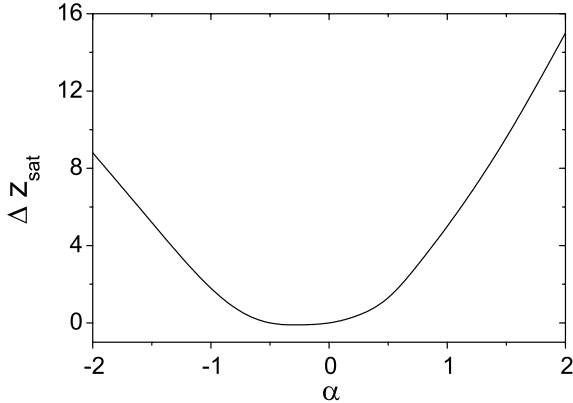


Figure 1: Increase of saturation length  $\Delta \hat{z}_{\text{sat}} = \hat{z}_{\text{sat}}(\hat{\alpha}) - \hat{z}_{\text{sat}}(0)$  versus parameter  $\hat{\alpha}$ . Here  $\hat{z}_{\text{sat}}(0) = 13$ .

$$G(\hat{z}, \hat{\alpha}) \simeq 2\sqrt{\frac{2}{\hat{\alpha}\hat{z}}}. \quad (15)$$

For large negative values of  $\hat{\alpha}$  we obtain:

$$\langle \hat{\eta} \rangle \simeq \frac{1}{27/4\pi^{1/2}|\hat{\alpha}|^{3/4}\hat{z}^{5/4}N_c} \exp\left(4\sqrt{\frac{2\hat{z}}{|\hat{\alpha}|}}\right), \quad (16)$$

$$G(\hat{z}, \hat{\alpha}) \simeq 2\sqrt{\frac{2}{|\hat{\alpha}|\hat{z}}} - \frac{5}{4\hat{z}}. \quad (17)$$

## NONLINEAR REGIME

We studied nonlinear regime of a chirped SASE FEL operation with 1-D version of the code FAST [7, 10]. Analytical results of two previous Sections were used to check how well we simulate energy chirp effect. Green's function was modelled by exciting density modulation on a short scale,  $\Delta \hat{s} \ll 1$ . SASE FEL initial conditions were simulated in a standard way [7]. The results of numerical simulations in all cases were in a good agreement with analytical results presented above. The main results of simulation of nonlinear regime are presented in Figs. 1,2. Saturation length and power are functions of two parameters,  $\hat{\alpha}$  and  $N_c$ . For our simulations we have chosen  $N_c = 3 \times 10^7$  - a typical value for VUV SASE FELs. Note, however, that the results, presented in Figs. 1,2, very weakly depend on  $N_c$ . Fig. 1 shows increase of saturation length with respect to unchirped beam case. In Fig. 2 the output power is plotted versus chirp parameter for two cases: when undulator length is equal to a saturation length for a given  $\hat{\alpha}$  and when it is equal to the saturation length for the unchirped beam case. One can see sharp reduction of power for negative  $\hat{\alpha}$  while a mild positive chirp ( $\hat{\alpha} < 0.5$ ) is beneficial for SASE.

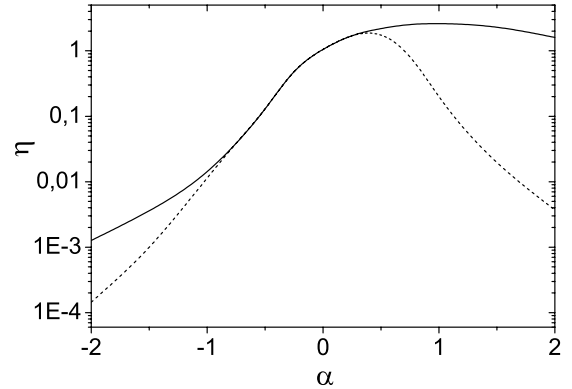


Figure 2: Normalized output power versus parameter  $\hat{\alpha}$ . Solid:  $\hat{z} = \hat{z}_{\text{sat}}(\hat{\alpha})$  (see Fig. 1); dash:  $\hat{z} = \hat{z}_{\text{sat}}(0) = 13$ .

## ENERGY CHIRP AND UNDULATOR TAPERING

Let us consider now the case when there is no energy chirp ( $\hat{\alpha} = 0$ ) and the detuning parameter changes linearly along the undulator [7]:  $C(\hat{z}) = \hat{b}_1 \hat{z}$ . This change can be due to variation of undulator parameters ( $K(\hat{z})$  and/or  $k_w(\hat{z})$ ) or due to an energy change  $\gamma_0(\hat{z})$ . We have found from numerical simulations that in such case the effect on FEL gain is exactly the same as in the case of energy chirp and no taper if  $\hat{\alpha} = 2\hat{b}_1$  for any value of  $\hat{\alpha}$  (Fig. 3 shows an example). Therefore, all the results of two previous Sections can be also used for the case of linear variation of energy or undulator parameters with the substitution  $\hat{\alpha} \rightarrow 2\hat{b}_1$ . The amplitudes of Green's functions are also the same while the phases are obviously different. In case of  $\hat{b}_1 = 0$ ,  $\hat{\alpha} \neq 0$  there is a frequency chirp along the bunch while in the case  $\hat{b}_1 = 0$ ,  $\hat{\alpha} = 0$  the frequency is changing along the undulator.

An effect of undulator tapering (or energy change along the undulator) on FEL gain was studied in [9] in the limit  $\hat{b}_1 \ll 1$ . Comparing our Eq. (12) (with the substitution  $\hat{\alpha} \rightarrow 2\hat{b}_1$ ) and Eq. (45) of Ref. [9], we can see that quadratic correction term in the argument of the exponential function is the same but the linear term is two times larger in [9]. The reason for discrepancy is that the frequency dependence of the pre-exponential factor in Eq. (42) of Ref. [9] is neglected.

A symmetry between two considered effects (energy chirp and undulator tapering) can be understood as follows. If we look at the radiation field acting on some test electron from an electron behind it, this field was emitted at a retarded time. In first case a radiating electron has a detuning due to an energy offset, in the second case it has the same detuning because undulator parameters were different at a retarded time. The question arises: can these two effects compensate each other? We give a positive answer based

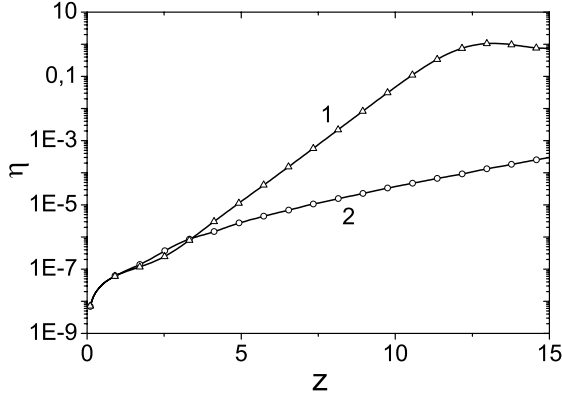


Figure 3: Normalized power versus undulator length. Solid line 1:  $\hat{\alpha} = 0, \hat{b}_1 = 0$ ; triangles:  $\hat{\alpha} = 4, \hat{b}_1 = -2$ ; solid line 2:  $\hat{\alpha} = 4, \hat{b}_1 = 0$ ; circles:  $\hat{\alpha} = 0, \hat{b}_1 = 2$ .

on numerical simulations (see Fig. 3 as an example): by setting  $\hat{b}_1 = -\hat{\alpha}/2$  we get rid of gain degradation, and FEL power at any point along the undulator is the same as in the case of unchirped beam and untapered undulator. This holds for any value of  $\hat{\alpha}$ . For instance, if one linearly changes magnetic field  $H_w$  of the undulator, the compensation condition can be written as follows (nominal values of parameters are marked with subscript '0'):

$$\frac{1}{H_{w0}} \frac{dH_w}{dz} = -\frac{1}{2} \frac{(1 + K_0^2)^2}{K_0^2} \frac{1}{\gamma_0^3} \frac{d\gamma}{cdt} \quad (18)$$

Of course, in such a case we get frequency chirped SASE pulse. Since compensation of gain degradation is possible also for large values of  $\hat{\alpha}$  (there is no theoretical limit on the value of chirp parameter, except for above mentioned condition  $\rho\hat{\alpha} \ll 1$ ), one can, in principle, organize a regime when a frequency chirp within an intensity spike is much larger than the natural FEL bandwidth (given by  $\rho\omega_0$ ).

## GENERATION OF ATTOSECOND PULSES

Many schemes for generation of femto- and attosecond pulses from X-ray SASE FELs are proposed. Here we mention the schemes considered in [11, 12] making use of energy modulation of a short slice in the electron bunch by a high-power few-cycle optical pulse in a two-period undulator. Due to energy modulation the frequency of SASE radiation in X-ray undulator (resonant to, say, 0.1 nm [11]) is correlated to the longitudinal position within the few-cycle-driven slice of the electron beam. The largest frequency offset corresponds to a single-spike pulse in time domain (about 300 as in [11]). The selection of single-spike pulses is achieved by using a crystal monochromator after the X-ray undulator [11].

Using the compensation effect, described in the previous Section, one can modify this scheme such that a monochromator is not required. Indeed, there is a strong energy chirp

around zero-crossing of energy modulation (for specific parameters of Ref. [11] the chirp parameter is  $\hat{\alpha} \simeq 2$ ). If one uses undulator tapering with  $\hat{b}_1 \simeq -1$  then only a short slice around zero-crossing produces powerful FEL pulse. The main part of the bunch is unmodulated and is, therefore, suffered from strong negative undulator tapering (from Fig. 2 one can estimate a suppression factor of  $10^4$ ). Therefore, a high-contrast attosecond pulse is directly produced in the undulator.

The fact that a SASE FEL can operate with a strong chirp parameter (in combination with undulator tapering) without gain degradation, opens up a possibility of a conceptual breakthrough: one can get from SASE FEL a radiation pulse which is much shorter than inverse FEL bandwidth. Indeed, in the case of  $\hat{\alpha} \gg 1$ , the idea of Ref. [4] can be generalized to time scales that are much shorter than a duration of intensity spike. In this case the frequency chirp inside an intensity spike (its duration is given by inverse FEL bandwidth) is much larger than FEL bandwidth. By appropriate choice of a monochromator bandwidth [6] one can select an X-ray pulse that is shorter by a factor  $\sqrt{2\hat{\alpha}}$  than inverse FEL bandwidth.

To illustrate a possible technical realization of this idea, we can suppose that the energy modulation by a few-cycle optical pulse in the scheme of Ref. [11] is increased by a factor 3 so that  $\hat{\alpha} \simeq 6$ . In combination with undulator tapering and a monochromator, this will allow to obtain intense X-ray pulses that are shorter than 100 as. Finally, without discussing technical limits, we should stress that a "fundamental" limit on pulse duration  $(\rho\omega_0)^{-1}$  can be overcome. That is the most important result of this paper.

## REFERENCES

- [1] M. Dohlus, et al., Nucl. Instr. and Methods A **530**(2004)217
- [2] V. Ayvazyan, et al., Phys. Rev. Lett. **88**(2002)104802
- [3] E.L. Saldin, E.A. Schneidmiller, M.V. Yurkov, DESY report TESLA-FEL-2004-06, July 2004
- [4] C.B. Schroeder, et al., Nucl. Instr. and Methods A **483**(2002)89
- [5] T. Shaftan, et al., Proc. of the 2004 FEL Conference, p. 282
- [6] S. Krinsky, Z. Huang, Phys. Rev. ST Accel. Beams **8**(2003)050702
- [7] E.L. Saldin, E.A. Schneidmiller, M.V. Yurkov, *The Physics of Free Electron Lasers* (Springer-Verlag, Berlin, 1999)
- [8] S. Krinsky and R.L. Gluckstern, Phys. Rev. ST Accel. Beams **6**(2003)050701
- [9] Z. Huang and G. Stupakov, Phys. Rev. ST Accel. Beams **8**(2005)040702
- [10] E.L. Saldin, E.A. Schneidmiller, M.V. Yurkov, Nucl. Instr. and Methods A **429**(1999)233
- [11] E.L. Saldin, E.A. Schneidmiller, M.V. Yurkov, Opt. Comm. **237**(2004)153
- [12] E.L. Saldin, E.A. Schneidmiller, M.V. Yurkov, Opt. Comm. **239**(2004)161

## DESIGN CONSIDERATIONS FOR THE 4GLS XUV-FEL

B. W. J. McNeil\*, G. R. M. Robb, University of Strathclyde, Glasgow G4 0NG, UK  
 N. R. Thompson, J. Jones and M. W. Poole,  
 ASTeC, Daresbury Laboratory, Warrington WA4 4AD, UK  
 C. K. M. Gerth, Deutsches Elektronen-Synchrotron DESY, D-22603 Hamburg, Germany

### Abstract

An XUV Free-Electron Laser operating in the photon energy range 10-100eV is a key component of the proposed 4th Generation Light Source (4GLS) at Daresbury Laboratory in the UK. The current design proposal is an amplifier FEL seeded by a High Harmonic Generation (HHG) source. In this paper we present and discuss the considerations that led to the current design. We also present 3D simulation results that illustrate the potential radiation output characteristics.

### INTRODUCTION

The Fourth Generation Light Source (4GLS) proposed for the UK's Daresbury Laboratory is designed to be a user facility to complement existing facilities within both the UK and Europe [1]. The 4GLS sources will provide synchronised ultra-high brightness pulsed radiation covering the FIR to the XUV regions of the spectrum. Previous FEL design considerations and the present design are discussed in this paper. The present design for the XUV uses an HHG seeded, high-gain FEL amplifier that will cover the photon energy range 10-100eV. Design work for a VUV source is considered elsewhere [2].

### DESIGN HISTORY

The XUV FEL branch of the 4GLS proposal began as a rather flexible specification for a coherent FEL source operating in the photon energy range 10-100 eV. Initially, attempts were made to design an FEL operating with a monoenergetic electron beam of 600 MeV corresponding to the main Energy Recovery branch and with a single undulator beam-line [3]. For a normal undulator of fixed period, tuning could therefore only be carried out by changing the undulator gap. At this beam energy it was not possible to achieve sufficiently short saturation lengths toward the higher photon energies while maintaining sensible undulator gaps at the lower photon energies.

A twin undulator, HHG seeded FEL scheme that had two separate modes of operation was also investigated. The two undulators were placed colinearly, with the first having a longer period than the second. In the first mode of operation, which would cover the lower photon energies, the first undulator acts as a high gain FEL amplifier seeded by an HHG source and achieves saturation in a relatively short length. This is possible as HHG sources currently

attain peak powers only approximately one to two orders of magnitude below FEL saturation powers for the photon energies 10eV and 50 eV respectively. The second mode of operation would use the second wiggler tuned to a harmonic of the first in an HGHG type configuration, to cover the higher photon energies. Design of such a scheme is quite complex and is complicated in the case of the first, lower photon energy mode of operation by the radiation transport out of the first undulator. Due to diffraction, the radiation cannot be transported through the second undulator and must be extracted at the end of the first undulator for transport to the experimental areas. A simpler option is to introduce further electron acceleration and electron energy tuning as described in the next section.

### PRESENT DESIGN

The present design concept for 4GLS incorporates three distinct electron beams driving three different FELs and a range of spontaneous sources. The first branch is a 50 MeV beam for driving an IR FEL oscillator operating at  $3 - 75 \mu\text{m}$ . The second and third branches are of higher energies at 600 MeV and 750-950 MeV respectively. The 600 MeV branch is of high average current supplying 80 pC pulses at up to 1.3 GHz and operating in an energy recovery mode. This branch will drive spontaneous sources and an FEL operating in the VUV [2]. The third 750-950 MeV branch is designed to give the high peak currents (1.5 kA, 1 nC pulses at 1-10 kHz) necessary to drive a single pass high gain FEL operating in the XUV. A schematic of the current conceptual design for the 4GLS XUV FEL is shown in Fig. (1). Only those components that have direct relevance to the XUV FEL are shown. From the photo-cathode gun, electron pulse acceleration is achieved in three separate stages by superconducting linac modules. Electron pulse compression is carried out in two stages between the main accelerator modules and is enhanced by a 3rd harmonic system. Not shown is the high average current energy recovery branch that has a separate 10 MeV photo-injector and shares the common 590 MeV accelerator stage. The different injector energies for the two branches mean that at the end of the 590 MeV linac the high average current branch has an energy of 600 MeV, while the high peak current branch has energy 750 MeV. This energy difference allows the two branches to be passively separated by a beam spreader immediately after the 590 MeV accelerator section. While the 600 MeV beam will continue through the spontaneous and VUV FEL sources and then on to energy recovery in the 590 MeV accelerator sec-

\* b.w.j.mcneil@strath.ac.uk

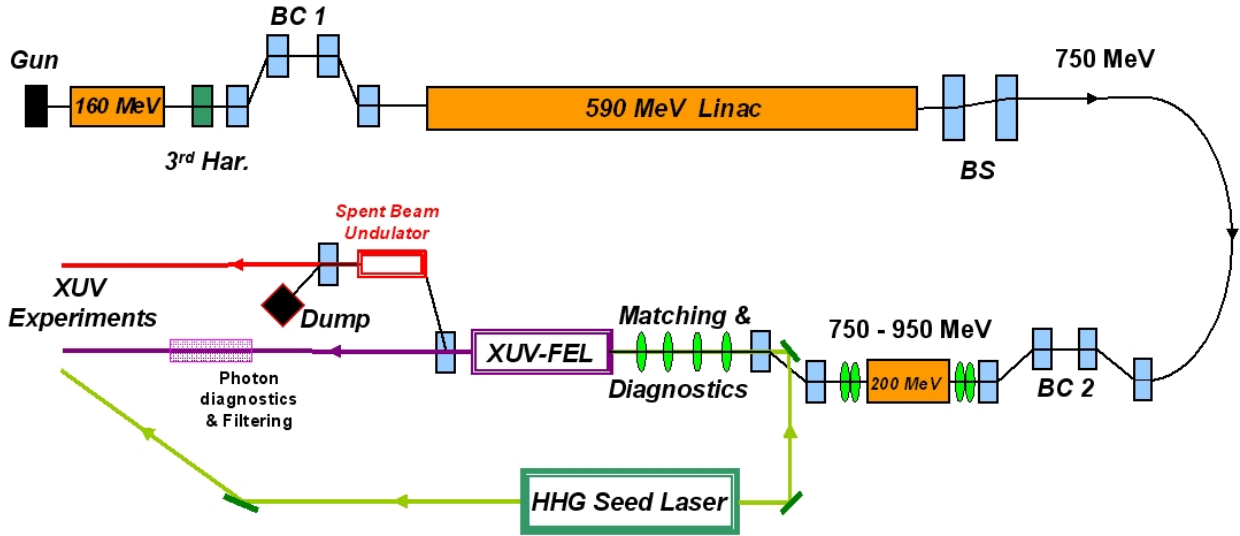


Figure 1: Schematic of the present conceptual design of the XUV FEL branch of 4GLS

tion, the 750 MeV beam takes a different path through a further bunch compressor and a final accelerator stage that may add a further 200 MeV to take the beam energy up to 950 MeV. Following the seeded XUV FEL stage, and before the beam dump, an option to pass the ‘spent’ electrons through a further spontaneous radiation source is included. A high degree of synchronisation is guaranteed between the XUV FEL and this source. The seed laser is shown schematically as a single unit, but may in reality be several High Harmonic Generation lasers. The facility to utilise these lasers as sources synchronised with the XUV FEL for use in user experiments is also included in the design.

### Design parameters

The electron beam parameters used for the conceptual design are summarised in Table 1. The additional 200 MeV

Pulse energy	750-950 MeV
Peak current	1.5 kA
Pulse charge	1 nC
Normalised emittance	$2\pi$ mm-mrad
Relative RMS energy spread	0.1%

Table 1: XUV FEL parameters.

accelerator module outside of the main ERL branch has significant beneficial effects. The additional beam energy tuning it affords, in addition to undulator gap tuning, allows one fixed period undulator to generate sufficient FEL coupling to achieve saturation over the design photon energy range 10-100 eV. Such tuning would be difficult to achieve by energy variation in the upstream injector, ERL accelerator and beam spreader sections which benefit from fixed energy operation. The parameters of Table 1 are used to optimise the undulator and focussing lattice that will cover the design photon energy range 10-100 eV. A Pure Perma-

nent Magnet (PPM) undulator has been chosen at this conceptual design stage although peak on-axis undulator fields may be improved by using a hybrid system. Hybrid undulators will be considered further as a future design option, as will variable polarisation undulators for the final few gain lengths such as the APPLE-II and APPLE-III type undulators. The magnetic field on axis of a PPM type undulator of period  $\lambda_w$  and pole gap  $g$  is given by [4]:

$$B_w = 2B_r \frac{\sin(\pi/M)}{(\pi/M)} (1 - \exp(-2\pi h/\lambda_w)) \times \exp(-\pi g/\lambda_w), \quad (1)$$

where the remnant field  $B_r = 1.3$ , the number of blocks per period  $M = 4$  and the block height as a fraction of undulator period  $h = 1/2$ . A minimum gap is set at  $g = 10$  mm.

The FEL design formulae of Xie [5] were used for the first parameter optimisation for generation of 100 eV photons. Table 2 gives the results of the optimisation. This optimisation is limited by, and fulfills, the requirement that the FEL must also be able to lase generating 10 eV photons at minimum undulator gap of 10 mm with electron beam energy of 750 MeV.

Undulator period, $\lambda_w$	45 mm
Undulator gap, $g$	$\sim 28$ mm
Beta-function, $\beta$	$\sim 2.2$ m
Gain length, $l_g$	$\sim 1.44$ m
SASE saturation length, $L_{sat}$	$\sim 27$ m
Seeded saturation length $L_{sat}$	$\sim 17$ m
Saturation power, $P_{sat}$	$\sim 2$ GW

Table 2: Optimised parameters of XUV FEL for 100 eV photons using Xie formulae [5].

Estimation of the seeded saturation length of Table 1 is calculated in the same way as that of the SASE case by

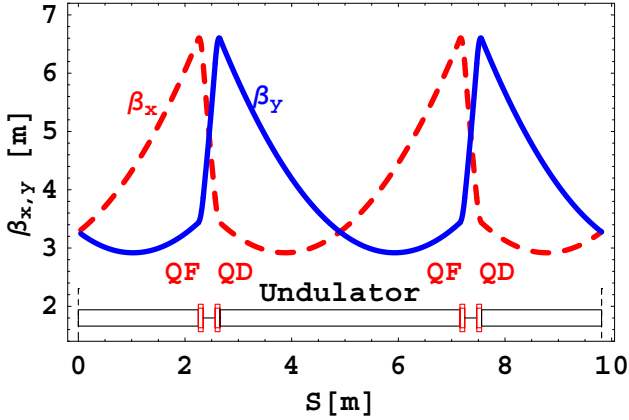


Figure 2: A section of the doublet focussing lattice showing the  $\beta$ -functions ( $\beta_x, \beta_y$ ) in the transverse plane and superimposed schematic of the undulator and quad. positions.

using equation (2) of [5] but with the effective input noise power,  $P_n \approx 30\text{W}$ , replaced by the seed power  $P_{seed} \approx 45\text{ kW}$ . This seed power is a conservative estimate based upon current High Harmonic Generation sources [6], and is clearly well above the noise level as required for a good seed source. It is worth noting that for an undulator length of 17 m, the Xie formula estimate that saturation can be achieved via SASE for photon energies up to  $\sim 35\text{ eV}$ .

The optimised  $\beta$ -function of the Xie formulation describes a constant, uniformly distributed focussing channel. The electron beam is therefore of constant radius  $r_b = \sqrt{\epsilon_n \beta / \gamma} \approx 49\mu\text{m}$ . The Xie formulae also show that the  $\beta$ -function may be increased from its optimised value of 2.2 m to 4 m with only small effects on the important parameters of Table 2. (E.g. the seeded saturation length is increased by only approximately 1 m.) For the same reasons as discussed elsewhere (see e.g. [7] which uses parameters similar to those discussed here), a discrete, non-uniform focussing lattice is more practical and leads to a design with focussing elements placed between separate undulator sections. Each undulator section has 100 undulator periods and so has total length 4.5 m. This length means a simple FODO lattice will result in significant variation in the  $\beta$ -function over the FODO period, and so a doublet quadrupole focussing lattice has been adopted at this stage. Again, as with [7], a triplet quadrupole lattice was investigated but was found in simulations to offer no significant benefit over the doublet. The undulator sections are separated by 9 undulator periods with each focussing quadrupole of length 2 undulator periods and gradient  $\approx 38\text{ T/m}$  placed at the beginning and end of each section. This leaves a length of 5 undulator periods between which other diagnostic, trimming coils, BPMs, phase matchers etc., may be placed.

The combined doublet focussing and undulator lattice used here was modelled and the electron beam at 950 MeV matched to it by the accelerator modelling code MAD [8]. The results are shown in Fig. (2). The mean  $\beta$ -function

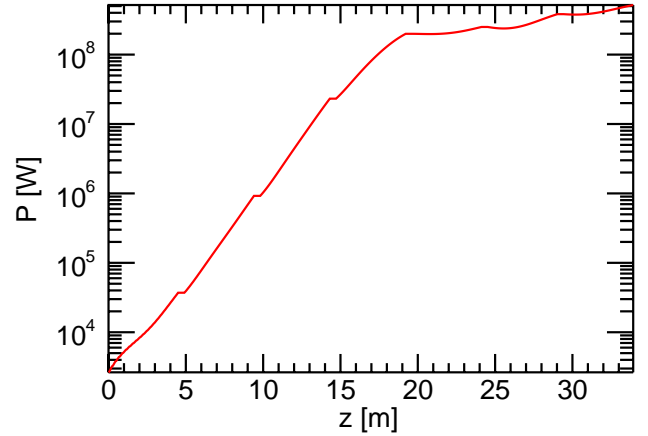


Figure 3: Plot of the average radiation power as a function of distance through the XUV FEL. The average is over the window of width  $\sim 500\mu\text{m}$  of Fig. (4).

within the undulators is  $\beta = 4\text{ m}$  and throughout the entire lattice, the mean  $\beta = 4.8\text{ m}$ .

### Design simulation

The 3-D FEL simulation code Genesis 1.3 [9] was used in its steady-state mode (neglecting slippage effects) with the above parameters and undulator/focussing lattice. The code estimates a saturation length of  $\sim 19.5\text{ m}$  and saturation power of  $\sim 2.5\text{ GW}$  which, when the  $\sim 1.2\text{ m}$  of gaps between undulator sections is taken into account, is in excellent agreement with the results of the Xie estimates of Table 1.

Genesis 1.3 has also been used to include the effects of pulse propagation. For a total charge of 1 nC and peak current of 1.5 kA, the Gaussian electron pulse has a temporal width of  $\sigma_t \approx 266\text{ fs}$ . A Gaussian radiation pulse was injected of peak power 60 kW (RMS power  $\sim 36\text{ kW}$ ) coincident with the peak of the current. The radiation pulse had a temporal width  $\sigma_t = 30\text{ fs}$ , typical of present HHG sources. The radiation was injected to a focus at 2.25 m into the first undulator section. The average FEL power, averaged over a window of width  $500\mu\text{m}$ , is shown in Fig. (3). It is seen that the power saturates toward the end of the fourth undulator section at  $z \approx 19\text{ m}$ . This agrees well with the results of the Xie formulation above despite the slightly smaller initial RMS input power. The structure of the radiation pulse power at saturation is plotted in Fig. (4) and shows a well defined pulse structure showing little of the noise associated with SASE. The relative slippage of the radiation with respect to the electron pulse is approximately  $4.8\mu\text{m}$  being just over half of the width of the seed  $\sigma_z \approx 9\mu\text{m}$  (30 fs). This slippage results in a slight increase in the width of radiation pulse width over that of the seed. Note that only that part of the electron pulse (current of peak 1.5 kA shown superimposed) that has been seeded has had any significant contribution to the FEL lasing. As the interaction proceeds, post saturation of the seeded re-

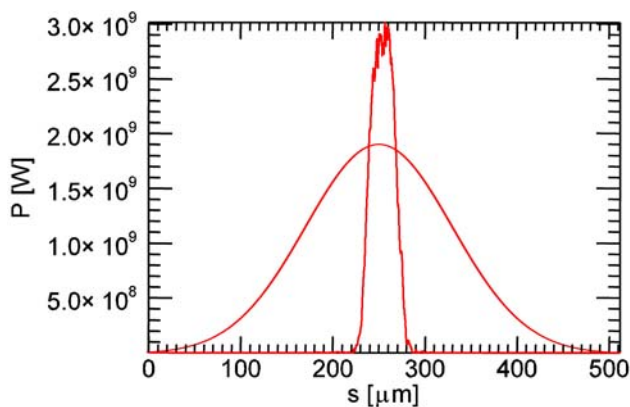


Figure 4: Radiation pulse power at saturation ( $z=19$  m) as a function of  $s=ct$ . The wider electron beam current of peak 1.5 kA is also shown.

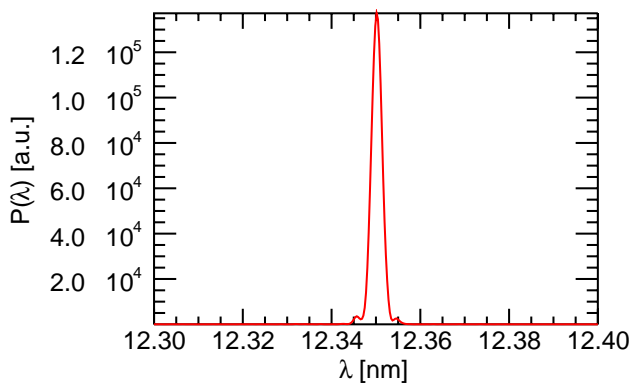


Figure 5: The spectral power at saturation as a function of radiation wavelength  $\lambda$ , confirms the enhanced radiation properties of a seeded FEL over that of SASE.

gion, then the remaining regions of the electron pulse begin to saturate via the SASE mechanism, spreading out from the centre of the electron pulse toward the lower current regions. This accounts, in large part, for the increasing average power for  $z \gtrsim 25$  seen in Fig. (3). The improved radiation pulse properties over that of SASE and suggested by the clean radiation pulse structure of Fig. (4) is confirmed in the plot of the spectral power at saturation of Fig. (5). Both the electron pulse current and seed radiation intensity will be subject to relative timing 'jitter' and therefore will not always be coincident. If this jitter is the width of the Gaussian electron pulse ( $\sigma_t \approx 266$  fs) then the current the seed interacts with is reduced to approximately 910 A. According to the Xie estimates this increases the seeded saturation length from 18 m to 24 m and reduces the saturated power from approximately 2 GW to 1.2 GW. (Of course, the correlation between the interaction current and timing jitter is determined by the shape of the current pulse and will require more detailed simulation of the complete system.)

## CONCLUSIONS

The ongoing design work for the 4GLS facility is an iterative process and is initially intended to lead toward a Conceptual Design Report, which will be published in the Spring of 2006, and thence to the Technical Design Report to be published toward the end of 2006. The present design remains a work-in-progress and will undoubtedly evolve further. Crucial to the final design will be a more detailed specification of the proposed HHG seed sources and further analysis of the stability of the FEL operation with respect to timing jitter within the system. Both of these issues will now be more closely studied. The use of other undulator systems that use hybrid magnets and variable polarisation (APPLE) also require further investigation. The former may allow extension of the FEL operation to lower photon energies while the latter will be required to provide users with variable polarised radiation. The current design proposal is relatively simple and therefore will hopefully have an inherent robustness built in that will ensure reproducible and stable operation for users. This also gives the design the scope for future upgrade e.g. addition of accelerator modules to further increase the electron energy or the addition of a modulator undulator for HHG type operation to higher photon energies. The latter may also provide a fall-back scheme to generate the higher photon energies up to 100 eV in the event that suitable HHG sources for direct seeding are not available.

We acknowledge the support of the CCLRC, and the Scottish Universities Physics Alliance and the valuable contributions of colleagues on the 4GLS International Advisory Committee.

## REFERENCES

- [1] M. W. Poole and E. A. Seddon, Proceedings of Particle Accelerator Conference, Knoxville, USA (2005)
- [2] N. R. Thompson and B. W. J. McNeil, *ibid* (2005)
- [3] M. W. Poole and B. W. J. McNeil, Nucl. Inst. Meth. Phys. Res. A, **507**, 489 (2003)
- [4] J. A. Clarke, *The science and technology of undulators and wigglers*, (Oxford University Press, 2004.)
- [5] Ming Xie, Proc. Of 1995 Part. Accel. Conf., 183 (1996)  
A MATLAB package for solving and displaying solutions can be found at <http://phys.strath.ac.uk/eurofel/rebs/desXie/desXie.htm>
- [6] Eiji J. Takahashi *et al*, IEEE J. OF Selected Topics in Quantum Electron., **10**, 1315 (2004)
- [7] B. Faatz, J. Pflüger, Nucl. Instr. and Meth. A **475**, 603 (2000)
- [8] H. Grote and F. C. Iselin, CERN/SL/90-13(AP) (Rev. 5), <http://hansg.home.cern.ch/hansg/mad/mad8/mad8.html>.
- [9] S. Reiche, Nucl. Inst. and Meth. A **429**, 243 (1999)
- [10] C. Gerth, *et al*, Proceedings of the 26th International Free Electron Laser Conference, Trieste (2004)

## BROADBAND SINGLE SHOT SPECTROMETER

H. Delsim-Hashemi, O. Grimm, J. Rossbach, H. Schlarb, B. Schmidt, DESY, Hamburg, Germany  
 P. Schmüser, Univ. Hamburg, Germany  
 A.F.G. van der Meer, FOM, Nieuwegein, The Netherlands

### *Abstract*

This paper summarizes the ongoing activities at DESY for the longitudinal phase space studies on ultra short bunches of VUV-FEL using infrared spectroscopy.

### INTRODUCTION

FEL facilities are pushing to achieve higher peak currents mainly by means of compressing bunches longitudinally. This process defines a machine parameter, longitudinal charge distribution that has to be fine-tuned empirically. Among the operational types of diagnostic tools for longitudinal phase-space are those based on infrared (IR) spectroscopy. The most commonly used IR spectrometers (e.g. Martin-Puplett interferometer) at the FEL facilities are inherently operating in a scanning mode and are not fast enough to be applicable for monitoring bunch compression versus machine settings on a bunch by bunch basis. On the other hand, any non-scanning single bunch spectrometer may suffer from the low amount of intensity that is available from Coherent Synchrotron Radiation (CSR) or Coherent Transition Radiation (CTR) or Coherent Diffraction Radiation (CDR) in short time intervals in different wavelengths.

The proposed single shot spectrometer is based on using gratings as dispersive elements. Pioneering tests with a Transmission Grating (TG) have shown the feasibility of the concept. The results of these measurements are in agreement with simulations that have been made using “THz-Transport”, a code which is developed at the FLA-group at DESY to simulate the radiation transport based on scalar diffraction theory [1].

In a second step, a version with Reflective Blazed Gratings (RBG) will be tested and should allow getting the maximum available signal for the whole spectrum and improved resolution.

Parallel to the study of optical parts, an array of pyroelectric detectors with integrated multi-channel readout is under development.

### SIMULATION CODES

#### *THz-Transport as simulation tool-box*

THz Transport generates the transition radiation from a single particle for a specified target geometry and frequency. It can propagate all kinds of radiations, including transition radiation, to optical elements using Fourier transformation optics. Optical elements which can be described include parabolic, elliptical, toroidal, spherical and flat mirrors, windows of different materials, and transmission gratings. The code provides the complex electric field amplitude at any plane perpendicular to the optical axis and allows simulating complex optical beam

lines with respect to transmission functions or propagation of THz pulses. It is written as a set of Mathematica routines and is able to handle frequencies in the range of a few GHz up to about 50 THz.

#### *GSolver as simulation code for gratings*

It is a well known result that for a ratio of wavelength over grating pitch larger than 0.4, scalar diffraction theory doesn't model the grating well. GSolver is a code which is based on a rigorous vector diffraction theory [2]. For all calculations for RBGs we have used this code [3].

### OPERATIONAL DIAGNOSTIC TOOLS AT TTF2

#### *Martin-Puplett Interferometer*

Two Martin-Puplett interferometers are currently operational at VUV-FEL at DESY. One equipped with DTGS pyroelectric detectors looks to CSR at Bunch Compressor 2 (BC2) [4]. The second interferometer that uses Golay-cell detectors looks at CDR at BC3. A routine which is integrated in the machine control system scans over path length of one arm and derives the interferogram and thereby the frequency spectrum.

#### *Bunch Compression Monitor (BCM)*

First-generation BCMs use pyroelectric detectors looking to polychromatic IR. Signal amplitude is dependent on the degree of compression. While this device is a good tool for an approximate tuning of the off-crest phase in the accelerating cavities preceding the bunch compressor chicane, it is not sensitive enough to adjust the optimum bunch compression.

### GRATINGS AS DISPERSIVE ELEMENTS

When a bunch of electrons is forced to radiate, electrons in the bunch radiate coherently at wavelengths longer than the bunch length. Therefore the range of the coherent radiation spectrum extends to shorter wavelengths as bunches become shorter, demanding for an efficient detection system that specifically covers this part of the spectrum. At VUV-FEL at DESY the bunch length is in the range of a few tens of fs, therefore coherent radiation extends from far-infrared to mid-infrared. One way to disperse such a polychromatic radiation to different components is based on gratings. TG and different types of RG (Reflective Gratings) are under study. RBG can be designed to give a very efficient (~90%) dispersive element that can reach the maximum possible signal for different components via appropriate optics. In the same

conditions TGs can reach efficiencies as large as 20% (equal to the half of the lamellar reflective grating).

### Transmission Grating (TG)-spectrometer at Bunch Compressor-2 (BC2)

Assuming plane waves illuminating a TG, it is not difficult to deduce a surprisingly simple relation between slit and pitch size that suppresses spectral orders above 1 and thus allows for broad free spectral range [5]. Based on this principle, a set of TGs were designed and manufactured at DESY. A collimating optics puts CDR at BC2 onto the TG, a paraboloid focuses the dispersed radiation into a line representing the wavelength spectrum. Since no fast multi-channel sensors of the required size exist for this wavelength range at the moment, we scan the spectrum with a single pyrodetector. The detector itself and the readout is fast enough to resolve individual bunches in the first spectroscopic order, that is selecting a specific, narrow wavelength range given by the diffractive power of the set up and the size of the detector element. An example is shown in Fig. 1. The achievable resolution in the focal plane is basically diffraction limited and the size of the detector element has to be properly adjusted.

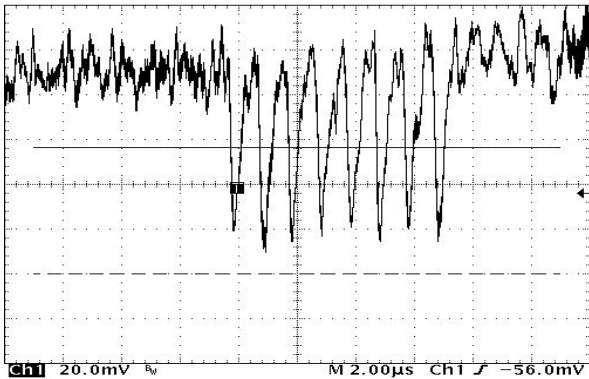


Figure 1: Signal from a Pyroelectric sensor for 8 subsequent bunches of InC charge in first spectroscopic order. The wavelength range covered by the detector is about 40  $\mu\text{m}$ .

Fig. 2 shows a picture of the TG spectrometer set up. Fig. 3 shows a reference spectrum using a CDR. In the front of the detector a 357  $\mu\text{m}$  band-pass filter is used to calibrate the wavelength axis. Position, width and intensity of the first order maxima are in agreement with the simulations using THz-Transport.



Figure 2: TG spectrometer at BC2 (Top view)

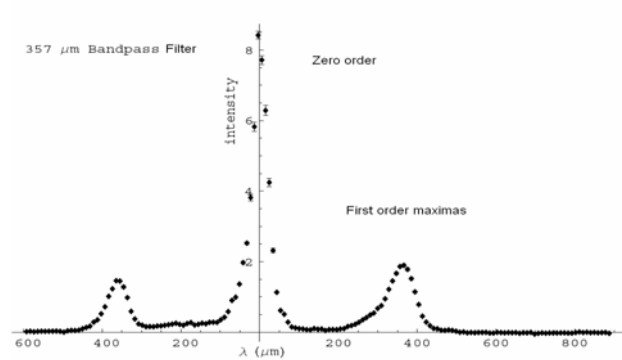


Figure 3: TG-Spectrometer is illuminated by CDR and a 357  $\mu\text{m}$  band-pass filter is in the front of the detector.

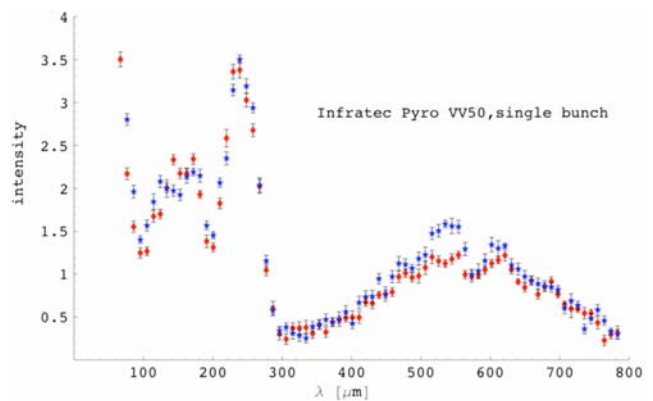


Figure 4: TG-Spectrometer is illuminated by CDR, no filters.

Fig.4 shows a full spectrum and its reproducibility in the range of device acceptance. The detector responsivity is not flat over far-infrared and it is the main reason for structures.

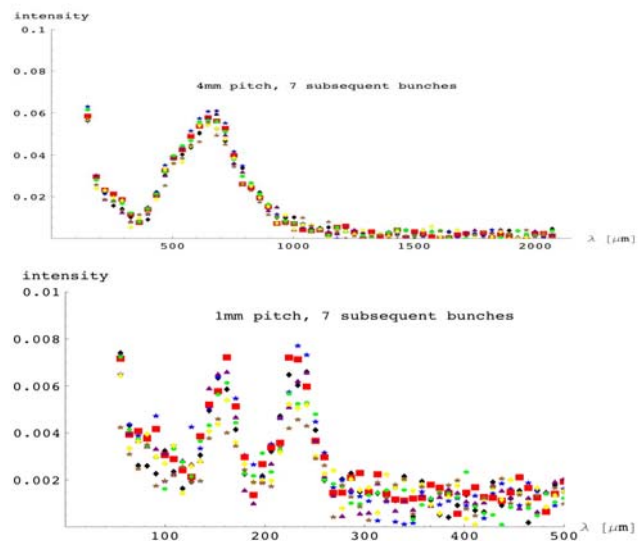


Figure 5. Bunch to bunch spectra made by TG spectrometer.

Fig. 5 shows two examples for spectra of the unfiltered CDR with TG of 4mm and 1mm pitch. The 0-order maximum and the left side of the spectra are suppressed.

The different symbols (colours) refer to 7 subsequent bunches from the same bunch train recorded simultaneously. The prominent structures at  $260\mu\text{m}$  and  $150\mu\text{m}$  wavelength seen in the short wavelength spectrum do not reveal bunch structures but are caused by the resonant behaviour of the responsivity for this specific pyroelectric sensor.

As a result of this pioneering measurement at VUV-FEL, the efficiency of TG turned out to be sufficient to get a detectable signal even from a single bunch of intermediate charge (using CDR).

### Reflective Blazed Grating (RBG) versus Transmission Grating (TG)

Efficiency curve of a properly designed RBG is illustrated in Fig.6. It is clear from that plot that the higher orders become excited below  $45\mu\text{m}$  wavelengths but above  $45\mu\text{m}$  all reflected power goes to zero and/or first orders. The  $45$  to  $85\mu\text{m}$  wavelength window is the dispersive region for this grating and for longer wavelengths it acts like a mirror. With a sequence of different such gratings, it is possible to cover a broad band of wavelengths without loss of intensity. The gain in intensity as compared to the best TG is at least a factor of four.

For calculation of the RBG efficiency curves, vector diffraction theory is used. The validity of calculations based on this theory for reflective grating has been widely proven. In fact the region of our interest, IR, is the safest region of electromagnetic spectrum for this theory [6].

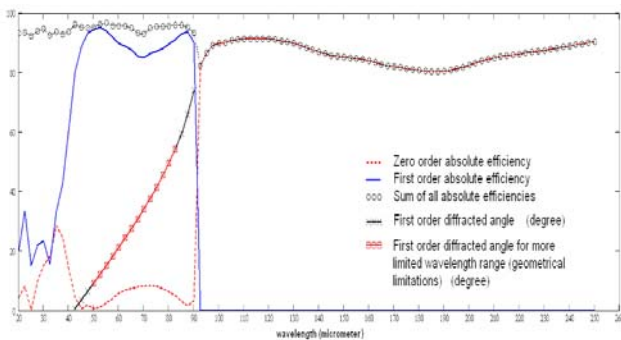


Figure 6. First and zero order efficiencies and first order diffracted angles for a RBG with 20 grooves/mm and blaze angle of  $26.75^\circ$  for S-polarization.

In order to evaluate our specific gratings and to compare their behaviour with theory, measurements were done at FELIX (Fig.7). The transition from dispersive to reflective behaviour (see Fig.6) for two different pitch size gratings in air and vacuum were tested. The incident radiation illuminates the grating with an angle of  $57^\circ$  from the normal to the grating plane (Fig. 8). For the lattice used for this test, grating equation shows that only zero and first orders are possible. Therefore measuring the zero order in the reflection (with much sharper peak, thus easier to measure) for different wavelengths seems sufficient to verify calculations. The prediction for the propagation direction of the first orders as a function of wavelength found to be in complete agreement with calculations. For

the zero order efficiency the agreement with theory is excellent. Furthermore, in the dispersive window region and for several wavelengths, the dispersed first order efficiencies were measured and they are in good agreement with the expected values.

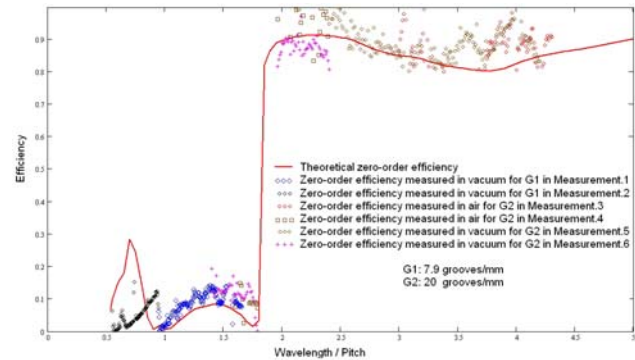


Figure 7. Theoretical zero-order (solid-red) and measured zero-order for two different gratings in air and vacuum.

Further studies with a non-scanning device were made. A large enough paraboloid with short focal length was focusing the dispersed first orders to an array of pyroelectric detectors. It was possible to see the narrow spectrum of the FELIX radiation and, changing the FEL wavelength, the spectrum was sliding on the array of detectors accordingly. No quantitative measurements were made with this device yet.

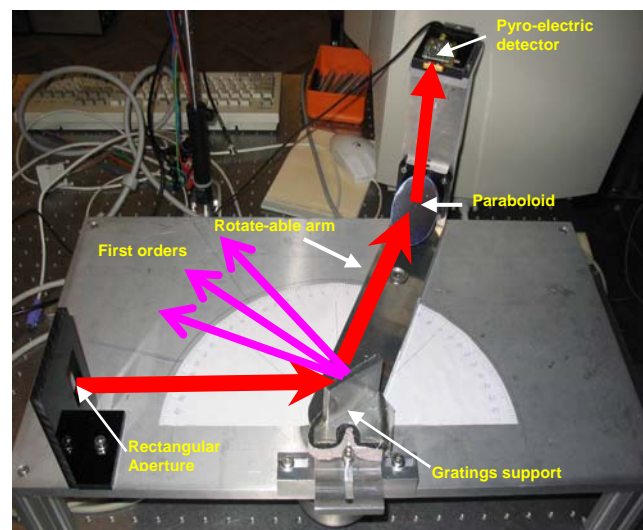


Figure 8. The mounting used for studies on distribution and efficiency of different orders at FELIX.

## CONCLUSION

A single shot spectrometer based on the grating as dispersive elements can give a full spectrum of the IR radiation of an individual bunch of intermediate charge. We were able to measure CDR spectra for individual successive bunches from a 7 bunch train with a scanning pyrodetector to demonstrate the feasibility of such a set up. The extension to a single shot device by developing a

fast multi-channel far-infrared detector is in preparation. First measurements have shown the power of the concept of RBG for this wavelength range and proven the validity of our simulation tools. A set of properly designed RBG together with multi-channel detectors should be able to cover a broad wavelength band for single bunches with high sensitivity.

### REFERENCES

- [1] S. Casalbuoni et. al. "Far infrared Transition and Diffraction radiation Part I: Production, Diffraction Effects and Optical Propagation", DESY TESLA Report 2005-15
- [2] D. Maystre, Opt. Commun. 6, 50 (1972)
- [3] GSolver available from [www.gsolver.com](http://www.gsolver.com)
- [4] L. Froehlich Diploma thesis, DESY-THESIS 2005-011, "Bunch Length Measurements Using a Martin-Puplett Interferometer at the VUV-FEL".
- [5] Talk by B. Schmidt on TG-Spectrometer: <http://tesla.desy.de/fla/crd/meetings/meetings.html>.
- [6] E. G. Loewen et. al. "Grating efficiency theory as it applies to blazed and holographic gratings", Appl. Opt. 16, 2711 (1977).

# COMMISSIONING OF TTF2 BUNCH COMPRESSORS FOR GENERATION OF 20 FEMTOSECOND SASE SOURCE

Yujong Kim\*, K. Flöttmann, S. Schreiber for VUV-FEL team, DESY, D-22603 Hamburg, Germany  
Dongchul Son and Y. Kim, The Center for High Energy Physics, Daegu 702-701, Korea

## Abstract

By the help of nonlinearity in the longitudinal phase space, the VUV-FEL at the TESLA Test Facility phase 2 (TTF2) is under operating in the femtosecond (fs) FEL mode which generates coherent and ultra-bright SASE source with photon pulse duration time of around 20 fs (FWHM) and wavelength of around 32 nm. For the fs FEL mode operation, bunch length of electron beams should be compressed by two bunch compressors to have a leading spike in the longitudinal beam density distribution or peak current. The required peak current at the spike is higher than about 1.0 kA, and the spike length is shorter than around 200 fs (FWHM). In this paper, we describe our commissioning experiences to optimize two TTF2 bunch compressors for the fs FEL mode operation.

## INTRODUCTION

Originally, Saldin *et al* proposed the fs FEL mode operation for the VUV-FEL due to the delayed installation of the 3rd harmonic cavities and users' request on a shorter pulse [1]. To generate more stable SASE source for a long time, recently, we increased single bunch charge from 0.5 nC to 1.0 nC and changed several other machine parameters from their original scheme [2]. One of our current nominal TTF2 machine layout for the fs FEL mode operation is shown in Fig. 1, where the 3rd harmonic cavities ACC39, the 6th TESLA superconducting accelerator module ACC6, and three seeding undulators SEEDING are not installed yet. Its detail linac parameters are summarized in Table 1. Note that here all parameters are projected ones, and with this machine layout and machine parameters, we could generate SASE source at a wavelength of around 32 nm on April 9th, 2005. Since nonlinearities in the longitudinal phase space can not be compensated without ACC39, two TTF2 bunch compressors (BC2 and BC3) compress bunch length nonlinearly [3]. In this case, a charge concentration or spike in the peak current is generated at the leading head region as shown in Fig. 2 [2], [3]. When the VUV-FEL generated the first lasing at 32 nm, there was no special diagnostic tool such as the LOLA cavity to measure fs range bunch length. However we could optimize two TTF2 bunch compressors (BCs) by comparing measured results with simulation ones and by measuring machine status and beam parameters with basic diagnostic tools such as pyroelectric detector and OTR screens. In this paper, we describe our commissioning experiences to optimize two TTF2 bunch compressors for the fs FEL mode operation.

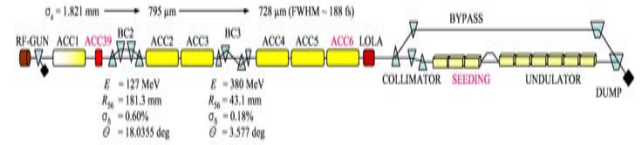


Figure 1: TTF2 layout for the fs FEL mode.

Table 1: TTF2 main linac parameters for the fs FEL mode.

Parameter	Unit	Value
single bunch charge	nC	-1.0
RF frequency of gun and TESLA module	GHz	1.3
gun peak gradient on the cathode	MV/m	40.25
gun phase from zero crossing	deg	38
low / high accelerating gradient in ACC1	MV/m	12.95 / 16.84
ACC1 phase from on crest	deg	~ -9.0
accelerating gradient in ACC2 / ACC3	MV/m	17.29 / 13.53
ACC2 / ACC3 phase from on crest	deg	~ 0.0
accelerating gradient in ACC4 / ACC5	MV/m	3.85 / 4.03
ACC4 / ACC5 phase from on crest	deg	0.0
beam energy after ACC5	MeV	445
rms relative energy spread after ACC5	%	0.16
horizontal / vertical emittance after ACC5	$\mu\text{m}$	3.17 / 2.05
bunch length (FWHM) after ACC5	fs	~ 188

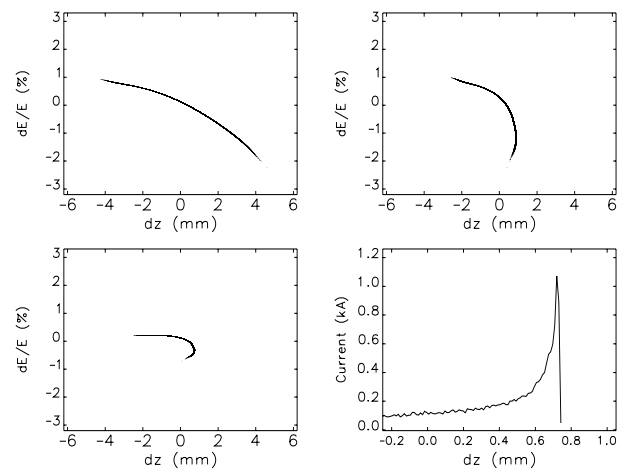


Figure 2: Longitudinal phase space before BC2 (top left), after BC2 (top right), after BC3 (bottom left), and peak current after BC3 (bottom right) for the machine layout in Fig. 1 and linac parameters in Table 1. Here positive  $dz$  means the leading head in a bunch.

\* E-Mail : Yujong.Kim@DESY.de

## BC COMMISSIONING EXPERIENCES

### Setup of Energy, Energy Spread, and $R_{56}$

As to two TTF2 BCs, detail design concepts for the nominal FEL mode operation are well described in reference [4]. To get the best BC performance for the fs FEL mode operation, we should properly choose beam energy at BCs, energy spread or RF phases of precompressor linacs (ACC1 for BC2, ACC2 and ACC3 for BC3), and the chicane strength  $R_{56}$  or bending angle of dipole magnet [3]. During the fs FEL mode operation, a charge concentration or a spike is generated within a local small area as shown in Fig. 2. Therefore beam energy at BCs should be high enough to avoid any possible beam dilution due to space charge effects in the spike. After considering the maximum available gradient of precompressor linacs, we chose 127 MeV and 380 MeV for the beam energy at BC2 and BC3, respectively. The exact beam energy at the BCs can be set up by positioning the beam image at the center of a screen in the chicane as shown in Fig 3(top row). Here 3BC2 screen is located at a point in BC2 where the horizontal dispersion is its maximum, and its horizontal beam position corresponds to beam energy at the bunch compressor. If beam energy is higher (or lower) than 127 MeV, horizontal beam position is at the left (or right) side of the 3BC2 screen. Although we can adjust bending angle or magnet current of chicane dipole, we fixed the bending angle of the chicane to measure beam energy at BC easily. From beam position on the screen and a calibration factor between chicane dipole current and beam energy, we can measure beam energy at BC easily.

To choose operational phase of precompressor linacs properly, we should consider various things such as projected and slice emittances, bunch length or peak current,

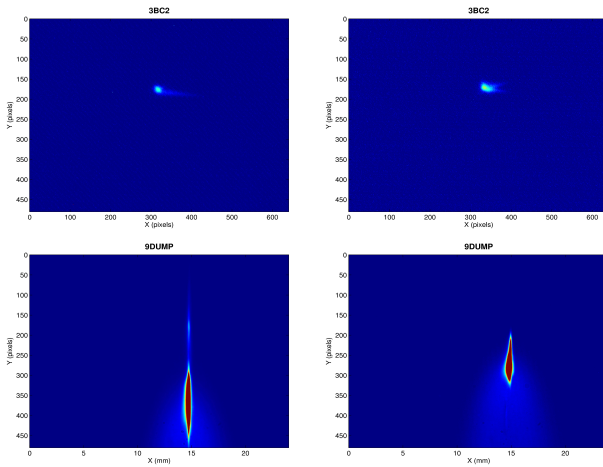


Figure 3: Beam images on 3BC2 and 9DUMP screens when ACC1 phase is on crest (top left), -2.0 degree off crest (top right), around -9.0 degree (bottom left), and around on crest (bottom right).

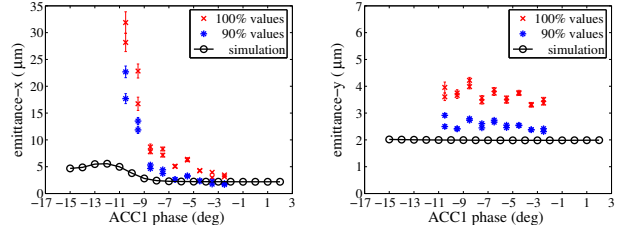


Figure 4: Simulation and measured results of projected emittance after BC2 for different ACC1 phase: (left) projected normalized rms horizontal emittance and (right) projected normalized rms vertical emittance.

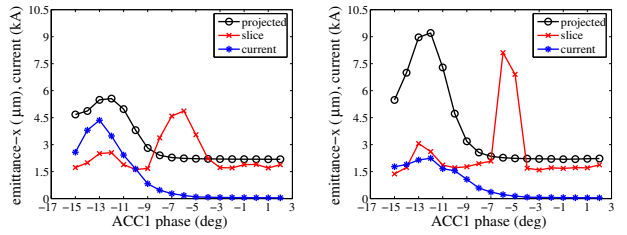


Figure 5: Simulation results of projected and slice normalized rms horizontal emittances and peak current after BC2 (left) and after BC3 (right).

projected and slice energy spread, beam loss in the collimator, and the longitudinal space charge force. After considering simulation and measured results of projected emittance after BC2 as shown in Fig. 4, we chose phases between -10 degree to -9 degree as the best operational phase of ACC1. In this case, slice emittance is around its minimum, and peak current is high enough as shown in Fig. 5(left), where slice emittance is the averaged slice emittance within the FWHM of the leading spike. Although we can choose more off crest phase to get a higher peak current after BC2, horizontal projected and slice emittance become worse due to stronger coherent synchrotron radiation (CSR) effects at BC2 as shown in Figs. 4(left) and 5(left). Since CSR attacks only in the bending horizontal plane, vertical projected emittance is almost constant though peak current is about a few kA as shown in Figs. 4(right) and 5(left). That constant vertical emittance also indicates that space charge effects at BC2 is weak enough though peak current is high. To reduce beam loss at the collimator and to reduce the projected and slice energy spread at the entrance of undulator, we chose on crest phase from ACC2 to ACC5 modules. In this case, ACC1 module and BC2 supply  $dz - dE/E$  chirping at BC3, and BC3 can continuously compress bunch length to get more higher peak current of around 1 kA as shown in Figs. 2 and 5. To compress the bunch length more strongly at BC3, we can choose somewhat off crest phase in ACC2 and ACC3 modules.

Note that there are two special things in Fig. 5: First, slice emittance is significantly increased if ACC1 phase

is between -8 degree and -4 degree off crest. This is related with the longitudinal position in a single bunch where compression is generated. For those off crest phases, the compression is generated around the head region where slice emittance is generally high [5]. But phases between -10 degree and -9 degree, compression position is shifted to the bunch core where slice emittance is low. Second, peak current after BC3 is not increased further if ACC1 phase is lower than -11 degree. This is related with the nonlinearity in the longitudinal phase space and the maximum compression at BC2. Since the maximum compression at BC2 is happened at around -13 degree off crest as shown in Fig. 5(left), and there is strong nonlinearity in the longitudinal phase space for ACC1 phase  $\leq -11$  degree, bunch length can not be compressed further by BC3. In this case, two or three spikes in peak current are generated by BC3, and the maximum peak current among spikes is always lower than that after BC2 as shown in Fig. 5.

Since bunch length or peak current after BC3 is significantly changed according to the ACC1 phase, it is important for us to know how to set up off crest phase of ACC1 exactly. Since a signal from the pyroelectric detector is proportional to the intensity of CSR, we can use the detector signal to find a phase which gives the maximum bunch length compression. At the TTF2, we find that there is always a constant phase difference between on crest phase and the maximum compression phase. At the BC2 (BC3), the maximum compression is always happened when ACC1 (ACC2 and ACC3) phase is about -13 degree (-42 degree) off crest as shown in Fig. 6. Therefore on crest phase can be exactly determined just by adding +13 degree (+42 degree) to the maximum compression phase of ACC1 (ACC2 and ACC3). There is the second method which can be used to find on crest phase of ACC1. Whenever ACC1 phase is around -2.0 degree off crest, we can find two symmetric branches at the tail region or lower energy region in the beam image on 3BC2 screen as shown in Fig. 3(top right). Here, we can clearly see those branches in the figure by zooming in with the Acrobat Reader. This is related with symmetric shape of longitudinal phase space when ACC1 phase is -2.0 degree. We can find its related longitudinal phase space from Y. Kim's presentation in reference [2]. By adding +2.0 degree to the phase which gives the symmetric two branches at the tail region on 3BC2 screen, we can find on crest phase of ACC1 module exactly.

In case of ACC4 and ACC5 modules, we can approximately find on crest phase by scanning phase while monitoring beam image on the 9DUMP screen or 5ECOL screen in the dog-leg. If vertical beam size on 9DUMP screen is close to its smallest one, and beam image on 9DUMP screen is located at the lowest vertical position, beam energy is highest, and the phase is close to on crest.

Since we fixed bending angles in BCs to measure beam energy easily,  $R_{56}$ s of two BCs are always constant as shown in Fig. 1. Instead of adjusting  $R_{56}$ , we change phases of precompressor linacs to adjust compression strength at BCs.

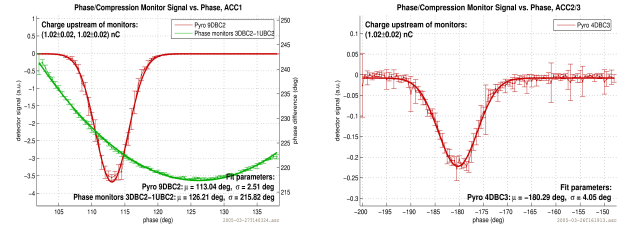


Figure 6: Measured signals of pyroelectric detector and phase monitor: (left) at 9DBC2 while ACC1 phase is scanned and (right) at 4DBC3 while ACC2 and ACC3 phases are simultaneously scanned for on crest ACC1 phase. Here 9DBC2 and 4DBC3 pyroelectric detectors are located at the downstream of BC2 and BC3, respectively.

### Fine Tuning for fs FEL Mode

Whenever we get the lasing, beam image at 9DUMP screen has a sharp leading beamlet at the top region as shown in Fig. 3(bottom left), which corresponds to the spike at the leading head in the peak current. When we do not compress bunch length or we lose SASE, beam image at 9DUMP screen is such as shown in Fig 3(bottom right). Therefore, for the fs FEL mode operation, we can finely tune phases and gradients of GUN and precompressor linacs by monitoring beam image at 9DUMP screen and the MCP gain of SASE source. With a similar machine layout as shown in Fig. 1 and similar machine parameters as summarized in Table 1, we could generate about 155 fs (FWHM) long electron spike in the leading head region, which was recently measured with the LOLA cavity for ACC1 phase  $\simeq -10$  degree off crest as shown in Fig. 7. This measured bunch length is well agreed with our simulation results; about 160 fs (FWHM) for -10 degree and about 188 fs (FWHM) for -9 degree off crest. With around 155 fs (FWHM) long electron spike, recently, we could generate coherent SASE source with peak photon energy of about several  $\mu\text{J}$  and photon pulse length of around 20 fs at 32 nm [6], [7].

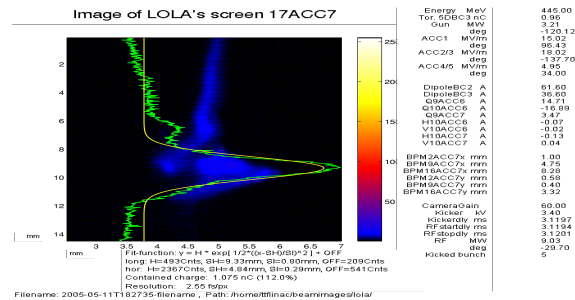


Figure 7: Electron beam image on LOLA screen 17ACC7 when ACC1 phase is about -10 degree and other parameters are such as summarized in Table 1. Here measured bunch length is about 155 fs (FWHM).

## Stability of Bunch Length

Even though we could generate 20 fs long SASE source during TTF2 commissioning period, we lost SASE source from time to time. This loss is generated mainly by the unstable RF low level system. Since unstable ACC1 RF phase

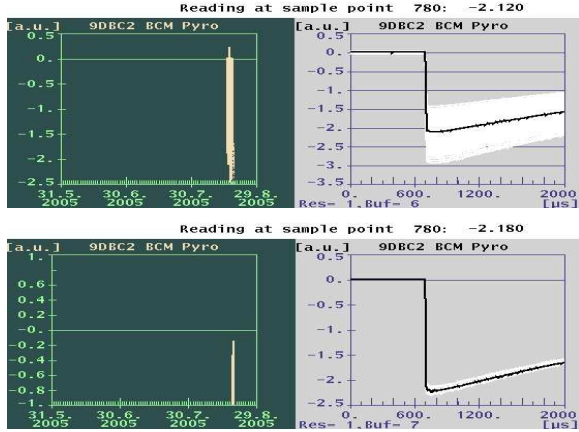


Figure 8: 9DBC2 pyroelectric detector signal: (top) when no slow feedback is applied to ACC1 RF phase and (bottom) when a slow feedback is applied to ACC1 RF phase to keep energy spread at BC2 constant and to generate stable bunch length at the downstream of BC2.

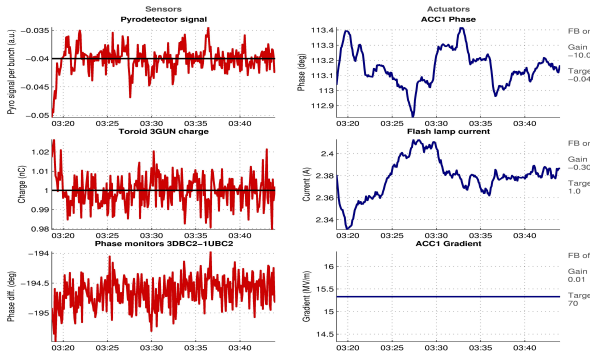


Figure 9: Three slow feedback systems to improve BC performance: (top left) 9DBC2 pyroelectric detector signal per bunch, (top right) a slow feedback system is applied to ACC1 RF phase to keep constant pyroelectric detector signal or bunch compression status at BC2, (middle left) 3GUN toroid signal at the downstream of RF gun, (middle right) a slow feedback system is applied to laser flash lamp current to keep constant single bunch charge at the 3GUN toroid, (bottom left) difference in signals of two phase monitors, which are located at the upstream and downstream of BC2, (bottom right) a slow feedback system can be applied to ACC1 gradient to keep beam energy at BC2 constant. Here last slow feedback system is turned off.

induces drift in energy spread at BC2, bunch length and

peak current after BC2 is continuously changed. This drifting bunch length is detected by the 9DBC2 pyroelectric detector as shown in Fig. 8(top), where white lines show history of drifting 9DBC2 pyroelectric detector signal or drifting bunch length. To solve drift in bunch length and peak current, we apply a slow feedback system in ACC1 RF phase as shown in Fig. 9(top). By applying the slow feedback in ACC1 RF phase in every a few tens seconds, we can effectively reduce drift in energy spread at BC2 and drift in 9DBC2 pyroelectric detector signal as shown in Fig. 8(bottom). Therefore we could generate stable bunch length and peak current after BC2, and we can keep stable SASE source for a longer time. To improve BC performance further, we apply three slow feedback systems to laser flash lamp current, ACC1 RF phase, and ACC1 RF gradient as shown in Fig. 9.

## SUMMARY

By using nonlinearities in the longitudinal phase space and by choosing proper RF phases in precompressor linacs, we could generate about 155 fs (FWHM) long spike at the leading head region of electron bunch. Even though we used several basic diagnostic tools, estimated bunch length with simulation was well agreed with measured one with the LOLA cavity. That means that our bunch compressors were optimized properly as we desired. Since estimated peak current and slice emittance at the leading spike are around 1 kA and  $2 \mu\text{m}$ , respectively, we can generate about 20 fs long SASE source from the spike. By applying slow feedbacks to the RF phase and amplitude of the precompressor linac and to laser flash lamp current, we can keep bunch length and peak current constant, which is helpful to generate stable SASE source for a longer time. We will optimize bunch compressors further by measuring bunch length and slice beam parameters with the LOLA cavity and by measuring projected emittance with OTR screens.

## ACKNOWLEDGEMENTS

We thank all operators who are working for TTF2 commissioning and DESY colleagues who are working for beam diagnostics; K. Honkavaara and F. Loehl for emittance measurement system with OTR, M. Huening and A. Bolzmann for bunch length measurement system with LOLA cavity, and O. Grimm and L. Froehlich for bunch compression monitor with pyroelectric detector.

## REFERENCES

- [1] E.L. Saldin *et al.*, DESY Report No. TESLA FEL 2004-06.
- [2] <http://commissioning2005.desy.de/>
- [3] Yujong Kim *et al.*, Nucl. Instr. and Meth. A 528 (2004) 421.
- [4] Ph. Piot *et al.*, in *Proc. EPAC2002*, 2002.
- [5] Yujong Kim *et al.*, in *Proc. EPAC2004*, 2004.
- [6] S. Schreiber, in these Proceedings.
- [7] M. Yurkov, in these Proceedings.

# OBSERVATION OF FEMTOSECOND BUNCH LENGTH USING A TRANSVERSE DEFLECTING STRUCTURE

Markus Hüning\*, Andy Bolzmann, Holger Schlarb (DESY, Hamburg),  
Josef Frisch, Douglas McCormick, Marc Ross, Tonee Smith (SLAC, Menlo Park, California),  
Jörg Rossbach (Universität Hamburg, Hamburg)

## Abstract

The design of the VUV-FEL at DESY demands bunch lengths in the order of 50 fs and below. For the diagnostic of such very short bunches a transverse deflecting RF structure (LOLA) has been installed which streaks the beam according to the longitudinal distribution. Tests in the VUV-FEL yielded a rich substructure of the bunches. The most pronounced peak in the has a rms length of approximately 50 fs during FEL operation and below 20 fs FWHM at maximum compression. Depending on the transverse focusing a resolution well below 50 fs was achieved.

## INTRODUCTION

To obtain enough gain for the SASE process it is necessary to produce peak currents in the order of 4 kA. With the present setup of the machine this can only be accomplished by compressing part of the bunch to 50 fs. Diagnosing such a short pulse poses a challenge to the beam instrumentation. Therefore a transversely deflecting structure is used to streak the beam.

For this purpose a structure formerly used for particle separation in secondary beams is utilized. It has been used before at SLAC under the name LOLA IV [1]. It is an S-band structure operating at a frequency of 2.856 GHz. Operating the structure close to the zero crossing of the field the bunches acquire no net deflection but are streaked vertically. Using a horizontally deflecting kicker one bunch per pulse is steered onto an OTR-screen. This way it is possible to diagnose parasitically one bunch out of a train of several hundred bunches. At SLAC this structure has been used for the same purpose [2,3,4]

## SETUP

The setup of the VUV-FEL is depicted in figure 1. The electron bunches are created in an RF-gun and then

accelerated in 5 superconducting modules up to presently 450 MeV. Behind the first and the third module there are two bunch compressors used to shape the longitudinal profile of the bunches. The initial bunch length is 1 ps (RMS) which is already long enough to probe the nonlinear rf curvature of the 1.3 GHz L-band cavities. This results in an incomplete compression in the first bunch compressor. The out coming bunch then has two main parts: A very short spike in the head and a tail which resembles the original distribution. The tail however still has an energy correlation imprinted in the first module and reshaped in the bunch compressor. Part of the tail is then compressed in the second bunch compressor to form a short spike with high peak current and good emittance. Depending on the exact phases in the modules #1-#3 the two bunch compressors produce a single or double spike at the exit of the linac. At the end of the acceleration sections, before the collimator system of the undulators, there is the transversely deflecting structure LOLA installed.

The structure is an S-band travelling wave structure. It operates in TE-TM-hybrid mode, so that a combination of electric and magnetic field produces a transverse kick. The maximum equivalent deflecting voltage is 20 MV over a structure length of 3.6 m. The fill-time is 680 ns, so that in a 1 MHz bunch train only one bunch is affected. A downstream OTR screen is utilized to analyse the streak. It is displaced from the centre of the beam pipe so that the beam can pass through. A kicker is used to steer only the bunch in question onto the screen.

To allow for a better synchronization with the master clock, LOLA is tuned to a frequency of 2.856059 GHz, which is an integer multiple of 1/11 of the master clock frequency of 9.027775 MHz. By means of an additional synchronization circuit it is guaranteed that the machine triggers always with a fixed phase relation to this reference [5]. At 9 MHz bunch rate this frequency offset

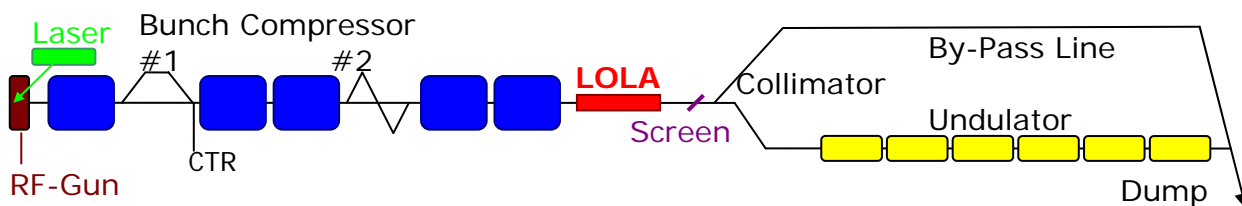


Figure 1: Schematic drawing of the VUV-FEL beam line. At the end of the accelerating section there is the transversely deflecting structure LOLA. It streaks the beam vertically so that on a downstream viewscreen the longitudinal profile of the bunches can be studied.

\*Corresponding author: markus.huening@desy.de

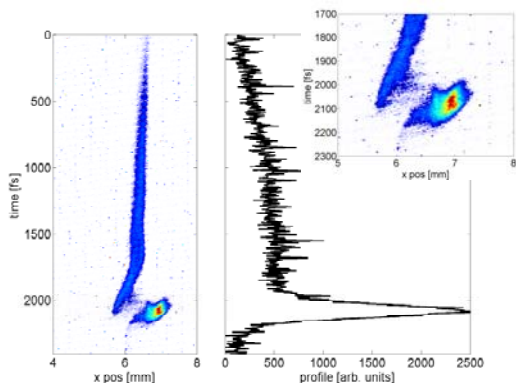


Figure 2: Image of the streaked bunch; inset: zoom on the spike at the head. The streak was approximately 4 fs/px.

results in a phase shift of  $36^\circ$  between neighbouring bunches. This way these bunches would miss the screen and not disturb the measurement.

Because an absolute calibration of the streak based on pure RF measurements did not seem precise enough, one power level was calibrated using the deflection of the beam. The calibration of the other power levels was then scaled according to the relative change of RF power. Relative power levels can be measured much more precisely than absolute levels, so that this method appeared accurate enough. For the calibration a relatively low power level was chosen, allowing for a phase shift of  $\sim 7^\circ$  before the bunch misses the screen. In this way the influence of phase jitter on the calibration is reduced. A streak of 74 pixel/degree or 13.2 fs/pixel was measured. One pixel of the CCD corresponds to  $26 \mu\text{m}$ . A maximum possible streak of 1.8 fs/pixel can be achieved. The optical setup allows for a better resolution than  $26 \mu\text{m}$ .

The beam size at this location is larger, however. The standard beam optics foresee  $200 \mu\text{m}$  spot size (RMS), which would then correspond to a resolution of approximately 15 fs. Unfortunately the spike is also the region of the largest energy spread in the bunch. An energy spread of  $\sim 1 \text{ MeV}$  (RMS) is not uncommon. In

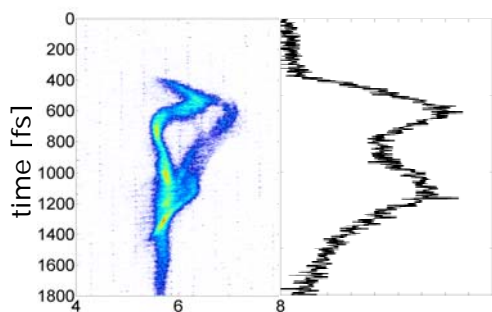


Figure 3: Bunch head with a double peak structure. There is a rich sub-structure of the bunch which shows not only longitudinally but transversely. Note that the streak is opposite to figure 2.

such a case each millimetre of vertical dispersion would contribute with 0.3 fs to above resolution.

## RESULTS

The transverse deflecting structure LOLA has been used to measure the longitudinal bunch profile while the machine was setup for SASE operation. Two examples are given in the figures 2 and 3. While the performance of the FEL was quite similar in the two cases (approximately  $1 \mu\text{J}$  photon pulse), the two profiles differ considerably. Both setups were started from a standard setting defined as follows: The acceleration in the first module was adjusted 6 degrees from the maximum compression phase, which is defined by the maximum of the coherent diffraction radiation at a station closely behind the first bunch compressor (see figure 1). The second and third module are adjusted for on-crest operation so that they do not add considerably to the longitudinal energy distribution. The second bunch compressor then creates the spike necessary for the high peak current at low emittance.

In the first case (figure 2) the module 1 phase was subsequently tuned for less compression, so that no strong peak was produced in the first bunch compressor but only in the second. This would also explain the relatively weak sub-structure of the bunch, because CSR would play a big role only after the second compression stage when it can not influence the longitudinal profile very much.

In the second case (figure 3) the phase was tuned to stronger compression in the first bunch compressor, so that both bunch compressors produce a spike. This results in the double peak structure that can be observed. At the same time there is even more structure to the bunch. This is probably due to wakefield and CSR effects in the first bunch compressor, which can then be translated into a longitudinal modulation in the second compressor stage.

In both cases the width of the peak in the projected profile is measured to be in the order of 120 fs (FWHM). This result however has to be considered preliminary because not all detrimental effects have been considered thoroughly yet. The true width will be smaller than that.

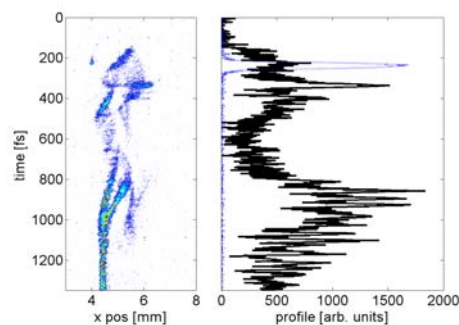


Figure 4: Bunch head with faster streak (2 fs/px) and optimized focusing. The dotted line in the right plot indicates the unstreaked beam size.

For the example in figure 4 the streak was increased and the unstreaked spot optimized for minimum vertical size. Consequently there was no lasing at that time, but the settings were somewhat close to the ones in figure 3. There is much more structure to be seen than in the previous cases. This appears in part enhanced by the lower intensity of the image which causes darker parts to vanish completely.

The effects that concern the most are the entanglement of the vertical and longitudinal structure of the bunch and the vertical dispersion. As can be seen from the figures 2 through 4 there is a strong variation of the horizontal profile along the bunch. This presumably has to be attributed to the two bunch compressors, which deflect horizontally. Nevertheless it can not be excluded that similar effects show vertically. Since the spike carries only a small fraction of the total bunch charge this can not be checked with the un-streaked beam. In this case the charge contained in the tail outshines the head.

A remedy to this problem might be a tomography in the z-y-plane. For this the voltage in the structure would have to be scanned while the change in profile would be recorded. This procedure is in preparation but is not finished yet. Likewise has the dispersion not been measured nor compensated yet.

The LOLA structure can also be used to monitor the jitter of the beam arrival time. This information is of special importance to pump-probe experiments to be performed with external lasers synchronized to the master

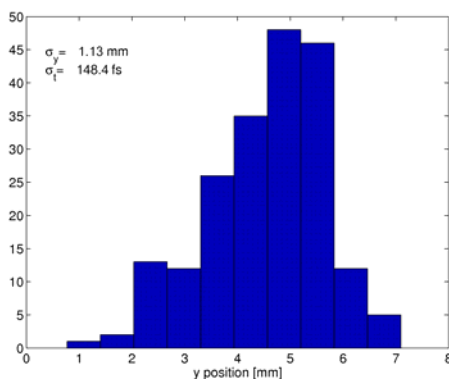


Figure 5: Phase jitter of the beam with respect to LOLA. The jitter due to the high power RF in LOLA is approx. 70 fs.

clock. The figure 5 shows the shot-by-shot jitter of the bunches measured with a BPM close to the viewscreen.

An RMS jitter of 145 fs (RMS) was measured. Note that this is the jitter of the beam with respect to the LOLA RF which can have a jitter by itself. The largest contribution will be the stability of the klystron, which was found to be in the order of 70 fs (RMS). A similar result for the beam jitter was found with electro-optical sampling (EOS) at a nearby diagnostic station [6]. The

main contribution to this timing jitter is expected to be the energy jitter in the first bunch compressor. Evaluation of this jitter delivered compatible results.

## CONCLUSION AND OUTLOOK

A transversely deflecting structure has been successfully applied to the beam in the VUV-FEL at DESY. Although some important contributions to the measurement error are not fully controlled yet, the achieved resolution surpasses most other methods already and it can be used in normal operation of the accelerator.

There are plans to exploit more capabilities of this measurement method as well as measurements of slice-emittances. A first attempt has already been made [7], but for best results tomographic measurements are foreseen.

In view of higher bunch repetition rates at later times and in future projects, shorter structures with a shorter fill-time are being envisioned.

## REFERENCES

- [1] O. H. Altenmueller, R. R. Larsen, and G. A. Loew, *Investigations of Traveling-Wave Separators for the Stanford Two-Mile Linear Accelerator*, The Review of Scientific Instruments, Vol. 35, Number 4, April 1964.
- [2] R. Akre, L. Bentson, P. Emma, P. Krejcik, A *Transverse RF Deflecting Structure for Bunch Length and Phase Space Diagnostics*, proceedings PAC 2001, p. 2353.
- [3] R. Akre et al, *Bunch Length Measurements Using a Transverse Deflecting Structure in the SLAC Linac*, EPAC'02, Paris, France, June 2002.
- [4] P. Krejcik et al, *Commissioning of the SPPS Linac Bunch Compressor*, proceedings PAC 2003, Portland, Oregon
- [5] A. Bolzmann, *Diploma Thesis*, Universität Würzburg
- [6] Bernd Steffen, Sara Casalbuoni, Ernst-Axel Knabbe, Bernhard Schmidt, Peter Schmäser, Axel Winter, *Spectral Decoding Electro Optic Bunch Length and Arrival Time Jitter Measurements at the DESY VUV-FEL*, this proceedings
- [7] Michael Roehrs, Markus Huening, Holger Schlarb, *Measurement of Slice-Emittance using a Transverse Deflecting Structure*, this proceedings

# Measurement of Slice-Emittance using a Transverse Deflecting Structure

Michael Röhrs\*, Andy Bolzmann, Markus Hüning, Katja Honkavaara, Holger Schlarb  
Deutsches Elektronen-Synchrotron DESY, D-22603 Hamburg, Germany

## Abstract

Among the very critical parameters for the operation of the VUV-FEL at DESY are slice emittance and slice Twiss parameters of the current peak in the electron bunch. Conventional tools for measuring the beam size are sensitive to projected properties of the bunch only and hence suffer from mixing of different parts of the bunch. A combination of streaking with a transverse deflecting rf structure and a quadrupole scan allows to measure slice parameters. Indeed the experiment reveals slice Twiss parameters changing gradually along the bunch and a significant increase in slice emittance in the head of the bunch.

## INTRODUCTION

Radiation generated by Free Electron Lasers based on the SASE phenomenon may be emitted only from a small fraction of an accelerated particle bunch. Emittance and charge of the total bunch are therefore not necessarily relevant parameters for the lasing process.

At the VUV-FEL at DESY, where first lasing at 32 nm has been achieved at the beginning of this year [1][2], experiments and simulations show that the bunches have the highest particle density in a spike at the front of the bunch we call the head [4]. The head is assumed to be the source for FEL radiation. For this reason it would be desirable to know the transverse emittance of thin slices of the bunch, especially in the front part. The development of the transverse slice emittance along the bunch would be an important information to understand the machine.

However, the standard methods for transverse emittance measurements are based on the measurement of projected particle distributions which do not allow to consider longitudinal fractions of the bunch separately. These methods may be supplemented by a transverse deflecting cavity, which deflects the particles in e.g. vertical direction depending on their longitudinal position [3]. The measured transverse projections then allow to distinguish longitudinal parts of the bunch and to reconstruct their transverse properties.

## SETUP OF THE EXPERIMENT

The presented experiment is the first one at the VUV-FEL aiming at the measurement of slice properties using a transverse deflecting cavity. The measurement has been performed at the end of the VUV-FEL accelerator at an energy of 445 MeV. The properties of the longitudinal density

profiles originate from two upstream magnetic bunch compressors “BC2” and “BC3” located at the 127 MeV and 380 MeV point of the accelerator, respectively. The particle distributions after compression sensitively depend on their energy distribution and therefore on the acceleration phase in module ACC1. The phase was set to  $-6.5^\circ$ , about  $-4.5^\circ$  from maximum compression. FEL-operation typically takes place between  $-6.5^\circ$  and  $-8^\circ$ . All other modules work on-crest. Using these settings, the longitudinal charge distribution is less distorted so the measurement as well as the evaluation is simplified.

The crucial part of the beamline is sketched in figure 1. The bunches pass a vertically deflecting cavity at zero crossing of the rf phase. This results in changes of the vertical particle momenta which depend linearly on the longitudinal position within the bunch and vanish at the center [3]. The rf power of the cavity is chosen so the main part of each bunch still hits the screen, and is therefore not set to the maximum value. A kicker is installed which deflects single bunches horizontally onto an off-axis OTR monitor. A constant transfer function from the cavity to the screen guarantees that the vertical offsets of the particles at the screen depend only on the kick applied in the cavity and thus on their longitudinal position in the bunch. The device can be calibrated by varying the cavity phase while monitoring the vertical movement of the beam at the screen.

In order to obtain emittance and Twiss parameters of the total bunch as well as of single slices, a quadrupole scan

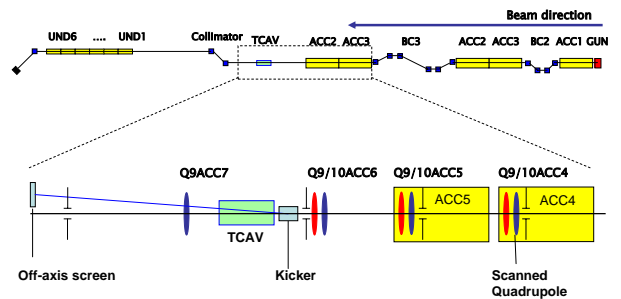


Figure 1: Sketch of the VUV-FEL beam line and the part used for the experiment. The beam passes a transverse deflecting cavity (TCAV) streaking it vertically and gets horizontally deflected by a kicker onto an off-axis OTR monitor. The Quadrupole Q9ACC4 is used for scanning.

\* michael.roehrs@desy.de

has been performed using the Quadrupole Q9ACC4 shown in figure 1. For each quadrupole current, ten bunch images have been taken to determine the average horizontal widths. To remove camera artefacts, an average background has been subtracted from the beam images. The transfer functions from the scanned quadrupole to the screen have been measured using steerers and beam position monitors to exclude large systematic errors.

## RESULTS

Figure 2 shows the image of a vertically streaked bunch on the OTR monitor. The dense head of the bunch (top) and the long trailing tail are clearly visible. A zoom into the head reveals a substructure characterized by horizontal offsets of the slice centroids. The tail appears to be nearly homogenous.

The conversion factor from vertical position on the monitor to time is  $16.6 \text{ fs / pixel}$ , the pixel width being  $27 \mu\text{m}$ . Using this conversion, the longitudinal charge density profiles can be obtained (figure 5). The spike at the front of the bunch contains roughly  $0.23\%$  of the total bunch charge of  $1 \text{ nC}$  and has a width of  $132.8 \pm 8.3 \text{ fs}$ . These values are both resolution limited, the resolution being determined by the vertical slice sizes. The images used for this evaluation have been taken with identical quadrupole settings and show the smallest spike width. Nevertheless, the given values are upper limits for the true ones.

Figure 3 shows the measured horizontal rms sizes of the total bunch during the quadrupole scan. Using the transfer matrices from the scanned quadrupole to the screen, bunch emittance and bunch Twiss parameters have been reconstructed by a least square fit method [5]. We have obtained a normalized horizontal emittance of  $8.04 \pm 2.81 \mu\text{m}$  (systematic error, see section “Error analysis”), and initial hor-

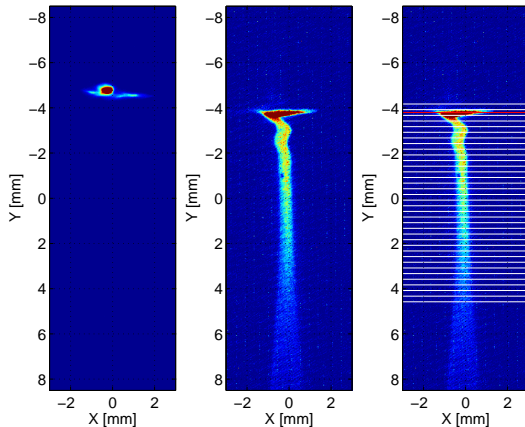


Figure 2: The monitor image on the left hand side shows a bunch without streak, the one in the middle a vertically streaked bunch. The head of the bunch is at the top. In the picture on the right the edges of the horizontal slices are drawn in. The reference point for slicing is the peak value in the vertical density profile (red line).

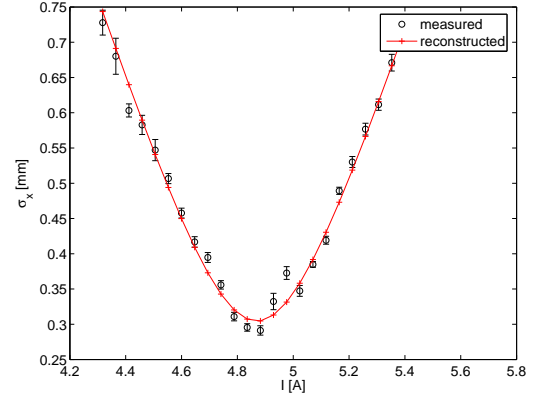


Figure 3: Measured and reconstructed horizontal bunch sizes for different quadrupole currents.

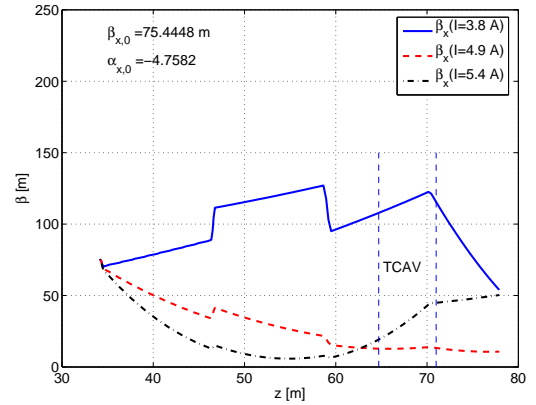


Figure 4: Reconstructed beta function of the total bunch for different quadrupole currents

izontal Twiss parameters  $\beta_x = 75.44 \pm 1.24 \pm 1.98 \text{ m}$  and  $\alpha_x = -4.76 \pm 0.08 \pm 0.65$  (statistical and systematic errors, respectively).

In order to determine slice parameters, the images of the streaked bunches have been subdivided into horizontal slices of  $0.25 \text{ mm}$  or  $154 \text{ fs}$  width each (figure 2). The peak value in the vertical profile has been used as reference in each image to correct for cavity phase jitter. From the horizontal rms sizes of these slices, slice emittance and slice Twiss parameters upstream of the scanned quadrupole can be reconstructed just as for the entire bunch.

Figure 6 shows that the resulting normalized slice emittance takes nearly constant values of roughly  $4.0 \mu\text{m}$  in the tail of the bunch and rises strongly up to  $11 \mu\text{m}$  in the head. The slice having the peak current has an emittance of roughly  $7.5 \mu\text{m}$ . The number of particles in the slice at the very front of the bunch which has the largest emittance value is clearly smaller than in most other slices and depends strongly on the vertical beta function of the head.

Restriction to the  $90\%$  - core of the horizontal profiles yields normalized emittances ranging from  $1.5 \mu\text{m}$  in the tail up to  $6.3 \mu\text{m}$  in the head. The  $90\%$  - value for the slice having the peak current is  $4.1 \mu\text{m}$ , the one of the total bunch

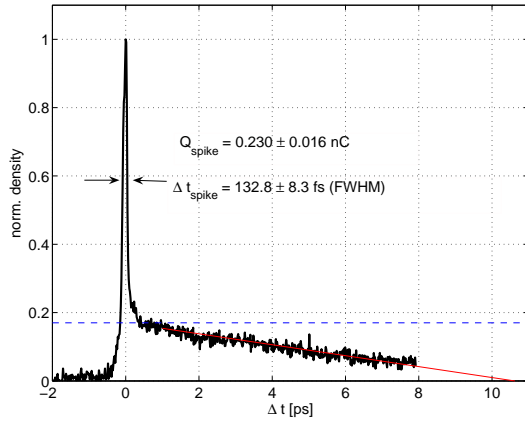


Figure 5: Measured longitudinal density profile. The charge density is normalized to its peak value. The region with densities larger than the threshold given by the dashed blue line defines the spike. The red line is a simple approximation for the part of the bunch that didn't hit the monitor.

4.0  $\mu\text{m}$ . All given values of course depend to a certain extent on the choice for the slice boundaries, especially in the front region.

The observed increase in slice emittance in the bunch head may have two different causes. The first one is a true increase in slice emittance. Slice emittance growth in the peak current region may originate from stronger nonlinear forces, especially due to space charge and coherent synchrotron radiation. There may also be a larger residual slice energy spread which effects the distribution of the transverse momenta at the horizontal kicker and thus the slice emittance. But since the slice energy spread is expected to be clearly smaller than 1% even for slices in the head [4], this is probably not a strong effect.

The second possible cause is an increase solely in projected emittance, since the slice width is finite. The observed slice centroid shifts in the head (figure 2) suggest that this effect largely contributes to the measured slice emittance in the front region.

The mismatch parameter  $B$  [5] of the slice Twiss parameters with respect to the Twiss parameters of the total bunch varies slightly in the range from  $B=1$  to  $B=1.5$  (figure 6). At the same time the mismatch phase  $\Theta_x$  [6] gradually decreases along the bunch from  $150^\circ$  in the head down to  $0^\circ$ . This indicates that the transfer functions for the single slices along the accelerator are different from each other, most likely because of chromaticity.

## ERROR ANALYSIS

Monte Carlo simulations have been performed in order to determine systematic errors caused by deviations of the integrated quadrupole gradients and the energy. We assumed a homogenous distribution of the integrated quadrupole gradients between  $\pm 3\%$  of the measured value, and a gaussian energy distribution with 2% standard deviation.

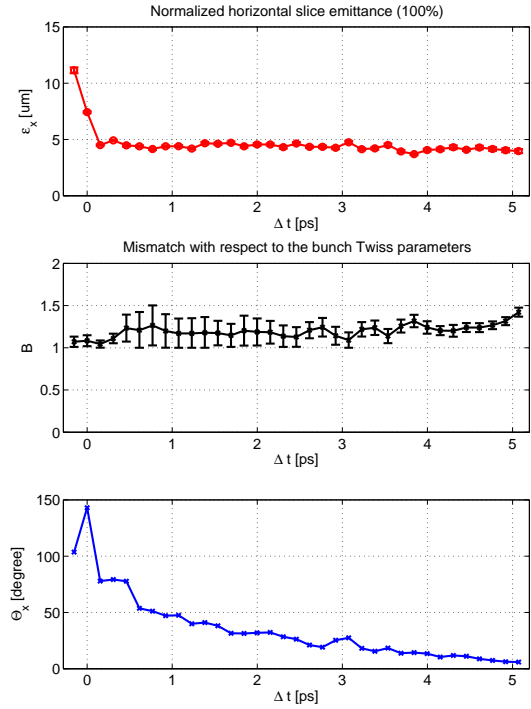


Figure 6: Horizontal slice emittance  $\epsilon_x$ , mismatch parameter  $B$  and mismatch phase  $\Theta_x$  along the bunch.  $\Delta t = 0$  refers to the peak density in the vertical profile. Mismatch parameter and phase are calculated with respect to the Twiss parameters of the total bunch. The error bars refer to statistical errors only.

tion.

We have found that the systematic errors of the mismatch parameters, the mismatch phases and the slice emittance ratios are neglectable compared to their statistical errors.

In case of the absolute emittance values the systematic error is about 35% (figure 8). It is also the dominating error of the reconstructed Twiss parameters. These deviations are mainly caused by errors of the integrated quadrupole gradients. They are rather large since there are seven quadrupoles with partly high gradients in the beamline and beta values up to 130  $m$ .

Chromaticity may effect the ratios of the slice emittance values and the mismatch parameters. A systematic correction of chromaticity requires a measurement of the energy distribution along the bunch, which unfortunately has not been done for this measurement. But assuming a residual correlated energy spread of less than 1% [4], the effect should be within the range of statistical errors.

The longitudinal resolution is mainly determined by the vertical size of the slices at the monitor. To estimate the vertical slice sizes, a scan of the same quadrupole has been performed without streaking the bunch. The measured vertical rms sizes of the total beam are presented in figure 7. The values range from  $160\mu\text{m}$  to  $340\mu\text{m}$ . The chosen vertical slice width is within the range of these values. This suggests that the dominating part of the particles in each

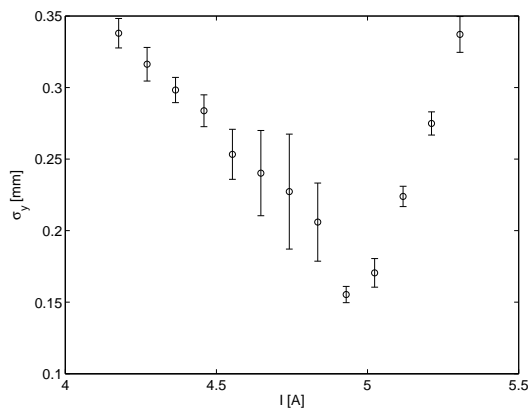


Figure 7: Measured vertical bunch sizes for different quadrupole currents.

vertical slice really is located in the assigned longitudinal slice. However, in case of strong variations of the longitudinal charge density, as e.g. in the region of the head of the bunch, this need not be the case.

## OUTLOOK

It is planned to repeat the measurement with a different optics. Thereby the intention is to scan multiple quadrupoles simultaneously in such a way, that a constant and small vertical beta function at the screen is guaranteed. This would improve the resolution.

The error analysis has shown that quadrupole gradient errors have a strong effect on the measurement. The goal is to determine the integrated quadrupole gradients as well as the beam energy with an accuracy of about 1%. To reduce the influence of these errors on the results, an optics with minimal horizontal beta values at the quadrupoles is to be worked out.

A variation of the vertical streak of the bunches may allow to reconstruct the particle distribution in the  $(y, z)$  - plane by tomography. The particle distribution could then be used to calculate the vertical slice emittances. Moreover, a calculation of the overlap of the projections of the slices and a corresponding correction of the horizontal slice widths may be possible.

## REFERENCES

- [1] S. Schreiber, "First Lasing at 32 nm of the VUV-FEL at DESY", this conference.
- [2] B. Faatz, "First Results from the VUV-FEL at DESY", PAC05, May 2005, Knoxville
- [3] M. Huening et al., "Observation of Femtosecond Bunch Length Using a Transverse Deflecting Structure", this conference
- [4] Y. Kim, "Commissioning of TTF2", PAC05, May 2005, Knoxville
- [5] M.G. Minty, F. Zimmermann, "Measurement and Control of Charged Particle Beams", Springer 2003

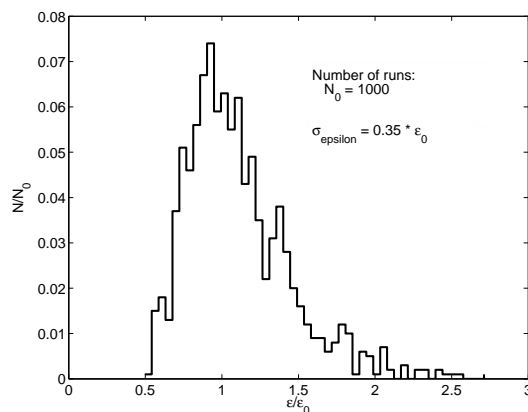


Figure 8: Result of a Monte Carlo simulation for the reconstruction of the emittance with random quadrupole strengths as specified in the text. The emittance values  $\epsilon$  are normalized to the value  $\epsilon_0$  obtained for the default quadrupole strengths.

- [6] M. Sands, "A Beta mismatch parameter", SLAC-AP-085, 1985.

# THE INJECTOR OF THE VUV-FEL AT DESY

S. Schreiber\*, DESY, Hamburg, Germany  
for the VUV-FEL team†

## Abstract

The VUV-FEL is a free electron laser user facility being commissioned at DESY in Hamburg. In the current configuration, the linac accelerates an electron beam up to 730 MeV. The injector is a crucial part of the linac, since it has to generate and maintain a high brightness electron beam required for SASE operation. The injector includes a laser driven RF gun, a booster section, a bunch compressor, and diagnostic sections. The good performance of the injector was crucial for the first lasing of the VUV-FEL at a wavelength of 32 nm in January 2005. We report on the present layout of the injector, the properties of the electron beam and on upgrade plans scheduled in the near future.

## INTRODUCTION

For the VUV-FEL project at the TESLA Test Facility (TTF) at DESY, the properties of the electron beam are of prime importance. The first user facility for VUV and soft X-ray coherent light provides impressive peak and average brilliance. This is only possible with a beam perfectly matched to the requirements to drive the SASE process in a single pass high gain FEL.

The basic injector concept, a laser driven RF gun with a booster, has already been successfully used in the TTF phase 1 FEL providing beam until end 2002 for user experiments in the wavelength range of 80 to 120 nm.

Drawbacks of the first design motivated a redesign [1] to meet the demands for the goals of phase 2, the lasing down to a wavelength of 6 nm. There are two major changes in the design: the booster is extended so that an energy of more than 100 MeV is reached, and a third harmonic cavity is included to correct non-linearities in the phase-energy phase space. In addition, an extended diagnostic section after the first bunch compressor has been included. The installation of the new injector has been completed in February 2004, with the exception of the third harmonic cavity. Its installation is foreseen in 2006.

The development of major components like the laser system, the RF gun, and the cathodes are performed at the photoinjector test facility PITZ. The advantage is, that well understood equipment is installed at the VUV-FEL and further R&D does not hamper the VUV-FEL runs.

The RF gun system has been commissioned at PITZ where with a full characterization of the system, an optimal working point for smallest transverse emittance has been determined [2, 3]. After the installation at TTF, only the solenoid current had to be slightly adjusted to match the beam into the booster section.

With the well commissioned injector, first lasing at a wavelength of 32 nm has been achieved in January 2005. See [4] and [5] for details.

## THE INJECTOR CONCEPT

Figure 1 gives a schematic overview of the present configuration, Fig. 2 shows a view from the RF gun down the accelerator. Table 1 summarizes main parameters.

The injector is based on a laser-driven photocathode RF gun and a booster section. The main goal is to achieve a transverse emittance smaller than 2 mm mrad for a charge of 1 nC. The working point is chosen such, that space charge induced emittance growth is as much reduced as possible. The RF gun design realizes a perfect symmetric field to reduce RF induced emittance growth. Since the transverse emittance scales with the laser spot size on the cathode, the reduction of space charge is realized choosing an initially long bunch (2 mm). The matching into the booster and the choice of accelerating gradients are such, that the transverse emittance is not only kept small, but is also damped to some extent (see [6] for details).

The bunch is compressed using magnetic chicane bunch compressors. The peak current of the uncompressed bunch of about 70 A is increased to more than 2 kA. The compression requires an energy chirp along the bunch which is generated by off crest acceleration. The compression is

\* siegfried.schreiber@desy.de

† W. Achermann, V. Ayvazyan, N. Baboi, J. Bähr, V. Balandin, B. Beutner, A. Brandt, I. Bohnet, A. Bolzmann, R. Brinkmann, O.I. Brovko, J.P. Carneiro, S. Casalbuoni, M. Castellano, P. Castro, L. Catani, E. Chiodroni, S. Choroba, A. Cianchi, H. Delsim-Hashemi, G. Di Pirro, M. Dohlus, S. Düsterer, H.T. Edwards, B. Faatz, A.A. Fateev, J. Feldhaus, K. Flöttmann, J. Frisch, L. Fröhlich, T. Garvey, U. Gensch, N. Golubeva, H.-J. Grabosch, B. Grigoryan, O. Grimm, U. Hahn, J.H. Han, M. v. Hartrott, K. Honkavaara, M. Hüning, R. Ischebeck, E. Jaeschke, M. Jablonka, R. Kammering, V. Katalev, B. Keitel, S. Khodyachyhh, Y. Kim, V. Kocharyan, M. Körfer, M. Kollwe, D. Kostin, D. Krämer, M. Krassilnikov, G. Kube, L. Lilje, T. Limberg, D. Lipka, S. Liu, F. Löhler, M. Luong, C. Magne, J. Menzel, P. Michelato, V. Miltchev, M. Minty, W.D. Möller, L. Monaco, W. Müller, M. Nagl, O. Napoly, P. Nicolosi, D. Nölle, T. Nuñez, A. Oppelt, C. Pagani, R. Paparella, B. Petersen, B. Petrosyan, J. Pflüger, P. Piot, E. Plönjes, L. Poletto, D. Proch, D. Pugachov, K. Rehlich, D. Richter, S. Riemann, J. Rönsch, M. Ross, J. Rossbach, M. Sachwitz, E.L. Saldin, W. Sandner, H. Schlarb, B. Schmidt, M. Schmitz, P. Schmüser, J.R. Schneider, E.A. Schneidmiller, S. Schnepf, H.-J. Schreiber, S. Schreiber, D. Sertore, S. Setzer, A.V. Shabunov, S. Simrock, E. Sombrowski, L. Staykov, B. Steffen, F. Stephan, F. Stulle, K.P. Sytchev, H. Thom, K. Tiedtke, M. Tischer, R. Treusch, D. Trines, I. Tsakov, A. Vardanyan, R. Wanzenberg, T. Weiland, H. Weise, M. Wendt, I. Will, A. Winter, K. Wittenburg, M.V. Yurkov, I. Zagorodnov, P. Zambolin, K. Zapfe

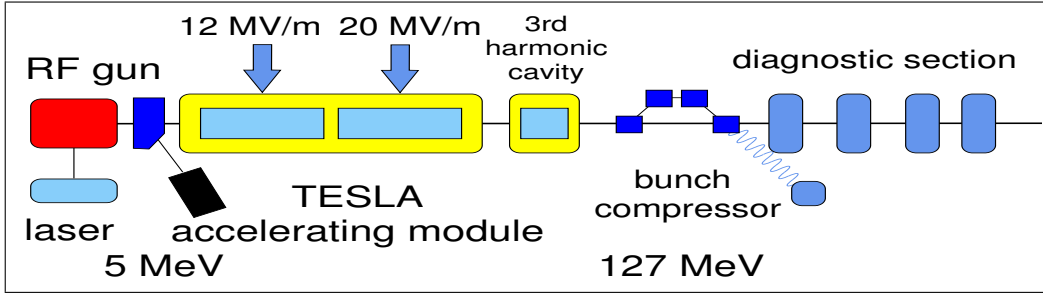


Figure 1: Schematic overview of the TTF VUV-FEL injector (not to scale). Beam direction is from left to right, the total length is 30 m. The third harmonic cavity is not installed yet.

Table 1: Present operating parameters of the VUV-FEL injector at start-up.

RF frequency	GHz	1.3
Energy	MeV	127
Bunch charge	nC	0.5 - 1.0
Nb. of bunches/train		30
Bunch train length	ms	0.03
Rep. rate	Hz	2
Laser spot size (rms)	mm	0.6
RF gun phase*	°	38
Acc. module phase**	°	-8
Emittance, norm. (x,y)	$\mu\text{m rad}$	1.4
Bunch length (rms, uncompressed)	mm	1.7
Spike length (rms, compressed)	$\mu\text{m}$	50
Uncorrelated energy spread	keV	< 25
$\Delta E/E$ (rms)	%	0.02

\* in respect to zero crossing

\*\* in respect to on crest



Figure 2: View of the VUV-FEL injector from the RF gun down the accelerator. The RF gun is inside the blue solenoids in the foreground. The yellow cryostat is the TESLA module used as a booster.

done in two steps at energies of 127 MeV and 370 MeV in order to avoid an unacceptable emittance growth due to space charge, wakefield, and coherent synchrotron radia-

tion effects.

Accelerating a bunch which is long in respect to the RF wavelength (a few degrees of RF phase) leads to a curvature in the energy-phase plane. This curvature can be removed by a third harmonic cavity following the accelerating section. A superconducting third harmonic cavity is under construction [7]. For the start-up phase, emphasis is on lasing at 30 nm which can be obtained similar to TTF1 by tailoring the longitudinal structure of the electron beam to produce a spike with the required peak current. See [8] for details.

## THE RF GUN AND BOOSTER

The RF gun is a 1.5 cell L-band cavity (1.3 GHz,  $\text{TM}_{010}$  mode) powered by a 5 MW klystron. To keep a perfect symmetry of the RF field, the gun is equipped with a longitudinal RF coupler. Moreover, it has no probes or tuning paddles which may distort the RF field. The gun is tuned by fine adjusting its temperature. The water cooling system is able to cope with an average RF power of 50 kW. During operation when the load on the gun is constant, the cooling system stabilizes the temperature to 0.05°C.

The RF gun is operated with a forward power of 3.1 MW yielding an accelerating field on the cathode of 41 MV/m. During the start-up phase of the VUV-FEL where a high repetition rate and long bunch trains are not required, the gun is operated at 2 Hz and an RF pulse length of 100  $\mu\text{s}$ . During the commissioning at PITZ and TTF [9], the gun has been operated up to 10 Hz with an RF power of 3 MW and an RF pulse length of up to 0.9 ms (27 kW average power).

The forward and reflected power is measured with a DSP based system enabling a low level control of the RF power. The forward power is stabilized to 0.1 % (rms), the phase stability achieved is better than 0.5° (rms).

We use a  $\text{Cs}_2\text{Te}$  photocathode which is inserted via a load-lock system to the back of the half cell. The quantum efficiency of the cathodes is initially high (in the order of 5-9 %) [10] and decreases slowly over several month to about 1 %.

A solenoid (0.163 T) focuses and matches the beam to the booster section. A bucking coil compensates the remnant magnetic field on the cathode surface to zero.

The booster accelerates the beam to 127 MeV. It is a TESLA module with eight 9-cell superconducting 1.3 GHz cavities. To avoid strong transverse focusing, the gradient of the first four cavities is chosen with 12 MV/m moderate. It is the optimum according to the emittance damping scheme. The last four cavities are operated with higher gradients, 19 MV/m in average. The module is powered by one 5 MW klystron. The RF power is split with a hybrid/phase-shifter combination.

## THE LASER SYSTEM

The laser is based on a Nd:YLF mode-locked pulse train oscillator synchronized to the 1.3 GHz RF of the accelerator. The diode pumped pulse train oscillator is operated at 27 MHz. Pockels cell based pulse pickers running at 1 MHz prepare the pulse train required for the VUV-FEL operation. The system is designed to produce pulse trains with up to 800  $\mu$ s length. The pulse spacing is usually 1  $\mu$ s (1 MHz), a 9 MHz mode is in preparation. The pulse train is amplified with a linear chain of amplifiers, two stages are pumped with laser diodes [11], the last two with flash-lamps. A system entirely pumped with laser diodes has been set-up and is being commissioned at PITZ.

The infrared wavelength of the laser is converted into the UV (262 nm) with two non-linear crystals (LBO and BBO). The beam is transported to the RF gun with an imaging system. Movable mirrors allow to control the position of the laser spot on the cathode. The last mirror is mounted in a vacuum chamber close to the gun and reflects the beam onto the cathode under a small angle (1.7°). To avoid charging up, and to avoid wakefield effects on the electron beam, the mirror is fabricated out of pure aluminum.

The temperature in the laser room is stabilized to 0.1 °C to reduce drifts as much as possible. The rms charge fluctuation measured after the RF gun is 2 % shot to shot, averaged over the pulse train 1 % (rms). The longitudinal pulse shape is gaussian, the pulses length measured with a streak camera is  $\sigma_L = 4.4 \pm 0.1$  ps (at 262 nm). The transverse laser pulse shape has a clipped gaussian shape with an homogeneity of about 20 %. Techniques to produce flat-hat transverse and longitudinal shapes with improved homogeneity are under development at PITZ [12].

## MEASUREMENT OF BASIC BEAM PARAMETERS

### *Energy and Energy Spread*

Directly after the RF gun, the beam momentum is measured in a dispersive section. The measured beam momentum as a function of the accelerating RF field in the gun agrees well with the expectation from simulations. For instance, for an RF power of 3 MW the momentum amounts to 4.7 MeV/c. After acceleration to 127 MeV, the energy and energy spread are measured in the dispersive section of the first bunch compressor using a view screen (optical transition radiation). Due to the initial long bunch length

of 1.7 mm, the beam shows a sharp core and a long energy tail. The width of the core is smaller than 25 keV (rms) and is a good estimate of the uncorrelated energy spread. A small uncorrelated energy spread is important for the development of a sharp temporal spike after the compression stage. The correlated energy spread could not be measured at the RF gun. Since the phase for minimum energy spread after acceleration in the booster is only 2° in phase away from the maximum energy gain, we conclude that the correlated energy spread is small.

With the low level RF feedback system regulating the phase and amplitude of the accelerating structures, the energy stability is measured to be  $dE/E = 2.6 \cdot 10^{-4}$  (rms). We also see drifts of the energy in the order of 0.08 %. These drifts are mainly due to temperature drifts in the electronics and cables. An improvement of the temperature stabilization is in preparation.

### *Emittance*

The emittance is evaluated from the beam sizes measured on four screens embedded in a FODO lattice. Digital CCD cameras record the optical transition radiation generated by the electron beam on the screens (silicon wafers with an Al coating). The resolution achieved is 10  $\mu$ m [13].

Fig. 3 shows the horizontal and vertical normalized transverse rms emittance measured at 127 MeV for a bunch charge of 1 nC repeated several times within 75 min. Two different methods are used to calculate the emittance (see [14] for details). The true rms emittance is calculated from the full and from 90 % of the intensity. A tomographic technique is also applied, which reconstructs the phase space. The tomographic method agrees well with the pure rms calculation.

In the example shown, the 90 % rms emittance 1.6 mm mrad. The data also show, that the emittance is maintained stable over a long time period, actually much longer than the measurement period in this example. Retuning of the injector is required only after major shut-downs. The rms fluctuation of the emittance is about 2 to 3 %. This corresponds to the statistical error of the measurements. The systematic error is estimated with 6 % mainly due to calibration error of the quadrupole fields and the uncertainty of the beam energy. With more data collected over the last months of running time, the geometrical average of the horizontal and vertical emittance is 1.4 mm mrad [15], with the measurement errors given above.

### *Bunchlength*

The uncompressed bunch is measured with a streak camera (Hamamatsu FESCA-200) using synchrotron radiation emitted by the last magnet of the first bunch compressor at 127 MeV. The length is  $1.7 \pm 0.2$  mm (rms) as expected. In the case of fully compression, the leading spike is expected to have a width in the order of 100 fs. Being close

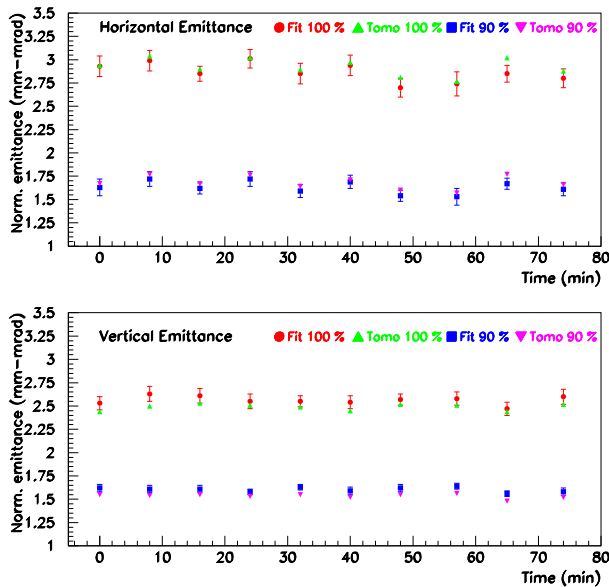


Figure 3: Transverse rms emittance measured at 127 MeV for a bunch charge of 1 nC repeated several times within 75 min. [13] Horizontal and vertical projected emittances are shown analyzed with two different methods (see [14] for details): the true rms calculated from the full and from 90 % of the intensity, and calculated using a tomographic technique.

to the resolution of the camera (100 fs rms), wavelength filters are required to reduce dispersion effects which reduce the number of photons reaching the camera. Currently, we work on the improvement of the photon yield of the synchrotron radiation beamline.

A deflecting cavity [16] is used after acceleration at 445 MeV to streak the electron beam. The streaked beam is measured with a view screen. The deflecting cavity provides a better signal to noise ratio and a better resolution of 10 to 50 fs (depending on the focusing of the beam). The compressed bunch shows the expected longitudinal bunch structure: a leading spike with a width of 120 fs (fwhm) and a long tail of 2 ps. See [17] for details.

The deflecting cavity has also been used to measure the emittance of a longitudinal slice of the beam. The data are still preliminary, They indicate, that the emittance is constant along the tail and increases at the high current spike.

Additional methods to measure the bunch length with interferometers and electro-optical sampling techniques are described in [18, 19].

## CONCLUSION

The injector of the VUV-FEL has been successfully commissioned in 2004 and brought into operation summer 2004. The projected beam parameters are well understood, a good working point in terms of small emittance and short bunches has been established. First measurements of the temporal structure after compression and the slice emittance

have been started. The excellent performance of the injector have been the bases for the first lasing at a wavelength of 32 nm.

## ACKNOWLEDGMENT

On behalf of the VUV-FEL group, I would like to thank all colleagues from DESY and the collaborating institutes for their enthusiastic commitment in the construction and installation of the VUV-FEL injector.

## REFERENCES

- [1] K. Flöttmann, P. Piot, "An upgraded injector for the TTF FEL-user facility," *Proc. EPAC 2002, Paris, 3-7 Jun 2002*
- [2] M. Krasilnikov *et al.*, "Optimizing the PITZ electron source for the VUV-FEL," DESY-M-04-03U, *Proc. EPAC 2004, Lucerne, 5-9 Jul 2004*
- [3] S. Schreiber, "Commissioning of the VUV-FEL injector at TTF," EPAC-2004-MOPKF022, *Proc. EPAC 2004, Lucerne, 5-9 Jul 2004*
- [4] S. Schreiber, "First Lasing at 32 nm of the VUV-FEL at DESY", these proceedings, FEL-2005-MOOB002.
- [5] V. Ayvazian *et al.*, "First operation of a Free-Electron Laser generating GW power radiation at 32 nm wavelength", submitted to Eur. Phys. J. D.
- [6] Y. Kim *et al.*, these proceedings, FEL-2005-THPP037
- [7] In cooperation between FNAL and DESY. See J. Sekutowicz *et al.*, DESY-TESLA-FEL-2002-05 for details on the design.
- [8] E. L. Saldin, E. A. Schneidmiller and M. V. Yurkov, DESY-TESLA-FEL-2004-06
- [9] J. Bähr *et al.*, DESY-TESLA-2003-33
- [10] S. Schreiber *et al.*, EPAC-2004-MOPKF021, *Proc. EPAC 2004, Lucerne, 5-9 Jul 2004*
- [11] I. Will *et al.*, Nucl. Instrum. Meth. A **541** (2005) 467
- [12] J. Bähr *et al.*, these proceedings, FEL-2005-MOPP034
- [13] K. Honkavaara *et al.*, DIPAC-2005-POM021, Proc. DIPAC 2005, Lyon, France, June 6-8, 2005
- [14] F. Löhl, "Measurements of the transverse emittance at the VUV-FEL", DESY-THESIS 2005-014 and TESLA-FEL 2005-03, Diploma Thesis, Hamburg University, 2005.
- [15] K. Honkavaara *et al.*, these proceedings, FEL-2005-WEOB001
- [16] The deflecting cavity project is a cooperation between SLAC and DESY.
- [17] M. Hüning *et al.*, these proceedings, FEL-2005-THPP035
- [18] L. Fröhlich, O. Grimm, these proceedings, FEL-2005-MOPP035
- [19] B. Steffen *et al.*, these proceedings, FEL-2005-THPP039

# Spectral decoding electro-optic measurements for longitudinal bunch diagnostics at the DESY VUV-FEL

B. Steffen\*, S. Casalbuoni, E.-A. Knabbe, B. Schmidt (DESY, Hamburg),  
P. Schmüser, A. Winter (Univ. Hamburg)

## Abstract

For the operation of a SASE FEL, the longitudinal bunch profile is one of the most critical parameters. At the superconducting linac of the VUV-FEL at DESY, an electro-optic spectral decoding (EOSD) experiment is installed to probe the time structure of the electric field of the bunches to better than 200 fs rms. The field induced birefringence of a ZnTe crystal is detected by TiSa laser pulses that are frequency chirped to  $\approx 2$  ps. The time structure is encoded on the wavelength spectrum of the chirped TiSa pulse. First results on the bunch length as function of the linac parameters and on time jitter measurements are presented.

## INTRODUCTION

Bunch length measurements in the 100 femtosecond regime are of high interest for VUV and X ray free electron lasers. The electro-optical technique provides the possibility to measure the longitudinal charge distribution with very high resolution, determined by the dispersion of the electric field pulse in the nonlinear optical crystal, the frequency bandwidth of the optical laser pulse, and the relative time jitter between electron bunch and laser pulse. At DESY, a titanium-sapphire (Ti:Sa) laser of 50 nm bandwidth is used to determine the birefringence which is induced in a nonlinear electro-optical crystal by the co-moving electric field of a relativistic electron bunch. In the EO crystal, the initial linear polarization of the laser pulse is converted into a slightly elliptical polarization which is then converted into an intensity modulation. Previous accelerator-related EO spectral decoding experiments have been carried out at the infrared free electron laser FELIX [1, 2].

## EXPERIMENTAL SETUP

The Ti:Sa laser has a minimum pulse width of 25 fs (FWHM), a central wavelength of 805 nm and a bandwidth of 50 nm. It is mounted on a vibration-damped optical table outside the tunnel. The pulse is stretched by a SF11 prism stretcher, resulting in a linearly chirped pulse of about 2 ps length (FWHM), and then guided into the linac tunnel by a 20 m long optical transfer line equipped with four mirrors and two lenses ( $f = 4$  m) which image the Ti:Sa laser onto a 300  $\mu\text{m}$  thick ZnTe crystal in the linac beampipe.

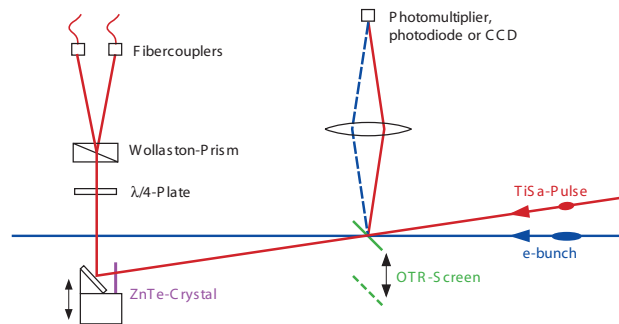


Figure 1: Schematic of the EO setup. An OTR screen can be moved into the e-beam to adjust the relative timing between the laser pulses and the electron bunches with  $\approx 200$  ps precision using a PMT or a photodiode.

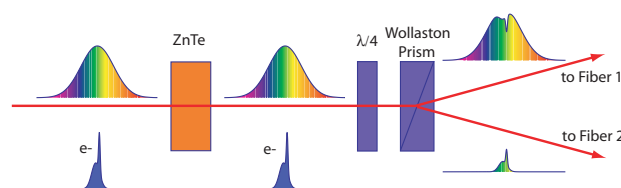


Figure 2: Simplified scheme of the EO spectral decoding. The laser and the field of the bunch are polarized horizontally, parallel to the  $(-1,1,0)$  axis of the ZnTe crystal. The Wollaston prism acts as crossed polarizer for the laser beam coupled into fiber 2.

Inside the linac tunnel an optical table is installed which holds the beampipe and the detector optics (see Fig. 1). A spherical mirror ( $f = 1$  m) focuses the laser on the ZnTe crystal. The laser beam is injected into the beampipe at an angle of  $6^\circ$  with respect to the e-beam. Thereby we avoid a mirror upstream of the crystal which might produce wakefields. Behind the crystal a mirror reflects the laser beam to the detector optics outside the vacuum chamber. An optical transition radiation (OTR) screen can be moved into the e-beam to adjust the relative timing between the laser pulses and the electron bunches with approx. 200 ps precision before starting an EO measurement.

A simplified view of the signal detection scheme is shown in figure 2. ZnTe is optically isotropic at vanishing field but acquires a birefringence in the presence of a strong electric field. The crystal is cut in the (110) plane with the crystallographic  $(-1,1,0)$  axis oriented horizontally. The electric field of the bunch and the Ti:Sa pulse

\* email: bernd.steffen@desy.de

are both polarized horizontally. The induced birefringence can be described by a refractive index ellipse whose large axis is rotated by  $45^\circ$  with respect to the horizontal axis. In the crystal, the laser polarization components along the two main axes of the index ellipse acquire a phase shift difference of  $\Gamma \propto r_{41}E_e$  where  $r_{41}$  is the electro optical coefficient of ZnTe and  $E_e$  the electric field of the bunch. Behind the ZnTe crystal the laser pulse will then be elliptically polarized. To measure this ellipticity a Wollaston prism is used as a polarizing beam splitter. The horizontal polarization component is coupled into fiber 1, the vertical (crossed) polarization component into fiber 2 (see figure 2). The quarter wave plate serves the only purpose to compensate the small intrinsic birefringence of the ZnTe crystal. The multimode fibers guide the two polarization components to a spectrometer (SpectraPro 150) located outside the linac tunnel. The image of the spectrum is recorded with a gated intensified camera (Andor DH720-18F). Single shot spectra of individual bunches can be taken with a repetition rate of up to 60 Hz. In the case of temporal overlap between the laser pulse and the electron bunch, the temporal profile of the electron bunch is encoded on the spectrum of the laser pulse from fiber 2, while the spectrum from fiber 1 can be used for normalization. Without temporal overlap no signal is transmitted into fiber 2.

## TEMPORAL RESOLUTION

The time resolution of the EOSD method is determined by [3]:

- the material and thickness of the electro-optical crystal. The lower limit for a  $300 \mu\text{m}$  thick ZnTe crystal was calculated to be approx. 250 fs (FWHM) [4].
- the bandwidth-limited length of the laser pulse  $\tau_0 = 25$  fs and the length  $\tau_c = 2$  ps to which it is stretched. For bunch lengths shorter than  $(\tau_0\tau_c)^{1/2} \approx 245$  fs (FWHM) the measured profile will be broadened and/or distorted [5].
- the distance  $r = 12$  mm from the electron beam to the EO crystal,  $\Delta t_d \approx 2r/\gamma_c \approx 90$  fs (rms) [6].
- the resolution of the spectrometer and camera which contributes about 40 fs.

The resulting total resolution is 400 fs (FWHM) or 175 fs (rms), which is approximately the same as the shortest peaks seen in the measurements presented here. Measurements with increased resolution using a thinner crystal and a laser with larger bandwidth are currently prepared.

The arrival time of the bunch at the EO crystal can in principle be measured to better than one quarter of the resolution ( $> 50$  fs), additionally the time jitter of the synchronization between the laser and the 1.3 GHz linac master oscillator of approx. 70 fs (rms) has to be taken into account [7].

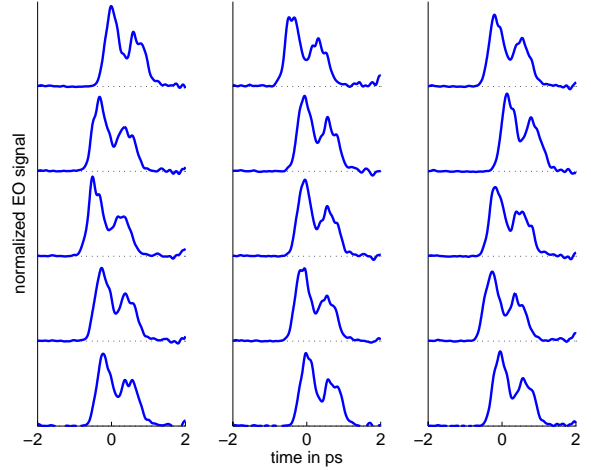


Figure 3: Single shot measurements of 15 consecutive bunches. The leading edge of the bunch is on the left.

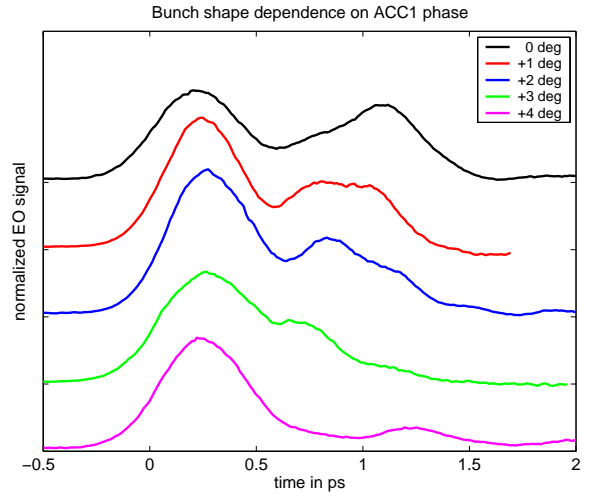


Figure 4: Measurement of the bunch field for different settings of the phase in the first accelerating module. Each line represents the average of 100 normalized and time jitter corrected single shot measurements. The leading edge of the bunch is on the left.

## MEASUREMENTS

Figure 3 shows single-shot measurements of 15 consecutive bunches. One observes longitudinal field distributions of approx. 1 ps length containing of two peaks that are  $\approx 700$  fs apart and 160 fs to 250 fs wide (rms). These data are in qualitative agreement with measurements using a vertically deflecting cavity, where similar bunch shapes were found at the same accelerator settings [8]. Changing the rf phase in the first accelerating module by  $4^\circ$ , the bunch could be compressed to a single peak (Fig. 4).

Figure 5 show averaged single-shot measurements for different bunch charges. An almost linear dependence of the signal amplitude on the bunch charge is observed with slight changes in the signal shape, probably due to different

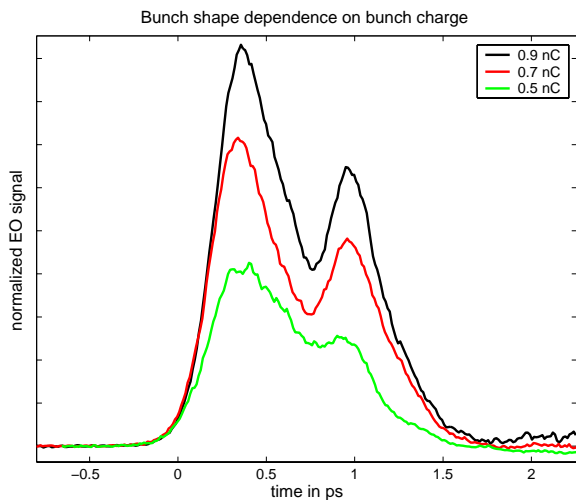


Figure 5: Measurement of the bunch field for different bunch charges. Each curve represents the average of 600 normalized and time-jitter corrected single-shot measurements. The leading edge of the bunch is on the left.

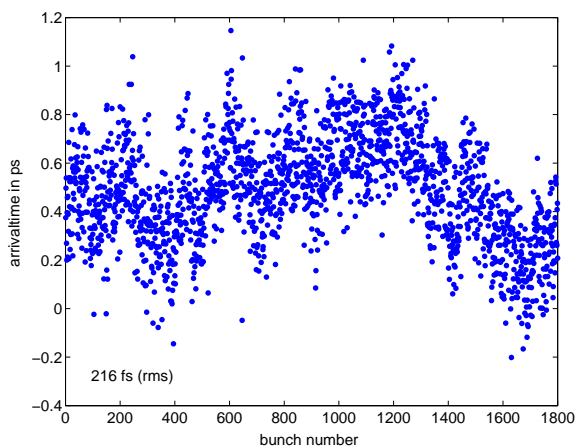


Figure 6: Arrival time of the electron bunches at the ZnTe crystal, measured with respect to the 1.3 GHz reference frequency. The rms time jitter is 216 fs.

space charge effects during the acceleration of the bunch.

For a series of measurements the arrival time of the bunches at the EO crystal, relative to the 1.3 GHz reference frequency, was determined by fitting a Gaussian to the first peak of the signal. The data in figure 6 cover a time interval of 15 minutes at a bunch repetition frequency of 2 Hz. The rms time jitter is 216 fs, including the above mentioned 70 fs time jitter of the synchronization between the laser and the 1.3 GHz linac master oscillator. Measurements ranging from 2 to 30 minutes show rms time jitters between 140 fs and 1 ps, including slow time drifts.

## CONCLUSION

The Electro-Optical Spectral Decoding technique offers the opportunity of an online non-destructive single-shot

measurement of the longitudinal bunch shape with a resolution of better than 175 fs, and simultaneous timing measurements with a resolution of better than 50 fs.

We are very grateful to LOT-Oriel, Darmstadt, Germany for lending us an Andor intensified ICCD camera to record the data presented here.

## REFERENCES

- [1] D. Oepts et al. Picosecond electronbunch length measurement using an electro-optic sensor. In *Proceedings of the 21st International FEL Conference*, Hamburg, 1999.
- [2] I. Wilke et al. Single-shot electron-beam bunch length measurements. *Phys. Rev. Lett.*, 88:124801–1, 2002.
- [3] G. Bernden et al. Chirped-laser based electron bunch length. In *Proceedings of the Pac 2003*, 2003.
- [4] S. Casalbuoni, H. Schlarb, B. Schmidt, B. Steffen, P. Schmüser, and A. Winter. Numerical studies on the electro-optic sampling of ultrashort electron bunches. In *Proceedings of the PAC 2005*, Knoxville, Tennessee, USA, 2005.
- [5] J.R. Fletcher. *Opt. Express*, 10:1425, 2002.
- [6] D. Oepts and G.M.H. Knippels. In *Proceedings of the 20th international FEL conference*, Williamsburg, 1998.
- [7] A. Winter, N. Ignachine, E.-A. Knabbe, A. Simonov, S. Simrock, B. Steffen, and S. Sytov. Femtosecond synchronisation of an ultrashort pulse laser to a microwave rf clock. In *Proceedings of the PAC 2005*, Knoxville, Tennessee, USA, 2005.
- [8] Markus Huening, Andy Bolzmann, Holger Schlarb, Josef Frisch, Douglas McCormick, Marc Ross, Tonee Smith, and Jrg Rossbach. Observation of femtosecond bunch length using a transverse deflecting structure. In *Proceedings of the FEL 2005*, Palo Alto, CA, USA, 2005.

# LONGITUDINAL PHASE SPACE STUDIES AT PITZ

J. Rönsch\*, J. Rossbach, Hamburg University, 22761 Hamburg, Germany  
 M.v. Hartrott, D. Lipka, BESSY, 12489 Berlin, Germany  
 K. Abrahamyan†, G. Asova‡, J. Bähr, G. Dimitrov§, H.-J. Grabosch, J.H. Han,  
 S. Khodyachykh, M. Krasilnikov, S. Liu, V. Miltchev, A. Oppelt, B. Petrosyan,  
 S. Riemann, L. Staykov, F. Stephan, DESY, 15738 Zeuthen, Germany

## Abstract

The main goal of the Photo Injector Test facility at DESY in Zeuthen (PITZ) is to test and to optimize photo injectors for Free-Electron Lasers (FELs). The demands on such a photo injector are small transverse emittances, short bunches and high bunch charge. A FEL is driven by an accelerator which consists of a RF gun followed by an acceleration section and a magnetic bunch compressor. For an effective bunch compression detailed studies of the longitudinal phase space have to be performed. The correlation between the positions of the particles in the bunch and their longitudinal momenta has to be understood and the non-linearities of the longitudinal phase space have to be analysed. A special apparatus for longitudinal phase space tomography at a momentum of around 5 MeV using a dipole, a Cherenkov radiator, an optical transmission line and a streak camera was developed. Results of longitudinal phase space measurements are presented and compared with simulations and the influence of the space charge force is discussed.

## INTRODUCTION AND SETUP

To measure the longitudinal phase space a correlated measurement of momentum and temporal distribution is required. In Fig. 1, a schematic of the PITZ1 setup [1] is shown. To measure the longitudinal distribution of the electron bunch a Cherenkov radiator (silica aerogel) [2] is used to transform the bunch into a light distribution at screen station 4 in the straight section (SS). This light distribution is imaged by an optical transmission line [3] onto the entrance slit of a streak camera (C5680 from Hamamatsu).

The momentum distribution is measured at screen station 5 on a YAG-screen in the dispersive arm (DA) by means of a spectrometer dipole [4]. To measure the longitudinal phase space both methods are combined. The YAG-screen in the DA can be replaced by silica aerogel using a movable actuator. The light pulse which presents the longitudinal phase space is transported to the streak camera. A description of the setup and the impact of the main com-

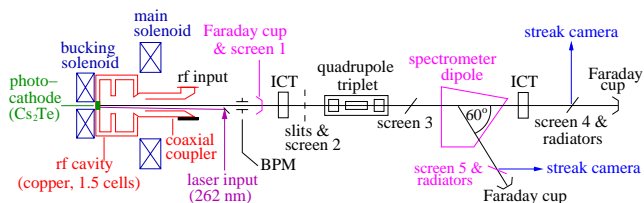


Figure 1: Schematic of PITZ1 setup.

ponents of the apparatus (as dipole magnet, streak camera and optical transmission line) on the results of the measurements of the longitudinal phase space can be found in Ref. [5].

## COMPARISON OF MEASUREMENT AND SIMULATION

First measurements of the longitudinal phase space were done at the end of 2004 in order to test the method. The measurements were done for flat-top and gaussian temporal laser distribution, bunch charges of 30 pC up to 1 nC and different phases between RF and laser (launch phases). In order to avoid including dispersion effects of the optical transmission line into the measurement, a spectral transmission filter with a bandwidth of 10 nm was inserted into the optical transmission line in front of the streak camera. The disadvantage of using filters is the strong reduction of the numbers of photons, thus the number of images to be taken increases and consequently the influence of jitter increases.

Figure 2 shows a result of these measurements compared to simulations, at a distance of 3.45 m downstream from the cathode, for standard operation conditions of PITZ, i.e. 1 nC bunch charge, flat-top longitudinal laser distribution (FWHM = 20 ps; rising time = 8 ps) and the launch phase is chosen such that the momentum gain in the gun is maximum (optimum launch phase). The electrons with negative time values represent the beginning of the bunch and the higher time values its tail.

The projections of the longitudinal phase space agree in principle with the direct measured distribution and the simulations. In the longitudinal distribution measured in the dispersive arm two minima can be found. These minima are caused by the assembling of different streak images.

\* author: jroensch@ifh.de

† on leave from YERPHI, 375036 Yerevan, Armenia

‡ on leave from INRNE, 1784 Sofia, Bulgaria

§ on leave from INRNE, 1784 Sofia, Bulgaria

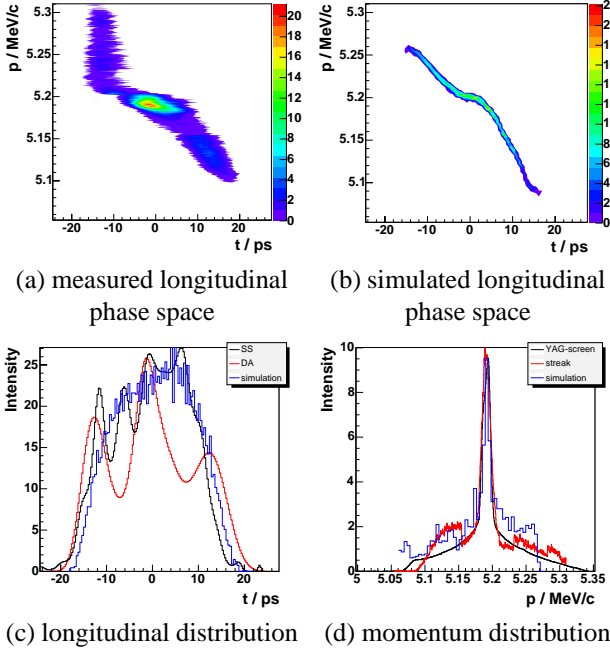


Figure 2: Measured (a) and simulated (b) longitudinal phase space and their projections: longitudinal (c) and momentum (d) distribution for 1 nC bunch charge, optimum launch phase and a flat-top laser distribution with about 20 ps FWHM pulse length. In (c) and (d) the black curves are direct measurements, the red ones are the projections of the measured longitudinal phase space and the blue ones are simulations.

This process has to be improved. Measured and simulated longitudinal phase space show a similar shape, but the measured one is wider than the simulated one. This is commonly observed for all used operation conditions. To estimate the impact of the resolution of the streak camera the simulated longitudinal phase space (2 (b)) was convoluted with the resolution function of the streak camera [6]. The resolution is given by the producer to be about 2 ps. In Fig. 3 (a) the convoluted distribution is shown. It bears a better resemblance to the measured one, but there is still a discrepancy due to jitter, noise and the fact that for the correction of the effects in the dipole only simulated distributions were used. For the measurement of the longitudinal distribution (bunch length) the resolution of 2 ps is sufficient, but for longitudinal phase space measurements it strongly impacts the measurement, because the longitudinal distribution of a certain energy is smaller than 2 ps. Therefore, the measured values of longitudinal emittance exceed the simulated ones.

Figure 3 (b) shows the longitudinal phase space for the same initial conditions as in Fig. 2 (b), but at a position close to the exit of the gun. The particles in the center of the bunch could reach the maximum energy gain. Due to space charge forces the particles in front of the bunch are slightly accelerated and the electrons in the end are slightly decelerated.

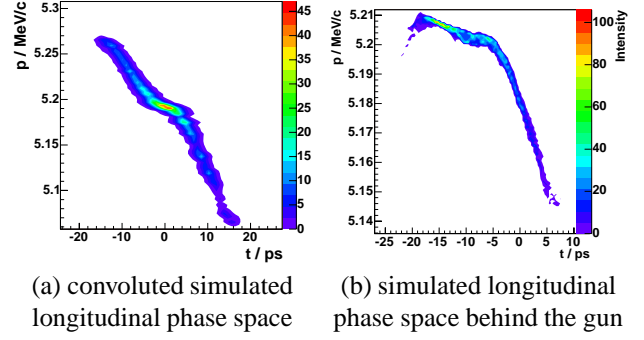


Figure 3: Simulated longitudinal phase space for optimum launch phase, flat-top laser distribution and 1 nC bunch charge (Fig. 2 (b)) convoluted with the resolution function of the streak camera (a). For studying the evolution of the longitudinal phase space the simulated longitudinal phase space for optimum launch phase, flat-top laser distribution and 1 nC bunch charge at the gun exit is shown (b).

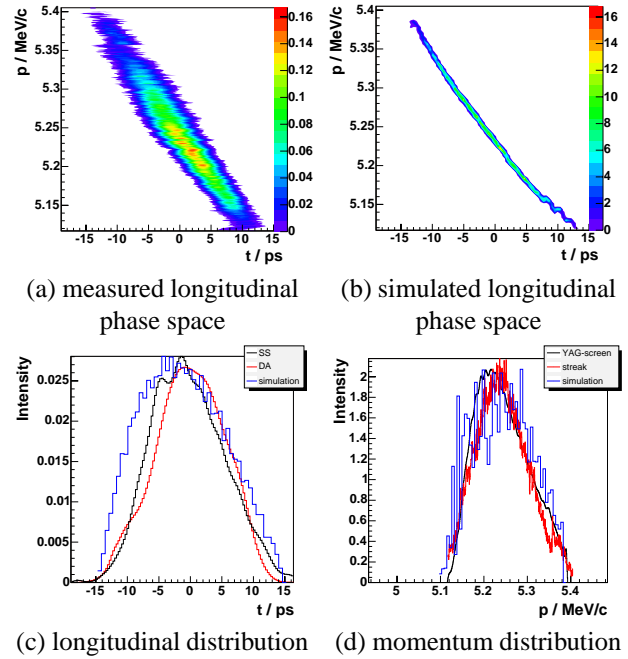


Figure 4: Measured (a) and simulated (b) longitudinal phase space and their projections: longitudinal (c) and momentum distribution (d) for 1 nC bunch charge, optimum launch phase and gaussian laser distribution with about 10 ps FWHM pulse length. In (c) and (d) the black curves are direct measurements, the red ones are the projections of the measured longitudinal phase space and the blue ones are simulations.

Figure 4 shows the results for optimum launch phase, 1 nC bunch charge and gaussian longitudinal laser distribution (FWHM = 10 ps). For this case the assembling of different streak images was working better, there is no minimum in the distribution visible as in Fig. 2. For longitudinal gaussian distribution the influence of the space charge

force is even higher than for flat-top, because the charge density in the bunch is higher. This leads to a strong increase of the momentum spread and an almost linear longitudinal phase space, with high energetic electrons in the head and lower energetic electrons in the tail. At TTF VUV-FEL further accelerating modules follow. A third harmonic cavity can remove the curvature of the longitudinal phase space, because the longitudinal phase space of the electron bunch which enters into the bunch compressor should be linear off-crest [7]. The influence of the space charge force to the main parameters of the longitudinal phase space is shown in Fig. 5 and 6.

## INFLUENCE OF THE SPACE CHARGE FORCE

Figure 5 shows the mean energy, the energy spread, the longitudinal emittance and the bunch length as a function of the bunch charge for flat-top and gaussian longitudinal laser distribution, each with and without space charge at the position of the dipole in the PITZ1 setup. When space

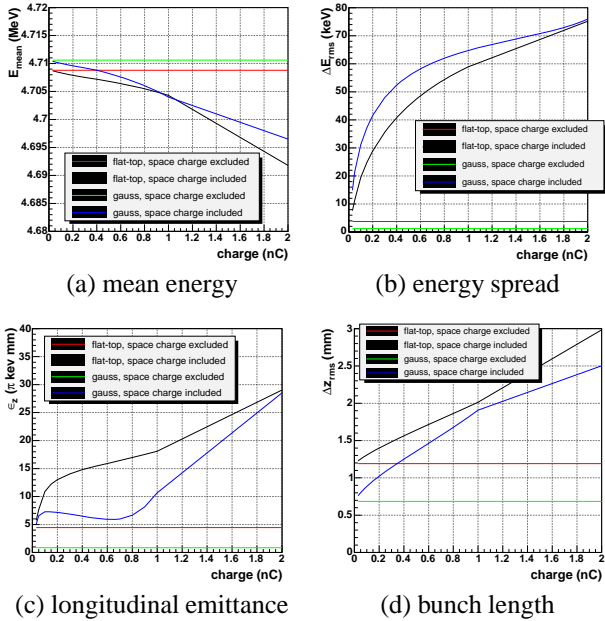


Figure 5: Simulated mean energy (a), energy spread (b), longitudinal emittance (c) and bunch length (d) as a function of the bunch charge.

charge effect is excluded from the simulation the longitudinal phase space does not change with the charge. Taking the space charge force into account for the simulation, charge increase signifies higher charge density for similar beam conditions. This impacts the momentum spread in the first instance but also the bunch length and consequently the longitudinal emittance. The mean momentum is decreased by about 1% for 1 nC bunch charge due to space charge effects. The longitudinal emittance for flat-top laser distribution increases with the charge, especially

for small charges there is a strong rise. For gaussian laser distribution a minimum of the longitudinal emittance is at about 0.65 nC. In practice the solenoid current is optimized to focus the beam on the screen in the dispersive arm. For all this simulations a solenoid current of 290 A has been used. For small charges the position of the focus is shifted towards the gun and the focusing leads to increasing space charge forces behind that point.

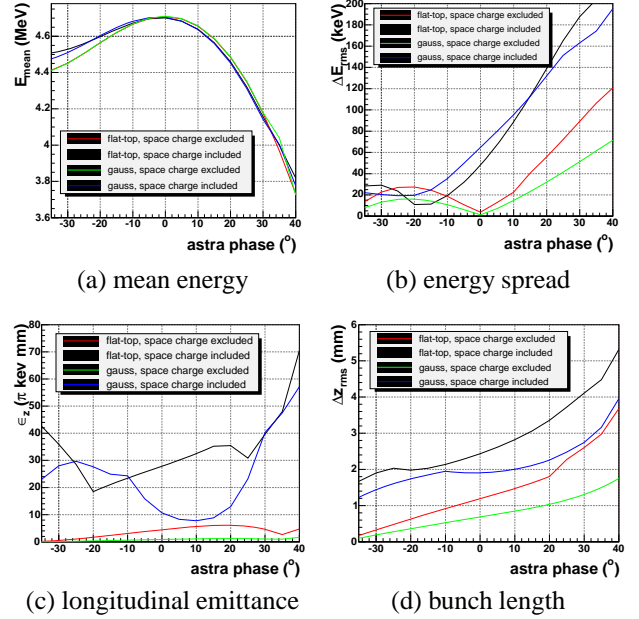


Figure 6: Simulated mean energy (a), energy spread (b), longitudinal emittance (c) and bunch length (d) as a function of the launch phase.

Figure 6 shows the same parameters but for different launch phases, for 1 nC bunch charge. Also for varying the launch phase the mean momentum is almost independent of space charge force, but the momentum spread shows a strong dependency. The launch phase of minimum momentum spread is shifted due to space charge force. The dependency of the mean momentum and the momentum spread on phase (as displayed in 6 (a) and (b)) and influence of the longitudinal laser distribution to these distributions are discussed in Ref. [8, 9, 10]. The smallest longitudinal emittance for flat-top laser distribution was reached for about the same launch phase as the smallest energy spread.

For a better understanding of the shape of the longitudinal phase space, a low bunch charge (of about 40 pC) has been used in order to reduce the influence of space charge force (Fig. 7). In Fig. 7 (c) the measurement result is shown, the result from the simulation is displayed in Fig. 7 (a) for the same position and in Fig. 7 (b) at the gun exit. Here it is visible that the electrons at the head of the bunch are accelerated due to the space charge forces, whereas the particles at the tail are slowed down. Due to

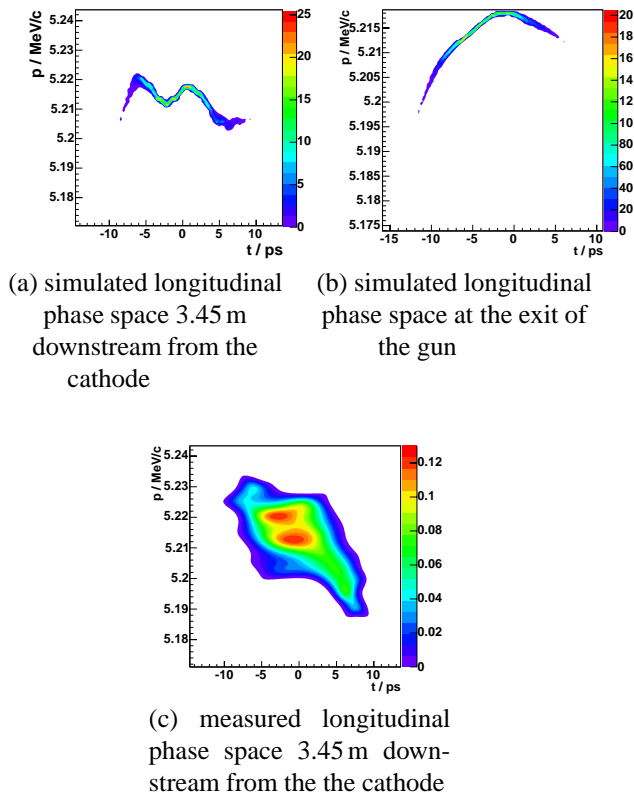


Figure 7: Simulated longitudinal phase space for optimum launch phase, flat-top laser distribution and about 40 pC bunch charge at dipole position (a) and at the exit of the gun (b). In (c) the measurement result is displayed.

the smaller space charge force the influence is not as strong as for 1 nC.

## CONCLUSION

Measurements of the longitudinal phase space for an energy around 5 MeV have been presented. The resolution of the longitudinal phase space measurement is restricted by the resolution of the streak camera. Therefore, the measured values of longitudinal emittance are in general noticeably higher than the simulated values. There is a significant influence of the space charge force to the longitudinal phase space even for charges of about 40 pC.

## ACKNOWLEDGEMENTS

This work has partly been supported by the European Community, contract numbers RII3-CT-2004-506008 and 011935, and by the 'Impuls- und Vernetzungsfonds' of the Helmholtz Association, contract number VH-FZ-005.

## REFERENCES

- [1] A. Oppelt et al, "The photo injector Test facility at DESY Zeuthen: results of the first phase", LINAC, Lübeck, 2004.
- [2] J. Bähr, V. Djordjadze, D. Lipka, A. Onuchin, F. Stephan,

"Silica aerogel radiators for bunch length measurements", NIM A 538 (2005) 597-607.

- [3] J. Bähr, D. Lipka, H. Lüdecke, "Optical transmission line for streak camera measurement at PITZ", Dipac, Mainz, 2003.
- [4] D. Lipka, "Momentum And Momentum spread Analysis (MAMA)", PITZ Note 01-04
- [5] J. Rönsch et al, "Measurement of the Longitudinal Phase Space at the Photo Injector Test Facility at DESY in Zeuthen (PITZ)", Dipac, Lyon, 2005.
- [6] Hamamatsu, "Test report C5680-21, Serial No. 040168".
- [7] K. Honkavaara, "Commissioning of the TTF Linac Injector at the DESY VUV-FEL", FEL, Trieste, 2004.
- [8] D. Lipka, "Untersuchungen zum longitudinalen Phasenraum an einem Photoinjektor für minimale Strahlemittanz", PhD thesis, Humboldt University Berlin, May 2004.
- [9] D. Lipka et al, "Measurement of the longitudinal phase space at the Photo Injector Test Facility at DESY Zeuthen", Dipac, Mainz, 2003.
- [10] D. Lipka et al, "Measurement of the longitudinal phase space at the Photo Injector Test Facility at DESY Zeuthen", FEL, Tsukuba, 2003.

# MODELLING THE TRANSVERSE PHASE SPACE AND CORE EMITTANCE STUDIES AT PITZ

V. Miltchev\*, DESY, Zeuthen, Germany

## Abstract

In this work we propose a method for reconstruction of the transverse phase space distribution of electron beams using data from slit scanning measurements. The suggested analysis procedure will be applied to slit scanning data taken at various operating conditions of the Photo Injector Test Facility at Zeuthen (PITZ). Transverse emittance values containing only a certain fraction of all particles in the distribution (core emittance) will be estimated and the results will be compared with simulations.

## INTRODUCTION

The high electron beam quality needed for SASE FEL processes requires considerable effort in the characterization and the improvement of the electron source. The main research goal of the Photo Injector Test Facility at Zeuthen (PITZ) is the development of electron sources with minimized transverse emittance like they are required for the successful operation of Free Electron Lasers and future linear colliders [1]. The experimental set-up used for the measurements is shown in Fig. 1. It consists of a 1.5 cell L-band rf gun with a Cs<sub>2</sub>Te photo-cathode, a solenoid system for compensating space charge induced emittance growth, a photo-cathode laser system capable of generating long pulse trains with variable temporal and spatial micro pulse shape, and an extensive diagnostics section. The transverse emittance measurements at PITZ are performed using a single-slit scan technique. A slit of 50 μm width is used to sample the initial transverse phase space distribution. The beam is transformed into small beamlets, which retain the uncorrelated divergence of the original beam. The beamlet profiles are observed on a screen situated at a distance L=1.01 m downstream, where the measured rms size  $\tilde{\sigma}_i$  of the *i*<sup>th</sup> beamlet image directly corresponds to uncorrelated divergence  $\tilde{x}'_i \cong \tilde{\sigma}_i/L$ . The goal is to evaluate the rms emittance defined as  $\epsilon_{x,rms} = \sqrt{\langle x^2 \rangle \langle x'^2 \rangle - \langle xx' \rangle^2}$ , which requires the computation of the total (correlated and uncorrelated) divergence  $\langle x'^2 \rangle$  as well as the correlation  $\langle xx' \rangle$ . For practical use it is more convenient to apply an equivalent definition as derived in[3]:

$$\epsilon_{x,rms} = \sqrt{\langle x^2 \rangle \langle \tilde{x}'^2 \rangle} = \sqrt{\langle x^2 \rangle \left\langle \frac{\tilde{\sigma}^2}{L^2} \right\rangle} \quad (1)$$

The rms size  $\sigma_x = \sqrt{\langle x^2 \rangle}$  is measured directly by observing the beam profile on a screen with scintillating material inserted at the position of the slit mask. The typical emittance measurement at PITZ, as it is illustrated in Fig. 2,

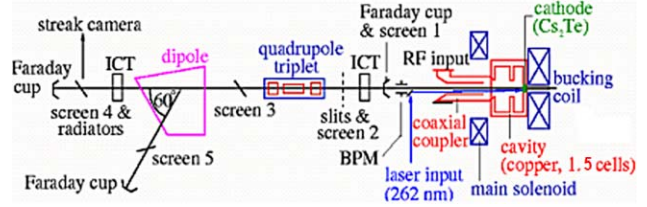


Figure 1: Schematic layout of PITZ.

consists of a beam size measurement at the slit mask position and of a transverse phase space sampling at three transverse positions [2] given by  $x_i = \langle x \rangle + 0.7\sigma_x \cdot i$ , where  $i = \{-1, 0, 1\}$ .

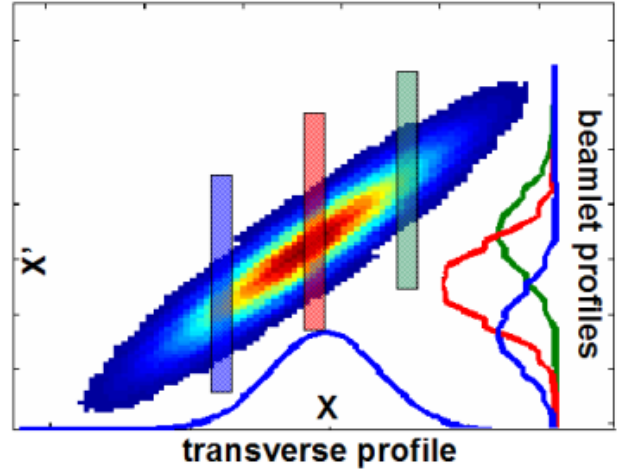


Figure 2: A schematic representation of the emittance measurement using the slit scanning technique at PITZ. The shaded stripes correspond to a phase space sampling by the slit. The beamlet profiles  $\eta_{meas}(x_i, x')$  produced by the slit are observed on a screen after about 1 m drift. The beam transverse profile  $\xi_{meas}(x)$  is measured at the position of the slit mask.

## PHASE SPACE RECONSTRUCTION

The measurement procedure briefly described above provides a good estimation of the full (100%) beam emittance, although the process of emittance calculation does not require a detailed reconstruction of the phase space. However, in some FEL applications the particles in the outermost phase space region might stay out of the amplifier bandwidth and hence only the core of the distribution takes part in the FEL process. For this reason one might be interested in calculating the emittance only of a certain fraction of the particles (core emittance), which corresponds to the

\* velizar.miltchev@desy.de

lasing part of the bunch. One possible approach to estimate the core emittance is to reconstruct the distribution  $f(x, x')$  of the electrons in the phase space using the data from the slit scan i.e. using the measured transverse beam profile  $\xi_{\text{meas}}(x)$  and the observed beamlet profiles  $\eta_{\text{meas}}(x_i, x')$ . The goal is to determine the function  $f(x, x')$  such, that its projection  $\xi_{\text{rec}}(x)$  onto the transverse axis fits to  $\xi_{\text{meas}}(x)$  as well as the beamlet profiles  $\eta_{\text{rec}}(x_i, x')$  sampled from  $f(x, x')$  should fit to  $\eta_{\text{meas}}(x_i, x')$ . Let  $\Lambda$  be a parameterization of  $f(x, x')$ . Then the phase space reconstruction reduces to a search of the parameters set  $\Lambda_0$ , which minimizes the sum:

$$R = R_\xi + R_\eta \quad (2)$$

where  $R_\xi$  and  $R_\eta$  are defined as:

$$R_\xi = \sum_n \left( \xi_{\text{rec}}(x_n, \Lambda) - \xi_{\text{meas}}(x_n) \right)^2 \quad (3)$$

$$R_\eta = \sum_{i=1}^3 \sum_m \left( \eta_{\text{rec}}(x_i, x'_m, \Lambda) - \eta_{\text{meas}}(x_i, x'_m) \right)^2 \quad (4)$$

In the expressions above a summation instead integration is used since the beam measurements are done with CCD cameras of finite pixel size and therefore  $\xi$  and  $\eta$  are non-continuous binned distributions. If one considers the electron bunch as an ensemble of longitudinal slices each of them with different orientation in the transverse phase space, then the projected beam emittance will be determined by the common phase space area occupied by all slices. For the purpose of the phase space reconstruction, one can imagine a model, which formally resembles the case with the longitudinal slices. One assumes, that the transverse phase space shape is a superposition of an ensemble of  $N$  ellipses, each of them characterized by its phase space angle  $\delta$ , semi axes  $\{a, b\}$  and charge  $Q$ . For the analysis presented in this paper the charge distribution in each ellipse was assumed to be gaussian in both  $x$  and  $x'$ . However, it is important to note that the final result of the phase space reconstruction and hence of the calculated core emittance depends on the assumed charge distribution, where the distributions with longer tails might generate smaller core emittances.

## CORE EMITTANCE ESTIMATIONS

In the proposed model the quantities  $\Lambda \equiv \{\delta_i, a_i, b_i, Q_i\}$ ,  $i = 1..N$ , are considered as free parameters, which have to be determined by the minimization of the quadratic sum given in Eq. 2. The proposed procedure to calculate the transverse core emittance consists of three steps. At first one performs a phase space reconstruction based on the slit scan data. Then one applies a thresholding (as illustrated in Fig. 6) of the phase space distribution in order to remove a given fraction (e.g. 10%) of the particles. The third step is a calculation of the emittance of the remaining (e.g. 90%) core. In the examples shown in Fig. 3 and Fig. 4, the reconstruction algorithm was applied to slit scan data

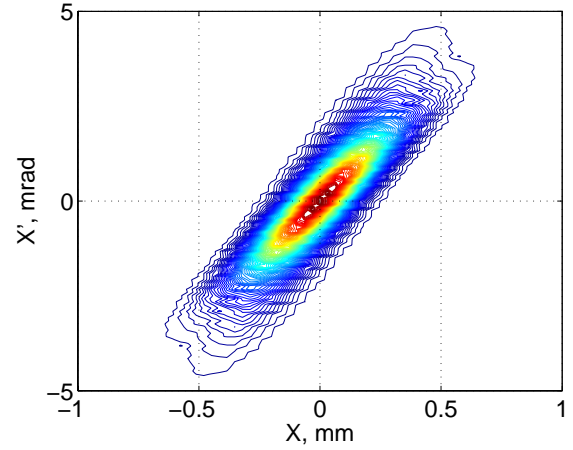


Figure 3: Reconstructed horizontal phase space based on slit scan data. The calculated 100% vertical emittance is  $\epsilon_x = 1.4$  mm mrad and the 90% core emittance is  $\epsilon_{x,90\%} = 1.0$  mm mrad. For comparison the measured 100% emittance is  $\epsilon_x = 1.3 \pm 0.1$  mm mrad.

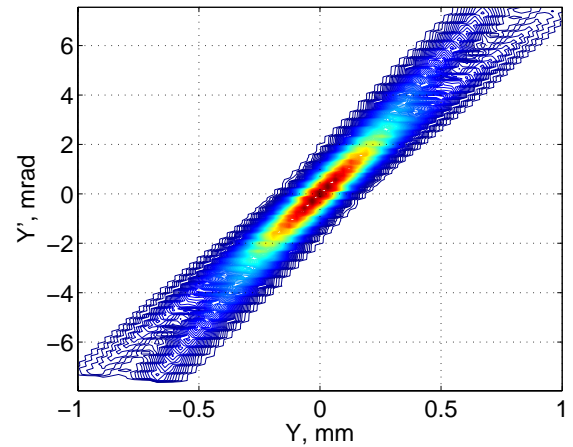


Figure 4: Reconstructed vertical phase space based on slit scan data. The calculated 100% vertical emittance is  $\epsilon_y = 2.3$  mm mrad and the 90% core emittance is  $\epsilon_{y,90\%} = 1.6$  mm mrad. For comparison the measured 100% emittance is  $\epsilon_y = 1.9 \pm 0.2$  mm mrad.

measured at a solenoid current, which corresponds to an over focused beam at the position of the emittance measurement system. The reconstruction was performed for both the horizontal and for the vertical phase space and the results are to be compared with the ASTRA [4] simulation, which is shown in Fig. 5. As a reasonable compromise between the needed computing time and the goodness of the fit, the number of the superimposed phase space ellipses was taken to be  $N = 3$ . A core emittance (90%) analysis was done using the slit scan data taken at PITZ, where the emittance at 1 nC bunch charge was measured as a function of the focusing solenoid current. The estimated 100%

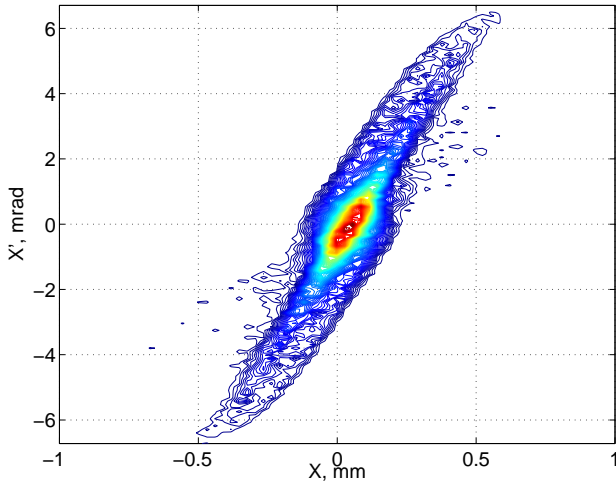


Figure 5: The phase space as predicted by ASTRA simulation for the same conditions as for the measurements analysed in Fig. 3 and Fig. 4: a gun gradient of about 45 MV/m, 1 nC bunch charge and rf phase corresponding to the phase of maximum energy gain  $\Phi_m$ . The current in the main solenoid is set to 326 A, which corresponds to an over focused beam at the position of the slit mask. The UV laser pulse shape was a flat top of about 20 ps FWHM and about 5 ps rise/fall time. The 100% emittance is  $\epsilon = 1.5$  mm mrad and the 90% core emittance is  $\epsilon_{90\%} = 0.8$  mm mrad.

and 90% emittance values are presented in Fig. 7, Fig. 8 and compared with corresponding ASTRA simulations for injector parameters like the ones observed during the emittance measurements.

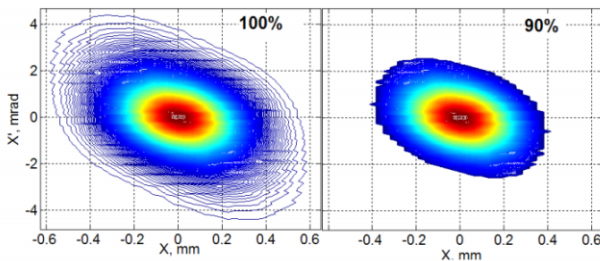


Figure 6: The figure shows the result of a thresholding of the phase space distribution. The graph in the left represents the full reconstructed distribution with an emittance of  $\epsilon = 1.95$  mm mrad. In the right the remaining points are those, where the phase space density is above a certain threshold determined so that 90% of the particles are left. The corresponding core emittance is  $\epsilon_{90\%} = 1.39$  mm mrad.

## SUMMARY

A method for reconstruction of the transverse phase space distribution of electron beams using data from slit scanning measurements was proposed. A procedure to estimate the transverse core emittance was discussed. Fol-

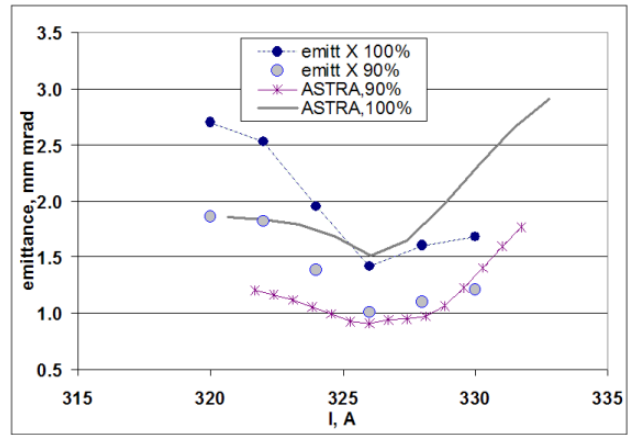


Figure 7: Estimated after phase space reconstruction 100% and 90% horizontal emittances are shown as a function of the solenoid current.

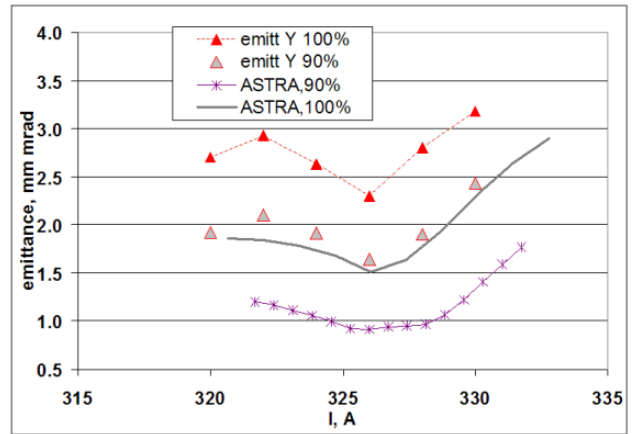


Figure 8: Estimated after phase space reconstruction 100% and 90% vertical emittances are shown as a function of the solenoid current.

lowing the suggested procedure slit scan data taken at PITZ were analyzed and 90% core emittance was calculated as a function of the solenoid current. Despite the good general agreement between the obtained results and the simulation one can think of further improvements in the model for the phase space reconstruction.

## ACKNOWLEDGEMENTS

This work has partly been supported by the European Community, contract numbers RII3-CT-2004-506008 and 011935, and by the 'Impuls- und Vernetzungsfonds' of the Helmholtz Association, contract number VH-FZ-005. I would like to thank to my colleagues from the PITZ group for supplying the slit scan data used in the analysis.

## REFERENCES

- [1] F. Stephan et al., "Photo Injector Test Facility under construction at DESY Zeuthen", FEL'00, August 2000, Durham,

North Carolina, U.S.A.

- [2] M. Krasilnikov et al., "Characterization of the Electron Source at the Photo Injector Test Facility at DESY Zeuthen", FEL'03, Sept, 2003, Tsukuba, Japan
- [3] K. Flöttmann, "Some basic features of the beam emittance", Phys. Rev. ST Accel. Beams , 2003, vol. 6.
- [4] K. Flöttmann, "A Space Charge Tracking Algorithm", <http://www.desy.de/~mpyflo>

# Measurements of thermal emittance for cesium telluride photocathodes at PITZ\*

V. Miltchev<sup>†</sup>, J. Baehr, H.-J. Grabosch, J. H. Han, M. Krasilnikov, A. Oppelt,  
B. Petrosyan, L. Staykov, F. Stephan, DESY, D-15738 Zeuthen, Germany  
M. v. Hartrott, BESSY GmbH, Berlin, Germany

## Abstract

The thermal emittance determines the lower emittance limit and its measurement is of high importance to understand the ultimate injector performance. In this contribution we present results of thermal emittance measurements under rf operation conditions for various  $\text{Cs}_2\text{Te}$  cathodes and different accelerating gradients. Measurements of thermal emittance scaling with the cathode laser spot size are presented and analyzed. The significance of the applied electric rf field in the emittance formation process is discussed.

## INTRODUCTION

The main research goal of the Photo Injector Test Facility at Zeuthen (PITZ) is the development of electron sources with minimized transverse emittance like they are required for the successful operation of Free Electron Lasers and future linear colliders [1]. The experimental set-up used for the measurements is shown in Fig. 1. It consists of a 1.5 cell L-band rf gun with a  $\text{Cs}_2\text{Te}$  photocathode, a solenoid system for compensating space charge induced emittance growth, a photo-cathode laser system capable of generating long pulse trains with variable temporal and spatial micro pulse shape, and an extensive diagnostics section. The emittance characterization at PITZ is performed using the slit scanning method [2], which was used also for the thermal emittance measurements.

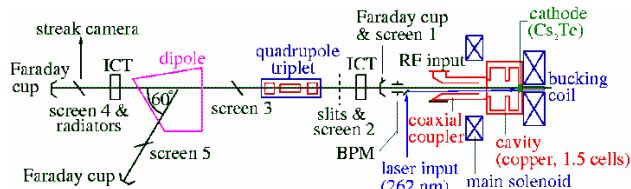


Figure 1: Schematic layout of PITZ.

The thermal emittance adds in quadrature to the other emittance contributions, thus it sets the lower limit for the transverse emittance of electron sources. Numerous theoretical and experimental studies have been dedicated to the

measurements of the thermal emittance as well as to solutions for reducing it. Everywhere the authors point out the high importance of thermal emittance measurements to understand and to improve the ultimate performance of injectors feeding linac driven FELs. Among the various possible photocathode materials, the semi conductive alkali telluride  $\text{Cs}_2\text{Te}$  shows high quantum efficiency, high robustness and long lifetime and therefore has been chosen for PITZ as well as for many other photoinjectors. For first time thermal emittance measurements for  $\text{Cs}_2\text{Te}$  photocathodes under real rf operating conditions were performed at PITZ and will be presented in the following sections. The thermal emittance depends [3] on the laser spot size, the momentum and the angular distribution of the emitted photoelectrons. Its typical value is small, usually in the range 0.3-0.7 mm-mrad and therefore it starts to play a significant role in the emittance formation, when the injector operating parameters have been fully optimized so that very low emittances of the order of 1 mm-mrad are about to be produced. It is important to note that the thermal emittance is a complex quantity influenced not only by the photocathode material properties but also by the parameters of the cathode UV laser and the accelerating field amplitude. In planning the measurements one has to consider the dependence on the laser spot rms size, on lowering the surface potential barrier due to the high rf field (Schottky effect) and on poisoning of the cathode due to increased vacuum pressure.

## THERMAL EMITTANCE CALCULATION

The photoemission in semiconductors takes place in the following sequence [4]: Step 1: Absorption of a photon in the bulk material and excitation of electrons to the conduction band (CB). Since  $\text{Cs}_2\text{Te}$  is a semiconductor material with a band gap of  $E_G = 3.3$  eV, a photon energy  $E_{ph} > 3.3$  eV is required. The UV laser put into operation at PITZ generates photons at a wavelength of  $\lambda = 262$  nm or  $E_{ph} = 4.72$  eV. Step 2: Transport of excited electrons to the first maximum of the CB density of states, which for  $\text{Cs}_2\text{Te}$  is located at an energy of 4.05 eV above the maximum of valence band (VB). Step 3: Escape of the electrons into vacuum. In order to escape from the conduction band to the vacuum, electrons have to overcome the surface potential barrier given by the electron affinity  $E_A$ , which is defined as the energy difference between the vacuum level  $E_{vac}$  and the bottom of the conduction band. Thus, the threshold energy  $E_T = E_{vac}$  for photoe-

\*This work has partly been supported by the European Community, contract numbers R113-CT-2004-506008 and 011935, and by the 'Impuls- und Vernetzungsfonds' of the Helmholtz Association, contract number VH-FZ-005

<sup>†</sup> velizar.miltchev@desy.de

mission is given by the sum of the band gap and the electron affinity:  $E_T = E_A + E_G$ . The threshold energy for  $\text{Cs}_2\text{Te}$  is measured [4] to be  $E_T = 3.5$  eV and hence the electron affinity for a very fresh cathode can be estimated by:  $E_A = E_T - E_G = 0.2$  eV (due to cathode contamination  $E_A$  might become larger). Since the electrons final state energy in Step 2 is on average  $E_{CB} = 4.05$  eV, after escaping into the vacuum the electrons will have a mean kinetic energy of  $E_k = E_{CB} - E_{vac} = 4.05 - 3.5 = 0.55$  eV. The above quoted value for the average kinetic energy of the emitted photoelectrons was estimated considering the measurements of Powell[4] performed with fresh cathodes and very low electric fields. However the actual value of  $E_k$  obtained when the cathode is operated in an rf gun with high accelerating gradient might be larger due to Schottky reduction of the electron affinity or lower due to poisoning of the cathode surface. Following the arguments in [3] one can derive a relation between the thermal emittance and photoemission parameters: the average kinetic energy of the emitted photoelectrons and the electron affinity. In the photoemission model considered in the following, one assumes that the electrons are emitted isotropically into the hemisphere over the cathode surface behind the potential barrier. The average kinetic energy of photoemitted electrons is defined as:

$$E_k = E_{CB} - E_G - E_A \quad (1)$$

The analysis presented in [3] yields the following relation for the normalized thermal emittance:

$$\epsilon_{th} = \sigma \sqrt{\frac{2E_k}{3m_0c^2}} \quad (2)$$

where  $\sigma$  denotes the rms laser spot size.

## OPERATION PARAMETERS

As it was discussed above the thermal emittance adds quadratically to the other emittance terms to form the total emittance:  $\epsilon_n \approx \sqrt{\epsilon_{th}^2 + \epsilon_{rf}^2 + \epsilon_{sc}^2}$ . This relation has to be taken into account in order to determine the operation conditions needed to perform thermal emittance measurements. The main problem is that with the PITZ set up one can not measure the thermal emittance directly at the photocathode (inside the rf gun), but at the position of emittance measurement system, which is located about 1.62 m downstream. This means that one measures not only the thermal emittance but the contributions of rf and space charge as well. Under proper operation conditions the last two terms should be minimized so that  $\epsilon_n \approx \epsilon_{th}$ . The space charge contribution to the emittance rapidly scales up with the charge, which implies that the bunch charge should be set as close as possible to zero. On the other hand one has to keep the signal-to-noise ratio during the emittance measurement sufficiently high, which sets a lower limit to the charge. According to the practical experience a charge of about 3 pC is a reasonable compromise between these contradicting requirements. According to ASTRA [6] for this charge, the relative emittance increase due to self-fields

should not be larger than 5%. Regarding the contribution of the rf field it is helpful to recall that  $\epsilon_{rf} \propto \sigma_t^2$ , hence the laser pulse length  $\sigma_t$  has to be shortened to the possible limit. The laser system of PITZ can generate gaussian pulses of  $\sigma_t \approx 3$  ps. A further reduction of the temporal extent of the laser pulses is not possible without major reconstruction of the system. According to the ASTRA simulation results the rf induced emittance growth is expected to be not more than 2% of the thermal emittance for pulse length of 3 ps. Taking into account that for the tiny charge of 3 pC the beam current  $I \simeq Q/\sigma_t$  is just about 1 A, one can consider to lower the accelerating rf gradient in order to minimize the dark current and its impact on the emittance and the data analysis. For that reason most measurements were done at an accelerating field of about 32-34 MV/m, since the PITZ gun (with inserted  $\text{Cs}_2\text{Te}$  photocathode) then produces a negligible dark current of about  $1 \cdot 10^{-4}$  A for a peak gradient of 34 MV/m. The gun rf phase for the measurements was always set to the phase of maximum mean energy gain  $\Phi_m$ , although a large emittance variation with the rf phase for that small charge is not expected.

## EMITTANCE SCALING WITH LASER SPOT SIZE

The final goal of these measurements is to estimate the average kinetic energy  $E_k$  of the electrons immediately after emission from the  $\text{Cs}_2\text{Te}$  photocathode. By differentiation of both sides of Eq. 2 one obtains a relation between energy of the electrons and the rate of increase of emittance with the laser spot size  $\sigma_r$ .

$$E_k = 1.5m_0c^2 \left( \frac{d\epsilon_{th}}{d\sigma_r} \right)^2 \quad (3)$$

Thus an estimate for  $E_k$  can be given, provided that the slope ( $d\epsilon_{th}/d\sigma_r$ ) is known. It can be determined by measuring the emittance as a function of the laser spot size and then fitting a straight line through the measured data points. The emittance was measured vs. laser rms spot size using the slit scanning technique at a small bunch charge of 3 pC and a moderate gradient of about 32 MV/m. The variation of the laser spot size was realized by passing the initial laser beam through a circular aperture of changeable diameter. Two sets of measurements were taken for two different  $\text{Cs}_2\text{Te}$  cathodes: cathode No.60 (see Fig. 2) with quantum efficiency (QE) of about 1% at the time of the measurements and cathode No.61 (see Fig. 3) with QE of about 1.5%. Straight line fits through the measured data for the horizontal as well as the vertical emittance yield the following results for cathode No.60:

$$\frac{d\epsilon_{th,x}}{d\sigma_x} \simeq 1.3 \text{ mrad} \quad \frac{d\epsilon_{th,y}}{d\sigma_y} \simeq 1.1 \text{ mrad} \quad (4)$$

Taking into account Eq. 3 and since there is no reason to expect the energies obtained for both transverse planes to differ, one takes the average of the two as a final result with

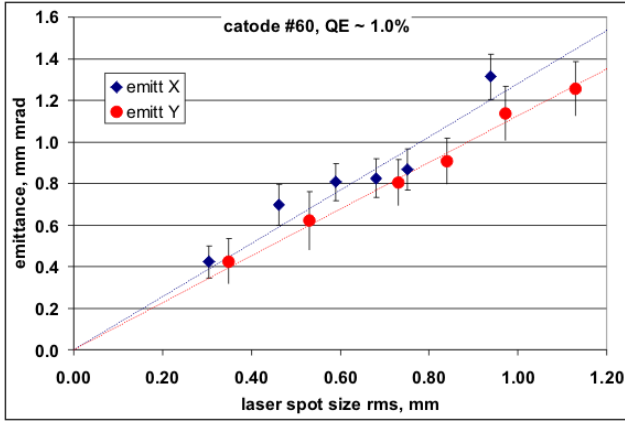


Figure 2: Measurements with cathode No.60.

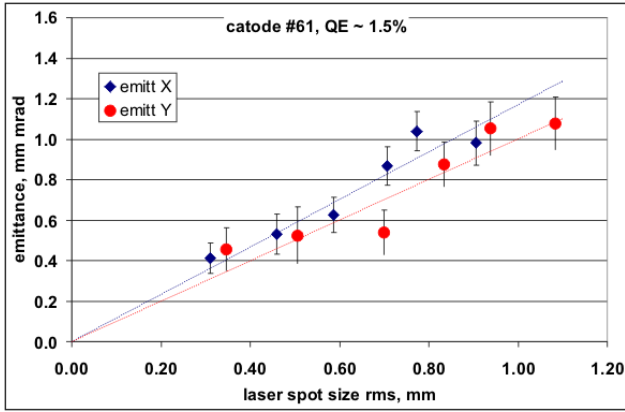


Figure 3: Measurements with cathode No.61.

an uncertainty equal to the standard deviation:

$$E_{k,\#60} = (1.1 \pm 0.2) \text{ eV} \quad (5)$$

The same analysis applied to the emittance data taken with cathode No.61 yields the following results:

$$\frac{d\epsilon_{th,x}}{d\sigma_x} \simeq 1.2 \text{ mrad} \quad \frac{d\epsilon_{th,y}}{d\sigma_y} \simeq 1.0 \text{ mrad} \quad (6)$$

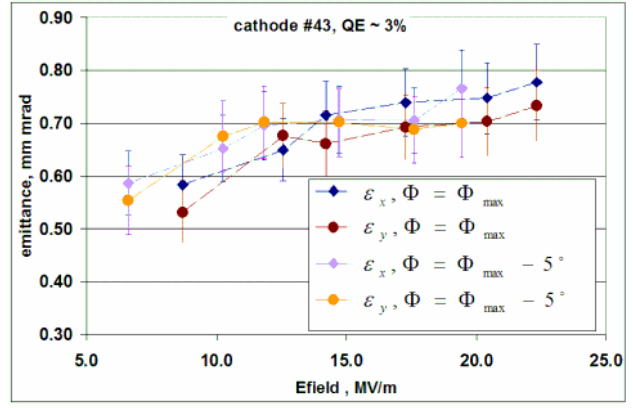
And the final result for cathode No.61:

$$E_{k,\#61} = (0.9 \pm 0.2) \text{ eV} \quad (7)$$

The average kinetic energy of the emitted photoelectrons was estimated to be in the range 4.2-4.4 eV above the top of the valence band, which corresponds to 0.9-1.1 eV relative to the vacuum level. The expected value was about 4.05 eV, where a symmetric energy distribution curve of the photoemitted electrons was assumed. The slightly higher experimental result might be assigned to an asymmetry in the energy distribution.

## THERMAL EMITTANCE DEPENDENCE ON ELECTRIC RF FIELD

The goal of these measurements is to study the dependence of the thermal emittance and hence the average ki-

Figure 4: Measurements with cathode No.43. RF phase set to  $\Phi_m$  and  $\Phi_m - 5^\circ$ . Laser spot size  $\sigma_{x/y} = 0.55/0.54$  mm

netic energy of the photoelectrons as a function of the electric field  $E$  in the moment of photoemission. The measurements were done using the PITZ slit scanning technique. Since the same general requirements for the operation parameters apply as described above, a similar measurement procedure was followed. The electric rf field amplitude  $E_0$  was varied in the range of 24 to 39 MV/m. For each value of  $E_0$  the rf phase was adjusted to the phase of maximum mean energy gain  $\Phi_m$ . Before each emittance measurement the beam charge was measured vs. rf phase. From the rising edge of that scan the zero crossing rf phase  $\Phi_0$  was determined and thus  $E = E_0 \sin(\Phi_m - \Phi_0)$ . The laser spot size was kept fixed. The bunch charge was set to 2-3 pC. Such measurements were done with a cathode of QE of about 3% and then repeated for a slightly different rf phase corresponding to  $\Phi_{\max} - 5^\circ$ . The laser spot size was adjusted to  $\sigma_{x/y} = 0.55/0.54$  mm. Results of these measurements are shown in Fig. 4. In all cases the thermal emittance increases with the accelerating field, which corresponds to a rising average kinetic energy of the photoelectrons. The experimental data can be analyzed assuming that the thermal emittance increase is due to a lowering of the electron affinity caused by the Schottky effect. The reduction of the electron affinity due to the Schottky effect for a semiconductor photocathode is described by the following expression [5] :

$$E_A = E_A(0) - \sqrt{\beta \frac{eE}{4\pi\epsilon_0}} \quad (8)$$

with  $\beta$  denoting an effective field enhancement factor and  $E_A(0)$  is the electron affinity at zero electric field. In summary from Eq. 1, Eq. 2 and Eq. 8 one expects the following general relation between thermal emittance and applied electric field:

$$\epsilon_{th}^2 = A + B\sqrt{E} \quad (9)$$

i.e. a linear dependence between square of thermal emittance and square root of electric field. It is well known that the main problem in using semiconductor photocathodes in

an rf gun is the relatively short, compared with metals, lifetime due to contamination caused by residual gases. This photocathode degradation appears as monotonic QE decay with the time and can be explained with electron affinity increase due to passivation of the photocathode surface. Therefore the value of electron affinity  $E_A=0.2$  eV, quoted before, is valid only for very fresh cathode. During the rf operation the electron affinity monotonically grows and might reach significantly larger values than the initial one [5]. The photocathodes used in the thermal emittance studies presented above were exposed to residual gases in the rf gun. For that reason it is interesting to give an estimate of their actual electron affinity at the time of the measurements. In order to do this, according to Eq. 9, one has to fit a straight line to the square of the measured thermal emittance  $\epsilon_{th}^2$  as a function of the square root of the rf field  $\sqrt{E}$ . The fit coefficient denoted as A in Eq. 9 is related to the actual value of the electron affinity at zero electric field. The replacement of Eq. 1, Eq. 2 into Eq. 8 and setting the electric field  $E=0$  yields:

$$E_A(0) = E_{CB} - E_G - \frac{3 Am_0 c^2}{2 \sigma_r^2} \quad (10)$$

where  $\epsilon_{th}(0) = \sqrt{A}$  denotes the thermal emittance at zero electric field. With these considerations the measured data for cathode No.43 were analyzed using the regression model introduced in Eq. 9. The results of the straight line  $\chi^2$  fits, plotted in Fig. 5 and Fig. 6, give the following value for A:

$$A = \epsilon_{th}^2(0) = (0.12 \pm 0.04) \mu m^2 \quad (11)$$

and subsequently by replacement in Eq. 10:

$$E_A(0) = (0.45 \pm 0.10) eV \quad (12)$$

The last result is in very good agreement with the value of 0.44 eV [5] obtained by measuring QE dependence on rf phase. The estimated high value of the electron affinity for cathode No. 43 (compared to 0.2 eV for very fresh not yet used cathode) is a clear indication of degradation of photoemissive layer due to residual gases in the rf cavity.

## SUMMARY

The transverse emittance was measured for a very low charge of 2-3 pC, short laser pulses of  $\sigma_t$  about 3 ps and moderate accelerating gradients. According to simulations space charge and rf field contributions to the emittance should be negligible. The scaling of the transverse emittance with the laser spot rms size was measured using the single slit scanning technique. The thermal emittance was measured as a function of the applied field at the cathode, where monotonic increase with electric field due to the Schottky effect was observed. The electron affinity at zero accelerating field was estimated to be  $0.45 \pm 0.10$  eV for a cathode with quantum efficiency of about 3%.

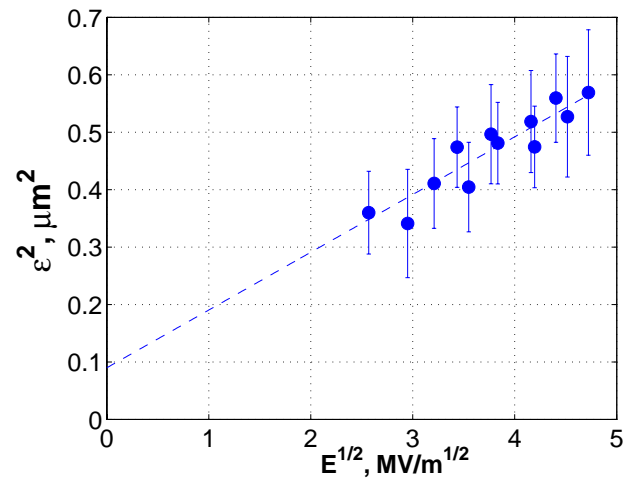


Figure 5: The fit yields:  $\epsilon_{th,x}^2 = 0.09 + 0.10\sqrt{E}$

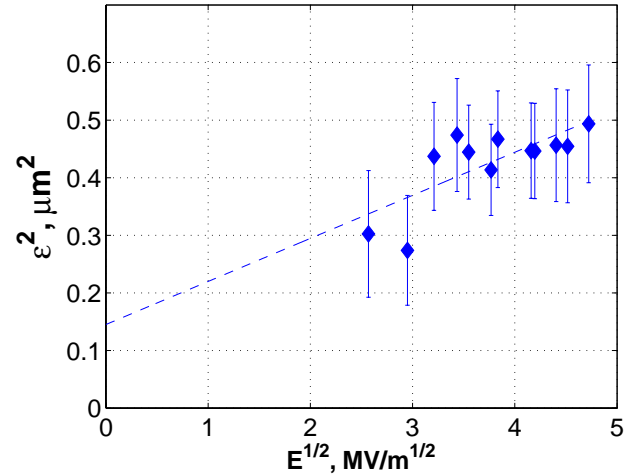


Figure 6: The fit yields:  $\epsilon_{th,y}^2 = 0.15 + 0.07\sqrt{E}$

## REFERENCES

- [1] F. Stephan et al., "Photo Injector Test Facility under construction at DESY Zeuthen", FEL'00, August 2000, Durham, North Carolina, U.S.A.
- [2] M. Krasilnikov et al., "Characterization of the Electron Source at the Photo Injector Test Facility at DESY Zeuthen", FEL'03, Sept, 2003, Tsukuba, Japan
- [3] Klaus Flöttmann, "Note on the Thermal Emittance of Electrons Emitted by Cesium Telluride Photo Cathodes", TESLA NOTE, 1997
- [4] R. A. Powell et. al., "Photoemission Studies of Cesium Telluride", Phys. Rev. B, 1973, 8
- [5] J-H. Han et al., "Emission mechanisms in a photocathode rf gun", PAC'05, May 2005, Knoxville, Tennessee, U.S.A.
- [6] K. Flöttmann, "A Space Charge Tracking Algorithm", <http://www.desy.de/~mpyflo>

# STATUS AND FIRST RESULTS FROM THE UPGRADED PITZ FACILITY

A.Oppelt\*, K.Abrahamyan†, G.Asova‡, J.Bähr, G.Dimitrov§, U.Gensch,  
 H.-J.Grabosch, J.H.Han, S.Khodyachykh, M.Krasilnikov, S.Liu, V.Miltchev, B.Petrosyan,  
 S.Riemann, L.Staykov, F.Stephan, DESY, 15738 Zeuthen, Germany  
 M.v.Hartrott, E.Jaeschke, D.Krämer, D.Lipka, F.Marhauser, D.Richter, BESSY, 12487 Berlin, Germany  
 K.Flöttmann, S.Schreiber, DESY, 22603 Hamburg, Germany  
 T.Garvey, LAL Orsay, 91400 Orsay, France  
 L.Catani, E.Chiadroni, A.Cianchi, INFN-Roma2, 00133 Roma, Italy  
 L.Palumbo, D.Alesini, M.Boscolo, G.Di Pirro, M.Ferrario, D.Filippetto, C.Vicario,  
 INFN-LNF, 00044 Frascati, Italy  
 P.Michelato, L.Monaco, C.Pagani, D.Sertore, INFN Milano, 20090 Segrate, Italy  
 V.Boccone, N.Pavel, Humboldt University, 12489 Berlin, Germany  
 V.V.Paramonov, INR Troitsk, 117312 Moscow, Russia  
 I.Tsakov, INRNE Sofia, 1784 Sofia, Bulgaria  
 G.Klemz, W.Sandner, I.Will, Max-Born-Institute, 12489 Berlin, Germany  
 W.Ackermann, W.F.O.Müller, S.Schnepp, T.Weiland, TU Darmstadt, 64289 Darmstadt, Germany  
 J.Rönsch, J.Roßbach, University of Hamburg, D-22761 Hamburg, Germany

## Abstract

Since December 2004, the photo injector test facility at DESY in Zeuthen (PITZ) has been upgraded. A normal conducting booster cavity has been installed and the diagnostics beamline was significantly modified. An extended water cooling system has been installed and was successfully taken into operation. Currently, the new diagnostics elements are being commissioned. Since the installation of the new 10 MW klystron in June/July, the gun is being conditioned towards higher peak and average power, and the whole beamline including the booster is being taken into operation. First results from the commissioning phase including gun and booster conditioning are reported.

## INTRODUCTION

The first phase of PITZ has successfully concluded in November 2003 with the full characterization of a gun that has been installed and is currently in operation at the VUV-FEL. In the year 2004, the gun was replaced, the PITZ1 setup has been improved, and the photo injector properties were optimized. The main results have been summarized in [1]. The PITZ1 facility stopped operation in November 2004 for a large upgrade of the water cooling system, the dismantling of the PITZ1 beamline, and the installation of the first diagnostics components that belong to the PITZ2 phase. Meanwhile, an intermediate setup (PITZ1.5, Fig. 1) was taken into operation with two main goals: (a) to run the gun at higher gradients with up to 60 MV/m, and

(b) to study the emittance conservation principle by using a booster cavity. In order to completely characterize the photo injector, the beamline will be continuously extended towards the final setup (PITZ2).

## COOLING UPGRADE

Since December 2004, the electrical power system as well as the water cooling system at PITZ have been upgraded in order to provide the necessary power and cooling for gun, booster, and two 10 MW klystrons. This is a basic precondition for doing high power gun tests and reaching a gradient of 60 MV/m as required for reaching the XFEL baseline parameters for beam quality.

Tests of this system have been done in July 2005 with maximum available power consumption, i.e. at power level of ~500 kW. Fine tuning of the parameters will happen when more cooling is needed (e.g. after the delivery of the second 10 MW klystron).

## 10 MW MULTI BEAM KLYSTRON

The 10 MW multi beam klystron from Thales has been delivered to Zeuthen on 9.6.05. During the first tests after its installation 10 MW at 1.2 ms rf pulse duration were reached when running on a load. In autumn, tests with longer rf pulses up to the design parameter (1.5 ms) are foreseen. For the moment, the currently reached parameters are sufficient for running the PITZ facility and doing high power tests of the gun.

The rf output of the 10 MW klystron is via two 5 MW arms. In order to combine the rf power from the two arms, a power combiner has been developed [2] and tested on a load up to two times 2.5 MW (5 MW combined) at a rf

\* presenting author: anne.oppelt@desy.de

† on leave from YERPHI, 375036 Yerevan, Armenia

‡ on leave from INRNE, 1784 Sofia, Bulgaria

§ on leave from INRNE, 1784 Sofia, Bulgaria

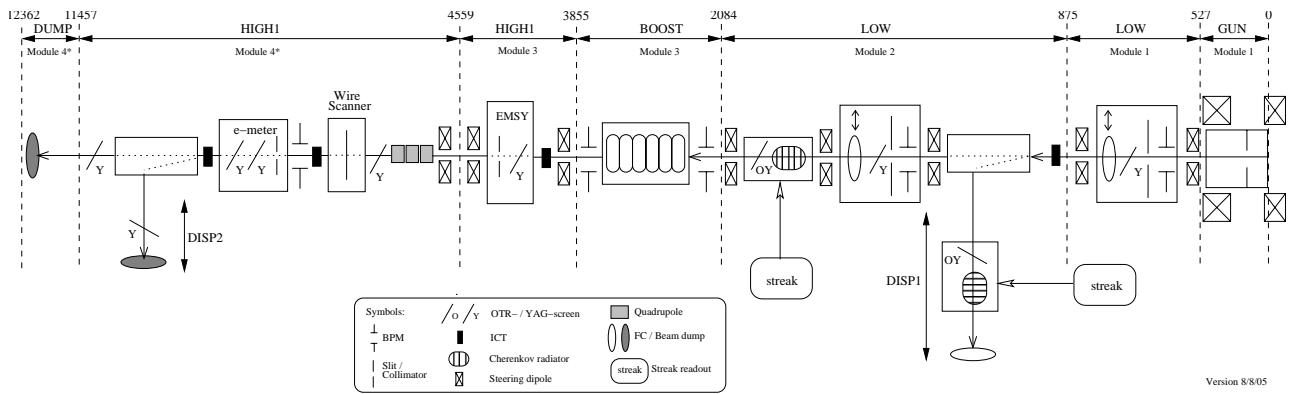


Figure 1: Scheme of the PITZ1.5 setup as it is currently realized.

pulse length of 200  $\mu\text{s}$  before its installation in the vacuum system of the PITZ gun.

The delivery of a second 10 MW klystron is foreseen for January 2006. Until then the booster is operated with the old 5 MW klystron.



Figure 2: Photograph of the power combiner.

## GUN CONDITIONING

After the power combiner has been installed at the gun, conditioning of power combiner and gun started on July 29, 2005 with the goal to reach a gradient of 60 MV/m in the gun: according to simulations, this is the necessary gradient to reach the XFEL emittance of  $0.9 \pi$  mm mrad. The conditioning is still ongoing. The following parameters have been reached so far: estimated input power of 4.3 MW at 10 Hz repetition rate with 100  $\mu\text{s}$  pulse length. In order to reach a gradient of 60 MV/m at the cathode, an input power of 6.7 MW is needed which requires still some conditioning.

## BOOSTER CONDITIONING

The preliminary booster cavity for PITZ is a normal conducting TESLA prototype cavity. It has been formerly used

with very short rf pulses and a maximum average power of 1.4 kW. Thus, only small cooling tubes are attached to the booster, limiting the use at PITZ to the same average power. The cleaning and tuning of the cavity has been done at Zeuthen in 2003/2004. A field flatness of 91 % and a maximum field imbalance of 6 % has been obtained, see Fig. 3.

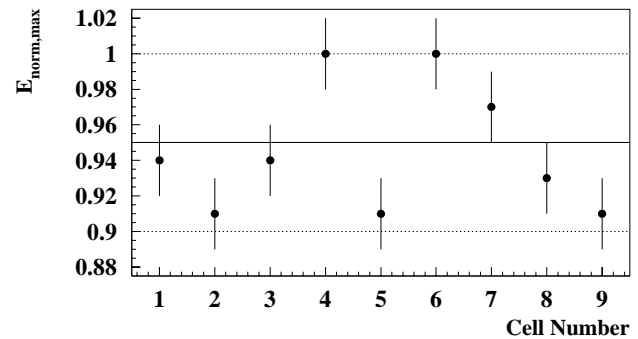


Figure 3: Field flatness obtained as a result of the booster tuning including measurement errors. The maximum field is normalized to 1. The average field is shown as full line.

In 2005, the booster has been fully conditioned at different repetition rates up to the cooling limit (maximum average power  $\sim 1.3$  kW, maximum peak power:  $\sim 3$  MW, table 1).

The reached maximum peak power of 3 MW corresponds to an average accelerating gradient of 16.4 MV/m which is far above the needed gradient of 12.5 MV/m (obtained with an input power of 1.7 MW).

Repetition rate (Hz)	10	5	2	1
Pulse length ( $\mu\text{s}$ )	50	85	250	500
Peak power (MW)	2.5	3.0	2.7	2.6
Mean power (kW)	1.25	1.27	1.32	1.29

Table 1: Maximum parameters obtained during the booster conditioning.

On August 11, the electron beam from the gun was accelerated through the booster for the first time and a mean momentum of 12 MeV/c was measured. Fig. 4 shows a more recent momentum measurement. More detailed studies of the field distribution and energy gain in the booster will follow in the run periods until the end of the year.

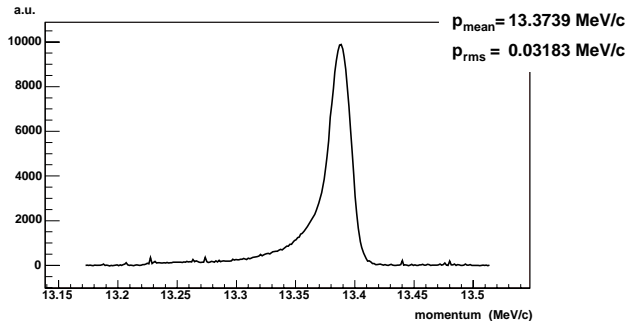


Figure 4: Measured momentum distribution after the booster. The momentum after the gun was 4.1 MeV/c.

## FACILITY OPERATION

In March 2005, the PITZ1 beamline was dismantled and the installation of the new diagnostics components according to Fig. 1 started. Commissioning of the diagnostics has been done in parallel to the booster conditioning and still continues. Since July 29, the facility is operated continuously: partly for gun conditioning, partly for beam measurements.

Apart from many other components, the new diagnostics beamline includes a movable emittance meter (e-meter) from LNF, which was temporarily installed at PITZ for beam tests and will be finally mounted at the SPARC facility in autumn 2005. The e-meter has been commissioned and first emittance measurements have been done with and without booster (i.e. at low and high energy). The measurements based on the slit mask technique have been compared with the data taken with the PITZ emittance measurement system (EMSY) [1] and a good agreement has been found. The cross-checks will continue until end of September. For more information on the e-meter see [3]. In addition to the beamline installation, an upgrade of the

laser happened: the laser system is now fully diode pumped and uses a different attenuation scheme which gives much more flexibility in choosing the charge while keeping the transverse and longitudinal laser profiles unchanged. The improvements related to laser and laser beamline are described in [4].

## PREPARATIONS FOR PITZ2

In autumn, the present beamline setup (PITZ1.5) will be extended and more diagnostics will be installed. Preparations towards the realization of the final setup (PITZ2) are continuing. A simplified scheme of the PITZ2 setup is shown in Fig. 5.

*Emittance measurement systems.* In a first step, the installation of three new emittance measurement systems at different distances from the cathode is planned for October. These systems, built by INRNE Sofia, are based on the slit mask technique. They allow characterizing the emittance evolution along the beamline, a necessary precondition for proving the emittance conservation principle and its experimental realization, one of the major goals of PITZ2. For cross-checking the emittance measurement results it is foreseen to use the quadrupole scan technique and the four screens method.

*High energy spectrometers.* The work on the design of two high energy spectrometers is in progress. For the first of them many different solutions were discussed. Fig. 6 shows two possible setups [5]. The big advantage of the system based on a 180° dipole magnet is the resolution control due to spot size changes on screen S1 using a quadrupole triplet placed in front of the dipole entrance [6].

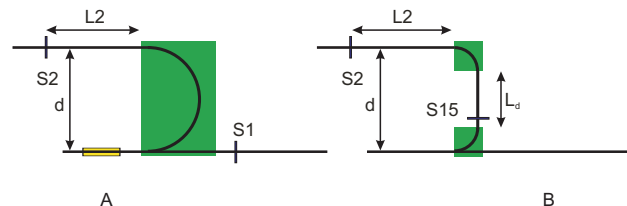


Figure 6: Two spectrometer setups under discussion. (A) A 180° dipole magnet followed by a drift space  $L_2$ . (B) Two 90° dipole magnets separated by a drift space  $L_d$  and followed by a drift space  $L_2$ .

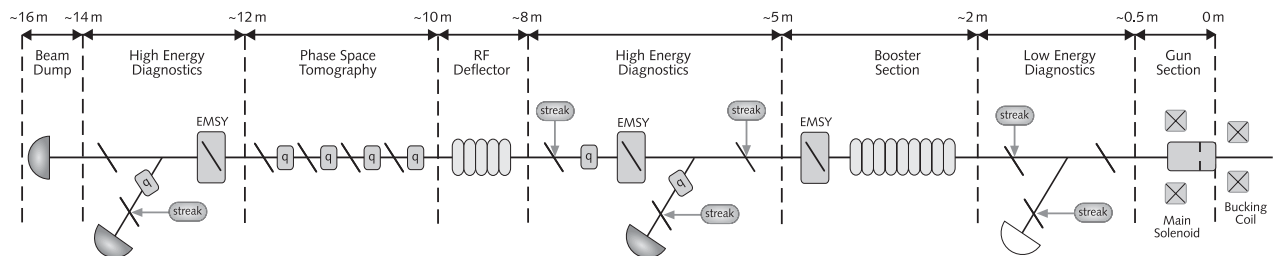


Figure 5: Preliminary layout scheme of the PITZ2 setup.

Due to space limitations in the PITZ tunnel and fabrication problems of this type of dipole, setup (B) is preferred: the  $180^\circ$  dipole magnet is split into two successive  $90^\circ$  magnets. By a proper choice of the bending radius and the distances  $d$  and  $L_2$  one can realize a system with a momentum resolution of about  $4 \cdot 10^{-4}$ , according to simulations. In this system, the resolution does not depend on the initial beam size but only on the initial beam divergence which can be additionally extracted from the measurements by comparing the beam spot sizes on screens S15 and S2.

*CDS Booster.* A booster cavity specially developed for PITZ has been designed [7] and is currently under construction at DESY in Hamburg. First rf measurements have been done with a couple of manufactured test cells. According to the time schedule, the CDS booster shall be installed in the PITZ facility by the end of 2006.

*Gun development.* The design of a new gun that can withstand higher power level is progressing. A first design of such a high gradient / high average power gun has been presented. Even if the cooling water distribution has been improved, recent simulations from BESSY show that still more cooling is needed, especially in the iris region.

## SUMMARY

The PITZ1 facility stopped operation in November 2004 for a large upgrade of the water cooling system, the dismounting of the PITZ1 beamline, and the installation of the first elements of the PITZ2 phase. A first 10 MW klystron was taken into operation and the commissioning of the PITZ1.5 setup has started. This includes full conditioning of a normal conducting booster cavity and first beam operation through the complete beamline. Preparations for the final PITZ2 setup are ongoing.

## ACKNOWLEDGEMENTS

The PITZ collaboration wants to thank the involved engineers and technical groups for their active engagement during the PITZ upgrade.

This work has been partly supported by the European Community, contract numbers RII3-CT-2004-506008 and 011935, and by the 'Impuls- und Vernetzungsfonds' of the Helmholtz Association, contract number VH-FZ-05.

## REFERENCES

- [1] A.Oppelt et al., The Photo Injector Test Facility at DESY Zeuthen: Results of the first phase, LINAC 2004, Lübeck, Aug.2004, p.375.  
F.Stephan et al., Recent results and perspectives of the low emittance photo injector at PITZ, FEL 2004, Trieste, Sept.2005, p.347.  
V.Miltchev et al., Modelling the Transverse Phase Space and Core Emittance Studies at PITZ, these proceedings (THPP041).
- [2] S.I. Sharamentov et al., Design of 10 MW L-Band Waveguide Transmission Line, Technical Design Report, PITZ internal report, 2000.
- [3] L.Catani et al., Commissioning of the SPARC Movable Emittance Meter and Its First Operation at PITZ, these proceedings (THPP073).
- [4] J.Bähr et al., Upgrades of the Photocathode Laser and Laser Beam-line at PITZ, these proceedings (MOPP034).
- [5] S.Khodyachykh, Comparison of dipole magnets, PITZ internal note 564.4, June 2005.
- [6] D.Lipka, Spectrometer design for the SRF Gun, BESSY internal note SRFgun-BESSY-003-12-2004.
- [7] V.Paramonov et al., The normal conducting booster cavity development for Photo Injector Test Facility, Technical Design Report, PITZ internal report, 2004.

## COMMISSIONING OF THE SPARC MOVABLE EMITTANCE METER AND ITS FIRST OPERATION AT PITZ

L.Catani, E.Chiadroni, A.Cianchi, INFN-Roma2, Via della Ricerca Scientifica 1, 00133 Roma, Italy  
 M.Castellano, G.Di Pirro, D.Filippetto, C.Vicario, INFN-LNF, Via E.Fermi 40, 00044 Frascati  
 (Rome), Italy

M.v.Hartrott, BESSY, 12487 Berlin, Germany

M.Krasilnikov, A.Oppelt, F.Stephan, DESY Zeuthen, Platanenallee 6, 15738 Zeuthen, Germany

### Abstract

For the SPARC Project a novel diagnostic device, called "Emittance-meter", has been conceived and constructed to perform a detailed study of the emittance compensation process in the SPARC photo-injector and to optimize the RF-gun and the accelerator working point. It consists of a movable emittance measurement system, based on the 1D pepper-pot method, installed between two long bellows with the possibility to scan a region 1.2 m long downstream the RF-gun. The construction of the device was completed in the first part of this year and a series of laboratory tests, to evaluate its performances, were carried out in Spring 2005. At the beginning of the summer the complete system was moved to DESY at Zeuthen to be installed on the Photo Injector Test Facility PITZ. After the commissioning it will be used for measurements of the PITZ electron beam in the framework of collaboration between the SPARC and PITZ Projects aiming on studies and operations with photo injectors.

### INTRODUCTION

The "SPARC emittance meter" ("SPARC e-meter" shortly) is a diagnostic device designed for a detailed analysis of the beam dynamics in the region of the SPARC injector where a significant evolution of transverse emittance occurs [1].

Design of SPARC e-meter has been optimized with respect to the design parameters of the SPARC electron beam, namely energy, nominal transverse emittance and size, charge per bunch etc. [2].

The construction of the device was completed in the first part of this year while the beam studies of SPARC Injector with the e-meter are scheduled for the end of 2005.

The evidence of a temporal gap between the completion of the e-meter and its first scheduled operations at SPARC suggested the possibility of a temporary installation at DESY Zeuthen for a round of measurements of the PITZ electron beam in the framework of a collaboration aiming on studies and operations with photo injectors.

To permit the installation of the SPARC e-meter at PITZ we modified the original design of the system to ensure its mechanical compatibility.

Before its shipment to DESY Zeuthen a number of test of the e-meter have been carried out to verify its performance and calibrate the components.

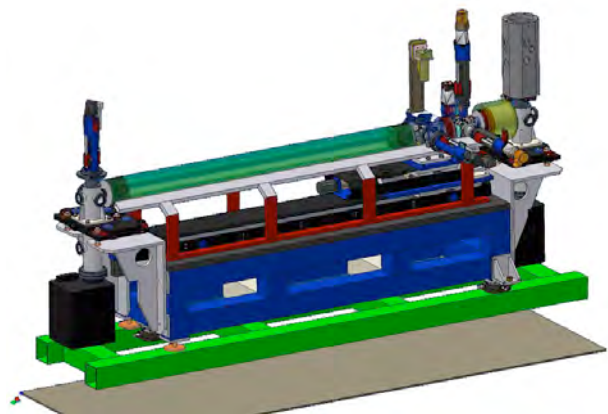


Figure 1. 3D mechanical drawing of the SPARC e-meter. In this drawing are also included one of the two alignment tools, to be installed during alignment on top of the end flanges (grey cylinders), and the PITZ girder (green structure).

### TESTS AND EVALUATION OF PERFORMANCE

#### Slits Mask

For the measurement of the emittance in the horizontal and vertical planes using the *1D pepper-pot method* we have two slit masks, mounted on two independent holders 90° with respect to each other. Each slits mask is assembled stacking single pieces made of 2 mm thick tungsten with a well defined profile. Once assembled these pieces form a mask with, in the upper part, two single slits 50 $\mu\text{m}$  and 100 $\mu\text{m}$  respectively and, in the lower part, an array of 7x50  $\mu\text{m}$  slits separated by 500 $\mu\text{m}$ .

The single slits will be used for multi-shot measurements, scanning transversally the beam and collecting together the images from different positions.

In 2004 a first prototype of slits mask has been realized precisely machining a tungsten piece, and removing in the central part 50  $\mu\text{m}$ , or 100  $\mu\text{m}$ , of metal. A preliminary analysis using a profile projector showed that agreement of average measured widths, with respect to the nominal value, was better than 5 $\mu\text{m}$  for 7 over 9 of the slits produced, thus compatible with the needed tolerances.

Nevertheless, a more accurate analysis with an optical microscope evidenced that while the average width was within the tolerances, irregularities of the profile due to roughness of edges might locally exceed, in some cases, 10% of the nominal width.

An alternative method for the preparation of slits we investigated is photo-chemical machining. Optical analysis of slits produced using this method showed higher uniformity of the slits and improved smoothness of edges consequence of the more precise etching process. It also eliminates irregularities produced by machining, due to the mechanical stress of material (Fig.2).

### *Screens and imaging system*

The transverse distribution of low-charge beamlets emerging from the slit-mask needs to be measured with high accuracy.

It means that radiator screens, used for this purpose, need to have a linear response with beam charge in the range of few tenths of pC and they must guarantee a spatial resolution better than 20  $\mu\text{m}$ .

Same performance are required from the imaging system that should not introduce any degradation to the figure above.

Doped-YAG radiators, either crystals or sintered screens, are good candidates because of their high resolution and efficiency.

For our application, we focused our attention on Ce:YAG radiators that we tested at the DAFNE Beam Test Facility.

We collect forward radiation emitted from Ce:YAG crystal with a mirror at 45° downstream the radiator. As result the radiator is observed at 90° with respect to the rear face thus minimizing the degradation of spatial resolution due to the non-negligible thickness of transparent crystal.

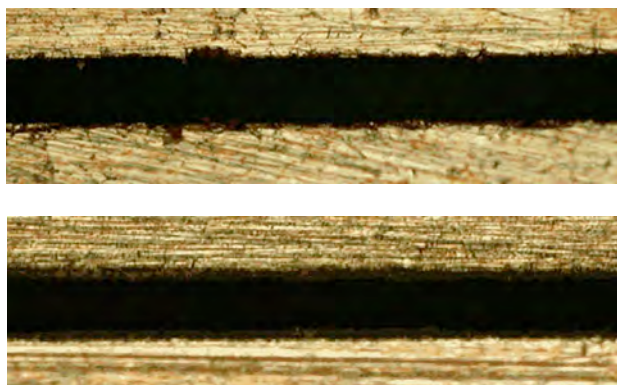


Figure 2. Optical microscope pictures of the single-slit obtained by mechanical machining (top) compared to single-slit produced by photo-chemical machining (bottom).

The performance of the Ce:YAG radiator has been compared to those of a Cr-oxide radiator used by our group in previous applications.

Both radiators have been installed at the same diagnostic station in the DAFNE Beam Test Facility and their performances measured under different beam conditions, within the range of values expected in the SPARC injector.

Analysis of results shows that performances of the Ce:YAG screen are superior: efficiency is a factor 2-3 higher than Cr-oxide and resolution is evidently better, as we can observe comparing the two pictures on Fig.3. At the same time we didn't report any evidence of a deviation from a linear correlation between the light yield from the two radiators varying the charge density of the beam in the range of values expected in the SPARC injector. This confirms a good linearity of the Ce:YAG radiator with charge density in the range of values of interest.

Imaging system includes a digital CCD cameras (Basler 311f) and a 105mm "macro" type objective from SIGMA. In the current set-up, the magnification, and the correspondent resolution, has been chosen to better adapt to the PITZ beam size. Being the distance of CCD from the object (the radiator surface) 300 mm, we calculated a magnification of 1:1.7 and the resolution of the optical system has been measured to be 17,2  $\mu\text{m}$  (Fig.4). It's worth to mention that tests of the imaging system previously made in our laboratory shown that a resolution better than 11  $\mu\text{m}$  can be achieved.

The digital cameras are connected to the e-meter control system by means of their built-in firewire (IEEE1394) interface that can be used for both images read-out and control of the camera settings.

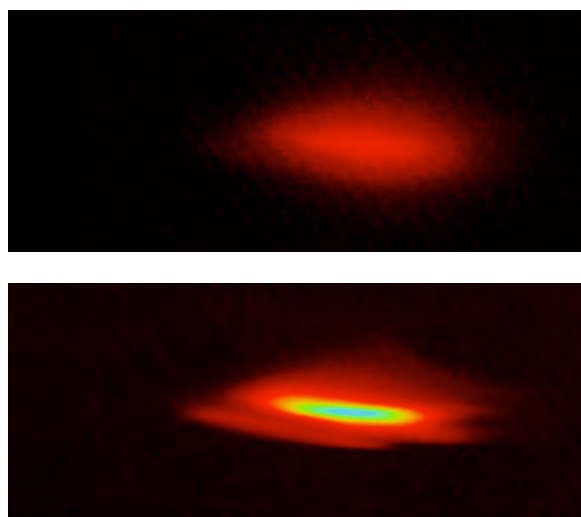


Figure 3. Electron beam imaging using Cr-oxide (top) and Ce-doped YAG radiators (bottom). Electronic gain of the CCD camera was approximately three times higher in the case of Cr-oxide screen to get comparable pixel values with the Ce:YAG.

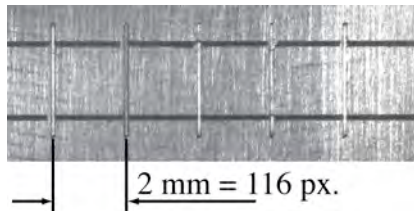


Figure 4. On-line measurement of resolution of the optical system can be done using the calibration marks on the screen holder.

In SPARC the digital cameras of the e-meter will be part of a larger system including those needed for other optical diagnostic stations.

It will be based on the solutions developed for the TTF VUV-FEL large camera system [3].

### *Motors and Actuators*

Motors and actuators are other important components of the SPARC e-meter. Linear actuators with stepper motors are used to control the insertion of screens and slits mask into the beamline. A differential encoder and a reference end switch guarantee reproducibility and accuracy of the movement, the latter being better than  $2\mu\text{m}$ . This value is compatible with resolution needed for multi-shot measurement using a single slit.

More powerful brushless motors are used to move longitudinally the complete measurement system located between the two long bellows and to change the distance between the two crosses housing the slits mask and the screen.

Absolute position of linear movements can be obtained by, or checked with, the value given by position transducer potentiometers.

The cross housing the two slits mask can be tilted around both x and y-axes to adjust the alignment of the slits with respect to the beam direction. A stepper motor having 200 steps per turn moves each stage.  $\mu$ -step movement is also possible (256  $\mu$ -steps per step).

Resolutions and accuracy of these movements have been tested and results obtained ( $\Delta\theta < 2.5 \mu\text{rad}$ ) are compatible with the needed resolution of the rotational movement. Improvements are also possible by fine-tuning the assembly of mechanical components.

## **OPERATIONS AT PITZ**

The original design of the SPARC emittance meter has been partially modified during the construction to permit its installation in the Photo Injector Test Facility PITZ at DESY Zeuthen. Mainly the table, being the support for the beamline, was modified by shortening its legs to allow installation on top of the PITZ girder. Legs extenders have been prepared and they will be used to adjust the height of the “modified” e-meter to that needed for SPARC. Furthermore we ensured mechanical compatibility between SPARC e-meter and PITZ vacuum beamline.

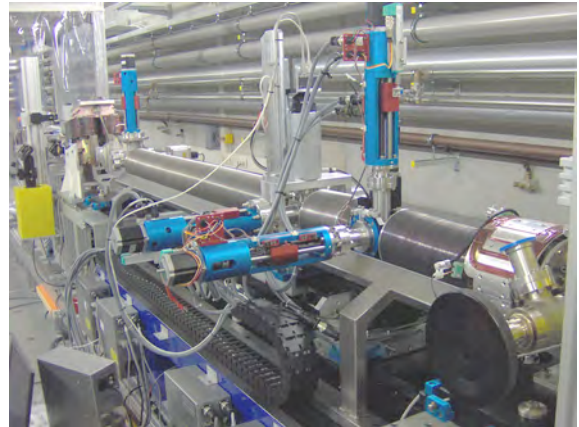


Figure 5. SPARC e-meter during installation at the Photo Injector Test Facility PITZ.

Alignment tools and procedures have been jointly defined.

The SPARC e-meter has been installed in the last section of the upgraded PITZ beamline [4], in the space located after the booster, before the electron beam spectrometer (Fig. 5).

The SPARC e-meter has its own control and acquisition system. Two PCs have been installed in the PITZ control room to run control panels and measurements programs. Motors are controlled via CAN bus or RS232 serial interfaces. PCs running control panels communicate with motor controllers via network using a network serial-port server. To connect a PC in the control room with digital cameras in the accelerator tunnel, because of limitation of the maximum cable length (4.5 meters), we used a fiber-optic firewire extender.

Magnetic steerers are installed at the beginning of the system, clamped around the upstream flange. They can be used to adjust the direction of the electron beam in the x and y plane.

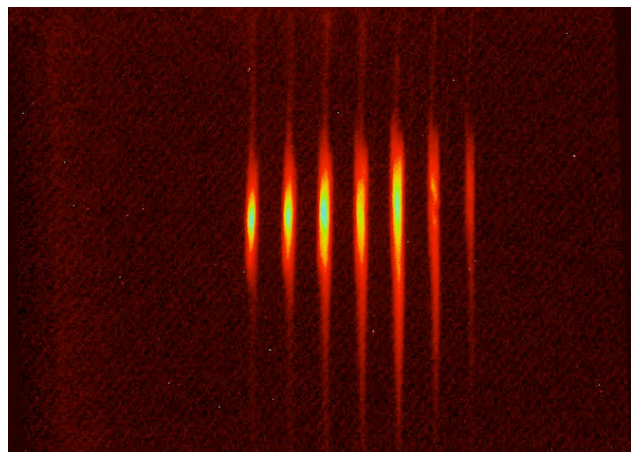


Figure 6: Picture of the beam at the YAG screen downstream the multi-slit mask.

Installation of the SPARC e-meter was completed in the beginning of July 2005 and commissioning started. Two rounds of commissioning and measurements shifts have been scheduled for the SPARC e-meter in the PITZ shift plan for July and August 2005.

The first days of operations have been dedicated to the optimization of components and to fix minor problems.

In the last part of that two-weeks shift characterization of the e-meter with low-energy beam started. We verified the reproducibility of measurements under different beam conditions and studied the strategies for the optimization of the measurements, e.g. adjusting the distance between the slits mask and the screen (Fig.6).

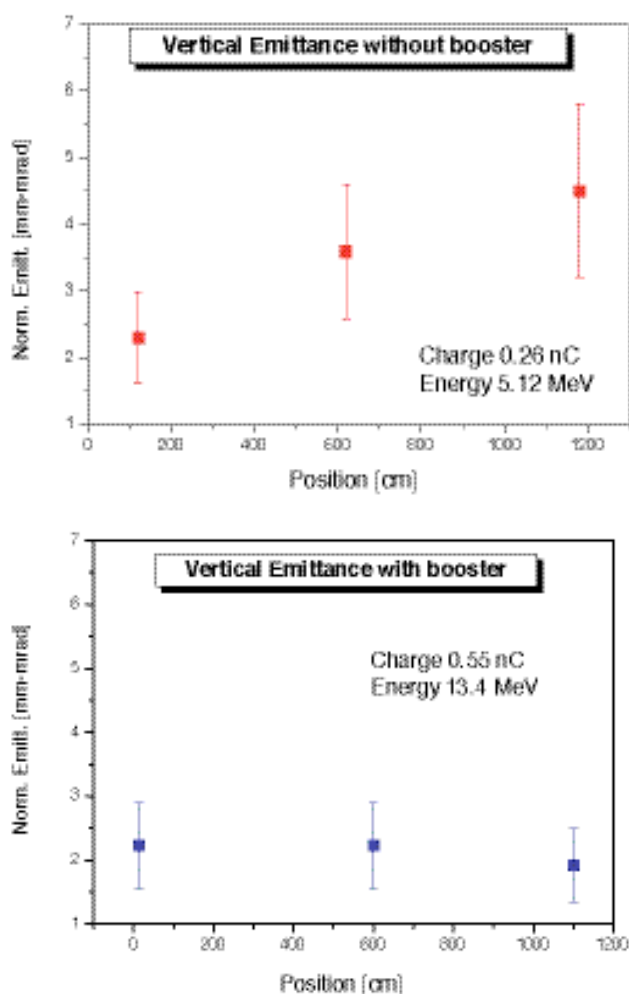


Figure 7: Preliminary result of vertical emittance measurements at PITZ with the SPARC e-meter under different conditions (booster off/on). Note that the three z-positions are not coincident in the two cases; also the beam charge is not identical.

Although the injector parameters and the transport of the beam are not yet optimized since commissioning of the upgraded PITZ facility is still in progress, preliminary measurements confirm the value of transverse emittance, as expected for the current injector settings, and its variation along the beamline. As an example we report the

measurements of the vertical emittance at three different positions along the e-meter (Fig.7). The measurements show a constant increase of the vertical emittance as function of longitudinal position in the case with booster off while for the higher energy beam accelerated by the booster the value stays almost constant (within the measurement errors). These results are in good agreement with simulations for the current injector settings [5].

## CONCLUSION

Construction of the SPARC Emittance-meter has been completed and it has been successfully commissioned at Photo Injector Test Facility PITZ in July 2005. Laboratory tests carried out at INFN-LNF before its shipment to DESY Zeuthen confirmed that design performances have been achieved.

Although the commissioning of the upgraded PITZ facility is still ongoing, preliminary emittance measurements have been obtained and show a good agreement with simulations for the current injector settings.

Operations with SPARC e-meter at PITZ are in progress and they will continue until the device will be shipped back to Frascati, in early Fall 2005, to be used for the measurements at the SPARC photo injector.

## Acknowledgements

Authors wish to thank all scientists and engineers of the SPARC collaboration that contributed to the design and commissioning of the emittance meter and all those at DESY Zeuthen that contributed to its installation and operation at PITZ.

Especially, we thank V. Lollo for his contribution to the mechanical design and engineering of the SPARC e-meter, F.Anelli and S. Fioravanti for their work with motor controllers and C.Ligi of INF-LNF for the design and calibration of magnetic steerers.

We also thank L.V.Vu, A.Donat, F.Tonisch for the preparation and installation at PITZ, and J. Bähr, S. Khodyachykh, V. Miltchev, J. Rönsch and L. Staykov for the support during the shifts.

This work has been partially supported by the EU Commission in the sixth framework programme, contract no. 011935 EUROFEL-DS1.

## REFERENCES

- [1] D. Alesini *et al.*: "Status of the SPARC Project", Proceedings of PAC2005, Knoxville, Tennessee, USA.
- [2] A. Cianchi *et al.*, "Design study of a movable emittance meter device for the SPARC photoinjector", Proceedings of EPAC04, Lucern (Switzerland) 2004
- [3] L. Catani *et al.*, "A Large Distributed Digital Camera System for Accelerator Beam Diagnostics", Rev. Sci.Instr. 76, 073303 (2005)
- [4] A.Oppelt *et al.*, "Status and First Results from the Upgraded PITZ Facility", these proceedings
- [5] M.Ferrario *et al.*, "Conceptual Design of the TESLA XFEL Photoinjector", TESLA-FEL 2001-03